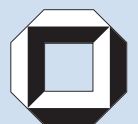


Imke Ludwig

Drying, Film Formation and Open Time of Aqueous Polymer Dispersions

An Investigation of Different Aspects
by Rheometry and Inverse-Micro-Raman-
Spectroscopy (IMRS)



Imke Ludwig

**Drying, Film Formation and Open Time
of Aqueous Polymer Dispersions**

An Investigation of Different Aspects by Rheometry
and Inverse-Micro-Raman-Spectroscopy (IMRS)

Drying, Film Formation and Open Time of Aqueous Polymer Dispersions

An Investigation of Different Aspects by Rheometry
and Inverse-Micro-Raman-Spectroscopy (IMRS)

by
Imke Ludwig



universitätsverlag karlsruhe

Dissertation, Universität Karlsruhe (TH)

Fakultät für Chemieingenieurwesen und Verfahrenstechnik, 2008

Impressum

Universitätsverlag Karlsruhe
c/o Universitätsbibliothek
Straße am Forum 2
D-76131 Karlsruhe
www.uvka.de



Dieses Werk ist unter folgender Creative Commons-Lizenz
lizenziert: <http://creativecommons.org/licenses/by-nc-nd/2.0/de/>

Universitätsverlag Karlsruhe 2008
Print on Demand

ISBN: 978-3-86644-284-9

Drying, Film Formation and Open Time of Aqueous Polymer Dispersions

**-An Investigation of Different Aspects by Rheometry
and Inverse-Micro-Raman-Spectroscopy (IMRS)-**

Zur Erlangung des akademischen Grades eines

Doktors der Ingenieurwissenschaften (Dr.-Ing.)

der Fakultät für Chemieingenieurwesen und Verfahrenstechnik der
Universität Fridericiana Karlsruhe (Technische Hochschule)

genehmigte

Dissertation

von

Dipl.-Ing. Imke Ludwig
geboren in Berlin-Wilmersdorf

Tag des Kolloquiums:	8. Juli 2008
Referent:	Prof. Dr.-Ing. Matthias Kind
Korreferent:	Prof. Dr. Norbert Willenbacher

Preface

This thesis is the final work of my Ph.D. study at the Institute of Thermal Process Engineering at the University of Karlsruhe (TH), which has been made from fall 2002 until spring 2007. The project is the result of a longlasting cooperation with the Rhodia Research and Technology Centers in Aubervilliers and Lyon (France): I started working on the new project entitled “Drying and Film Formation of Aqueous Dispersion Formulations” in October of 2002. It required the use of the measurement technique of Inverse-Micro-Raman-Spectroscopy (IMRS) that was brought to the institute by Wilhelm Schabel shortly before. By the success of the IMRS-technique, the research group grew to a size of ~4-5 PhD students.

What I present in the following chapters is the result of the work that I did together with students, technicians and other colleagues. I like to use this to thank all the people who contributed to this work, and my colleagues who created a pleasant and inspiring atmosphere to work in. I very much enjoyed working in Karlsruhe and in the Raman group.

First of all, I thank Prof. Dr.-Ing. Matthias Kind. He has been a very stimulating advisor who gave me a lot of freedom. It was very motivating that he was as excited about the research as I was. I am very grateful for setting up the long-lasting cooperation with Rhodia (France), that enabled this very interesting project. Besides, he gave me the opportunity to participate regularly in international conferences.

I would also like to thank Prof. Dr. Norbert Willenbacher for his interest in this project and for serving as a second censor for this work.

During my Ph.D. work, Dr.-Ing. Wilhelm Schabel became a second Ph.D. advisor for me. I would like to thank him for the many discussions and important suggestions concerning the progress of my work.

I enjoyed being the advisor of a number of students: I like to thank Peter Demarez and Jason Chan, for the excellent work during their diploma theses and also Özgül Gedikli and Karsten Pabst for their hard work during their seminar theses. Natalia Bylik, Markus Wetzels and Steffen Waglöhner must be mentioned because of the great job they did to obtain experimental results when working as a student researcher. Thank you for the good collaboration and the excellent results that were essential for the success of this work.

Many other colleagues in Karlsruhe contributed to this work with help, critical questions, stimulating discussions, and being friends during and after work. I would like to mention Gisela Schimana, Prof. Dr.-Ing. Holger Martin, Prof. Dr.-Ing. Ernst-Ulrich Schlünder, Prof. Dr.-Ing. Volker Gnielinski and Lothar Eckert who must be named in connection with the day-to-day work at the institute. The support from several technicians in our institute has been indispensable for getting results.

Especially I want to mention Patrick Ferlin, Jean-Christophe Castaing and Philippe Olier of Rhodia (France) and would like to say thank you for the scientific discussions in Paris, Lyon and in Karlsruhe.

Most notably, I like to thank my parents for always following and supporting my work with great interest.

Table of Contents

Symbols and Abbreviations	VII
1 Introduction	1
1.1 Introduction	1
1.2 State of the Art	3
1.3 Aim of this Work/Investigated Aspects	8
2 Aqueous Polymer Dispersions	11
2.1 Latex Dispersions	11
2.1.1 Composition	11
2.1.2 Investigated Dispersions	12
2.2 Polyurethane (PU) Emulsions	15
2.2.1 Composition	15
2.2.2 Emulsion Preparation	15
3 Rheology of Polymer Dispersions	17
3.1 Rheological Characteristics of Concentrated Polymer Dispersions	17
3.1.1 Viscoelastic Properties	18
3.1.2 Liquid-Solid Transition and Gelation	19
3.1.3 The Cox-Merz Rule	20
3.1.4 Theoretical Description of the Viscosity Function	20
3.1.5 Mean Particle Separation and Polymer Volume Fraction	24
4 Mechanism of Film Formation	27
4.1 Latex Dispersions: Film Formation by Physical Driving Forces	27
4.1.1 The Different Stages of Film Formation	27
4.1.2 The Driving Forces for Film Formation	29
4.2 PU Emulsions: Film Formation by Chemical Crosslinking	29
4.3 Horizontal Inhomogeneous Drying	31
5 Local Concentration Measurements (by IMRS)	33
5.1 Experimental Setup	33
5.1.1 Air Conditioning	33
5.1.2 Inverse-Micro-Raman-Spectrometer (IMRS)	34
5.2 Spectra Calibration	35
5.2.1 Raman Spectra of Relevant Components	35
5.2.2 Concentration Measurements	38
5.2.3 Spectra Evaluation	40

5.3	<i>Signal Intensity Loss by Scattering in Polymer Dispersions</i>	42
5.3.1	Particle Size Effect.....	45
5.3.2	Solid Content of the Dispersion.....	48
5.3.3	Appraisal of these Effects on the Quantitative Data Evaluation	48
6	Model Calculations	53
6.1	<i>Film Leveling</i>	53
6.2	<i>Film Drying</i>	55
6.2.1	Mass Transport in the Gas Phase (Constant-Rate-Model)	56
6.2.2	Water Sorption and Phase Equilibrium	56
6.2.3	Water Diffusion in the Film.....	57
6.2.4	Mathematical Description of Drying (Vertical Direction)	58
6.2.5	Mathematical Description of Drying (Horizontal Direction).....	61
7	Results and Discussion	65
7.1	<i>Rheology of Aqueous Latex Dispersions</i>	65
7.1.1	Rheological Investigation of the Concentrated Dispersions.....	65
7.1.2	Rheological Properties as a Function of the Water Content X.....	68
7.1.3	Viscosity Functions.....	71
7.1.4	Liquid-Solid Transition.....	72
7.1.5	Influence of Additives on the Rheological Properties.....	74
7.1.6	Investigation of Film Leveling	78
7.1.7	Influence of Additives on the Leveling of AS-H-1a	81
7.1.8	Conclusions on Dispersion Rheology and Film Leveling	82
7.2	<i>Water Evaporation and Film Drying</i>	82
7.2.1	Parameters Necessary to Describe Drying	83
7.2.2	Film Drying Experiments using Inverse-Micro-Raman-Spectroscopy	88
7.2.3	Homogeneous Drying in Vertical Direction of the Film.....	89
7.2.4	Influence of Different Drying Parameters on the Evaporation Rate	91
7.2.5	Inhomogeneous Drying in Horizontal Direction of the Film	92
7.2.6	Drying of Polymer Solutions	102
7.3	<i>Irreversible Particle Contact and Particle Deformation</i>	104
7.3.1	Redispersion Experiments using IMRS.....	105
7.3.2	2-Film-Experiments using IMRS.....	107
7.3.3	Conclusions on Particle Contact and Deformation.....	108
7.4	<i>Particle Coalescence and Film Ageing</i>	109
7.4.1	Surfactant Distribution in Vertical Direction of the Dry Film	109
7.4.2	Water Permeation in the Dry Film.....	111
7.4.3	Conclusions on Particle Coalescence and Film Ageing	114
7.5	<i>The Influence of Pigments on Drying and Film Formation</i>	114
7.5.1	Conclusions on the Influence of Pigments	116

7.6	<i>Influence of Additives on Drying and Film Formation</i>	117
7.6.1	Plasticizer (Texanol TM)	117
7.6.2	Surfactant (Sodium-Dodecyl-Sulfate, SDS)	125
7.7	<i>Aqueous Polyurethane (PU) Dispersions</i>	126
7.7.1	Water Concentration in Vertical Direction of the Film during Drying ..	126
7.7.2	Inhomogeneities in the Dry Film	127
7.7.3	Chemical Crosslinking	131
7.7.4	Water Permeation in Fully Crosslinked PU Films	133
7.7.5	Conclusions on PU Dispersions	134
8	Conclusions	135
8.1	<i>Summary</i>	135
8.2	<i>Outlook</i>	140
9	References	143
9.1	<i>Publications in Connection with this Work</i>	148
9.2	<i>Proceedings</i>	148
9.3	<i>Student's Theses</i>	149
Appendix I	Emulsion Polymerization	151
Appendix II	Dispersion Stabilization	153
Appendix III	Latex Dispersion Characteristics	159
1)	<i>Particle Size</i>	159
2)	<i>Glass Transition Temperature T_g</i>	160
3)	<i>Particle Volume Fraction ϕ</i>	160
4)	<i>Average Particle Separation in the Original Dispersion</i>	163
5)	<i>Surface Tension of the Dispersion</i>	163
6)	<i>Static Contact Angle</i>	165
7)	<i>Summary of the Characteristic Dispersion Parameters</i>	166
Appendix IV	Theoretical Basics of Rheology	173
1)	<i>Elastic Solids</i>	173
2)	<i>Viscous Fluids</i>	174
3)	<i>Linear Viscoelasticity</i>	175
4)	<i>Theoretical Basics of Rheometry</i>	176
5)	<i>Experimental Setup for the Rheological Measurements</i>	178

Appendix V	Driving Forces of Film Formation	181
1)	<i>“Dry Sintering” (Dillon, Matheson, Bradford (1951))</i>	<i>181</i>
2)	<i>“Wet Sintering“ and Capillary Forces (Brown (1956))</i>	<i>181</i>
3)	<i>„Skin Formation“ (Sheetz (1965))</i>	<i>183</i>
Appendix VI	Microscopy and Spectroscopy	185
1)	<i>Light Diffraction and Optical Resolution</i>	<i>185</i>
2)	<i>Light Refraction and Depth Resolution</i>	<i>186</i>
3)	<i>Spectroscopy</i>	<i>191</i>
Appendix VII	Mass Transfer: Gasphase.....	199
Appendix VIII	Parameter Equations	201
1)	<i>Antoine Equation for Water</i>	<i>201</i>
2)	<i>Fuller Equation.....</i>	<i>201</i>
Appendix IX	Sorption Theories.....	203
1)	<i>Localized Sorption Theories</i>	<i>203</i>
2)	<i>Dissolution Theories</i>	<i>207</i>
3)	<i>Water Sorption: Fitting Parameters.....</i>	<i>208</i>
Appendix X	Saturated Salt Solutions	209
Appendix XI	Diffusion Coefficients in Latex Films.....	211
Appendix XII	Influence of Different Drying Parameters.....	213
Appendix XIII	Viscosity Models.....	217
Appendix XIV	Characteristic Raman Peaks.....	219
1)	<i>Saturated Hydrocarbons (s = strong; m = medium; w = weak).....</i>	<i>219</i>
2)	<i>Olefins (s = strong; m = medium; w = weak).....</i>	<i>219</i>
3)	<i>Hydroxy Groups (s = strong; m = medium; w = weak)</i>	<i>219</i>
4)	<i>Amines, Amids, Ammonium Salts and Mercaptans (b = broad).....</i>	<i>220</i>
5)	<i>Carbonyl Groups (sat. = saturated; aryl = aryl).....</i>	<i>220</i>
6)	<i>Carbon-Carbon Double-Bonds in Aromatic Molecules.....</i>	<i>220</i>
7)	<i>Ether Groups</i>	<i>221</i>
8)	<i>Bonds with Sulfur, Nitrate and Phosphate</i>	<i>221</i>

Symbols and Abbreviations

(I) Latin Letters:

a	particle radius	m
a_w	water activity	-
A	area	m^2
	<i>Einstein</i> parameter	-
A_H	<i>Hamaker</i> constant	J
b	empirical constant	-
c	velocity of light ($2.9979 \cdot 10^8$)	m/s
c_i	concentration of component i	kg/m^3
C	empirical constant	-
	detector efficiency	-
c.o.g.	center of gravity	m
d.o.f.	depth of focus	m
d	particle diameter	m
	distance	m
d_w	diameter of focal tube	m
E	elastic modulus (<i>Young</i> modulus)	N/m^2
	electrical field	N/C
f	focal distance	m
F	<i>Faraday</i> constant ($9.648 \cdot 10^7$)	-
	force	N
	projected area	m^2
g	gravity constant (9.81)	m/s^2
G	shear modulus	N/m^2
	relaxation modulus	N/m^2
	<i>Gibbs</i> enthalpy	J
G_i	weighting factor	N/m^2
G'	storage modulus	N/m^2
G''	loss modulus	N/m^2
h	<i>Planck</i> constant ($6.626 \cdot 10^{-34}$)	J s
	specific enthalpy	J/kg
	mean particle separation	m
	film height	m
H	nearest distance of particles	m
	enthalpy	J
I	intensity of radiation	W/m^2
k	<i>Boltzmann</i> constant ($1.381 \cdot 10^{-23}$)	J/K
	self-crowding factor	-
	constant	-

K	calibration constant	-
K_S	<i>Stefan</i> correction term	-
L	characteristic length	m
m	ratio of the radii of the objective (r/r_{\max})	-
	mass	g
\dot{m}_i	specific mass flow of component i	kg/m ² s
M	torque	Nm
\tilde{M}_i	molar mass of component i	kg/mol
n	ratio of refractive indices	-
	number of moles	mol
n_i	refractive index of component i	-
\dot{n}_i	specific molar flow of component i	mol/m ² s
N	number of molecules in a sampling volume	-
N_A	<i>Avogadro</i> constant ($6.023 \cdot 10^{23}$)	mol ⁻¹
NA	numerical aperture	-
p	pressure	Pa
p_i	partial pressure of component i	Pa
p_i^*	vapour pressure component i	Pa
P	number of scattering centers at the particle surface	-
r	radius/distance in radial direction	m
\tilde{R}	universal gas constant (8.314)	J/Kmol
Re	<i>Reynolds</i> number	-
s	constant	-
S	entropy	J/K
Sc	<i>Schmidt</i> number	-
Sh	<i>Sherwood</i> number	-
t	time	s
T	temperature	K
T_g	glass transition temperature	K
T_{mfft}	minimum film formation temperature	K
u	velocity	m/s
v	velocity	m/s
v_0	particle volume	m ³ /mol
v_f	free volume	m ³ /mol
V	volume	m ³
V_0	surface potential	mV
V_A	attractive potential energy	J
V_R	repulsive potential energy	J
V_S	<i>Stern</i> potential	mV
x	length	m
x_i	mass fraction in the liquid phase	-
\tilde{x}_i	molar fraction in the liquid phase	-

X_i	content of solvent i in the polymer	-
y	length	m
\tilde{y}_i	molar fraction of i in the gas phase	-
z	direction normal to the film surface	m
z_i	charge number of i	-
z_1	nominal position of the laser focus	m
z_2	true position of the laser focus	m
(II) Greek Letters:		
α	angle	-
	leveling rate	m/s
	polarization	C^2m^2/N
$\bar{\alpha}(\tilde{\nu}_0)$	average molecular polarizability	C^2m^2/N
$\beta_{w,g}$	binary mass transfer coefficient of water in air	m/s
γ	shear strain	-
	deformation	-
γ_i	activity coefficient of component i	-
$\dot{\gamma}$	shear rate	1/s
δ	phase angle	-
	surface disturbance	m
δ_{ji}	diffusion coefficient	m^2/s
Δ	thickness of adsorbed monolayer	m
$\Delta\alpha(\tilde{\nu}_0)$	anisotropic molecular polarizability	C^2m^2/N
$\Delta\tilde{\nu}_k$	vibrational wavenumber	cm^{-1}
ε	relative dielectric constant	-
	strain	-
ε_0	electric field constant ($8.854 \cdot 10^{-12}$)	F/m
ε_λ	extinction coefficient	-
ϕ	particle volume fraction	-
ϕ_c	critical particle volume fraction	-
ϕ_{eff}	effective particle volume fraction	-
ϕ_{max}	maximum particle volume fraction	-
Φ	filling factor of an optical lense	-
η	dynamic viscosity	kg/ms
η_0	dynamic viscosity of aqueous medium	kg/ms
η_r	relative viscosity	-
$[\eta]$	intrinsic viscosity	-
φ	contact angle	-
	relative humidity	-
	volume fraction (water)	-
κ^{-1}	<i>Debye-Hueckel</i> screening length	m
λ	relaxation time	s

λ	disturbance wavelength	nm
	spacing of brushmarks	m
	factor	-
μ	reduced mass	-
	dipole moment	Cm
ν	kinematic viscosity	m ² /s
	frequency of oscillation	cm ⁻¹
$\tilde{\nu}_0$	wavenumber of incident light	cm ⁻¹
θ	contact angle	-
	fraction of occupied sites	-
ρ	density	kg/m ³
$\tilde{\rho}_g$	molar density of the gas phase	kg/mol
σ	normal stress	N/m ²
	surface tension	N/m
σ_{ext}	extinction cross-section	m ²
$\partial\sigma/\partial\Omega$	differential scattering cross-section	m ² /sr
τ	shear stress	N/m ²
	turbidity	-
ω	rotational speed	1/s
Ω_{obs}	observation angle of objective	sr
ζ	zeta-potential	mV
χ_{ij}	<i>Flory-Huggins</i> interaction parameter	-

(III) Indices:

g	gas phase
i, j, k, s	indices
p	polymer
ph	phase boundary
t	time
w	water
∞	infinite

1 Introduction

1.1 Introduction

The current expansion of waterborne polymer dispersions in the coatings market is the result of the pressure, induced by environmental legislation, to reduce the amount of volatile organic compounds in coating formulations. Compared to solvent-based formulations, aqueous latex dispersions, aqueous polyurethane (PU) emulsions and alkyd emulsions are environmentally-friendly alternatives. Already today, water-based latex paints compromise more than 85% of all coatings currently used in interior and exterior wall painting.

Generally, water-based paints and varnishes are colloidal dispersions that consist of the dispersion medium (= water), of binders, surfactants, organic co-solvents and further additives. Polymer particles in the nanometer size form the binder which is responsible for film formation and the surface-active species are necessary to prevent polymer particle agglomeration within the dispersion. Further additives like plasticizers (= organic solvents), thickeners (= rheology modifiers) or anti-foaming agents improve the application properties of the dispersion. In paint formulations, pigments are added for colour and/or opacity.

After the application of a fresh paint layer, the coating dries and film formation takes place. During film formation, the repulsive forces between the binder particles in the colloidal dispersion are overcome which results in close contact of the polymer particles. In the case of aqueous latex dispersions, physical driving forces - mainly interfacial tension and capillary pressure - are responsible for particle deformation. The mechanical stability of the final polymer film is the result of polymer chain interdiffusion. Aqueous polyurethane (PU) emulsions are chemical crosslinking systems in which the mechanical strength of the final coating is the result of a chemical reaction between the two compounds polyalcohol and polyisocyanate.

Compared to solvent-based formulations, water-based coatings show poor application properties, expressed by a short open time, inhomogeneities in the film thickness and component distribution and different coating defects. The open time is the period after coating application, during which the particle mobility is sufficiently high to allow corrections on the film without that coating defects like the stroke of the brush, lap lines from overlapping film layers or edge effects are visible in the final dry coating.

Both, industry and academia invest significant time and effort to develop water-based systems, that show a drying behaviour comparable to that of the established solvent-based formulations. To further improve the application properties of water-based formulations - open time, film quality and compound distribution, it requires a fundamental understanding of the drying and film formation mechanism of colloidal dispersions.

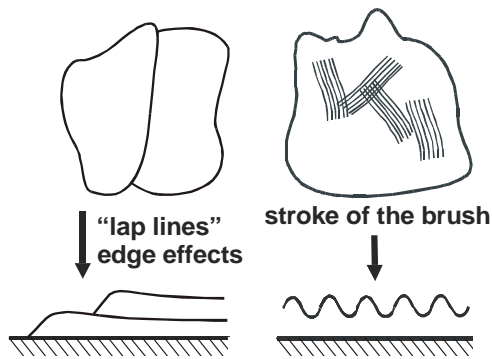


Figure 1-1: Typical defects in a dry coating

This is where this work wants to make a contribution. The measurement technique of Inverse-Micro-Raman-Spectroscopy (IMRS) used in this study, combines a high space and time resolution. It is therefore perfectly suited to measure water concentration profiles during film drying and film formation.

With the help of IMRS, different aspects could be identified and are subsequently discussed that prove responsible for the poor application properties and coating quality of aqueous polymer dispersions. They are summarized in the following figure:

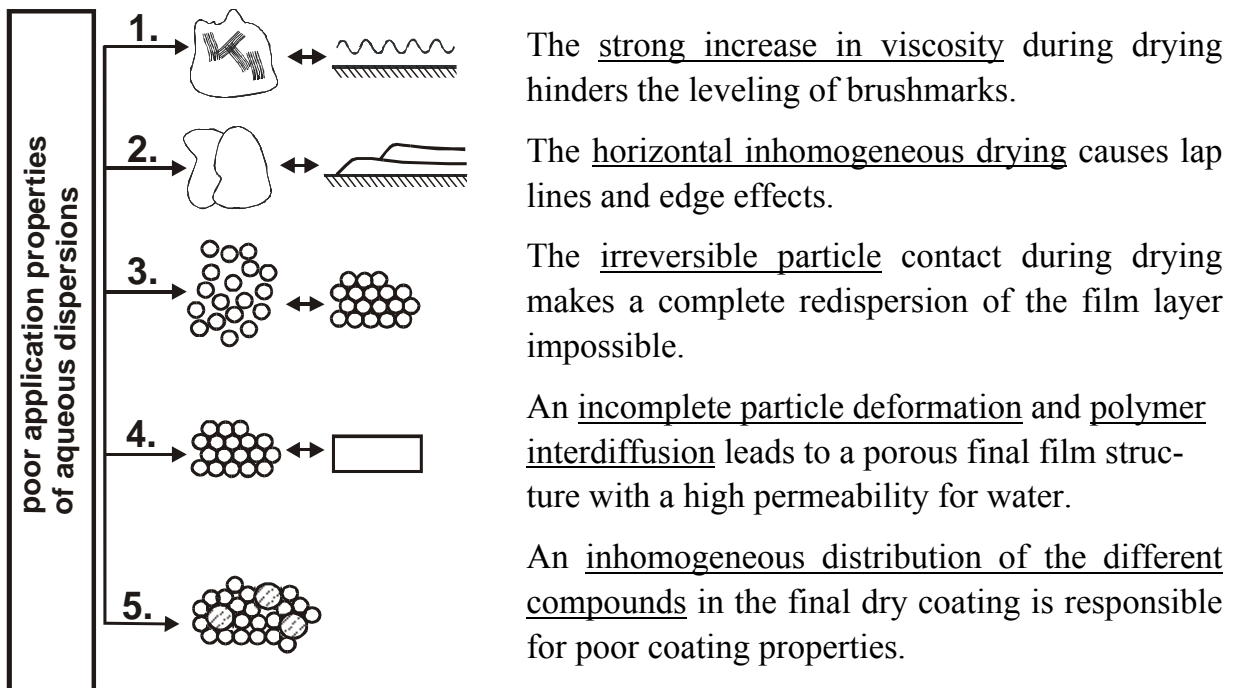


Figure 1-2: Reasons for the bad application properties of aqueous polymer dispersions

The experimental data obtained from IMRS are compared with theoretical considerations and calculations and the change of viscosity during drying of aqueous latex dispersions is investigated by rheological experiments.

1.2 State of the Art

Experimental studies on a large variety of latex dispersions prepared and dried under many different conditions and conducted by a large number of different methods have led to a flood of information about the details of latex film formation. This knowledge though is often not transferable even to closely related systems. Most studies on latex film formation concentrate on only one detail of the complex mechanism.

Good review articles on latex film formation were published by e.g. *Keddie (1997)*; *Winnik (1997)* and *Steward et al. (2000)*, but to my best knowledge, a systematic investigation of the different reasons for the minor application and coating properties of aqueous polymer dispersions is lacking. This is where this work wants to make a contribution. Based on the main reasons for the short open time and poor film quality of aqueous dispersions, (I) the strong increase of viscosity during drying, (II) the horizontal inhomogeneous drying and (III) the moment of irreversible particle contact, an overview of the state of the art is given below.

(I) Strong Increase in Viscosity:

Opposite to ordinary liquids and solutions, colloidal dispersions show non-Newtonian rheological behaviour. A good review article about the rheology of monodisperse latices was written by *Krieger (1972)*.

Much has been published about the viscoelastic properties of concentrated latex dispersions (e.g., *Milkie et al. (1982)*; *Tadros et al. (1990)*; *Nashima et al. (1991)*; *Raynaud et al. (1996)*; *Chu et al. (1998)*, *Hone et al. (2000)*...). Linear viscoelastic measurements of concentrated latex dispersions give information about their microstructure. At moderate to high concentrations, monodisperse latices form highly ordered but liquid-like, structured dispersions (*Goodwin et al. (1982)*). The structure depends on the potential of the mean force between the particles which is the result of repulsion by overlapping electrical double layers and attraction by van-der-Waals-forces (*Verwey, Overbeek (1948)*; *Derjaguin, Landau (1941)*). With increasing particle concentration, the rheological character of the dispersion changes from primarily viscous to elastic. The viscosity at low shear rates mainly depends on colloidal interaction whereas, for high shear rates, hydrodynamic factors dominate. The viscosity of concentrated latices decreases with increasing shear stress (*Krieger (1972)*), which is in the case of electrostatic stabilization ascribed to a reduced Coulombic interaction between the double-layers of the different particles at high shear. *Molenaar et al. (1997)* investigated the effects of the binder type, dispersion composition, plasticizer and thickener on the rheology of latex dispersions during drying and related them to the evaporation kinetics and to latex particle swelling. Most recently, *Pishvaei et al. (2005)* presented developments in the comprehension of the rheological behaviour of concentrated latex dispersions with different electrostatic properties as a function of volume fraction ϕ . They showed that at a critical volume fraction ϕ_c , the steady shear viscosity, the dynamic modulus and

the dynamic shear viscosity change dramatically. The percolation theory is extensively used to understand the rheology of latices that show long-range connectivity due to physical interaction caused by functional groups at the particle surface. At a certain polymer volume fraction, - the so-called percolation threshold -, all latex particles participate in a physical network and the system begins to behave like an elastic solid (*Winter et al. (1997)*).

A simplification to theoretically describe polymer dispersions is the hard-sphere model in which latex particles are treated as rigid spheres in a liquid. This was first adopted by *Einstein* in his study of the viscosity of diluted suspensions (*Einstein (1905), (1906), (1911)*). Based on *Einstein's* theory, several models have been developed to describe the rheological behaviour of monodisperse latex dispersions as a function of the volume fraction of latex particles (e.g. *Mooney (1951); Doolittle (1951); Quemada (1989); ...*) Although originally introduced to describe hard-sphere dispersions, the volume-fraction-dependence of the viscosity of a wide variety of dispersions is well described by the *Krieger-Dougherty* equation (*Krieger and Dougherty (1959)*). Deviations occur for soft particles and also for hard particles surrounded by thick layers of surfactants (*Mewis et al. (1989)*). They can be accounted for by an effective volume fraction which also includes the volume of the stabilizing layer (*Horn et al. (2000)*).

The physics and mechanics of film leveling have been studied for many decades. A review of the work is given by *Quach (1973)*. The driving forces for film leveling are a combination of surface tension and gravity, although the latter can safely be neglected in many applications. Most of the work has been focussed on surface leveling of horizontal films of finite thickness and infinite extent where the amplitude of the disturbances is small compared to the film thickness and inertial forces can be neglected compared to viscous forces. Historically, *Waring (1931)* was the first to analyze leveling of thin dispersion films. He found that the major factors that influence leveling are the yield stress of the polymer dispersion and the width of the brushmarks. *Patton (1964)* derived an expression for the leveling rate of surface corrugations having the geometry of alternating circular arcs. A formal stress analysis, based on the elastic theory of plain strain for brushmarks with sinusoidal wave profile, was conducted by *Smith et al. (1961)*. The analysis was later generalized by *Orchard (1962)* for arbitrary surface irregularities. *Keunings and Bousfield (1987)* presented a linear analysis of the surface-driven leveling of a *Newtonian* fluid and of one- and multi-mode *Maxwell* fluids. They also included a non-linear finite element analysis of the problem. In recent years, not much has been published on the leveling of viscoelastic thin films and the few papers that exist are normally based on the above mentioned theories, e.g. *Wilson (1993)*.

(II) Horizontal Inhomogeneous Drying:

Two-dimensional ordering of micrometer-size latex spheres on a glass plate investigated by optical microscopy has been reported by *Denkov et al. (1992)*: Particle

ordering in a highly diluted dispersion starts as soon as the thickness of the water layer has decreased to the size of the latex particle diameter. In the highly diluted dispersion, attractive capillary forces due to the menisci around the particles are identified as the main driving force for particle ordering and transport towards the ordered regions. Since then, horizontal inhomogeneous drying of latex films, where drying starts at the thinnest point of the film, has often been observed and reported of (e.g. *Keddie (1997); Winnik (1997)*).

Routh et al. (1998) developed a model in which the film thickness and the solid volume fraction in horizontal direction of the film was derived from overall momentum and conservation equations: As a first step, the capillary pressure was incorporated into the model as the driving force for horizontal inhomogeneous drying of rigid spheres (*Routh et al. (1998); Salamanca et al. (2001)*). As a next step, particle deformation was included by a viscoelastic function that describes the deformation of a pair of particles (*Routh et al. (2001); Tirumkudulu (2004)*). For a finite capillary pressure, the model considers three different zones: (I) a dry zone of deformed particles at the edge of the polymer film, (II) a zone of closely packed particles and (III) a zone of dispersed particles in the center of the film. Going from the edge of the film towards its center, the different zones are separated by the receding water front (I→II) and the particle front (= particle contact and packing, II→III).

Obviously, a lot of scientific work has already been done in the field of horizontal inhomogeneous drying of latex films. Nevertheless, experimental data which can be used to evaluate and improve the model calculations seem to be rare. A recent study reports the comparison of horizontal concentration profiles obtained from magnetic resonance experiments with model calculations (*Ciampi (2000)*).

(III) Drying, Film Formation and Irreversible Particle Contact:

Many authors have discussed the main driving forces for film formation. Different theories exist: *Dillon et al. (1951)* state that drying and particle deformation/film formation occur separately and that therefore, deformation is due to the polymer-air interfacial tension. On the contrary, *Brown (1956)* observed that water evaporation finishes at the same time as does film formation. Therefore, he states that both, the polymer-water interface and also the water-air interface, must be of importance for the film formation process. And *Sheetz (1965)* introduced a model of osmotic pressure-driven film formation which describes the formation of a thin layer of deformed particles at the latex surface, driven by capillary pressure. This layer then exerts a compressive force onto the particles below (perpendicular to the surface). Depending on the conditions and polymer properties, there exist experimental data to prove any of the above discussed film formation mechanisms.

A large number of studies exist on different aspects of spacing and deformation of the latex particles: Structural changes in films cast from soft particles which are protected by hydrophilic membranes have been studied by small-angle neutron scattering

(SANS) (*Joanicot et al.* (1990), (1993); *Chevalier et al.* (1996), (1999)). The same technique has also been applied to study particle coalescence and surfactant desorption during film formation of carboxylated acrylic latices (*Belaroui* (2003)). The use of transmission spectrophotometry has been reported to follow variations in the interparticle distance and displacement during the film formation of acrylic latices (*van Tent* (2000)). These studies show that completely deformed particles form a space-filling, highly ordered structure in which the number of functional groups incorporated into the particle surface and the amount of adsorbed surface-active material influence the existence of strong interparticular boundaries.

The impact of the functional groups at the surface of acrylic latex particles on the kinetics of polymer interdiffusion has been investigated by fluorescence decay measurements (*Kim et al.* (1995)). Attenuated total reflectance (ATR) *Fourier* transform infrared (FTIR) spectroscopy has been utilized for the study of surfactant-latex molecular-level interactions (*Niu et al.* (1998)) and the distribution of surfactant in the final latex film (*Zhao et al.* (1987)). Dynamic mechanical analysis was used to study polymer interdiffusion (*Richard et al.* (1992)). The studies show that a high number and certain types of functional groups at the latex particle surface can considerably slow down polymer chain interdiffusion across the individual particle boundaries. In the final polymer film, experimental data often give a higher level of surfactant near the film surface and the film-substrate interface.

Microscopic techniques have been applied to characterize the deformation and coalescence of the particles at the film surface. High-resolution cryogenic scanning electron microscopy (CSEM) has been used to investigate a microstructure development during drying of monodisperse and bimodal latex coatings (*Ma et al.* (2005)). Information about the surface morphology of waterborne pressure-sensitive adhesives, manufactured from acrylic ester copolymers has been obtained using tapping-mode atomic force microscopy (AFM) (*Mallegol et al.* (2001)). With both techniques, different stages towards the highly ordered structure of completely deformed, individual latex particles and subsequent particle coalescence could be visualized.

To my knowledge, so far, confocal Raman spectroscopy has only been applied to the field of latex film drying to investigate the distribution of water-soluble and surface-active species in acrylic latex films (*Belaroui et al.* (2000), (2003)).

Obviously, the major part of the existing experimental data deals with aspects of particle ordering and deformation during latex film formation. Although there is fundamental interest in the role of water during drying, experimental data dealing with this aspect are rare. Apparently, this is due to a lack of experimental methods, which can detect water and which have a space and time resolution that is high enough to measure the local water concentration in the film.

The investigation of film drying by means of gravimetric measurements at defined conditions is state-of-the-art (*Dobler et al.* (1992)). Apparently, there exist only two

studies dealing with water distribution in latex films. Solid-state nuclear magnetic resonance (NMR) spectroscopy has been used to investigate the influence of different amounts of surfactants on the drying process of thick films ($\sim 5\text{ mm}$) and the formation of water concentration gradients in vertical direction of the film (*Rottstegge et al.* (2003)). Excellent data have been obtained from magnetic resonance (MR) profiling which was used to monitor vertical water concentration profiles in thin films ($\sim 300\text{ }\mu\text{m}$) of alkyd emulsions (*Gorce* (2002)). In both studies, water gradients in vertical direction of the film were measured.

Due to the lack of experimental data on the water distribution in thin films not much can be found about the theoretical description of latex film drying. In general, a theoretical description compromises the mass transfer in the gas phase, the phase equilibrium at the interface and the diffusion of water in the polymer film.

Gas phase diffusion of a binary system is commonly described by the linear *Fick's* law of diffusion. This is valid as long as the partial pressures of the diffusing components are low and the influence of a convective drag flow is small. A calculation of the binary mass transfer coefficient $\beta_{w,g}$ can be found in *Schlünder* (1984). For the calculation of diffusion coefficients in the gas phase $\delta_{i,j}$ *Fuller et al.* (1966) developed a method which is flexible and easy to use.

A number of models exist to describe polymer-solvent phase equilibria. For aqueous systems generally two different approaches are described in the literature: (I) In localized sorption theories the polar penetrant is considered to bind at specific sites in the polymer structure, e.g. cracks, pores or polar groups. The presence of a dynamic equilibrium where condensation of molecules on bare sites equals evaporation from occupied sites is assumed (e.g. *Brunauer, Emmett, Teller* (1938); *Brunauer et al.* (1949); *Guggenheim* (1940); *Anderson* (1946); *de Boer* (1968)). (II) So-called dissolution theories use a more “macroscopic” approach to describe the water uptake of the film. Although often questionable for water-polymer systems, a homogeneous dissolution of the penetrant in the polymer is assumed and the “polymer solution” is treated as a three-dimensional lattice of spheres (e.g. *Flory* (1941); *Huggins* (1941)).

The water-permeability of films cast from polymer dispersions is usually higher than that of solvent-cast films due to the often observed existence of a hydrophilic diffusion network along the still existing particle interfaces. Binary diffusion coefficients of water in the polymer matrix can be obtained from gravimetric water sorption measurements using *Fick's* second law (*Arce* (2004)). *Guttoff* (1994) describes water diffusion in polymer films by a simple exponential approach.

1.3 Aim of this Work/Investigated Aspects

The application properties and the final coating properties of waterborne polymer dispersions are poor compared to the ones of polymer solutions with organic solvents. This is expressed by a short open time and by coating inhomogeneities and defects that are visible in the final dry coating. Such defects are not aesthetically pleasing and can even make the coating useless for an intended purpose.

Aim of this work is an investigation and discussion of the different aspects that are responsible for the poor application and coating properties of aqueous polymer dispersions by experiments and model calculations.

Different latex dispersions and one polyurethane emulsion are provided by RHODIA (France) for the investigation of film drying and film formation. The dispersions differ in the polymer composition, polymer glass transition temperature, particle size, particle surface functionality, kind of stabilization and amount of surfactant. The characteristic dispersion properties that are necessary to describe and understand the above mentioned aspects are presented in Appendix III.

In Karlsruhe, a new measurement technique, called Inverse-Miro-Raman-Spectroscopy (IMRS) has been developed by combining an inverse microscope with a confocal Raman spectrometer (*Schabel (2005); Schabel et al. (2005)*). With the technique it is possible to quantitatively measure water concentration profiles in vertical and horizontal direction of thin polymer films. With an optical resolution of $2-3 \mu\text{m}$ and a time resolution of $\sim 1 \text{ s}$, the IMRS data possess a quality not yet presented by others. New to this work is the use of the IMRS technique to investigate drying and film formation of thin films of aqueous polymer dispersions (instead of polymer solutions).

Below is an outline of the different reasons for the poor film quality and application properties of aqueous polymer dispersions:

(I) Strong increase of the dispersion viscosity and film leveling

After the application of a paint layer, the leveling of the brushmarks and the formation of a smooth surface is dictated by both, the rheological and surface tension properties of the material. During drying, there are strong changes of the rheological properties of the polymer dispersion, in particular the viscosity, which can hinder complete film leveling. In this work, the change of the viscosity and the elastic moduli as a function of the particle volume fraction are monitored by rheological measurements and the obtained viscosity function is then incorporated into a mathematical model of film leveling. This helps to describe the conditions that still allow complete leveling of the coating surface.

(II) Film drying and horizontal inhomogeneous drying

Although there is fundamental interest in the role of water during drying, experimental data dealing with this aspect are rare. In this work, IMRS is used to monitor water distribution in vertical direction of the film during drying and at different drying conditions. In the case of skin formation at the coating

surface, the formation of steep concentration gradients towards the film surface would be expected like it was found for solvent-based coatings (*Schabel et al.* (2003)). The experimental data are compared with model calculations of film drying (*Guttoff* (1984)).

For the investigation of horizontal inhomogeneous drying of waterborne polymer films, the water concentration at different positions in horizontal direction of the film is measured by IMRS during drying. Existing drying mechanisms which propagate the formation of a water front that moves towards the center of the film are validated. The experimental data are compared with model calculations of film drying (*Guttoff* (1984)).

(III) Irreversible contact of the polymer particles during drying

The moment of irreversible particle contact during drying is investigated by so-called redispersion- or two-film-experiments. For this, a thin coating layer is prepared and dried for a defined time before a second film layer or a reservoir of dispersion is applied on top of the first coating layer. With IMRS, the formation of water concentration gradients, the increase of the water content in the bottom layer and the equilibrium water concentration in both film layers is investigated. The experimental data are discussed with regard to the dispersion characteristics and are compared with theoretical considerations.

(IV) Incomplete particle deformation and polymer interdiffusion

A continuing problem with water-based coatings is their high permeability for water and other potentially harmful pollutants. A network of pores and hydrophilic surface-active materials in the film does account for the high permeability noted for latex films although already dry and transparent. Here, besides the investigation of drying, IMRS is used to monitor water diffusion into dry latex films cast from the different dispersions. In combination with atomic force microscopy (AFM) one can obtain information about the film structure at the dry coating surface.

In connection with the comprehensive investigation of film drying and film formation, the influence of additives like plasticizers (TexanolTM) or higher amounts of surfactant (sodium-dodecylsulfate, SDS) on the coating properties is investigated by IMRS measurements.

(V) Distribution of different dispersion components

Apart from aqueous latex dispersions, waterborne polyurethane (PU) emulsions are another option for environmentally-friendly coatings. PU emulsions are chemically crosslinking systems. Chemical crosslinking gives the film higher mechanical stability and makes it less permeable for water and other harmful substances. For the coating to show these properties, it is essential to have an even distribution of reactive compounds and a homogeneous degree of cross-linking. Here, the distribution of the different components of the PU emulsion is

obtained from IMRS measurements (I) during drying and (II) in the dry film. In addition, the onset, distribution and the degree of crosslinking with time is measured and discussed.

2 Aqueous Polymer Dispersions

The chapter gives an overview of the composition and characteristics of the investigated aqueous polymer dispersions: (I) latex dispersions (film formation by physical particle interaction and polymer interdiffusion) and (II) polyurethane (PU) emulsions (film formation by chemical crosslinking). The main characteristics and differences between the investigated latex dispersions are shown in Figure 2-1.

Appendix I and Appendix II give the theoretical background of the preparation and stabilization of aqueous polymer dispersions; more details on the dispersion characteristics are given in Appendix III.

2.1 Latex Dispersions

2.1.1 Composition

Generally, latex dispersions are colloids that consist of sub-micron polymer particles in an aqueous medium, stabilized by surfactants.

In aqueous latex dispersions, water forms the dispersion medium (= continuous phase). The advantage of water is the mostly unproblematic availability at low costs and its eco-friendliness. The disadvantage is, that a dispersion of polymer particles in pure water would not be stable due to the polar character of water compared to the apolar polymer. This calls for the use of surfactants to stabilize the dispersion. Besides surfactants, rests of non-reacted monomer and dissolved salts are normally present in the liquid phase.

The polymer particles in the dispersion - mostly acrylic or styrene by nature - are also called binder component since they are responsible for the film formation once water has evaporated. The kind and the composition of different monomers will influence the final coating properties. In paints, pigments (= inorganic substances like e.g. titanium dioxide) are added for colour and/or opacity. They are non-soluble particles that absorb and/or scatter light of a certain wavelength.

Additives can improve the application properties of the dispersion, e.g. plasticizers, rheology modifiers and anti-foaming agents. Plasticizers are low-volatile organic solvents (= VOCs) that mainly lower the polymer's glass transition temperature which facilitates particle deformation and film formation. Due to the low volatility, a plasticizer needs considerable time to evaporate from the coating which makes it potentially harmful for the environment. Since 2004, there exists a federal guideline for the European Union to stop the use of VOCs in paint formulations¹. Thickeners

¹ Directive 2004/42/EG of the European Union; Official Journal of the European Union; L143/87, 2004

modify the rheological properties of dispersions. They are important to assure an easy application, to improve the leveling of brushmarks in the film and to avoid sagging.

A typical composition of an aqueous latex paint would consist of around 30% of binder, 10% of pigments and 60% of water with additives.

2.1.2 Investigated Dispersions

In this work, aqueous latex dispersions as used in commercial formulations of paints and varnishes are investigated. They consist of water, polymer particles and a combination of different surfactants. Compared to full paint formulations, the dispersions do not contain additives like plasticizers and thickeners or pigments. The absence of pigments is pre-requisite for the use of the IMRS measurement technique which can only be employed for the investigation of at least nearly-transparent coatings. For an investigation of the influence of plasticizers on drying and film formation different amounts are given to the basic formulation.

The polymer particles used here are (I) co-polymers of different acrylic esters (butyl-acrylate, ethyl-hexyl-acrylate, methyl-methacrylate) and (II) co-polymers of acrylic esters (butyl-acrylate) and styrene. They show variations in the kind and amount of monomers, which accounts for the different glass transition temperatures T_g . Generally, one can differentiate between dispersions of hard polymer particles with a glass transition temperature above $16\text{ }^\circ\text{C}$ and soft latices with a T_g of $0\text{--}2\text{ }^\circ\text{C}$. In all dispersions, the particle surface is functionalized by different amounts and combinations of pH-dependent ionizable groups, ionic groups and hydrophilic alcohol or acid groups. The particle size - with one exception - is in the range of $90\text{--}165\text{ nm}$ and is a function of pH, depending on the amount of functional groups at the particle surface.

The dispersions contain different amounts and combinations of anionic and non-ionic surfactants and also vary in the amount and type of anions and cations present in the aqueous medium. The combination of different particle surface functionalities, a different surfactant level and amount of ions makes that the dispersion and film formation characteristics of the different formulations are considerably different. Generally, the necessary amount of surfactant for dispersion stabilization is inverse to the particle surface charge, being low when many functional groups are incorporated into the particle surface. This is responsible for a varying dominance of either long-distance electrostatic repulsion or shorter-range steric repulsion between the particles.

Below is a short description of the different latices under investigation (see also Figure 2-1). The letters in the name of each dispersion indicate their properties: **A** and **AS** symbolize the kind of monomer, where **A** means pure acrylic copolymers and **AS** stands for acrylic-styrene copolymers. The letters **H** and **S** are an abbreviation for the hard or soft polymer particles, referring to the polymer's glass transition temperature T_g .

AS-H-1a, AS-H-1b are acrylic-styrene copolymers of high glass transition temperature. Many pH-dependent, ionizable groups and hydrophilic functional groups are incorporated into the particle surface and the surfactant level is low. Both dispersions are very similar in their formulation but in the case of AS-H-1a the large cation amino-methyl-propanol is present in the medium. Amino-methyl-propanol is water-soluble and is often used as a pH-buffer in hair styling gels.

AS-S-1 is an acrylic-styrene copolymer of low glass transition temperature. The amount of pH-dependent, ionizable groups at the particle surface is lower than for AS-H-1a,b. For AS-S-1, the amount of ions in the medium is less than for AS-H-1a,b but the amount of surfactant is higher.

A-H-1 is an acrylic copolymer of high glass transition temperature. The amount of pH-dependent, ionizable groups is again less than for any of the AS copolymers. The level of ions in the dispersion medium is relatively low, whereas the amount of surfactant in this formulation is high. Also, free carboxylic acid is present in the aqueous medium.

A-S-1 is an acrylic copolymer of low glass transition temperature. The dispersion has a low amount of pH-dependent, ionizable groups at the particle surface but also an amount of ionic non-pH-dependent functional groups. The level of ions in the dispersion medium is low and compared to the other dispersions the amount of surfactant is medium.

A-S-2 is an acrylic copolymer of low glass transition temperature and small particle size of around 30 nm (so-called “nano”-latex). This latex has a number of ionic, pH-dependent ionizable groups incorporated into the particle surface and the amount of surfactant in this formulation is the highest of all dispersions.

Appendix III gives more information about the dispersion characteristics like particle size, glass transition temperature, particle volume fraction and average particle distance, surface tension and static contact angle. A table with a summary of the characteristic data of each dispersion can be found at the end of that chapter (Appendix III 8)). An analytical investigation of the dispersions to the bond level is not aim of this work.

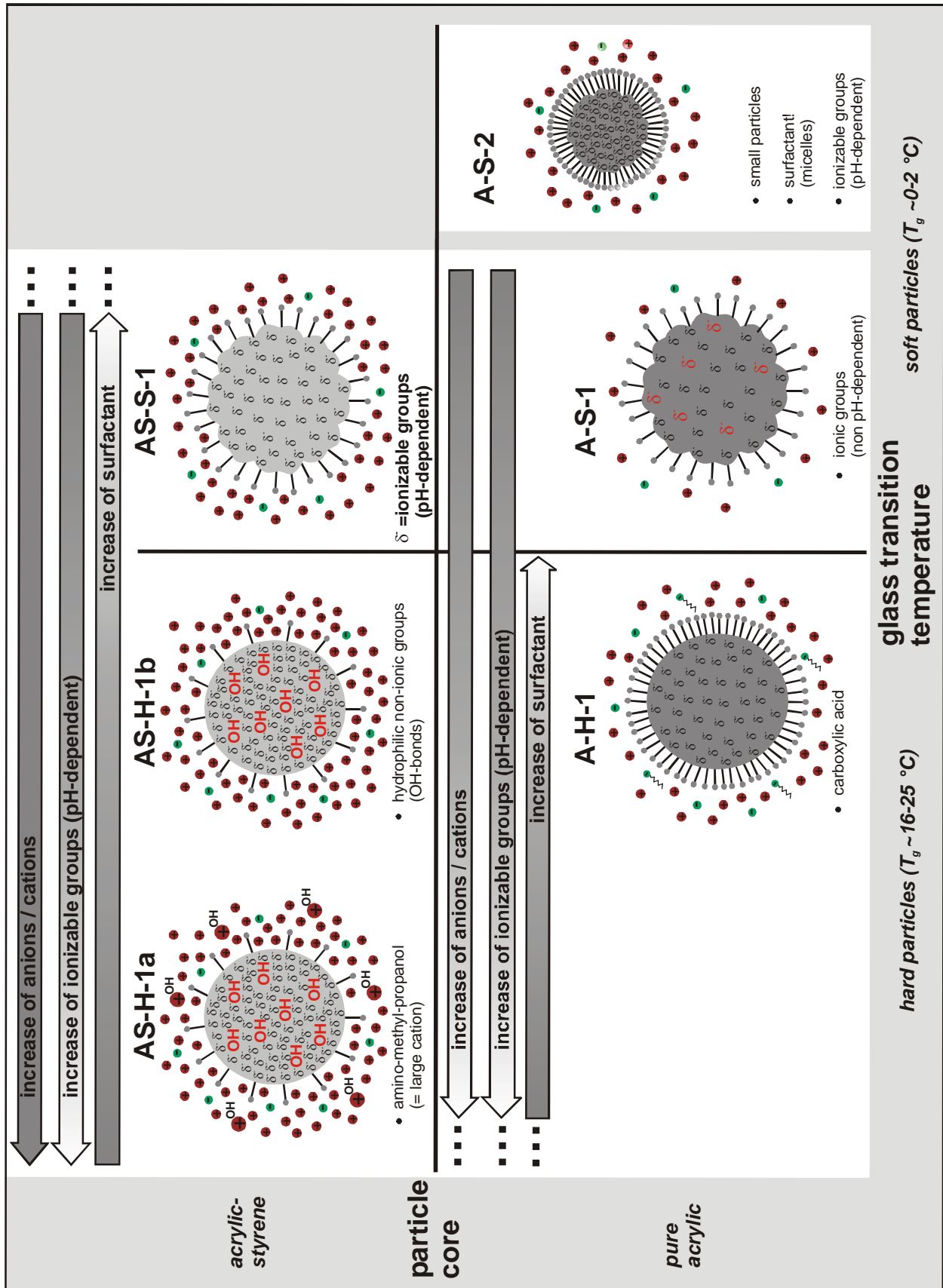


Figure 2-1: Overview of the different latex dispersions

2.2 Polyurethane (PU) Emulsions

2.2.1 Composition

Aqueous polyurethane emulsions consist of two reactive compounds – polyalcohol and polyisocyanate – dispersed in water and stabilized by surfactants. In this study, the polyalcohol (= polyol) is an aqueous dispersion of submicron polymer particles with a large number of OH-groups incorporated into the particle surface. Depending on the emulsion preparation, the other reactive component, the polyisocyanate, consists of nano- to micrometer-size droplets of aliphatic polyisocyanate, stabilized by a large amount of surfactant.

2.2.2 Emulsion Preparation

Usually, varnishes that consist of two-component polyurethane emulsions are prepared by the customer by mixing the different components directly before application. It is therefore essential to have a preparation route which is (I) easy to follow for the customer and which (II) guarantees the functionality of the final coating. Depending on the order of mixing of the different components, one can differentiate between three preparation routes: Although the dispersions have the same chemical composition, they show different characteristics. Most important is the droplet size and distribution of the two reactive components. The different preparation routes can be visualized in a phase diagram (Figure 2-2).

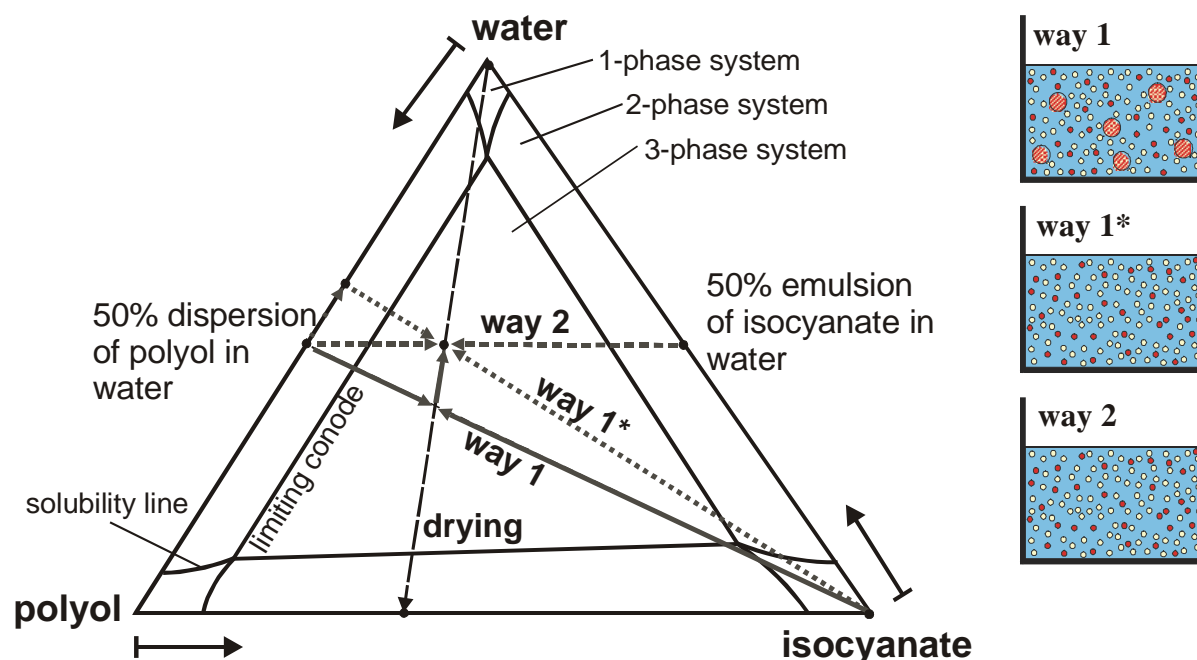


Figure 2-2: Representation of the phase diagram for the three-component-system water, polyisocyanate, polyalcohol and the different preparation routes

For preparation route 1 (Figure 2-2) pure polyisocyanate, containing surfactants, is given to an aqueous polyol dispersion under stirring. The high-viscosity emulsion is subsequently diluted with water to obtain a dispersion, which, after a short time of

stirring and rest, is ready to use. The advantage of this preparation route is that the emulsion viscosity can be easily adjusted in the final preparation step of dilution. The disadvantage is an inhomogeneous droplet size distribution with small polyol and isocyanate droplets of around 100 nm in size but also large drops of almost pure isocyanate having a size of about $1\ \mu\text{m}$.

A second preparation route, - indicated by way 2 in the phase-diagram -, is the preparation of an emulsion of polyisocyanate in water which is subsequently added to a $50\text{ mass}\%$ polyol dispersion. Way 2 gives a homogeneous size of polyol particles and polyisocyanate droplets of around 100 nm . Despite the advantage of homogeneity, way 2 is often not the first choice to prepare PU emulsions: The preparation route is not easy to follow for the customer since the preparation of two milky colloidal media, (I) polyol in water and (II) polyisocyanate in water, can cause confusion. Besides, the dispersion viscosity cannot be adjusted during the final step.

A third alternative, indicated by way 1* in Figure 2-2, is the dilution of the $\sim 50\text{ mass}\%$ polyol dispersion with water before the polyisocyanate is added. This preparation route gives a more homogeneous particle size distribution than is achieved by way 1, but the emulsion viscosity cannot be adjusted by a final dilution step.

3 Rheology of Polymer Dispersions

Rheometry generally means the quantitative investigation of the rheological properties of materials. Typical rheological characteristics of concentrated latex dispersions are e.g. their viscoelastic behaviour and the liquid-solid transition during drying. The chapter ends with a survey of the large number of model-equations that describe the dispersion viscosity as a function of polymer volume fraction. Some theoretical basics of rheology and the experimental setup are described in Appendix IV.

3.1 Rheological Characteristics of Concentrated Polymer Dispersions

During its lifetime, a latex dispersion as used in paints and varnishes may be subject to a number of deformation processes, e.g. pumping (= moderate to high shear), storage and transport (= low shear), application by brushing (= moderate shear), roller coating (= moderate to high shear), spraying (= high shear) or dipping (= low shear). Therefore, a dispersion paint must possess certain rheological properties to fulfill its function. For the easy application of a thin paint film, the dispersion must exhibit shear thinning behaviour. Typical shear rates for brushing are 1000 to $10\,000\text{ s}^{-1}$.

When applied to vertical walls, the dispersion viscosity must be sufficiently high to avoid sagging or the formation of “teardrops”. However, the viscosity of the coating at rest must also be low enough to allow the flow out of striations, caused by e.g. the stroke of the brush. Flow out of striations or film leveling would require a low yield stress and a high surface tension. In the effort to understand practical paint properties related to rheology (= sagging and leveling), the rheological changes in highly concentrated dispersions as they apply for drying and film formation are often overlooked or not measured due to experimental difficulties.

The common structural feature of latex dispersions is the presence of flow units, the colloidal particles, whose dimensions are large compared to the molecules of the suspending medium while still small enough to undergo *Brownian* motion. Polymer dispersions display viscoelastic properties (e.g. *Goodwin et al.* (1974), (1982); *Buscall* (1982)): Depending on the imposed deformation, rheological phenomena like shear thinning and/or shear thickening behaviour, thixotropy and the existence of a yield stress are observed. Parameters that influence the dispersion rheology are the diameter, the shape and the size distribution of the particles. In addition, the rheology is controlled by the particle volume fraction and the hydrodynamic and thermodynamic particle interactions which depend on the number of electrical charges in the medium and at the particle surface and also on the amount of surfactant present. For the rheology of highly concentrated dispersions, the complex many-body hydrodynamic interactions are of secondary importance relative to the hard-sphere geometric effects (*Woodcock* (1985)).

3.1.1 Viscoelastic Properties

Long range particle ordering driven by the interplay of attractive and repulsive forces between the particles is observed for concentrated latex dispersions (e.g. *Hiltner and Krieger (1969)*; *Brown et al. (1975)*; *Alexander et al. (1983)*). The interparticular forces are the result of particle repulsion (overlapping electrical double layers, electrical charges at the particle surface and adsorbed surfactants) and attractive forces (*van-der-Waals* forces, hydrogen-bonding). The presence of electrical charges at the particle surface and in the medium causes an augmentation of the intrinsic viscosity, because of the increased energy dissipation in the electrical double layer around the particles (*von Smoluchowski (1916)*). The intrinsic viscosity is a measure for the capability of the polymer particles to enhance the dispersion viscosity. It is a function of the hydrodynamic radius of the latex particles and is defined by:

$$[\eta] = \lim_{\phi \rightarrow 0} \left(\frac{\eta}{\eta_0} - 1 \right) / \phi \quad \text{Equ. 3-1}$$

with:

η	= dispersion viscosity
η_0	= viscosity of the aqueous medium
$[\eta]$	= intrinsic viscosity
ϕ	= particle volume fraction

Three electroviscous effects are distinguished (*Conway and Dobry-Duclaux (1960)*):

(I) the first electroviscous effect is caused by a distortion of the electrical double layer around the particles. This effect is only observed for dilute dispersions and is masked by the other effects at higher particle concentrations.

(II) the second electroviscous effect further increases the viscosity of concentrated dispersions. A surplus of counterions caused by overlapping electrical double layers of different particles leads to an osmotic pressure causing particle repulsion. This effect can alter the viscosity by an order of magnitude and is strongly affected by traces of electrolytic impurities.

(III) the third electroviscous effect is caused by electrical charges at the particle surface.

Apart from electroviscous effects, the presence of water-soluble molecules can also increase the viscosity of pure water. At sufficiently high shear stresses, the viscosity is independent of the electrolyte content, but for lower stresses a viscosity minimum is observed for a certain electrolyte concentration c_{\min} . It represents the electrolyte level that provides maximum shielding of the repulsive *Coulombic* forces without destabilizing the dispersion (*Krieger (1972)*). In the case of steric stabilization, the lowest viscosity is exhibited for a surfactant level that corresponds to a 100% monolayer coverage of the particle surface. An increase in viscosity for higher surfactant concentrations is due to the formation of micelles and for lower surfactant concentrations it can be the result of bridging between the polymer particles.

At low shear rates, where colloidal forces are dominant, polymer dispersions show a *Newtonian* plateau of constant viscosity. This means, that for low shear rates and small deformations, the *Brownian* motion of the particles is high enough so that the relative positions of the latex particles during flow are identical to those at rest. Above a critical shear rate, hydrodynamic factors become more effective. This is when the shear rate is high enough to disturb the distribution of interparticle spacing from its equilibrium level. This will cause a reduction of the flow resistance in the dispersion, expressed by a decrease in viscosity (= shear thinning). For dispersions at high shear rates, a second *Newtonian* plateau of constant viscosity exists which mainly depends on the polymer particle volume fraction ϕ . Under certain conditions, e.g. high shear rates and high particle volume fractions, shear thickening can occur, being the result of so-called hydrocluster formation. The reversible formation of particle clusters can lead to an increased effective particle volume fraction due to trapped solvent, combined with an increase in the dispersion viscosity (*Laun (1984)*).

Generally, a yield stress appears when the particle repulsion is strong enough to induce a regular arrangement of particles or a sort of “macro-crystallization”. This is often the case for higher particle concentrations. But also the formation of aggregates in highly concentrated, unstable suspensions can be a reason for the existence of a yield stress.

3.1.2 Liquid-Solid Transition and Gelation

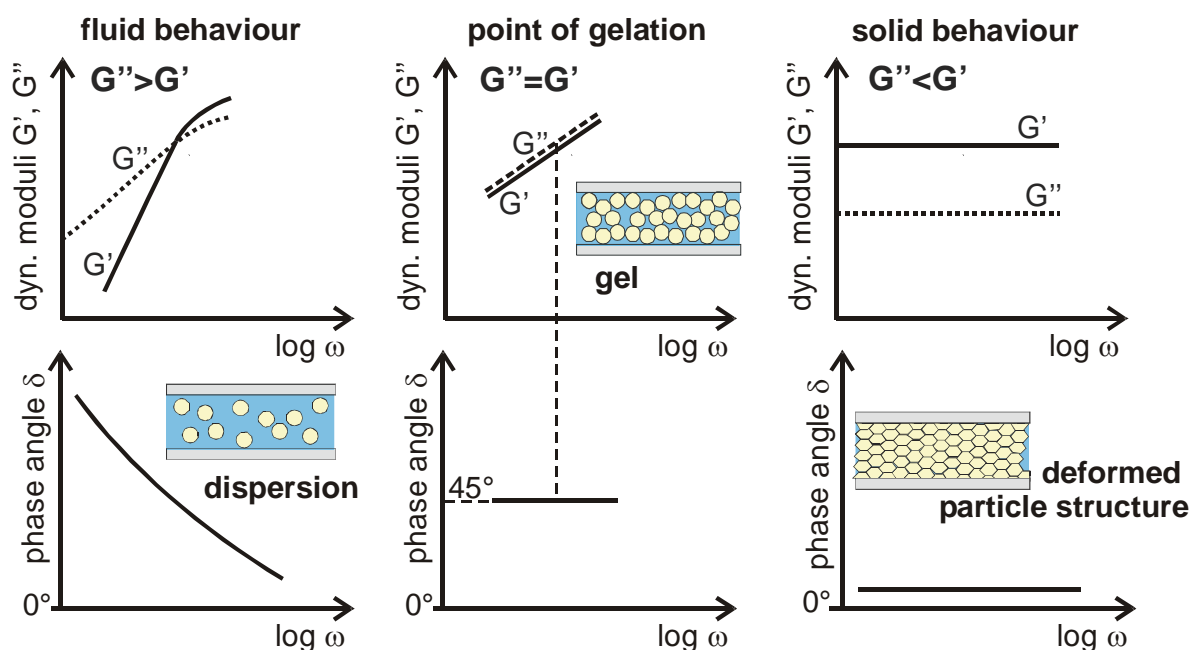


Figure 3-1: Dynamic moduli for different water contents X

During drying, the rheological behaviour of a latex dispersion changes from primarily viscous at lower particle concentrations to elastic at high particle concentrations. The moment where the solid and liquid properties of the dispersion are equally dominant is called the rheological gel point. It can be obtained from an experimental investigation

of the dynamic moduli G' and G'' at different water contents. A representation of the dynamic moduli during liquid-solid transition is given in Figure 3-1.

At the gel point, both dynamic moduli have the same value and slope (Figure 3-1). Below the gel point, the dynamic moduli G' and G'' are proportional to ω^2 and ω^1 showing liquid-like behaviour at low frequencies (*Winter et al. (1997)*). The process of gelation is the result of particle interaction and contact. As the particle concentration is increased, the frequency where G' crosses G'' decreases rapidly. This is caused by an increase of the relaxation time with particle volume fraction ϕ . The plateau of the elastic modulus G' means that all particles participate in a physical network, giving a rubber-like response.

3.1.3 The Cox-Merz Rule

The rule states that in highly diluted polymer dispersions, the complex viscosity $\eta^*(\omega)$ obtained from oscillatory shear experiments is equal to the steady shear viscosity $\eta(\dot{\gamma})$ for the same low value of angular frequency and steady shear rate.

$$\left| \eta^*(\omega) \right|_{\omega \rightarrow 0} = \eta(\dot{\gamma})_{\dot{\gamma} \rightarrow 0} \quad \text{Equ. 3-2}$$

This was first reported by *Cox and Merz (1958)*. *Gleissle and Hochstein (2003)* found that the *Cox-Merz* rule is not valid for concentrated suspensions of various glass beads. *Flickinger (1999)*, (2000) showed for aqueous polyurethane emulsions that the *Cox-Merz* rule is only obeyed at strains in the linear viscoelastic region and at concentrations below the gel point, where the system shows a *Newtonian* shear plateau. In the regions of shear thinning, the dynamic viscosity is always higher than the simple shear viscosity. The failure of the rule can be explained by the fact, that for steady shear flow, as opposed to dynamic shear flow, the shear distortion of the particle arrangement with increasing shear rate could be more severe than in dynamic experiments where the possibility of a rearrangement of the distorted structure is higher.

3.1.4 Theoretical Description of the Viscosity Function

The viscosity of polymer dispersions is an exponentially increasing function of the particle volume fraction. The shape of the viscosity function is determined by the requirements that (I) for the dilute dispersion, the slope equals that of the intrinsic viscosity and that (II) for approaching the maximum packing fraction of particles, the viscosity will diverge. The nature of the viscosity function $\eta(\phi)$ had been subject of many theoretical and experimental studies:

Famous is *Einstein's* study of the viscosity of a dilute dispersion of rigid spheres (*Einstein (1905)*, (1906), (1911)). In the theoretical treatment of the dispersion viscosity, he successfully adapted the hard-sphere model, originally developed to describe transport properties of gases. In this, *Einstein* took certain assumptions, like (I) the incompressibility of the fluid and (II) an equal particle and fluid density. He

also neglected (III) particle or wall interactions or slip between the particles and the fluid. *Einstein* describes the dispersion viscosity by:

$$\eta = \eta_0 \left(1 + \frac{5}{2} \phi\right) \quad \text{Equ. 3-3}$$

with:

η	= dispersion viscosity
η_0	= viscosity of the aqueous medium
ϕ	= particle volume fraction

Re-arrangement of Equ. 3-3 gives the intrinsic viscosity of the dispersion, which reflects the capability of the polymer particles to enhance the dispersion viscosity.

$$[\eta] = \lim_{\phi \rightarrow 0} (\eta_r - 1) / \phi = \frac{5}{2} \quad \text{Equ. 3-4}$$

with:

$$\eta_r = \frac{\eta}{\eta_0} \quad = \text{relative viscosity} \quad \text{Equ. 3-5}$$

According to *Einstein's* theory, the intrinsic viscosity has a value of 5/2 regardless of size and size distribution of the latex particles.

Based on *Einstein's* theory, several models have been developed to describe the rheological behaviour of monodisperse latex dispersions as a function of the particle volume fraction (*Mooney* (1951); *Doolittle* (1951); *Krieger* and *Dougherty* (1959); *Quemada* (1989); ...). All of the models introduced below are empirical descriptions of the dispersion viscosity for non-interacting, hard-sphere particle dispersions.

Mooney extended *Einstein's* basic viscosity analysis of dilute dispersions of rigid spheres to be also applicable to dispersions of finite concentrations. For a monodisperse system, the solution of the functional equation that *Mooney* employed in his theory is:

$$\eta = \eta_0 \exp\left(\frac{A \cdot \phi}{1 - k \cdot \phi}\right) \quad \text{Equ. 3-6}$$

with:

A	= <i>Einstein</i> parameter
k	= so-called self-crowding factor

The theory describes first-order interactions of the particles by a crowding effect, taking into account a reduction of the total volume by the particles. The so-called self-crowding factor k is empirical and cannot be derived from hydrodynamic theory.

The so-called *Doolittle* equation is based on the idea that, in a liquid, the resistance to flow depends upon the relative volume of the molecules present per unit of free space. It was empirically derived from the free-volume theory, which assumes that the volume can be divided into a part that is occupied by the molecules (v_0) and a part in which the molecules are free to move, termed the “free volume” (v_f). The theory further supposes that a supercooled liquid can be described by a distribution of liquid-like and solid-like cells, with or without enough free volume for molecular diffusion. The free volume is considered to be partitioned randomly among the cells and hence the viscosity is given by the following expression:

$$\eta = C \cdot \exp\left(b \frac{v_0}{v_f}\right) = C \cdot \exp(b\phi) \quad \text{Equ. 3-7}$$

with:

C, b	= empirical constants
v_0	= volume of the particles
v_f	= free volume (= volume of the surrounding medium)

Although originally introduced to describe hard sphere dispersions, the volume fraction dependence of the viscosity of a wide variety of dispersions is well described by the *Krieger-Dougherty* equation (*Krieger and Dougherty (1959)*).

$$\eta = \eta_0 \left[1 - \frac{\phi}{\phi_{max}} \right]^{-[\eta]\phi_{max}} \quad \text{Equ. 3-8}$$

with:

η	= dispersion viscosity
η_0	= viscosity of the aqueous medium
$[\eta]$	= intrinsic viscosity
ϕ	= particle volume fraction
ϕ_{max}	= maximum particle volume fraction

In this model, the intrinsic viscosity $[\eta]$ has the value of $5/2$, as introduced by *Einstein*. The maximum packing fraction ϕ_{max} depends on the particle size, shape and particle size distribution, shear rate and on the state of aggregation of the dispersion. Typical for randomly packed spheres is a maximum particle volume fraction $\phi_{max} = 0.58-0.63$. *Krieger and Dougherty* further developed their theory to take explicit notice of adsorbed monolayers at the particle surface which are incorporated by a factor λ . Then, the equation terms:

$$\eta = \eta_0 \left[1 - \frac{\lambda \cdot \phi}{\phi_{max}} \right]^{-[\eta]\phi_{max}} \quad \text{with: } \lambda = 1 + 6\Delta/\bar{d} \quad \text{Equ. 3-9}$$

with:

$\frac{\Delta}{\bar{d}}$	= thickness of an adsorbed monolayer
\bar{d}	= average particle diameter

The *Quemada* (1989) model was developed in search for a theoretical description of stationary flow of concentrated dispersions with a non-uniform particle volume concentration, e.g. a tube with a concentration profiles $c(r)$. It is (I) based on *Newtonian* flow behaviour (at high shear rates) and (II) diffusion effects are neglected. The *Quemada* viscosity function is deduced from an optimization of the viscous energy dissipation and is expressed by:

$$\eta = \eta_0 \left[1 - \frac{\phi}{\phi_{\max}} \right]^{-2} \quad \text{Equ. 3-10}$$

Here, the product of $[\eta] \cdot \phi_{\max}$, being around 1.5 for the *Krieger-Dougherty* equation, is replaced by the constant factor 2.

Pishvaei et al. (2005) used the percolation theory, generally employed for crosslinked polymer networks, to describe the viscosity data of concentrated polymer dispersions, obtained from dynamic shear experiments. They state, that in a dispersion the long-range connectivity results from the physical interaction of charged particle surfaces, but that the liquid-solid transition of dispersions has the same features as chemical gelling: it is expressed by the divergence of the longest relaxation time. The transition occurs during a random aggregation process of subunits into larger molecules.

The definition of a percolation threshold is that (I) the storage modulus G' crosses over the loss modulus G'' and (II) that, at that point, G' and G'' show the same power law dependence. From a viscoelastic analysis, *Pishvaei et al.* (2005) obtained a percolation threshold for particles that do not behave like rigid non-interacting spheres. They further applied the concept of percolation to determine the dynamic zero-shear viscosity which is defined by:

$$\eta = \lim_{\omega \rightarrow 0} \eta^*(\omega) = \lim_{\omega \rightarrow 0} \frac{G''(\omega)}{\omega} \quad \text{Equ. 3-11}$$

According to the percolation theory the dynamic zero-shear viscosity can be expressed by:

$$\eta = k(\phi_c - \phi)^{-s} \quad \text{for } \phi < \phi_c \quad \text{Equ. 3-12}$$

with:

- η = dynamic zero-shear viscosity
- k, s = constants
- ϕ = particle volume fraction
- ϕ_c = critical particle volume fraction ($\eta \rightarrow \infty$)

The model of *Pishvaei et al.* can be applied to describe dispersions of interacting and deforming particles, but is limited to low shear rates.

3.1.5 Mean Particle Separation and Polymer Volume Fraction

The mean particle separation \bar{h} in hard-sphere dispersions can be derived from geometrical considerations and is a function of the particle volume fraction ϕ . A comparison of the maximum particle volume fraction at both, low and high shear rates, reveals a strong increase of ϕ_{max} with shear which is attributed to the structure formation at low shear rates. Therefore, the maximum particle volume fraction ϕ_{max} of low-shear experiments has to be used in the following expression:

$$\frac{\bar{h}}{2a} = \sqrt[3]{\frac{\phi_{max}}{\phi}} - 1 \quad \text{or} \quad \frac{\phi_{max}}{\phi} = \left(1 + \frac{\bar{h}}{2a}\right)^3 \quad \text{Equ. 3-13}$$

with:

\bar{h}	= mean particle separation
a	= particle radius
ϕ	= particle volume fraction
ϕ_{max}	= maximum particle volume fraction

The Woodcock equation (Woodcock (1985)), derived from the osmotic equation of state for a hard-sphere dispersion, is another way to express the mean particle separation in polymer dispersions.

$$\frac{\bar{h}}{2a} = \left[\left(\frac{1}{3\pi\phi} + \frac{5}{6} \right)^{1/2} - 1 \right] \quad \text{Equ. 3-14}$$

Due to the electrical double layer and/or steric stabilization, latex particles of real polymer dispersions occupy a larger volume than is expressed by the particle volume fraction ϕ (Horn *et al.* (2000)). Low ionic strength, for example, results in long range particle repulsion which causes a large effective particle volume. A high effective volume fraction is also found for small particle dispersions. To take this extra volume into account, an effective particle volume fraction ϕ_{eff} is formed by the same geometrical considerations as used above to describe ϕ_{max} .

$$\frac{\phi_{eff}}{\phi} = \left(1 + \frac{\Delta}{a}\right)^3 \quad \text{Equ. 3-15}$$

with:

Δ	= dimension of the repulsive layer
----------	------------------------------------

By the use of effective volumes ϕ_{eff} , the charged particles are regarded as effective hard spheres. Then, real dispersion data can be fitted well by the above described viscosity models when the volume fraction ϕ is replaced by the effective volume fraction ϕ_{eff} . The effective volume fraction can also be determined from a comparison of the experimental data with the hard sphere data:

$$\phi_{\text{eff}} = \phi \left(\frac{\phi_{\text{max, hard-sphere}}}{\phi_{\text{max, exp.}}} \right)$$

Equ. 3-16

Then, a plot of the different experimental zero-shear viscosity data η_0 as a function of ϕ_{eff} form a mastercurve, independent of particle size, electrostatic effects or surface charges.

4 Mechanism of Film Formation

The chapter gives a description of the different, widely accepted stages of film formation for (I) physical particle interaction (= aqueous latex dispersions) and for (II) chemical crosslinking formulations (= aqueous polyurethane emulsions). A survey of possible driving forces of film formation is given in Appendix V. The chapter ends with the description of horizontal inhomogeneous drying of aqueous polymer dispersions.

4.1 Latex Dispersions: Film Formation by Physical Driving Forces

4.1.1 The Different Stages of Film Formation

Common understanding is, that the process of film formation can be described by a mechanism of consecutive stages which consist of (I) water evaporation, (II) particle ordering, (III) particle contact and deformation and (IV) particle coalescence (e.g. Winnik (1992), (1997); Keddie (1997); Toussaint (1997);...). Coalescence is defined as the step during film formation where the particles lose their individuality by interdiffusion of polymer chains. The general mechanism of film formation is illustrated in Figure 4-1.

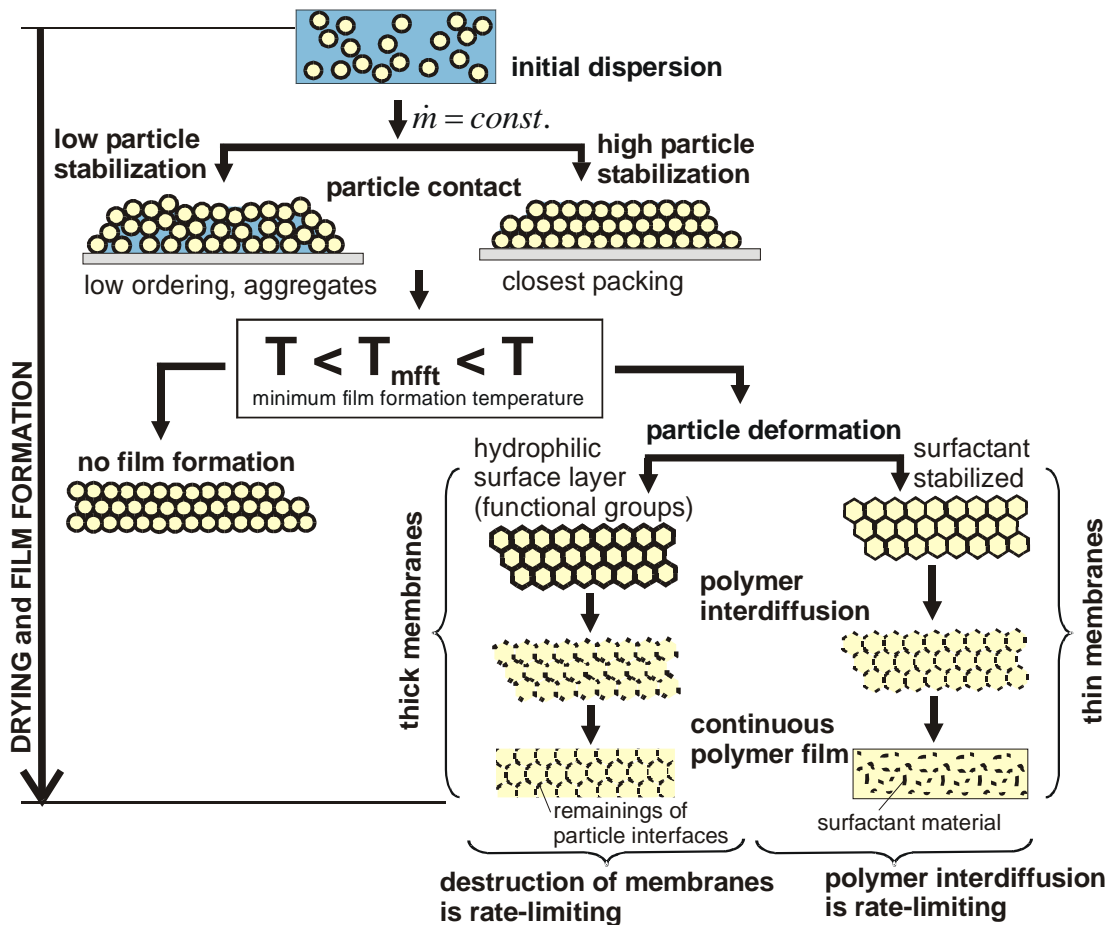


Figure 4-1: The different stages of latex film formation

The formation of a coherent, transparent and mechanically stable polymer film only occurs for drying above a certain temperature. In the coating business, this is called the **minimum film formation temperature** T_{mfft} . Practically, the T_{mfft} is the temperature, obtained from drying experiments, above which the dry polymer film is optically clear as a result of particle contact and deformation and does not show any cracks or defects. In scientific terms, the T_{mfft} is nothing else than the polymer's glass transition temperature T_g being a function of humidity: Due to the plasticizing effect of water, the T_g in the polymer dispersion is lower than in the dry polymer film.

During the initial stage of water evaporation, the milky-white dispersion dries at a constant rate of water loss. The initial dispersion has a concentration of $\sim 50 \text{ mass } \%$ polymer and is prevented from agglomeration by electrostatic and steric stabilization. During drying, the concentration of the latex particles continually increases and, - depending on the drying conditions, the nature and strength of particle stabilization and the ionic strength of the serum -, the particles come closer and arrange in a more or less ordered way. A high level of ions, initially present in the serum, would prevent particle ordering because it reduces interparticular repulsion and leads to early particle agglomeration.

After a certain drying time, the proximity of the particles and the increased concentration of ions in the remaining liquid reduce the existing particle repulsion which leads to irreversible particle contact and deformation. The particles ideally adopt a densest lattice packing (e.g. **face-centered-cubic** packing (fcc)) and deform into space-filling dodecahedrons. The deformability of the particles depends on the temperature difference between the ambient temperature and the minimum film formation temperature T_{mfft} . A larger temperature difference makes the particles more flexible. The extent of particle deformation in dependence of T_{mfft} has been studied by *van Tent* (2000) using turbidity measurements: Depending on the kind of particle stabilization and the drying temperature, particle deformation can occur prior to first particle contact. Transparency of the polymer film is observed as soon as the interstices between the deformed particles become smaller than the wavelength of light.

At this stage, the deformed particles are surrounded by a more or less thick layer of hydrophilic, surface-active material that prevents direct particle contact. If the particles have a hydrophilic surface layer which is the result of functional groups incorporated into the particle surface, this layer will be thicker than if it was made from surfactants adsorbed at the particle surface (*Visschers* (1997)). According to many authors (e.g. *Joanicot et al.* (1990); *Chevalier* (1996); *Winnik* (1997); *Stuard et al.* (2000);...), the rupture of the surfactant layer is pre-requisite for polymer interdiffusion which gives mechanical strength to the film (*Toussaint et al.* (1997)). In the case of a hydrophilic surface layer made from functional groups, the rupture of the membranes is the rate-limiting step towards coalescence, whereas for a surfactant layer it is the polymer interdiffusion (*Kim* (1995)).

The polymer chain mobility which controls coalescence is again a function of T_{mft} . If drying is well above the T_{mft} , particle deformation and polymer diffusion are strong enough to destroy the network of surfactant material to form a non-porous film. Then, islands of surfactant material will form in the film or the surfactant will be transported to the coating interfaces. If the drying temperature is close to the T_{mft} , particle deformation will be incomplete. Although the final film appears transparent, it is a porous structure of individual particles with a network of surfactant material present at the still existing particle-particle interfaces. Such a coating is susceptible to water permeation. The final film properties are fully obtained long after water has been removed from the film. Full mechanical strength of the film is only obtained after the hydrophilic layers between the particles have been destroyed. This is the case after polymer chains have diffused a distance that corresponds to half of the radius of gyration of the latex particles (*Winnik (1997)*).

4.1.2 The Driving Forces for Film Formation

There exist different theories and opinions regarding the driving forces for film formation. Review articles on this topic can be found in the literature (e.g. *Keddie (1997)*; *Winnik (1997)*; *Steward et al. (2000)*). In the different theories, the polymer/air surface tension (*Dillon (1951)*), the polymer/water interfacial tension and capillary forces (*Brown (1956)*) and capillary forces and osmotic pressure (*Sheetz (1956)*) are considered as driving forces. Depending on the experimental conditions and the material's properties, there exist experimental data that prove particle coalescence by any of the above mentioned driving forces. A recently developed model predicts the conditions necessary for the different driving forces to be dominant during film formation (*Routh and Russel (1999)*). A short survey of the main theories is given in Appendix V.

4.2 PU Emulsions: Film Formation by Chemical Crosslinking

To my best knowledge, there exist no papers dealing with the different stages of film formation of chemical crosslinking polyurethane (PU) emulsions. The experimental data of this study show that the general mechanism of film formation of aqueous PU emulsions can as well be described by several consecutive stages (see Figure 4-2).

Like for aqueous latex dispersions, drying of the initial PU emulsion is gasside controlled, i.e. the drying rate is controlled by the ambient drying conditions. The dispersion characteristics, like e.g. the droplet size of the different components, depend on the chosen preparation route (see Chapter 2.2.2). The initial emulsion, consisting of OH-functionalized acrylic polymer particles (= polyalcohol) and polyisocyanate droplets, has a solid content of ~50 mass % polymer, in which the two reactive compounds are prevented from particle agglomeration and chemical reaction by a large amount of surfactant. During drying, the emulsion droplets or particles come closer.

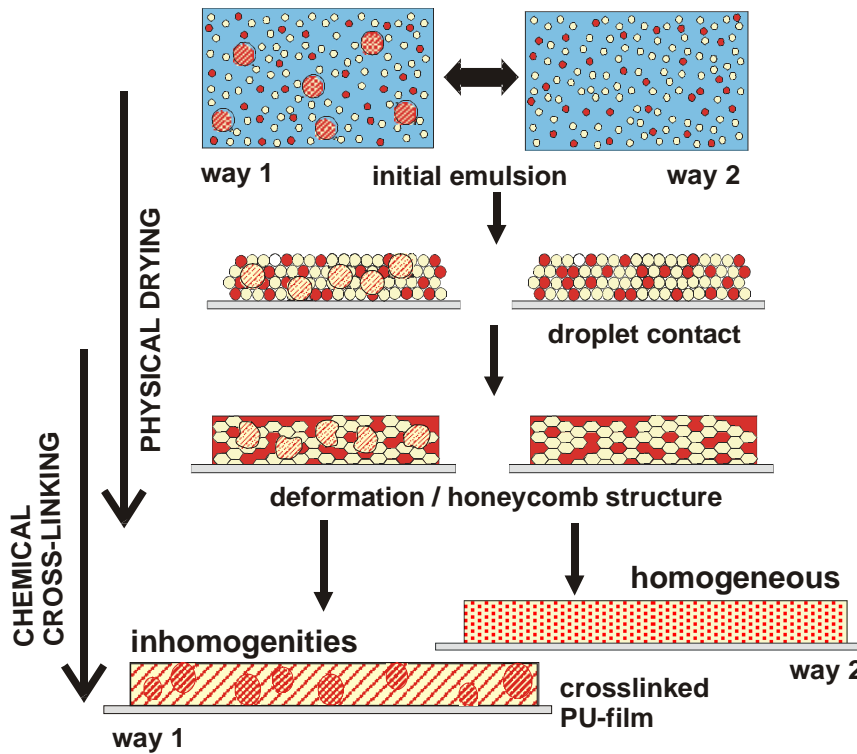


Figure 4-2: The stages of film formation of PU emulsions

Essential for the final coating quality and the mechanical stability is a homogeneous distribution of both components. In the concentrated emulsion, the droplets are forced into contact, deform and form a so-called honeycomb structure. At this moment, the particles are still separated by the surfactant material located at the interfaces, originally intended to stabilize the emulsion. The surfactant layer prevents, - or at least slows down -, crosslinking and some water is trapped in between the deformed droplets.

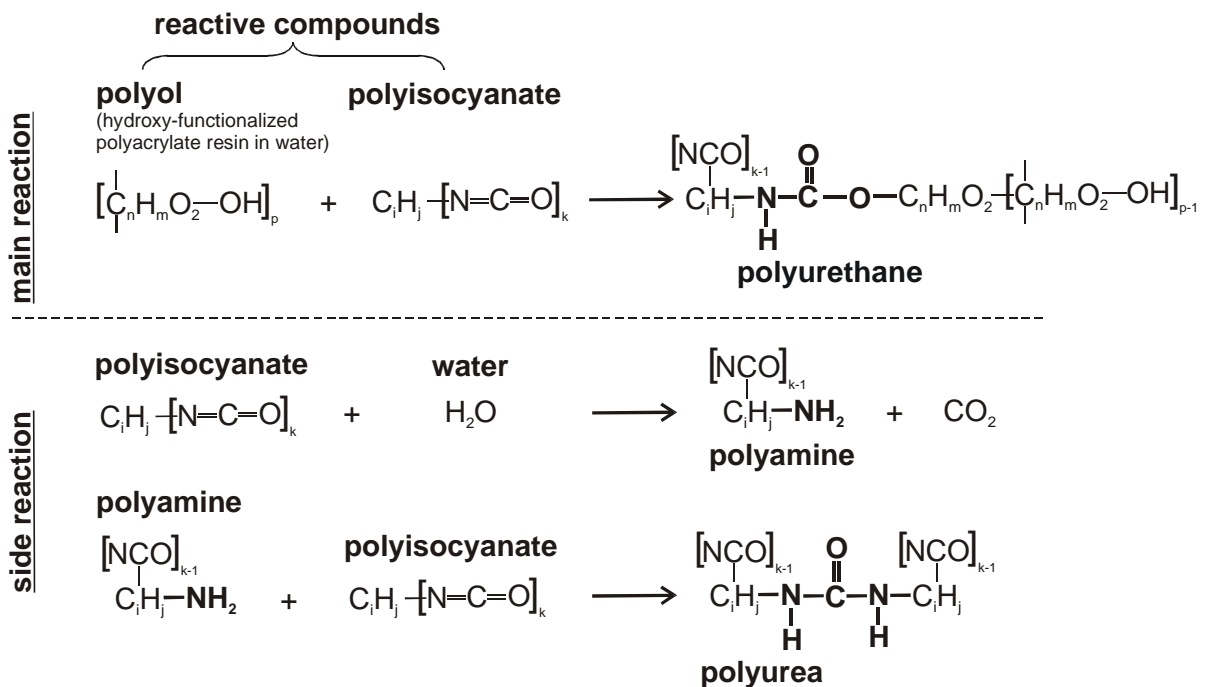


Figure 4-3: Formation of polyurethane and polyurea

The formation of polyurethane is by chemical reaction of an alcohol group with an isocyanate group. Diffusion processes across the surfactant layer will bring the reactive components into contact and lead to a destruction of the surfactant layer. Due to remaining water in the film, a side reaction can occur during which water reacts with isocyanate to form polyurea. The side reaction is taken into account by the initial ratio of functional groups, OH : NCO. Both reactions are shown in Figure 4-3.

Chemical crosslinking is slow compared to drying. Maximum crosslinking is only obtained after several days at room temperature or in a shorter time, when exposed to elevated temperatures (= higher activation energy for the chemical reaction).

4.3 Horizontal Inhomogeneous Drying

In connection with water-based polymer dispersions, horizontal inhomogeneous drying is the reason for coating defects, i.e. edge-effects and the existence of lap lines in the final dry coating. In industrial coating processes, the border area of aqueous coatings has normally to be disposed of because of such effects. Therefore, industry has fundamental interest in how to influence and avoid lateral inhomogeneous drying.

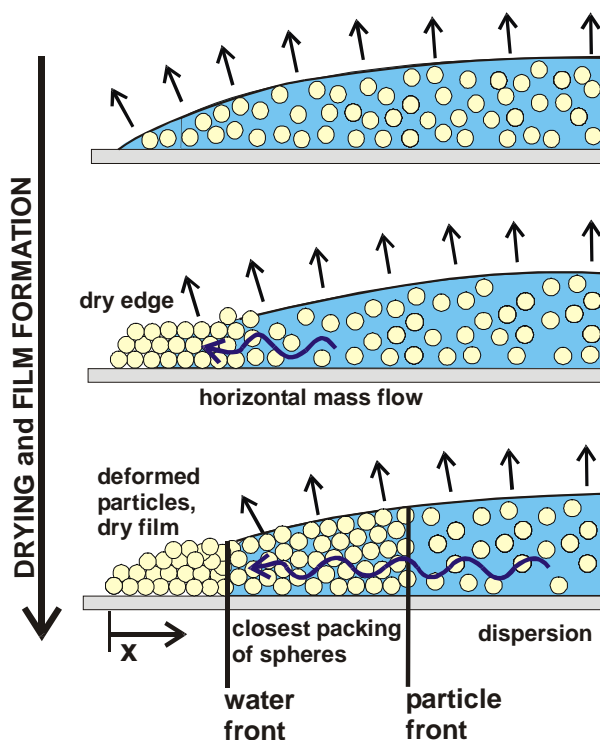


Figure 4-4: Different stages of horizontal inhomogeneous drying of aqueous polymer dispersions

Observations show, that drying is faster at the edge of a film layer due to the larger evaporation area and, - depending on the wetting properties of the dispersion -, due to a reduced film thickness. An ordered structure of closely-packed polymer particles first forms at the edge of the film. The reduced water content at the edge and a capillary pressure difference cause a horizontal flux of water and a limited flux of particles. In highly concentrated dispersions, the flow of polymer particles is limited

from the very beginning of drying. In aqueous polymer dispersions containing a large amount of surfactant, local surface tension gradients can normally be neglected as driving forces for horizontal mass flow. Once the capillary pressure difference is not large enough to wet the entire film surface, a drying front forms and starts to recede into the film towards its center.

The different stages of horizontal inhomogeneous drying are illustrated in Figure 4-4. For a finite capillary pressure, different zones form: (I) a dry zone of deformed particles at the edge, (II) a zone of closely packed particles and (III) a zone of dispersed particles in the center. The zones are separated by a particle front and a water front respectively. Water exclusively evaporates from the wet surface area. Horizontal mass flux towards the edge of the film is caused by water concentration gradients and a capillary pressure difference.

5 Local Concentration Measurements (by IMRS)

With the measurement technique of Inverse-Micro-Raman-Spectroscopy (IMRS) it is possible to quantitatively measure water concentration profiles in vertical and horizontal direction of thin polymer films online during drying. The chapter shows the experimental setup of the IMRS technique. For a better understanding, the theoretical basics of Raman spectroscopy and microscopy are explained in Appendix VI. The calibration method for a quantitative evaluation of the water concentration in thin films of concentrated polymer dispersion is explained. At the end of the chapter, problems with and limitations for spectroscopic measurements in turbid media (like dispersions) are discussed.

5.1 Experimental Setup

5.1.1 Air Conditioning

Within a drying channel located above the inverse microscope (= part of the IMRS setup), defined drying conditions, i.e. air humidity, drying temperature and air velocity can be adjusted. Figure 5-1 shows a flow chart of the complete setup.

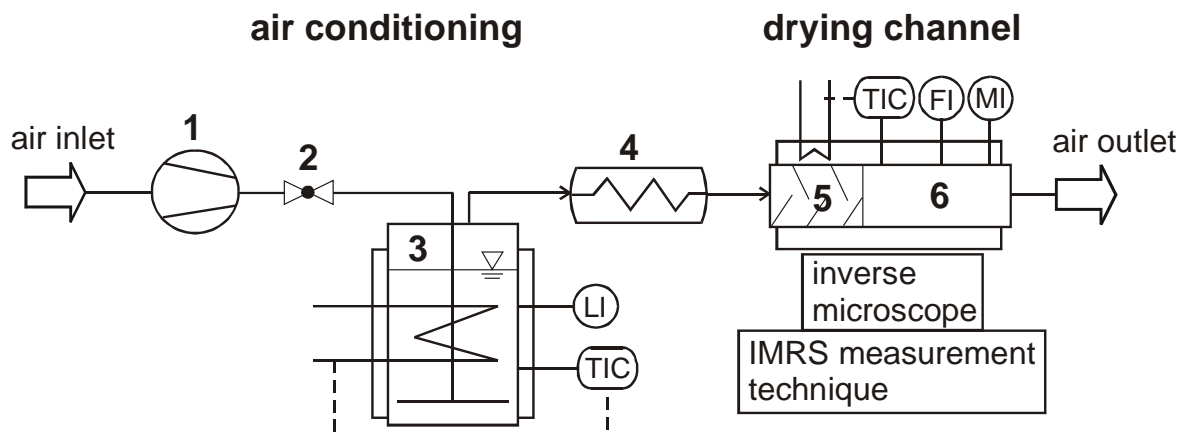


Figure 5-1: Flow chart of the experimental setup

Compressed ambient air, but also inert air of higher nitrogen content, can be used as process gas (1). The air humidity can be adjusted by complete saturation of the process gas with water at lower temperatures (3) and subsequent heating to the desired temperature (4). The air humidity in the channel is monitored by a moisture control. To assure isothermal drying conditions, the double-jacket drying channel (6) which is connected to a thermostate, is kept at the experimental temperature. In addition, the brazen sample holder which is centered in the drying channel above the inverse microscope, is also temperature-conditioned. The temperature in the drying channel directly above the sample holder is controlled by an external temperature sensor (PT100, $\varnothing 1\text{ mm}$).

The air velocity in the channel is adjusted by a needle valve (2) and is controlled at the measurement position by a hot-wire anemometer of accuracy ± 0.01 m/s. To assure a homogeneous flow pattern, flow straighteners are included into the drying channel (5).

5.1.2 Inverse-Micro-Raman-Spectrometer (IMRS)

Below the drying channel, an inverse microscope (Olympus IX50) is coupled with a confocal Raman spectrometer (Labram, Jobin Yvon). Both components are arranged on an optical table being designed to absorb external vibrations. Three lasers of different wavelength can be used in combination with the Raman technique. A He-Ne laser ($\lambda = 632$ nm) of 25 mW output power is integrated into the Labram spectrometer. Two external lasers, (I) an Argon laser ($\lambda = 514$ nm) with a continuously adjustable power output between 5 and 175 mW and (II) a solid-state laser ($\lambda = 532$ nm, up to 300 mW) can also be coupled with the measurement technique. The different lasers allow an optimization of the signal quality using either a higher laser intensity or light of a different wavelength (see also Appendix VI).

During a film drying experiment, a monochromatic, parallel laser beam is focused into the sample film by a system of mirrors and optical lenses. Within the polymer film, the laser light is scattered, - elastically (*Rayleigh*) and inelastically (*Raman*) -, due to the interaction of the laser light with the molecules of the sample. Then, the backscattered light is collected by the objective and is reflected back onto a notch filter. Notch filters are gels with an engraved interference pattern. Light of a certain (= the incident) wavelength is reflected, whereas light which differs from this wavelength can pass. Here, only the inelastically scattered light, the Raman light, having a different frequency compared to the incident laser light, can pass the interference pattern of the notch filter. High spatial resolution is reached by a confocal pinhole, which is optically coupled with the objective's focus. Only backscattered light from the plane of focus can pass. Finally, the filtered Raman light is spectrally fractionized by an optical grid and is detected by a peltier-cooled CCD-detector (**C**harge-**C**oupled **D**evice). In such a detector, the photons are absorbed by deuterated silica crystals which unleash electrical charges. These signals are used by the measurement software to generate the corresponding Raman spectrum. A representation of the principle of Inverse-Micro-Raman-Spectroscopy is given in Figure 5-2.

In the described setup, the position of the polymer film on the sample holder is fixed. A thin glass cover plate ($\varnothing 110$ mm, 170 μ m thickness), being the substrate for the sample film allows a non-invasive investigation of the sample film by IMRS. To measure concentrations in vertical direction of the film, a so-called piezo-nano positioning system (Physic Instruments) is employed. It is fixed at the microscope revolver and allows vertical positioning of the laser focus with an accuracy of 0.3 μ m (value provided by the supplier). The technique is based on the piezo-electrical characteristics of quartz crystals, which make them change their dimensions proportional to the connected voltage. The piezo-focus used here can move the objective's

focus between 0 and $350\ \mu\text{m}$ which corresponds to an applied control voltage between 0 and $100\ \text{V}$. Measurements at different horizontal positions of the film can be obtained by manual adjustment of the lateral measurement positions.

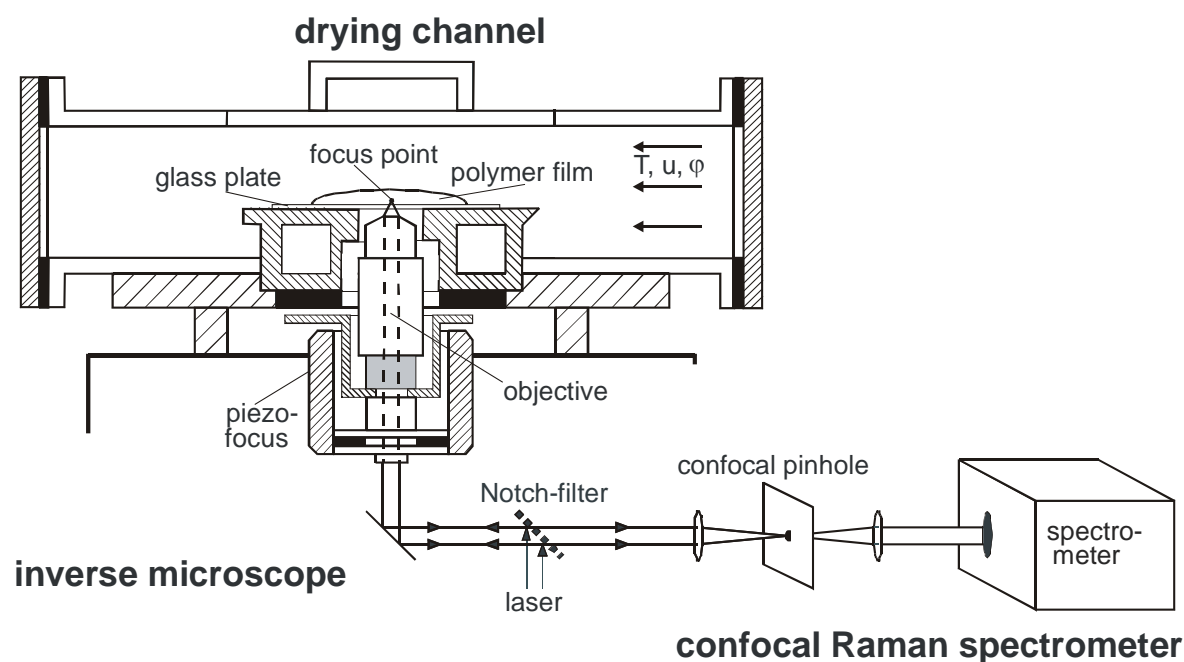


Figure 5-2: Inverse-Micro-Raman-Spectroscopy (IMRS) (Schabel (2004))

Abberations due to light fraction at any phase boundary (air-glass plate and glass plate-polymer film) can be minimized if all penetrated media are of similar refractive index. Therefore, a glass plate-corrected immersion oil objective is used in this study. It has a working distance of $200\ \mu\text{m}$ and has a large numerical aperture of 1.3 . Here, instead of air ($n = 1.0$) the space between the objective and the glass cover plate is filled by the immersion oil, having the same refractive index as the glass cover plate ($n = 1.51$). The refractive index of the initial aqueous dispersion is in the range of $n = 1.43$ and increases continually during drying. This means, that the optical resolution increases throughout the drying experiment.

5.2 Spectra Calibration

5.2.1 Raman Spectra of Relevant Components

The peaks of a Raman spectrum represent the frequency shift caused by the interaction of the laser light with the chemical bonds of a molecule. Therefore, Raman spectra are characteristic for the chemical species under investigation. The other way round, one can obtain information about the chemical structure of an unknown species from its Raman spectrum. Raman spectra of a mixture of different species are, as long as there is no strong interaction between the different molecules, the sum of the pure component's Raman spectra.

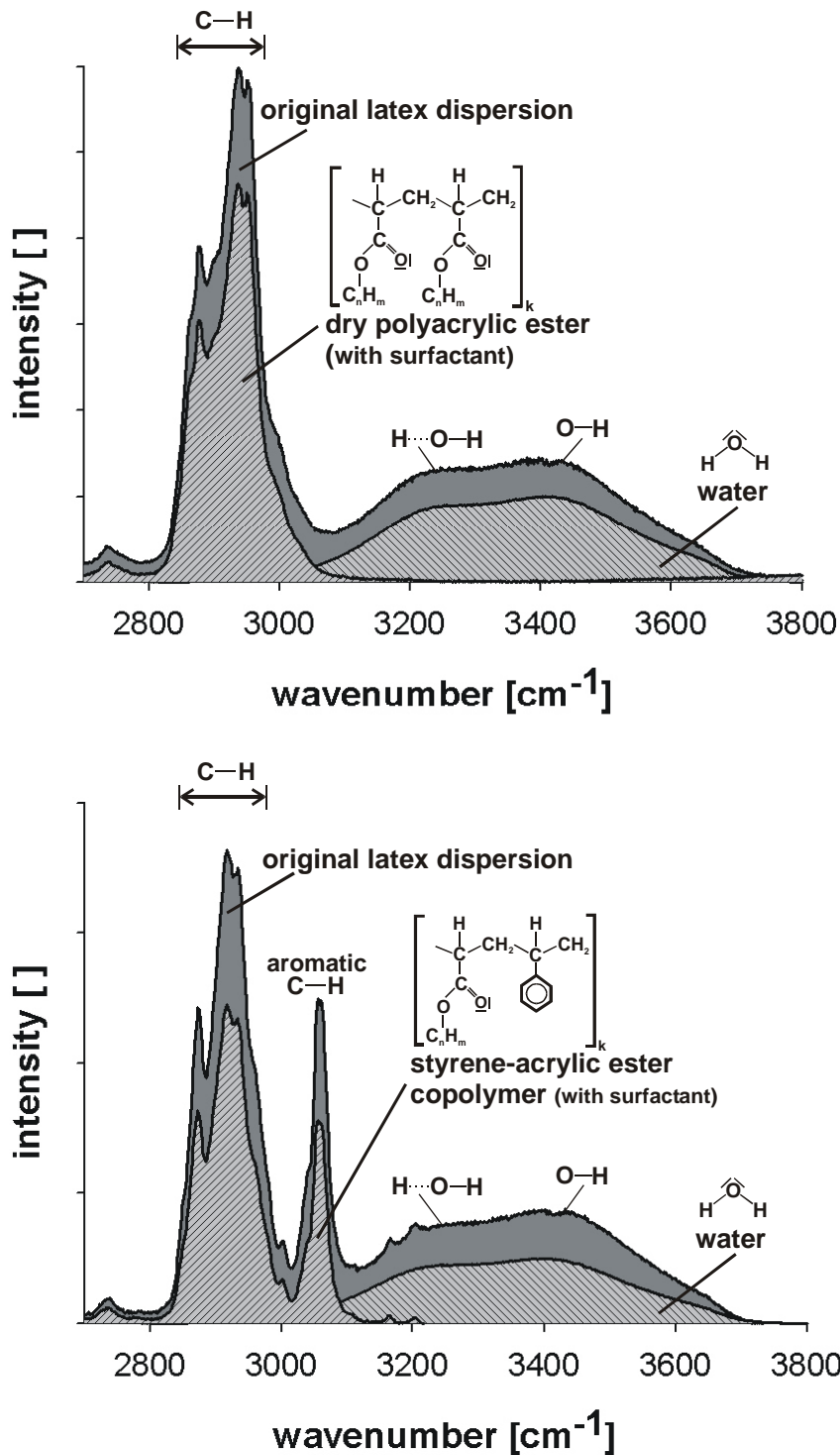


Figure 5-3: Raman spectra of the quasi-binary systems. Top: a pure acrylic latex dispersion; bottom: an acrylic-styrene latex dispersion

In this study, aqueous latex dispersions are treated as “quasi-binary” systems of (I) water and (II) polymer particles with surfactant. Figure 5-3 (top) shows the Stokes-Raman spectra of (I) the dry acrylic polymer with additives, (II) water and (III) the initial aqueous dispersion. The chemical structure of the molecules and the wavenumbers of the characteristic peaks are indicated. In Figure 5-3 (bottom), the Raman spectra of the single components are given for an acrylic-styrene latex dispersion.

The O-H bonds of water give one broad double peak at around 3500 cm^{-1} . The left shoulder represents the amount of hydrogen bonding and the right peak is from covalent O-H-bonds. The ratio of the two water peaks is therefore a measure for the amount of hydrogen bonding in the aqueous dispersion. Symmetrically oscillating bonds have especially high Raman signals, e.g. C-H and C=O bonds. A table with a number of characteristic Raman peaks is given in Appendix XIV.

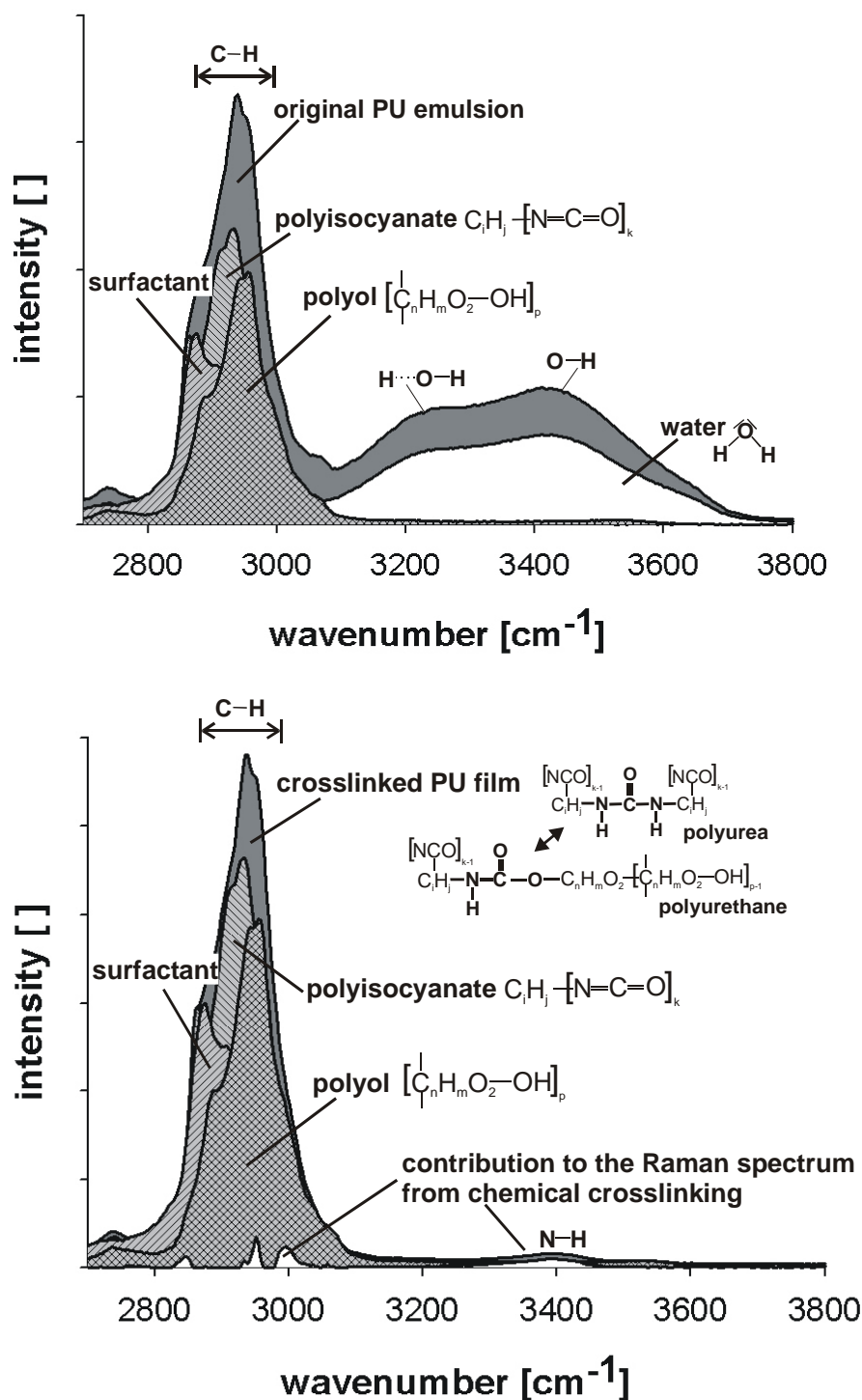


Figure 5-4: Raman spectra of the quasi-quaternary system (PU emulsion). Top: during drying; bottom: in the crosslinked PU film

Polyurethane (PU) emulsions are chemical crosslinking systems, meaning that their Raman spectrum changes not only due to water evaporation during drying, but also due to the formation of new chemical bonds. By the formation of polyurethane from a polyalcohol and a polyisocyanate, N=C double-bonds are broken and N-H bonds are formed. Unfortunately, both bondings display only weak Raman signals and, - as long as water is present -, the N-H peak is masked by the broad peak from O-H bonding (compare the Stokes-Raman spectra in Figure 5-4 (top)). It is therefore impossible to observe the beginning of crosslinking as long as water is present in the coating. Fortunately, crosslinking takes much longer time than drying, which makes it possible to treat both processes independently. This is done by the separate evaluation of the Raman spectra of (I) the aqueous emulsion and (II) the dry and crosslinked film. In both cases, the systems are regarded as “quasi-quaternary”.

The aqueous PU emulsion consists of the two reactive compounds, polyalcohol (= polyol) and polyisocyanate, and further of surfactant and water. Figure 5-4 (top) shows the component's Stokes-Raman spectra and the spectrum of the initial PU emulsion. Again, the chemical structure of the molecules and the wavenumbers of the characteristic peaks are indicated.

The dry and crosslinked film is treated as a system which consists of the polyol, polyisocyanate, surfactant and of reacted functional groups (= chemical crosslinking). The crosslinking is represented by the Raman spectrum of the bonds that form during chemical crosslinking. The component's Stokes-Raman spectra and the spectrum of a fully crosslinked PU film are shown in Figure 5-4 (bottom).

5.2.2 Concentration Measurements

The intensity of a Raman signal is linear proportional to the number of scattered photons in the volume that is illuminated by the laser (*Mayinger (1994)*). Therefore, the Raman intensity of a chemical species *i* can be expressed by the following simple equation which shows a linear dependence on concentration (*Moritz (1999)*):

$$I_i = \underbrace{\left(\frac{\partial \sigma}{\partial \Omega} \right)_k}_{\text{specific for investigated species}} \cdot \frac{c_i}{\tilde{M}_i} \cdot \underbrace{N_A \cdot V \cdot \Omega_{\text{obs}} \cdot F^{-1} \cdot C \cdot I_0}_{\text{experimental factor}} \quad \text{Equ. 5-1}$$

with:

- $(\partial \sigma / \partial \Omega)_k$ = differential scattering cross-section for vibration *k*
- c_i = concentration of component *i*
- \tilde{M}_i = molar mass of component *i*
- N_A = *Avogadro* constant
- V = sample volume
- Ω_{obs} = observation angle of the objective
- F = projection screen of the detector aperture onto the sample volume
- C = constant (considers the detector efficiency)
- I_0 = intensity of incident laser light

The primary parameter characterizing the vibrational Raman spectrum is the differential scattering cross-section. It is defined by the probability to observe a scattered photon in a given quantum state per solid angle unit, if the target is irradiated by a flux of one photon per surface unit. In other words, the differential scattering cross-section is a measure for the Raman activity of the vibration k of a molecule under investigation. It can be obtained from a geometric derivative of the electric dipole polarizability, evaluated at the frequency of the incident laser light. For diatomic molecules, *Pecul* and *Rizzo* (2002) give the following expression for a harmonic approximation of $\partial\sigma/\partial\Omega$ (Stokes) perpendicular to the linear polarized incoming beam:

$$\left(\frac{\partial\sigma}{\partial\Omega}\right)_{k(\text{Stokes}, \perp)} = \frac{2\pi^4}{45} \frac{h}{8\pi^2 c \tilde{\nu}_0 \mu} \left(\frac{(\tilde{\nu}_0 - \Delta\tilde{\nu}_k)^4}{\Delta\tilde{\nu}_k (1 - \exp[-hc\Delta\tilde{\nu}_k/kT])} \right) \quad \text{Equ. 5-2}$$

$$(45(\nabla_e \bar{\alpha}(\tilde{\nu}_0))^2 + \frac{7}{4}(\nabla_e \Delta\alpha(\tilde{\nu}_0))^2)$$

with:

c	= velocity of light
h	= <i>Planck's</i> constant
$\tilde{\nu}_0$	= laser wavenumber
μ	= reduced mass
$\Delta\tilde{\nu}_k$	= vibrational wavenumber
$\nabla_e \bar{\alpha}(\tilde{\nu}_0)$	= bond length derivative of $\bar{\alpha}(\tilde{\nu}_0)$
$\nabla_e \Delta\alpha(\tilde{\nu}_0)$	= bond length derivative of $\Delta\alpha(\tilde{\nu}_0)$
$\bar{\alpha}(\tilde{\nu}_0)$	= average (isotropic) molecular polarizability
$\Delta\alpha(\tilde{\nu}_0)$	= anisotropic molecular polarizability

The unknown concentration of a species could be obtained from calibration measurements at constant testing conditions, like laser volume, observation angle, detector efficiency and laser light intensity. However, these parameters are almost impossible to be kept constant, even for two consecutive measurements. Besides, they are difficult to obtain from experiments. Especially in polymer-solvent systems, where the polymer component is non-volatile, one is less interested in absolute concentrations (= intensity of the pure components) but in the content of water in the polymer (= relative intensities). In this case, one can form relative intensities, taken from the same Raman spectrum, to obtain good quality concentration data, regardless of experimental conditions. By the formation of the intensity ratio of solvent and polymer component all experimental factors cancel out according to:

$$\frac{I_i}{I_p} = \frac{\left(\frac{\partial\sigma_i}{\partial\Omega}\right) \cdot \frac{c_i}{\tilde{M}_i}}{\left(\frac{\partial\sigma_p}{\partial\Omega}\right) \cdot \frac{c_p}{\tilde{M}_p}} \cdot \underbrace{\frac{N_A \cdot V \cdot \Omega_{\text{obs}} \cdot F^{-1} \cdot C \cdot I_0}{N_A \cdot V \cdot \Omega_{\text{obs}} \cdot F^{-1} \cdot C \cdot I_0}}_{=1} \quad \text{Equ. 5-3}$$

And with the definition of the solvent content per polymer,

$$X_i = \frac{m_i}{m_p} = \frac{m_i/V_{\text{total}}}{m_p/V_{\text{total}}} = \frac{c_i}{c_p} \quad \text{Equ. 5-4}$$

Equ. 5-3 has the following simple form:

$$\frac{I_i}{I_p} = \underbrace{\left(\frac{\partial \sigma_i / \partial \Omega}{\partial \sigma_p / \partial \Omega} \right)}_{=K} \cdot \frac{\tilde{M}_p}{\tilde{M}_i} \cdot X_i = K \cdot X_i \quad \text{Equ. 5-5}$$

The proportionality factor K can be obtained from the Raman spectrum of one single calibration sample of known concentration, independent of the conditions and the exact experimental setup.

5.2.3 Spectra Evaluation

According to Equ. 5-4 and Equ. 5-5, a quantitative evaluation of the Raman signal can be obtained from the intensity ratio of the Raman peaks that are specific for the chemical species under investigation. A measure for the Raman intensity is either the maximum peak height, or the area below the peak which, however, gives more accurate results.

For the data evaluation by peak area, the definition of a spectral window with distinct peaks is necessary. For aqueous polymer dispersions, this is the range represented by a Raman shift of 2700 to 3800 cm^{-1} which contains the sharp peak of the C-H vibration of the polymer and the broad peak, resulting from the O-H-bonds of water (Figure 5-3 and Figure 5-4). In the selected window, the intensity curve is baseline-corrected to separate the spectral noise from the Raman signal. As stated above, the dispersion is treated as a quasi-binary mixture of stabilized polymer particles and water. In the Raman spectrum of an aqueous polymer dispersion, the distinct peaks, being specific for the one or the other component, normally overlap. From the spectrum of the mixture, it is therefore not readily clear which part of the total area below the curve contributes to the concentration of the solvent and which to the concentration of the polymer. There are two ways to obtain the relative areas that contribute to the intensity of the polymer and the one of water:

One possible way is described by *Schabel et al.* (2003) who use a certain wavenumber to subdivide the spectral window into two areas A, B that are dominated by either component, the polymer or the solvent, and are influenced by the other component. The formation of relative parts per total area from the pure spectra of each component in A, B is necessary to come up with an expression for the part of the total area of the mixture that contributes to the concentration (intensity) of each of the two components. The method can also be applied for three- and multi-component systems. A comprehensive explanation of the method can be found in *Schabel* (2005).

The second way employs a computer algorithm developed by *Scharfer* (2006) and realized in VBA (= Visual Basic for Application). The routine is based on the fact that, in many cases, a multi-component Raman spectrum can be obtained from the sum of the pure component Raman spectra, multiplied by so-called weighting factors x_i . The weighting factors x_i are obtained from a least-square-fit of the normalized multi-component Raman spectrum by normalized pure component spectra in the selected spectral window. The NAG Fortran library E04FYF is used to calculate the weighting factors x_i that minimize the sum of the differences between the Raman experimental intensity and the calculated intensity for each wavenumber of the spectral window. It is an algorithm for finding an unconstrained minimum of a sum of squares of m non-linear functions of n variables. In addition, the measured Raman spectrum is shifted in steps of 0.1 cm^{-1} to lower and higher wavenumbers to find the global minimum of that sum between the measured and the calculated spectrum. For the weighting factors in the normalized spectrum, the following constraint holds:

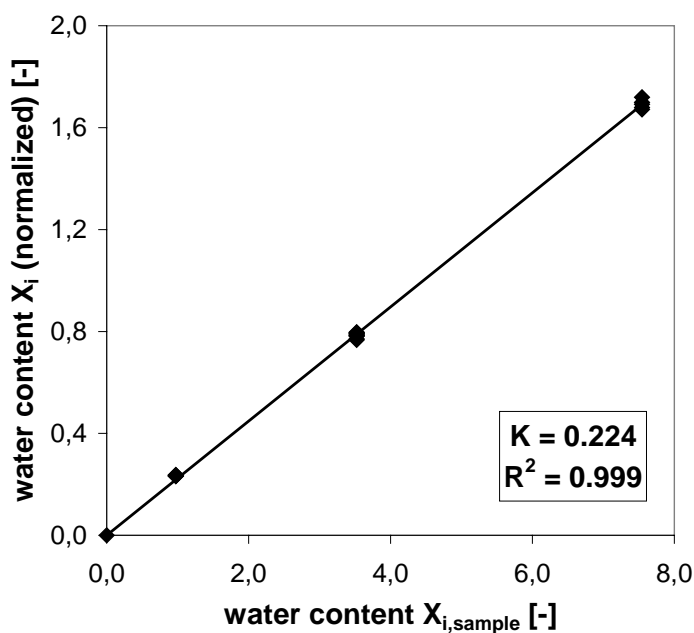
$$\sum_i x_i = 1 \quad \text{Equ. 5-6}$$

From this, the relative content of each component i with regard to the polymer component p can be calculated from:

$$X_i = \frac{x_i}{x_p} \quad \text{Equ. 5-7}$$

The absolute content of component i per polymer in the sample is expressed by:

$$X_{i,\text{sample}} = \frac{X_i}{K} \quad \text{Equ. 5-8}$$



In Equ. 5-8, K is the calibration constant, which is obtained from a plot of X_i over $X_{i,\text{sample}}$ for samples of known concentration. K is specific for the investigated dispersion.

The VBA routine is used in this work for the quantitative evaluation of the spectral data.

Figure 5-5: Calibration constant K of A-H-1 (obtained by the VBA-routine)

5.3 Signal Intensity Loss by Scattering in Polymer Dispersions

In the case of heterogeneous systems, such as latex dispersions, the light scattering properties of the medium can seriously influence the intensity of the Raman signal. The incident laser beam is not only transmitted, but also reflected and diffracted by single and multiple scattering at the particles. In the following chapter, the influence of particle size and particle concentration on light scattering and signal intensity loss in polymer dispersions is investigated experimentally. This shall prove the validity of the above described quantitative evaluation method of spectroscopic data also for scattering media like concentrated latex dispersions. Light scattering is influenced by the particle size, shape and interparticle distance.

The absolute Raman signal is very sensitive to the position of the laser focus in the polymer dispersion, expressed by an exponential decrease of the signal intensity with increased focal depth in the film. This is illustrated in Figure 5-6 and Figure 5-7 which give Raman spectra at different positions in a thin film of aqueous polymer dispersion and show the integral intensity of the polymer peak at 3000 cm^{-1} as a function of focus position.

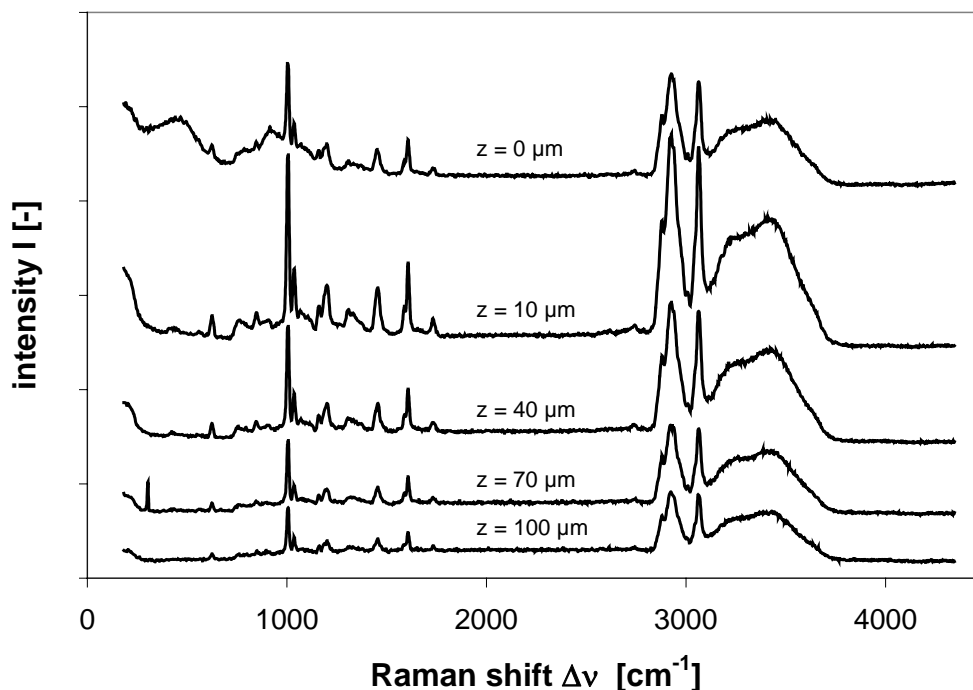


Figure 5-6: Selected Raman spectra at different focal positions in a wet film

The decrease in laser light intensity is due to a loss of photons, caused by one or both of the following elastic photon-particle scattering effects (*van den Brink et al. (2002)*):

- (I) Incoming (= unshifted) photons scatter off their path into the sampling volume, causing a lower effective photon density at the measurement position.
- (II) The collection of the Raman signal may be influenced by the elastic scattering of Raman-scattered photons at the latex particles. If this is the case, it also influences the

relative intensities in the Raman spectrum, since scattering of light varies with the wavelength to the power of minus four. Blue light is scattered more strongly than light of higher wavelength. This may result in a significantly stronger attenuation of the Raman spectrum at lower wavelength.

If one would use light excitation in the near-infrared region (750 - 1400 nm), a so-called self-absorption effect of the Raman scattered photons would cause a decrease of the laser light intensity (e.g. *Agarval et al. (2005)*). The effect occurs when water absorption bands overlap with the Raman spectrum, causing the spectrum to change in a non-linear way, due to the difference in path length, from multiple light scattering.

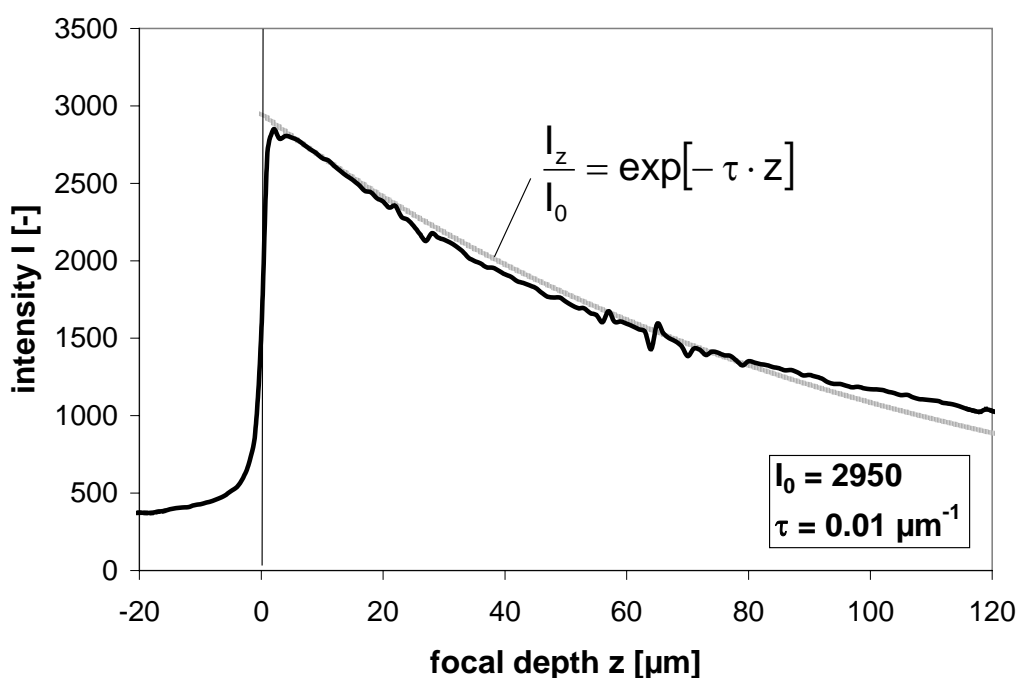


Figure 5-7: Raman intensity as a function of the focal depth ($X \sim 1.0$ g water/g pol.). The decay of intensity can be well described by exponential turbidity laws

The measured absolute intensity strongly depends on the concentration of the particles and the light scattering properties of the medium. Changes in the particle size by e.g. aggregation can cause changes in the turbidity, even though the solid content remains constant. In general, for small particle sizes and dilute dispersions, the absolute signal intensity can be described by the *Lambert-Beer* law:

$$I_z = I_0 \exp[-\varepsilon_\lambda \cdot c \cdot z] \quad \text{Equ. 5-9}$$

with:

- I_z = transmitted light after length z
- ε_λ = extinction coefficient
- c = particle concentration

In higher concentrated dispersions, the classic light scattering theory is no longer obeyed and departures from linearity can occur because of multiple-scattering effects, which makes a theoretical description rather complex. Multiple-scattering of photons is highly analogous to diffusion, which is why diffusion models are often successfully

employed to describe multiple-scattering behaviour (e.g. *Weitz et al. (1989); Zhu et al. (1992)*). *Riebel (1991)* used statistical analysis to describe the extinction of radiation in dispersions of a large concentration range.

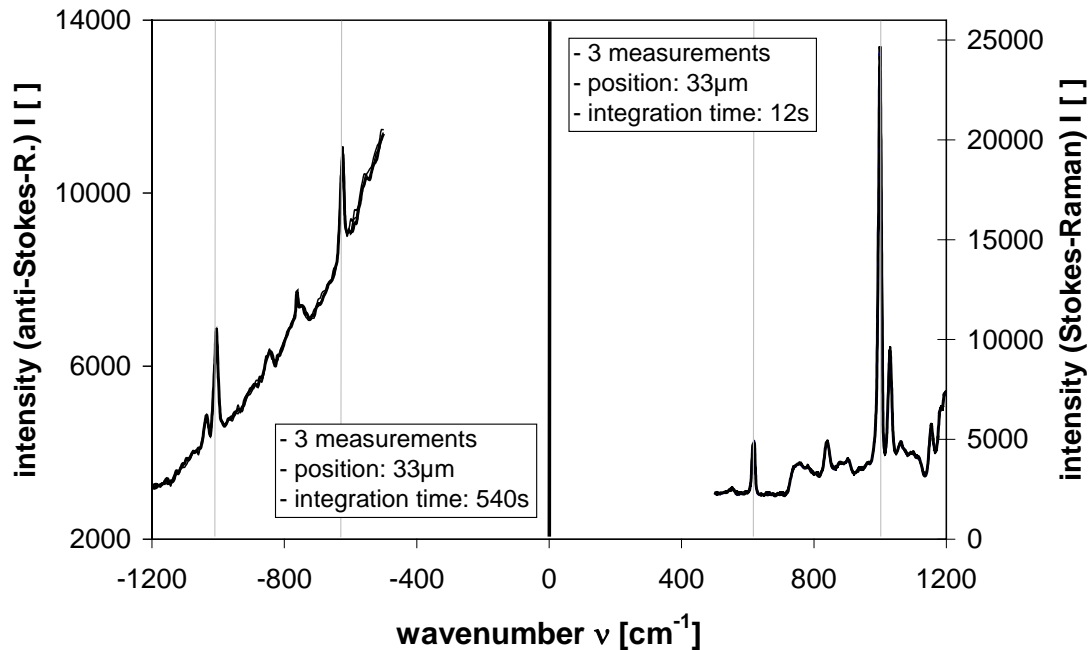


Figure 5-8: Anti-Stokes-Raman and Stokes-Raman spectrum of an aqueous polymer dispersion

Typical for higher concentrated dispersions is, that the experimental transmission is higher than predicted from the *Lambert-Beer* law and the deviation can be attributed to multiple-scattering (*van den Brink et al. (2002)*).

Nevertheless, in many cases the decay of the transmitted intensity in highly concentrated dispersions can still be described by an exponential decay according to:

$$\frac{I_z}{I_0} = \exp[-\tau \cdot z] \quad \text{Equ. 5-10}$$

with:

$$\tau = \text{turbidity of the medium}$$

The turbidity is related to the number of particles in the sampling volume and the individual particle extinction cross-section:

$$\tau = n \cdot \sigma_{\text{ext}} \quad \text{Equ. 5-11}$$

Extinction may originate from both, absorption and scattering. If there would be energy dissipation in the polymer film caused by laser light absorption, the temperature-dependent anti-Stokes Raman part of the spectrum would change. But, repeated measurements at one position of the film show, that the spectra always coincide (compare Figure 5-8).

Considering the above observations, the wavelength ($\lambda = 514 \text{ nm}$) of the laser and the material under investigation (= an aqueous dispersion, of a particle size $\sim 100 \text{ nm}$), it can be assumed that extinction is solely due to scattering at the particles and the following will be valid:

$$\sigma_{\text{ext}} = \sigma_{\text{scatter}}$$

Equ. 5-12

The above approach to describe τ doesn't take into account the increase of the sampling volume with focal depth which may cause a systematic error.

5.3.1 Particle Size Effect

Different latex dispersions of same polymer content but different particle size are used to illustrate particle size effects on the Raman signal intensity.

Figure 5-9 and Figure 5-10 show normalized Raman intensities at different focus positions as a function of the particle diameter d . The data are given for two different polymer solid contents of ~ 35 and $\sim 50 \text{ mass } \%$ polymer, corresponding to $X = 1.8$ and $X = 1.0 \text{ g water/g polymer}$. The figures show, that the data can be well described by exponential turbidity laws, even for concentrated latex dispersions of up to $\sim 50 \text{ mass } \%$ polymer and for a particle size ranging between $d = 35 \mu\text{m}$ and $d = 160 \mu\text{m}$. One can see that the decay of intensity is stronger for larger particles and for lower polymer contents. This can be explained by a multiple-scattering effect, causing a reduced transport mean free path of the photons in direction of the objective's lense in the more diluted dispersion (see also Chapter 5.3.3 below).

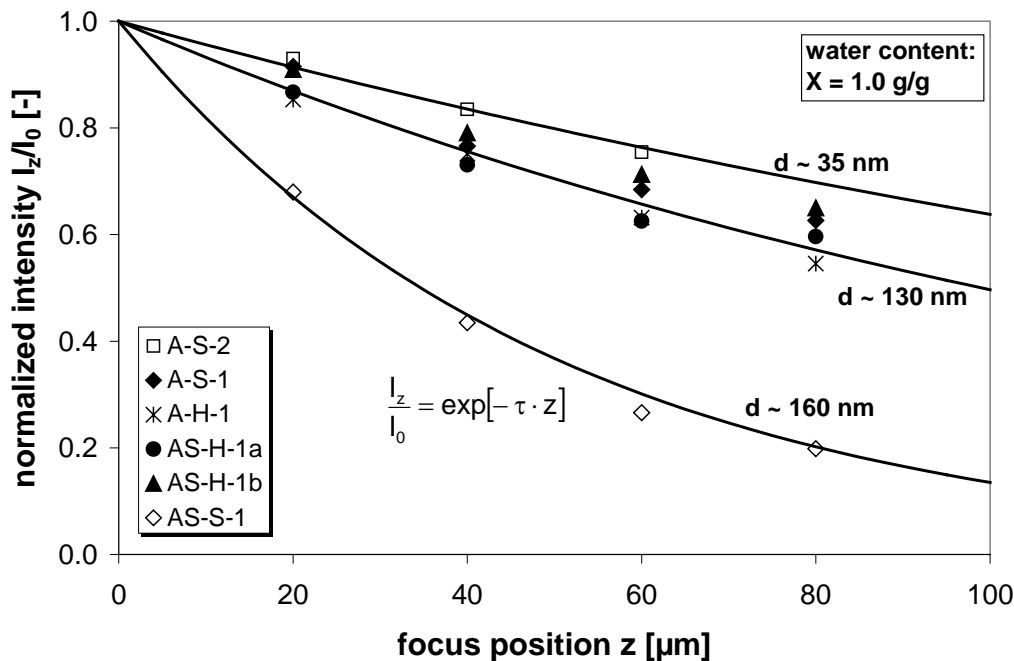


Figure 5-9: The decay of intensity in the film as a function of particle size d ($X = 1.0 \text{ g water/g polymer}$)

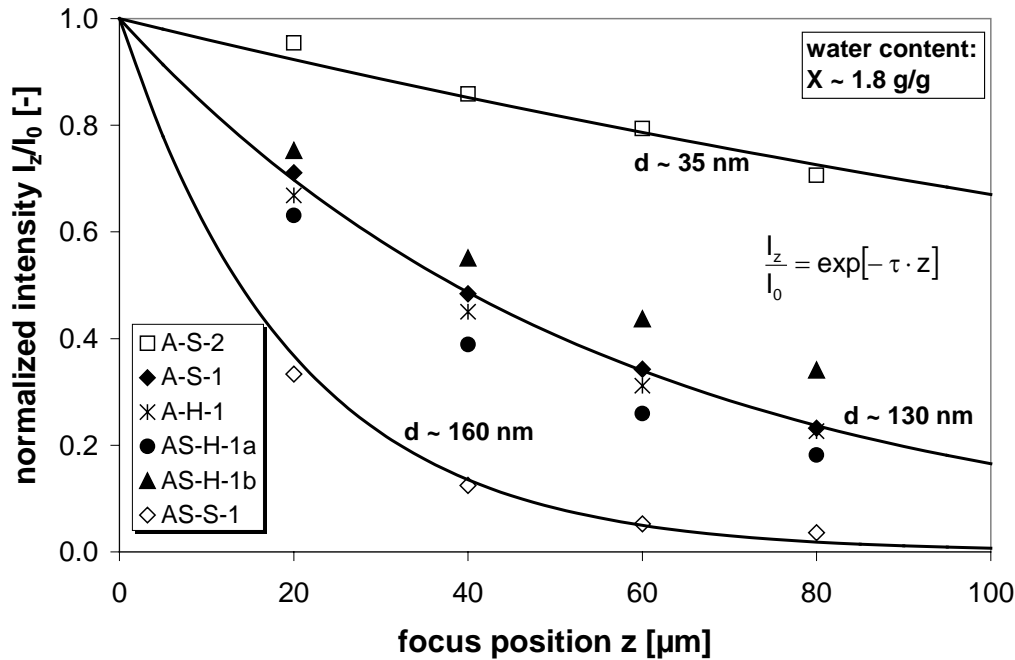


Figure 5-10: The decay of intensity in the film as a function of particle size d ($X = 1.8$ g water/g polymer)

According to the *Mie-Rayleigh* theory, the scattering intensity I_s and scattering cross-section σ_s are proportional to the particle diameter d to the power of six. This is explained by the fact that for particles, being small compared to the wavelength of light, scattering is coherent everywhere on the particle surface. Since the number of scattering centers on a particle is proportional to the particle volume, the following holds:

$$P \sim d^3 \quad \text{and} \quad I_s = (P \cdot E)^2 \sim d^6 \quad \text{Equ. 5-13}$$

with:

P = number of scattering centers on a particle surface
 E = electrical field

The same also holds for the extinction τ .

$$\tau \sim n \cdot d^6 \quad \text{Equ. 5-14}$$

with:

n = quantity representing the scattering events in the dispersion

Therefore, the normalized intensity at focus position z can be described by:

$$\frac{I_z}{I_0} = C \cdot \exp[-n \cdot d^6 \cdot z] \quad (C = \text{constant}) \quad \text{Equ. 5-15}$$

According to Figure 5-11 and Figure 5-12, the power-six-dependence on the particle diameter is well fulfilled by the latex dispersions under investigation. Here, the intensity ratio at different focal positions I_z/I_0 is shown for a water content of $X = 1.0$

and $X = 1.8 \text{ g water/g polymer}$. For the experiment a laser with an excitation wavelength of $\lambda = 514 \text{ nm}$ was used and the data evaluation was done with the characteristic C-H Raman peak at $k \sim 3000 \text{ cm}^{-1}$. Data fitting gives a value of $n = 350$ for the dispersion of $X = 1.0 \text{ g water/g polymer}$ ($n = 2400$, $X = 1.8 \text{ g/g}$), meaning that the transport length in the more concentrated dispersion ($X = 1.0 \text{ g/g}$) is longer and light is less scattered.

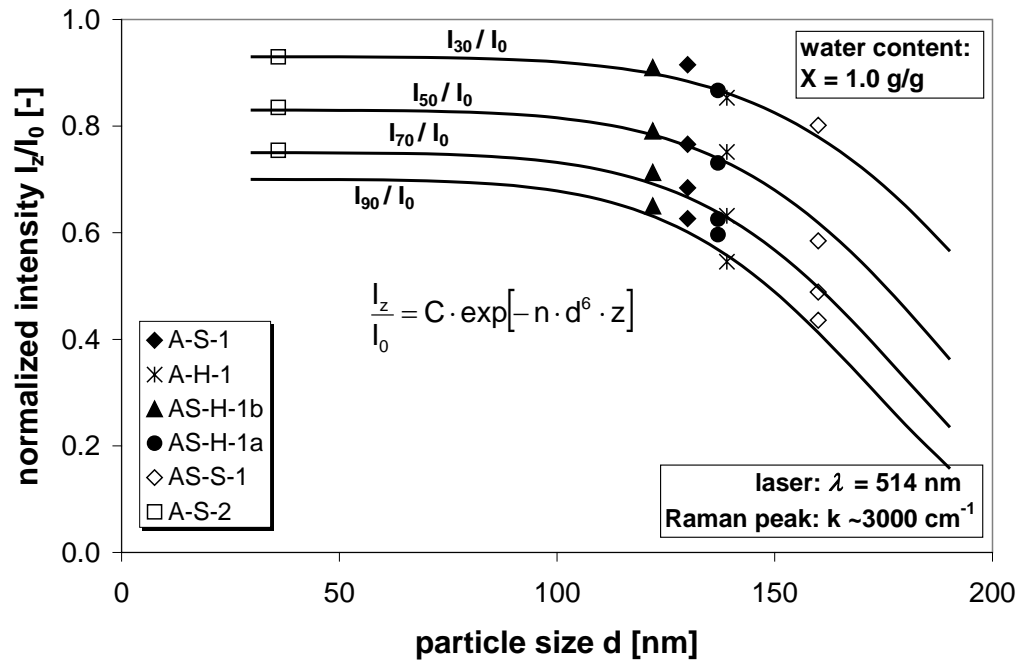


Figure 5-11: Normalized Raman intensity I_z/I_0 at different focus positions z as a function of the particle diameter d ($z = 30, 50, 70, 90 \mu\text{m}$; $X = 1.0 \text{ g/g}$)

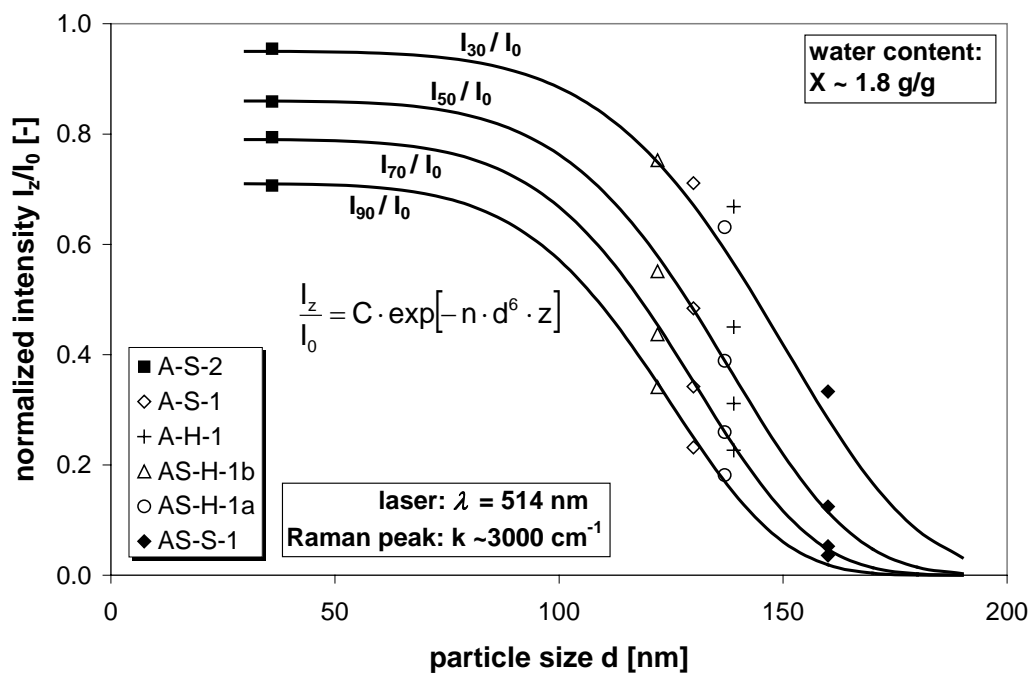


Figure 5-12: Normalized Raman intensity I_z/I_0 at different focus positions z as a function of the particle diameter d ($z = 30, 50, 70, 90 \mu\text{m}$; $X = 1.8 \text{ g/g}$)

5.3.2 Solid Content of the Dispersion

Figure 5-13 shows the normalized Raman intensity I_{50}/I_{\max} taken at a focal position of $z = 50 \mu\text{m}$ as a function of the water content X . Whereas for a water content below $X \sim 1.2 \text{ g water/g polymer}$ the expected linear relation between Raman intensity and concentration $I \sim X$ is observed, it is not the case at higher water contents X . Above $X \sim 1.2 \text{ g water/g polymer}$, the Raman intensity shows a minimum constant value that is insensitive to certain changes in the water content X , but strongly depends on the latex particle size. For $d \sim 35 \mu\text{m}$, the decay of intensity is only around 10%, meaning that multiple-scattering of photons at small particles is less important. For a particle size of $d \sim 160 \mu\text{m}$, the decrease of intensity is more than 80%.

The latex dispersions used in this work to investigate the different aspects of film formation have an initial water content of $X \sim 1.0 \text{ g water/g polymer}$ (exception: A-S-2 where $X \sim 2.5 \text{ g/g}$). Investigations of drying and film formation are therefore always performed in the region, where the linear dependence of the Raman intensity on concentration is valid.

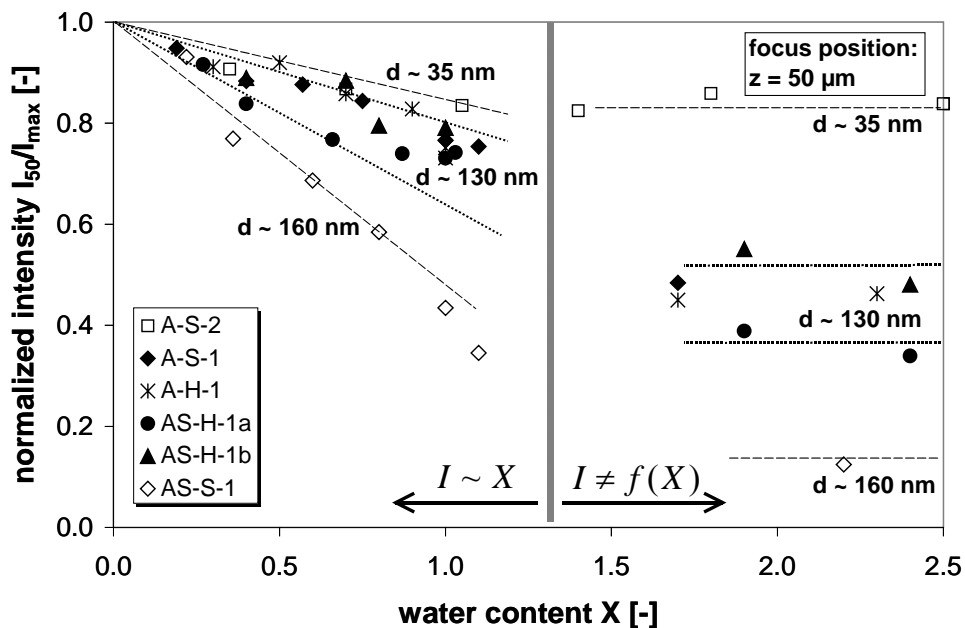


Figure 5-13: The decay of intensity as $f(\text{water content } X; \text{ particle size } d)$

5.3.3 Appraisal of these Effects on the Quantitative Data Evaluation

Owing to the discrete nature of the particles, the signals emerging from extinction measurements in concentrated dispersions and other multi-phase media are subject to spatial fluctuation, caused by multiple particle-scattering. Garg *et al.* (1997) investigated the transmittance of highly concentrated dispersions of polymer volume fractions of up to $\phi = 0.55$ by 100 fs laser pulses. They found, that in the dilute limit the transport length of the photons in the dispersion decreases linearly with increasing particle concentration. For higher concentrations, the decrease in the transport length is

less than linear as a result of correlated scatterers. Above a critical concentration, at which the interparticle spacing becomes comparable to or less than the wavelength of the incident light, an again increased transport scattering mean-free-path is observed, expressed by a less severe decay of intensity.

As stated above, the loss of signal intensity is mainly caused by scattering of either incoming, unshifted photons or of Raman-scattered photons. In the first case, all photons have the same wavelength, corresponding to the incident laser light; in the second case, the inelastically scattered photons have a different wavelength to the excitation wavelength. From theory it is known, that the extent of light scattering strongly depends on the wavelength ($I \sim \lambda^{-4}$). If the decrease in detected Raman intensity was due to photon-particle scattering of Raman-shifted photons, there would be considerable differences in the number of scattered photons depending on wavelength. This may result in a significantly stronger attenuation of the Raman spectrum at lower wavelengths. Figure 5-14 and Figure 5-15 show the original Raman data of an aqueous polymer dispersion obtained from different focal positions z in the film for water contents of $X = 1.0$ and $X = 1.8 \text{ g water/g polymer}$. In addition, they show the normalized peak intensity as function of focus position for selected Raman shifts in the spectral window used for evaluation.

Obviously, scattering of incoming, unshifted or of Raman-scattered photons strongly depends on the interparticle distance: The more dilute dispersion of $X = 1.8 \text{ g water/g polymer}$ doesn't show any long-range particle ordering or beginning particle contact. According to Equ. 3-13, the particles have a large average interparticle distance of $\bar{h} \sim 75 \text{ nm}$. However, the distance is inhomogeneous due to *Brownian* motion of the particles. Scattering is caused by the large refractive index difference between the particles and the medium. The interparticle distance is large enough to scatter a considerable amount of photons off the way so that they are not recollected by the objective, resulting in a strong decrease of the signal intensity with focus position z . Therefore, in the dilute dispersion of $X = 1.8 \text{ g water/g polymer}$, the relative intensity is a function of wavenumber (Figure 5-14). The strong decay in intensity is even stronger for light of lower Raman shift (= lower wavelength), meaning that not only incident unshifted photons are scattered off the path, but also Raman-scattered photons of different wavelength. According to the considerations above, this will severely influence the quantitative data evaluation.

In the higher concentrated dispersion, the average particle distance is in the range of $\bar{h} \sim 15 \text{ nm}$ (Equ. 3-13), meaning that the particles are fixed in their position and that, depending on the particle stabilization, a long-range, ordered structure of particles exists. The decrease in intensity with focus position is less than for the more dilute dispersion, which is in accordance with what was also observed by *Garg et al.* (1997). The smaller interparticle distance makes, that less photons are scattered off the path. Figure 5-15 also shows, that in the less dilute dispersion of $X = 1.0 \text{ g water/g polymer}$ the relative intensity is independent of the wavenumber. The normalized intensities

taken at different Raman shifts give the same value, meaning that the decay of intensity is mainly caused by the scattering of incoming laser photons, while the efficiency of collecting Raman-shifted photons is not hindered by photon-particle scattering. According to the considerations above, in the concentration range below $X \sim 1.0$ g water/g polymer, a quantitative evaluation is not affected by photon scattering.

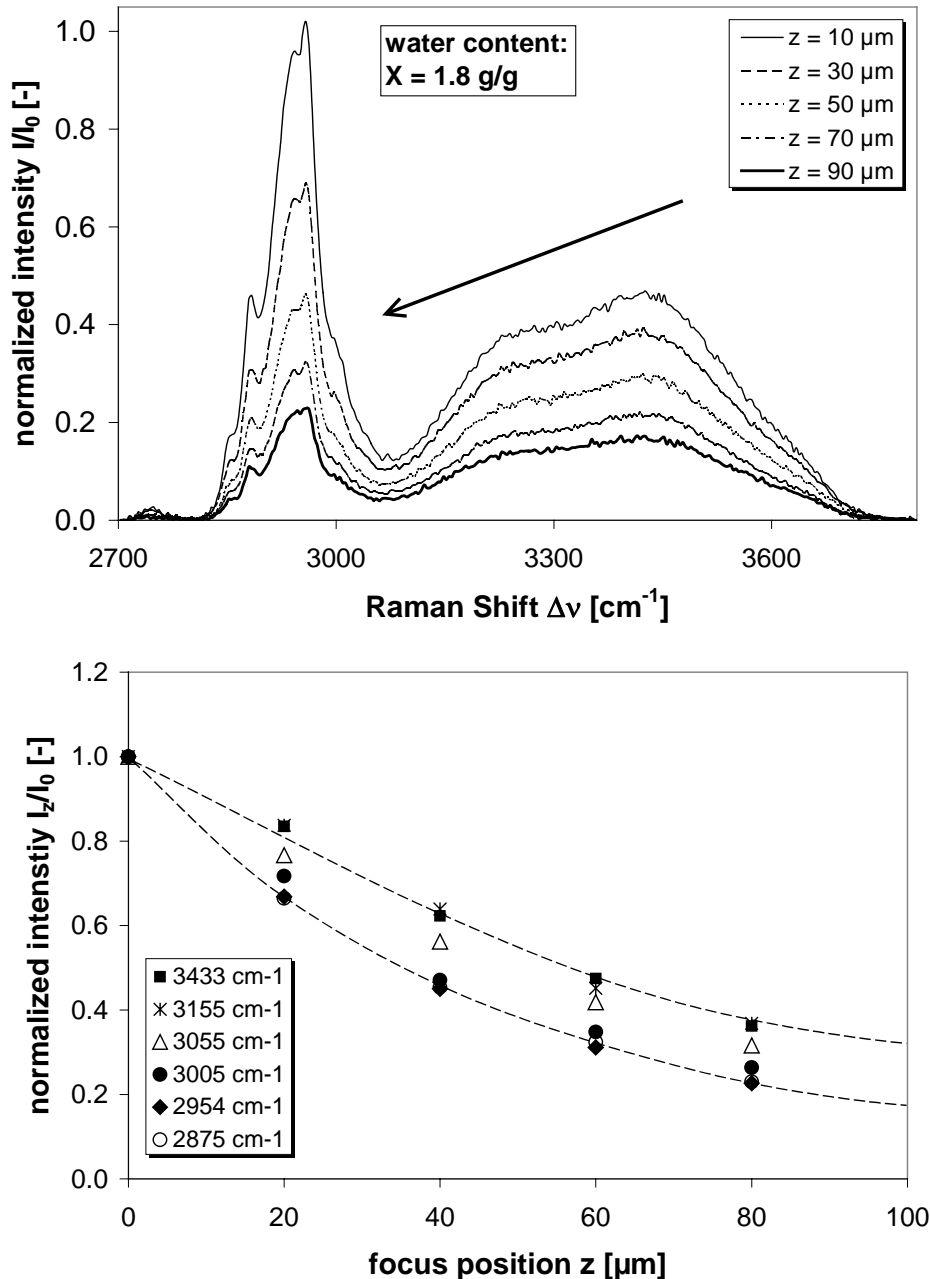


Figure 5-14: Aqueous polymer dispersion of $X = 1.8$ g water/g polymer. Top: Raman spectra at different positions; bottom: The decrease of intensity in the spectral window is wavenumber-dependent. The decrease is stronger for smaller wavelengths

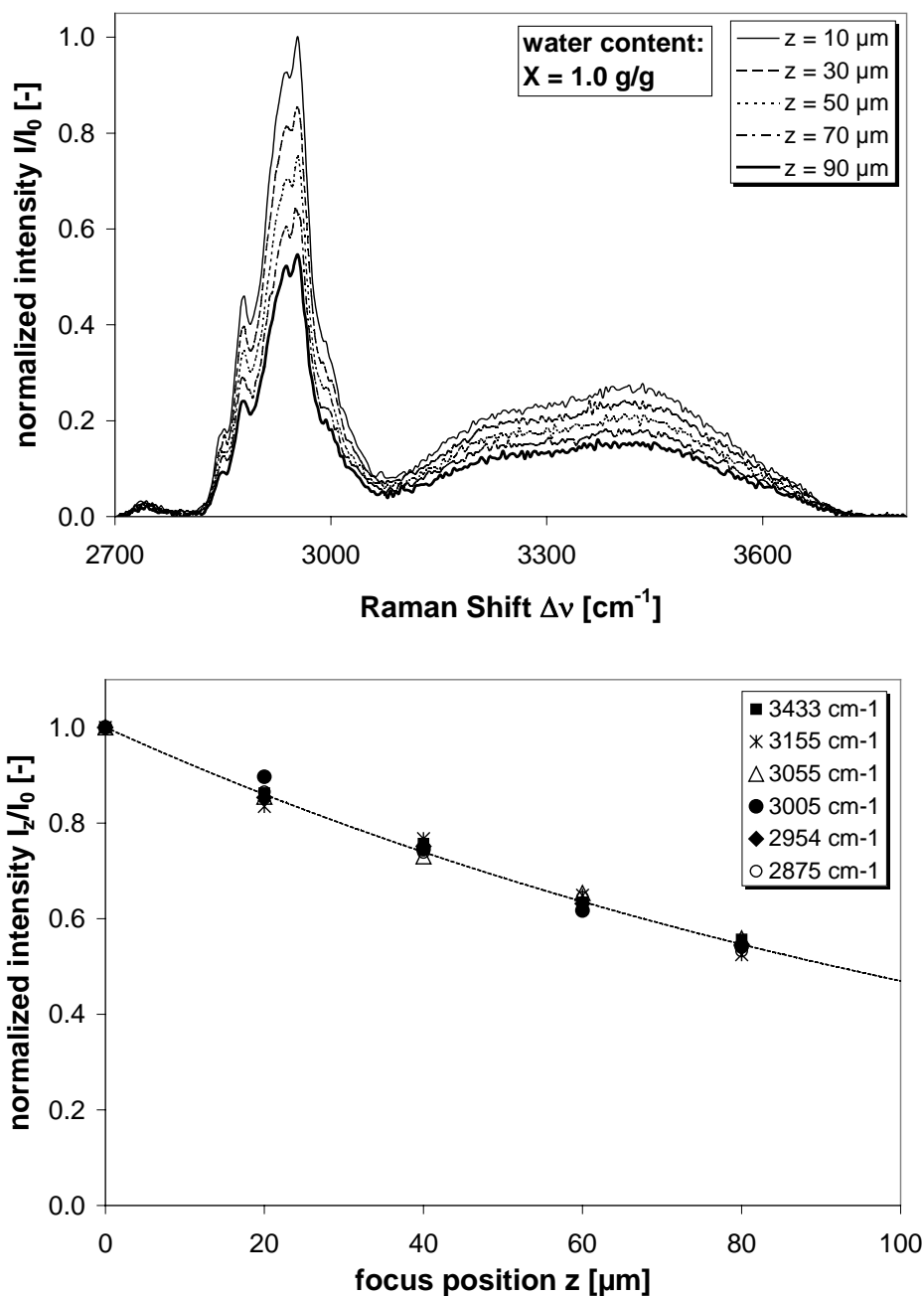


Figure 5-15: Aqueous polymer dispersion of $X = 1.0$ g water/g polymer. Top: Raman spectra at different positions; bottom: The decrease of intensity in the spectral window is wavenumber-independent

The quantitative evaluation of the Raman spectra of polymer dispersions is only possible as long as the relative peak intensities are not affected by scattering effects at the polymer particles. Obviously, this is only fulfilled for highly concentrated dispersions, where the interparticle distance is small enough so that multiple-scattered photons are still collected by the objective. For the investigated dispersions, this is the case for water contents of up to $X = 1.0$ g water/g polymer, but not for $X = 1.8$ g/g.

It means that in the typical concentration range for many coating applications ($X = 0$ -1.0 g water/g polymer), the quantitative evaluation of Raman spectra is possible by the method described in chapter 5.2.3 above.

6 Model Calculations

This chapter deals with model calculations of film leveling and drying. Film leveling describes the surface tension-driven flow-out of small striations of the coating surface which evolve during the application of a film layer. The ability of the dispersion to flow-out is characterized by the leveling rate α which is derived from conservation equations of momentum and mass.

Film drying describes the evaporation of water from the film surface, driven by concentration gradients. The thermodynamic equilibrium at the interface couples the mass transport in the gasphase with the water transport in the polymer film. Each aspect is discussed separately. In chapter 7, the model calculations are compared with experimental data.

6.1 Film Leveling

When applied to a substrate, the coating surface normally shows striations, that are caused by the application tool e.g. a brush or an air gun. Such “brushmarks” are nearly sinusoidal in nature. Within a limited time after application, the striations need to flow-out to form a smooth and shiny surface – this process is known as leveling. The driving forces for leveling are generally a combination of surface tension and gravity, although gravity can be safely neglected in many applications. The steep increase in viscosity in connection with water evaporation is the limiting factor for film leveling. On porous substrates, the diffusion of water into the substrate can affect film leveling even more than does water evaporation.

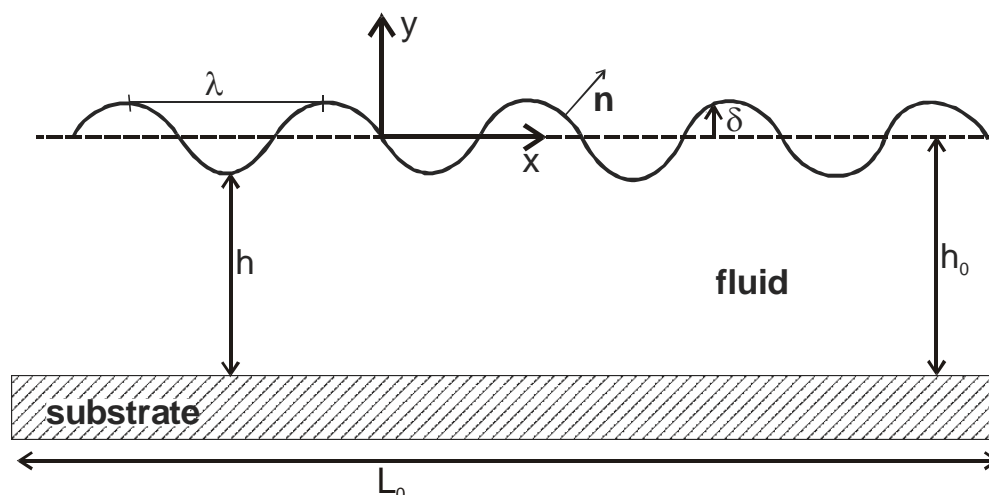


Figure 6-1: Sketch of a thin film with sinusoidal surface disturbances

The ability of a dispersion to flow-out is characterized by its leveling rate α which can be derived from conservation equations of momentum and mass. In their paper, *Keunings and Bousfield (1987)* give a detailed derivation of an analytical expression for α , which is based on certain justified simplifications: They consider an

incompressible dispersion, isothermal conditions and a two-dimensional leveling problem (Figure 6-1). Inertial and body forces are neglected and the constant surface tension is the main driving force. Often, the level of surfactant in latex dispersions is close to or above the critical micelle concentration (c_{cmc}) and therefore the assumption of a constant surface tension is valid.

Depending on how accurate the viscoelastic properties of the dispersion are described, one of the following expressions for the leveling rate α is used:

- (I) The leveling rate α of a general Maxwell fluid with several relaxation times λ_i is given by:

$$\alpha = \frac{\sigma k}{2\eta_v(\alpha)} \psi(\xi) \quad \text{Equ. 6-1}$$

where $\eta_v(\alpha)$ is defined by:

$$\eta_v = \sum_{i=1}^N \frac{\eta_i}{1 - \alpha\lambda_i} \quad \text{Equ. 6-2}$$

k is a factor and $\psi(\xi)$ is a trigonometrical function.

- (II) For a Newtonian fluid, *Keunings and Bousfield* (1987) give the following solution for the leveling rate as a function of the constant surface tension σ and the constant viscosity η :

$$\alpha_{Newton} = \frac{\sigma k}{2\eta} \psi(\xi) \quad \text{and for } \xi \ll 1 \quad \alpha_{Newton} = \frac{16\pi^4 \sigma h_0^3}{3\eta\lambda^4} \quad \text{Equ. 6-3}$$

- (III) The one-mode Maxwell fluid possesses one single relaxation time λ in addition to its *Newtonian* viscosity. The leveling rate of a *Maxwell* fluid with one relaxation time is described by:

$$\alpha_{Maxwell} = \frac{\alpha_{Newton}}{1 + \lambda\alpha_{Newton}} \quad \text{Equ. 6-4}$$

Since α_{Newton} is always positive, $\alpha_{Maxwell} < \alpha_{Newton}$ holds, indicating that viscoelasticity exerts a retardation effect on leveling.

Unfortunately, in reality, most fluids expose a very complex rheological behaviour and are therefore best described by a multi-mode *Maxwell* model.

With the help of α , the surface disturbance δ after time t (Figure 6-1) can be calculated from:

$$\delta(x, t) = \bar{\delta} e^{ikx - \alpha t} \quad \text{Equ. 6-5}$$

and the surface disturbance δ_{end} after leveling time t_{end} can be obtained from:

$$\frac{\delta_{end}(x, t_{end})}{\delta_0(x, t_0)} = \frac{\bar{\delta} \cdot e^{ikx - \alpha t_{end}}}{\bar{\delta} \cdot e^{ikx - \alpha t_0}} \quad \delta_{end}(x, t_{end}) = \delta_0(x, t_0) \cdot e^{-\alpha(t_{end} - t_0)} \quad \text{Equ. 6-6}$$

Then, the leveling time t_{end} after which brushmarks have decreased to δ_{end} is:

$$t_{end} = -\frac{1}{\alpha} \ln\left(\frac{\delta_{end}}{\delta_0}\right) \quad t_0 = 0 \text{ s} \quad \text{Equ. 6-7}$$

A time-dependent viscosity function $\eta(t)$ can be obtained from a calculation of the change of water content $X(t)$ that is linked to the polymer volume fraction ϕ and the corresponding viscosity function $\eta(\phi)$ (see also Chapters 3.1.4 and 7.1.3).

To describe film leveling of the investigated aqueous dispersions, a multi-mode Maxwell fit of the low-shear dynamic moduli G' and G'' for different particle volume fractions ϕ is used to obtain an expression for $\eta(\phi)$. Inserted into Equ. 6-1, this results in an expression for the leveling rate α (compare Chapter 7.1.6).

6.2 Film Drying

Any mass flow is driven by gradients in concentration, density or surface tension. In this work, mass transport phenomena in thin polymer films are investigated, independent of the influence of heat transport. This is assured by isothermal drying conditions during the experiment (compare also Chapter 7.2.1). In the mathematical description of film drying, the mass transport in the gas phase (Chapter 6.2.1) is coupled with that in the film (Chapter 6.2.4) by the thermodynamic equilibrium at the interface (compare Figure 6-2). In this work, a finite-difference-model (Guttoff (1994)) is used for the calculation of water concentration profiles in the polymer film.

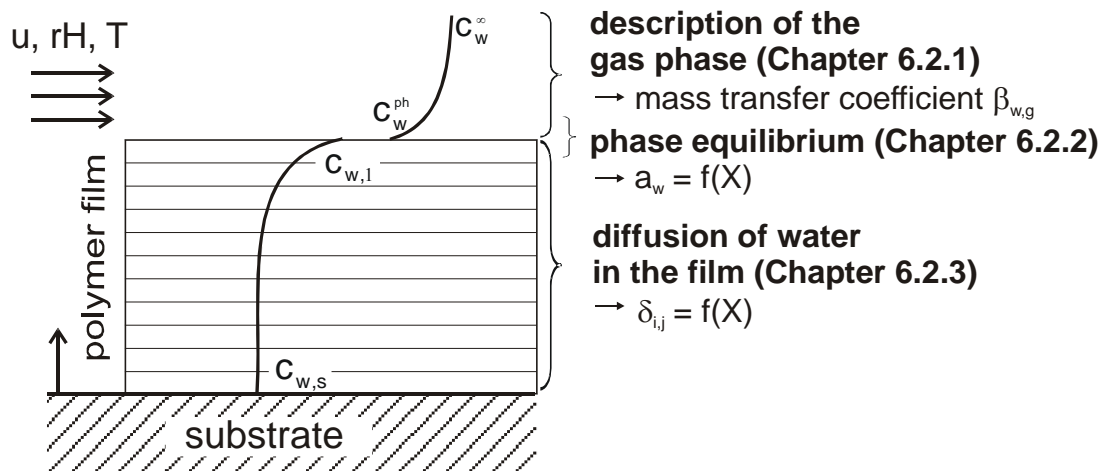


Figure 6-2: Concentration gradients in thin films: (I) water evaporation into the gas phase, (II) phase equilibrium at the interface and (III) water diffusion in the polymer film

6.2.1 Mass Transport in the Gas Phase (Constant-Rate-Model)

For the case of uni-directional diffusion of water in air (= binary system, semipermeable interface, diffusion of one component) and a low partial pressure of water, a linear approach can be used to describe water evaporation from the polymer film:

$$\dot{m}_w = \tilde{M}_w \cdot \tilde{\rho}_g \cdot \beta_{w,g} (\tilde{y}_w^{\text{ph}} - \tilde{y}_w^\infty) \quad \text{Equ. AVII-10}$$

Or expressed in terms of concentration:

$$\dot{m}_w = \beta_{w,g} (c_w^{\text{ph}} - c_w^\infty) \quad \text{Equ. AVII-11}$$

For a derivation of Equ. AVII- 10 see Appendix VII. The mass transfer coefficient $\beta_{w,g}$ is calculated from a *Sherwood*-correlation $Sh = f(Re, Sc, \text{geometry})$. According to the VDI-Wärmeatlas (2005), for fully developed laminar flow and plate geometry an average mass transfer coefficient $\overline{\beta_{w,g}}$ versus the length of the plate is obtained from:

$$Sh = \frac{\overline{\beta_{w,g}} \cdot L}{\delta_{w,g}} = 0.664 \cdot \sqrt{Re} \cdot \sqrt[3]{Sc} = 0.664 \cdot \sqrt{\frac{u \cdot L}{\nu_g}} \cdot \sqrt[3]{\frac{\nu_g}{\delta_{w,g}}} \quad \text{Equ. 6-8}$$

with:

L	= characteristic length (distance from the edge of the plate to the center of the sample film in the direction of flow)
Re	= <i>Reynolds</i> -number
Sc	= <i>Schmidt</i> -number
u	= air velocity above the sample film
ν	= kinematic viscosity

The diffusion coefficient $\delta_{w,g}$ of water in air is calculated from the *Fuller*-equation (*Fuller et. al.* (1966), see Appendix AVIII).

6.2.2 Water Sorption and Phase Equilibrium

Sorption isotherms describe the equilibrium water content of polymer materials as a function of the water activity a_w , including water adsorption and capillary condensation. They are necessary for a complete mathematical description of the water transport in the polymer film. From the shape of the sorption isotherm, conclusions can be drawn about the structure of the latex film, e.g. the existence of pores and of a network of hydrophilic material.

A number of models exist to describe polymer-solvent phase equilibria. For aqueous systems, generally two different approaches are used:

(I) In localized sorption theories, which are basically modifications of *Langmuir's* sorption isotherm, the polar penetrant is considered to bind on specific sites in the polymer structure, e.g. cracks, pores or polar groups. The presence of a dynamic equilibrium where condensation of molecules on bare sites equals evaporation from occupied sites is assumed. The classical BET-model (*Brunauer, Emmet, Teller* (1938)), which describes five different types of sorption isotherms, is the famous

representative of localized sorption theories. A more flexible model to describe non-ideal water sorption in polymers for a large range of activities is the so-called GAB-model (*Guggenheim* (1966), *Anderson* (1946), *de Boer* (1968)). In this model, the ratio of the heat of adsorption of water molecules to the heat of liquefaction k is an additional parameter and is assumed to be less than one.

(II) So-called dissolution theories use a more “macroscopic” approach to describe sorption. Although questionable for many water-polymer systems, a homogeneous dissolution of the penetrant in the polymer is assumed. In connection with water sorption equilibria, normally such dissolution theories are used, in which the polymer solution is treated as a three-dimensional lattice of spheres. In the lattice, the water molecules are represented by single spheres, whereas the polymer is described by a chain of spheres. Due to its simple structure, the Flory-Huggins model (*Flory* (1941); *Huggins* (1941)) is widely used even for aqueous systems.

A more detailed description of the BET- and GAB-model representing the localized sorption theory and a discussion of the *Flory-Huggins* model, representing the dissolution theory, can be found in Appendix IX.

For reasons of simplicity, the experimental sorption data are fitted by the following parameter equations for $a_w(X)$ to be incorporated into the mathematical model of film drying (see Appendix IX 3) and Chapter 6.2.4):

$$a_w = \left(\frac{X}{A}\right)^B \quad \text{for } X < 0.015 \quad \text{Equ. 6-9}$$

$$a_w = \frac{1}{\exp\left[\left(\frac{C}{X}\right)^D\right]} \quad \text{for } 0.015 < X < 0.03 \quad \text{Equ. 6-10}$$

with:

a_w = water activity
 A, B, C, D = fitting parameters

6.2.3 Water Diffusion in the Film

The diffusion coefficient of water in the polymer film is a function of the water content X and temperature T . Due to the isothermal experimental conditions, the dependence of $\delta_{w,p}$ on T is not investigated in this work. As employed by *Gutoff* (1994) in his finite-difference-model, the following exponential equation is used to describe the diffusion coefficient of water in the film:

$$\delta_{w,p} = A(T) \cdot \exp\left[-\frac{B}{1 + 2X \frac{\rho_p}{\rho_w}}\right] \quad \text{with: } T = \text{const.} \quad \text{Equ. 6-11}$$

For the description of the experimental data by model calculations, the diffusion coefficient is used as a fitting parameter.

Water diffusion in the latex film, expressed by $\delta_{w,p}$, strongly depends on the age and structure of the film:

- (I) In the case of incomplete film formation, diffusion will proceed along the still existing particle-particle interfaces, where functionalized particle surfaces and the surfactant material form a hydrophilic diffusion network. In this case, the diffusion coefficient $\delta_{w,p}$ describes water diffusion in the surfactant material along the interfaces.
- (II) In the case of complete film formation, the hydrophilic network no longer exists and the diffusion coefficient $\delta_{w,p}$ describes water diffusion in the polymer.
- (III) For high- T_g polymer particles, the additional effect of water transport in a porous structure has to be considered.

6.2.4 Mathematical Description of Drying (Vertical Direction)

Gutoff's finite-difference-model is used to describe the water concentration profiles in vertical direction of the film during drying (see also Figure 6-3): For this, the film is subdivided into slices of equal mass content of polymer. Their sum gives the overall mass of polymer of the film. The diffusion coefficient of water in each slice and the height of each slice are a function of the water content (and drying time) and are therefore subject to change.

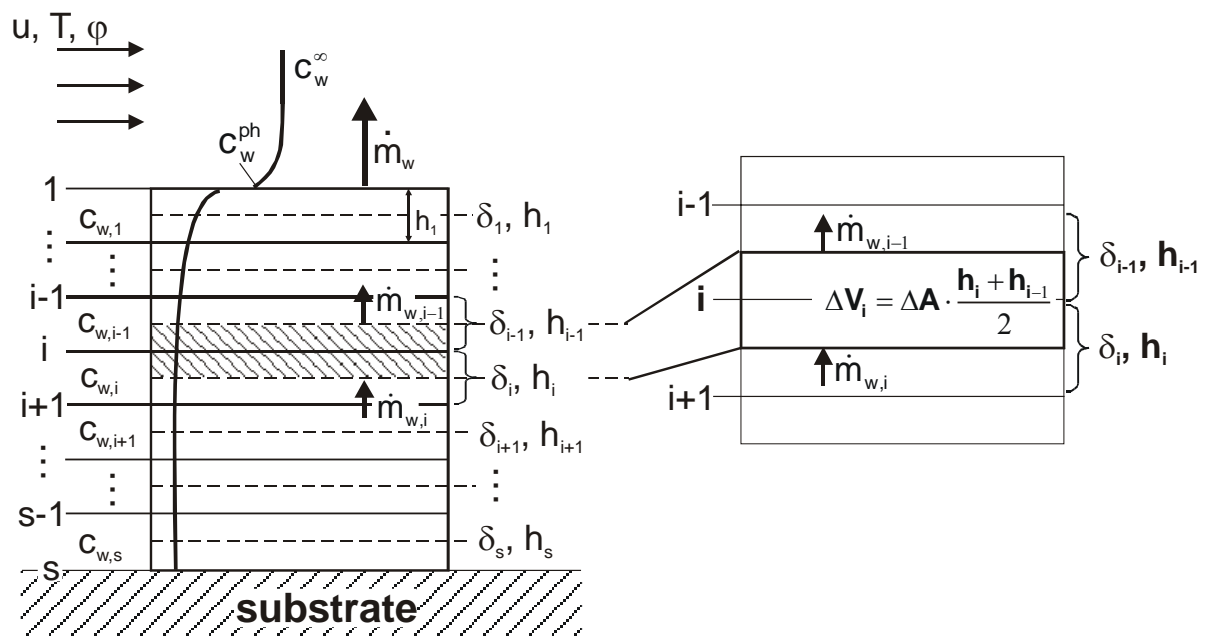


Figure 6-3: Left: drying model as described by Gutoff (1994) in vertical direction of the film. Right: mass balance around a slice i of the film

The water concentration of each slice is obtained from the respective diffusion equations. The rate of water accumulation is equal to the rate of water transport into the slice minus the rate of water transport out of the slice:

$$\frac{dm_{w,i}}{dt} = \dot{m}_{w,i} - \dot{m}_{w,i-1} \quad \text{Equ. 6-12}$$

Figure 6-3 illustrates the notation used to describe each slice. The concentration of any middle slice of the film can be obtained from the mass balance around the slice with:

$$\dot{m}_{w,i} = -\delta_i \left. \frac{dc_{w,i}}{dz} \right|_i \quad \text{and } h_i = f(X) \quad \text{Equ. 6-13}$$

$$\frac{h_i + h_{i-1}}{2} \cdot \frac{dc_{w,i}}{dt} = \delta_i \cdot \left. \frac{dc_w}{dz} \right|_i - \delta_{i-1} \cdot \left. \frac{dc_w}{dz} \right|_{i-1} \quad \text{Equ. 6-14}$$

The change of concentration of the investigated slice is:

$$\frac{dc_{w,i}}{dt} = \frac{c_{w,i,t+1} - c_{w,i,t}}{\Delta t} = \frac{2}{h_{i,t} + h_{i-1,t}} \left[\frac{\delta_{i,t}}{h_{i,t}} (c_{w,i+1,t} - c_{w,i,t}) - \frac{\delta_{i-1,t}}{h_{i-1,t}} (c_{w,i,t} - c_{w,i-1,t}) \right] \quad \text{Equ. 6-15}$$

And solving Equ. 6-15 for $c_{w,i,t+1}$ results in:

$$c_{w,i,t+1} = c_{w,i,t} + \frac{2 \cdot \Delta t}{h_{i,t} + h_{i-1,t}} \left[\frac{c_{w,i+1,t} \delta_{i,t}}{h_{i,t}} - c_{w,i,t} \left(\frac{\delta_{i,t}}{h_{i,t}} + \frac{\delta_{i-1,t}}{h_{i-1,t}} \right) + \frac{c_{w,i-1,t} \delta_{i-1,t}}{h_{i-1,t}} \right] \quad \text{Equ. 6-16}$$

with:

$c_{w,i,t}$	= water concentration in slice i at time t
$h_{i,t}$	= height of slice i at time t
t	= time
$\delta_{i,t}$	= diffusion coefficient in slice i at time t
$\beta_{w,g}$	= mass transfer coefficient
c_w^{ph}	= water concentration at the film surface
c_w^∞	= water concentration in the air

For the slice at the film surface (index 1), the mass balance gives:

$$\frac{h_1}{2} \cdot \frac{dc_{w,1}}{dt} = \delta_1 \cdot \left. \frac{dc_w}{dz} \right|_{i=1} - \beta_{w,g} \cdot \Delta c_w \quad \text{Equ. 6-17}$$

$$\frac{dc_{w,1}}{dt} = \frac{c_{w,1,t+1} - c_{w,1,t}}{\Delta t} = \frac{2}{h_{1,t}} \left[\frac{\delta_{1,t}}{h_{1,t}} (c_{w,2,t} - c_{w,1,t}) - \beta_{w,g} (c_w^{ph} - c_w^\infty) \right] \quad \text{Equ. 6-18}$$

Solving Equ. 6-18 for $c_{w,1,t+1}$ results in:

$$c_{w,1,t+1} = c_{w,1,t} + \frac{2 \cdot \Delta t}{h_{1,t}} \left[\frac{\delta_{1,t}}{h_{1,t}} (c_{w,2,t} - c_{w,1,t}) - \beta_{w,g} (c_{w,t}^{ph} - c_w^\infty) \right] \quad \text{Equ. 6-19}$$

Assuming, that there is no mass transfer into the substrate, the water concentration of the bottom slice (index s) only changes by the flow of water which leaves this slice:

$$\frac{h_s}{2} \cdot \frac{dc_{w,s}}{dt} = -\delta_s \cdot \frac{dc_w}{dz} \Big|_{i=s} \quad \text{Equ. 6-20}$$

$$\frac{dc_{w,s}}{dt} = \frac{c_{w,s,t+1} - c_{w,s,t}}{\Delta t} = -\frac{2}{h_{s,t}} \frac{\delta_{s,t}}{h_{s,t}} (c_{w,s,t} - c_{w,s-1,t}) \quad \text{Equ. 6-21}$$

The concentration in the bottom slice after time t+1 is:

$$c_{w,s,t+1} = c_{w,s,t} - \frac{2 \cdot \Delta t \cdot \delta_{s,t}}{h_{s,t}^2} (c_{w,s,t} - c_{w,s-1,t}) \quad \text{Equ. 6-22}$$

Expressions for the unknown parameters in Equ. 6-14 to Equ. 6-22 are as follows:

- (I) The diffusion coefficient δ_i is described by Equ. 6-11 (Chapter 6.2.3)
- (II) The water flux in the gas phase is described by a simple linear equation (Equ. AVII- 11, Chapter 6.2.1) in which the water concentration at the interface c_w^{ph} is calculated from:

$$c_w^{ph} = a_w \cdot \frac{P^*(T_{film})}{p} \cdot \tilde{\rho}_{air} \cdot \tilde{M}_{water} \quad \text{Equ. 6-23}$$

- (III) The phase equilibrium is described by the fit of the parameter equations Equ. 6-9 and Equ. 6-10 to the experimental sorption data, obtained from gravimetric experiments (compare Chapter 6.2.2 and Appendix X).

- (IV) The height of each slice is calculated from:

$$h_{i,t}(X) = h_{i,start} - \Delta h_{w,i,t}(X) \quad \text{Equ. 6-24}$$

$$h_{j,t}(X) = h_{j,start} \left(1 - (X_{j,start} - X_{j,t}) \cdot \frac{\rho_{dispersion}}{\rho_w} \cdot X_{dispersion} \right) \quad \text{Equ. 6-25}$$

with:

$h_{i,t}$	= height of slice i after time t
$h_{i,start}$	= height of slice i at t = 0 s
X_{start}	= water content at t = 0 s
$X_{i,t}$	= water content after time t
$\rho_{dispersion}$	= viscosity of the original dispersion
ρ_w	= viscosity of water
$X_{dispersion}$	= mass content of the original dispersion

6.2.5 Mathematical Description of Drying (Horizontal Direction)

For the calculation of water concentration profiles in horizontal direction of thin latex films during drying, the same finite-difference-method (*Gutoff (1994)*) is used as described above.

The model is based on diffusion processes only and capillary forces are not included. It is therefore not suited to fully describe the mechanism of horizontal inhomogeneous drying as depicted in Chapter 4-3, but a comparison between the experimental data and model calculations would allow conclusions about the importance of the capillary forces on horizontal inhomogeneous drying.

The calculation of water concentration profiles in horizontal direction can still be treated as a 1-dimensional problem: For the mathematical description of the concentration profiles in horizontal direction, the film is subdivided into slices of the same, constant width b (Figure 6-4). The width of one cell is $b = 100 \mu m$, being a distance, over which no concentration gradients are observed for the applied drying conditions. All cells have a defined initial volume V_j and the decreasing water content is considered by a reduction in the cell height h_j . For a start, the initial water concentration $c_{w,start}$ and the film height as a function of the horizontal position $h_{j,start}$ are given.

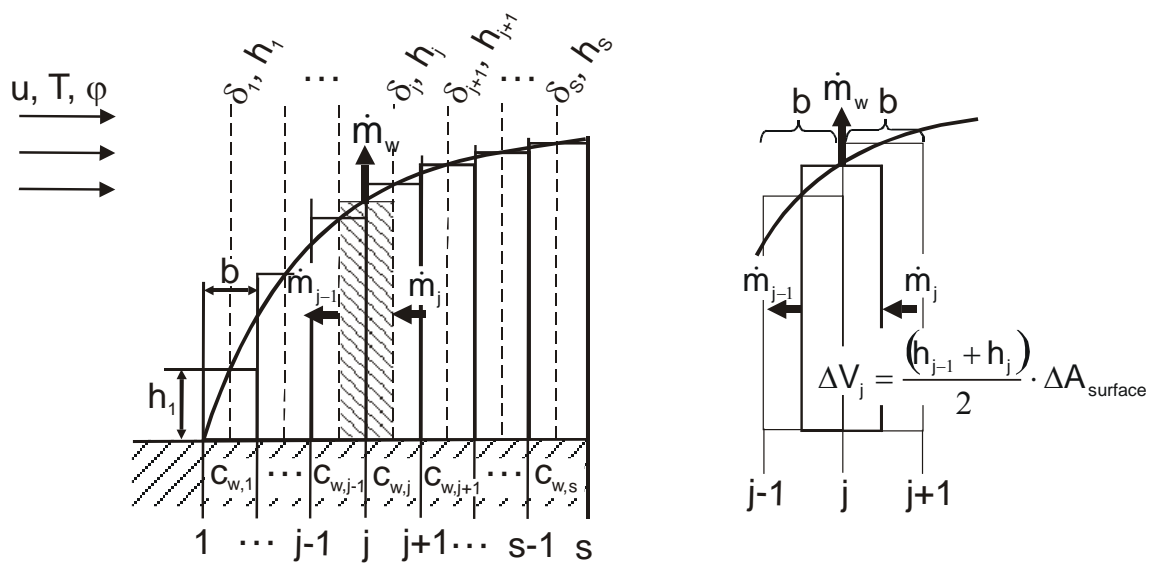


Figure 6-4: Left: drying model in horizontal direction of the film; right: mass balance around a slice i of the film

Again, the water concentration of each slice $c_{w,j}$ is obtained from the respective diffusion equations. The water concentration can be obtained from the flow of water into the slice (being transported from the center), the flow that evaporates from the film surface and the one out of the slice towards the edge of the film:

$$\frac{h_{j-1,t} + h_{j,t}}{2} \cdot \frac{c_{w,j,t+1} - c_{w,j,t}}{\Delta t} = \frac{h_{j,t}}{b} \cdot \delta_{j,t} \frac{(c_{w,j+1,t} - c_{w,j,t})}{b} - \frac{h_{j-1,t}}{b} \cdot \delta_{j-1,t} \frac{(c_{w,j,t} - c_{w,j-1,t})}{b} - \beta_{w,g} (c_{w,t}^{ph} - c_w^\infty)$$

Equ. 6-26

Taken together, this gives the following expression for the water concentration $c_{w,j}$ of slice j at the time $t+1$:

$$c_{w,j,t+1} = c_{w,j,t} + \frac{2\Delta t}{h_{j,t} + h_{j-1,t}} \left[\frac{h_{j,t}}{b^2} \delta_{j,t} (c_{w,j+1,t} - c_{w,j,t}) - \frac{h_{j-1,t}}{b^2} \delta_{j-1,t} (c_{w,j,t} - c_{w,j-1,t}) - \beta_{w,g} (c_w^{ph} - c_w^\infty) \right]$$

Equ. 6-27

For the slice at the edge of the film, the summation of all fluxes gives the following equation:

$$\frac{h_{1,t}}{2} \cdot \frac{c_{w,1,t+1} - c_{w,1,t}}{\Delta t} = \frac{h_{1,t}}{b} \cdot \delta_{1,t} \frac{(c_{w,2,t} - c_{w,1,t})}{b} - \frac{h_{1,t}}{b} \cdot \beta_{w,g} (c_{w,t}^{ph} - c_w^\infty) - \frac{1}{2} \cdot \beta_{w,g} (c_{w,t}^{ph} - c_w^\infty)$$

Equ. 6-28

Solving Equ. 6-28 for $c_{w,1,t+1}$ leads to:

$$c_{w,1,t+1} = c_{w,1,t} + \frac{2\Delta t}{b} \left[\frac{\delta_{1,t}}{b} (c_{w,2,t} - c_{w,1,t}) - \beta_{w,g} (c_{w,t}^{ph} - c_w^\infty) \left(1 + \frac{b}{2 \cdot h_{1,t}} \right) \right]$$

Equ. 6-29

Assuming a symmetrical shape of the film, there will be no mass flow to the center slice; instead, the water concentration of the slice changes by the flow of water out of this slice and the one caused by water evaporation:

$$\frac{h_{s,t}}{2} \cdot \frac{c_{w,s,t+1} - c_{w,s,t}}{\Delta t} = -\frac{h_{s,t}}{b} \cdot \delta_{s,t} \frac{(c_{w,s,t} - c_{w,s-1,t})}{b} - \frac{1}{2} \cdot \beta_{w,g} (c_{w,t}^{ph} - c_w^\infty)$$

Equ. 6-30

Finally, the concentration of the center slice s at time $t+1$ is expressed by:

$$c_{w,s,t+1} = c_{w,s,t} - \frac{2\Delta t}{b} \left[\frac{\delta_{s,t}}{b} (c_{w,s,t} - c_{w,s-1,t}) + \beta_{w,g} (c_{w,t}^{ph} - c_w^\infty) \frac{b}{2 \cdot h_{s,t}} \right]$$

Equ. 6-31

After each time step, the film thickness $h_{j,t}$ at the respective position j is calculated from:

$$h_{j,t}(X) = h_{j,\text{start}} \left(1 - (X_{j,\text{start}} - X_{j,t}) \cdot \frac{\rho_{\text{dispersion}}}{\rho_w} \cdot X_{\text{dispersion}} \right) \quad \text{Equ. 6-25}$$

In Equ. 6-32, the water content X_j is obtained from the concentration $c_{w,j}$:

$$X_{j,t} = \frac{1 - x_{j,t}}{x_{j,t}} \quad \text{and: } x_{j,t} = 1 - \frac{c_{w,j,t}}{\rho_{\text{dispersion}}} \quad \text{Equ. 6-32}$$

For the diffusion coefficient δ_j , the values as obtained from the fit of the vertical concentration profiles at the same (= ambient) drying conditions (see Chapter 6.2.3) are used.

7 Results and Discussion

7.1 Rheology of Aqueous Latex Dispersions

To display good application properties (= good leveling, long open time, no sagging,) a coating formulation has to display certain rheological characteristics like e.g. shear thinning, no yield stress and a well-designed viscosity function $\eta(\dot{\phi})$. In this chapter, the rheological characteristics of the different industrial formulations are compared and discussed (Chapter 7.1.1). The experimental data show how the dispersion properties depend on the water content X (Chapter 7.1.2) and how they can be influenced by (I) an additional amount of surfactant or (II) different amounts of plasticizer (Chapter 7.1.5). One goal is to derive an expression of the viscosity function $\eta(\dot{\phi})$ from the experimental data of each dispersion using model calculations. In Chapter 7.1.6, the viscosity functions are used to calculate the film leveling rate α of the different dispersions as described in Chapter 6.1. All of the above findings are considered to identify the dispersion with the best application properties.

A short description of the latex dispersions is given in Chapter 2.1.2. More characteristic dispersion parameters like e.g. particle size, particle volume fraction, average particle distance in the original dispersion, dispersion surface tension and contact angle, as well as a tabular summary of all data can be found in Appendix III.

7.1.1 Rheological Investigation of the Concentrated Dispersions

A dispersion paint is required to give a smooth (= glossy) coating on many substrates to be aesthetically pleasing to the customer. The formation of a smooth surface is dictated by both, the rheological properties and the surface tension properties of the material.

When applied to a substrate, the coating will have striations in its surface caused by the way of application, e.g. brushing, rolling or spraying. Typical shear rates for brushing are in the range of 1000 to 10000 s^{-1} . After the application, the striations need to flow out to form a smooth surface – this process is known as leveling. If the paint is applied to a vertical surface, extensive flow will cause sagging, which means the formation of so-called “teardrops”. Typical shear rates for leveling and sagging are in the range of 0.01 – 1 s^{-1} . Therefore, a paint formulation needs well-balanced viscoelastic properties. On the one hand, - during the application -, the dispersion paint should predominantly have fluid-like behaviour to allow leveling, but on the other hand it should restructure within a short time to avoid sagging. This is fulfilled by dispersion paints that display shear thinning behaviour.

Figure 7-1 shows shear thinning behaviour for all the dispersions under investigation, but the zero-shear viscosity and the slope of the viscosity curve of the different

formulations differ strongly. For dispersions, the height of the zero-shear viscosity plateau is an indication of the activation energy, required to change the random *Brownian* motion of the particles into an ordered motion induced by the shear field. For clarification, the typical shear rate ranges of brushing and leveling and also the viscosity of water are indicated. With the higher water content X , the small particle dispersion A-S-2 has the lowest viscosity, independent of shear rate.

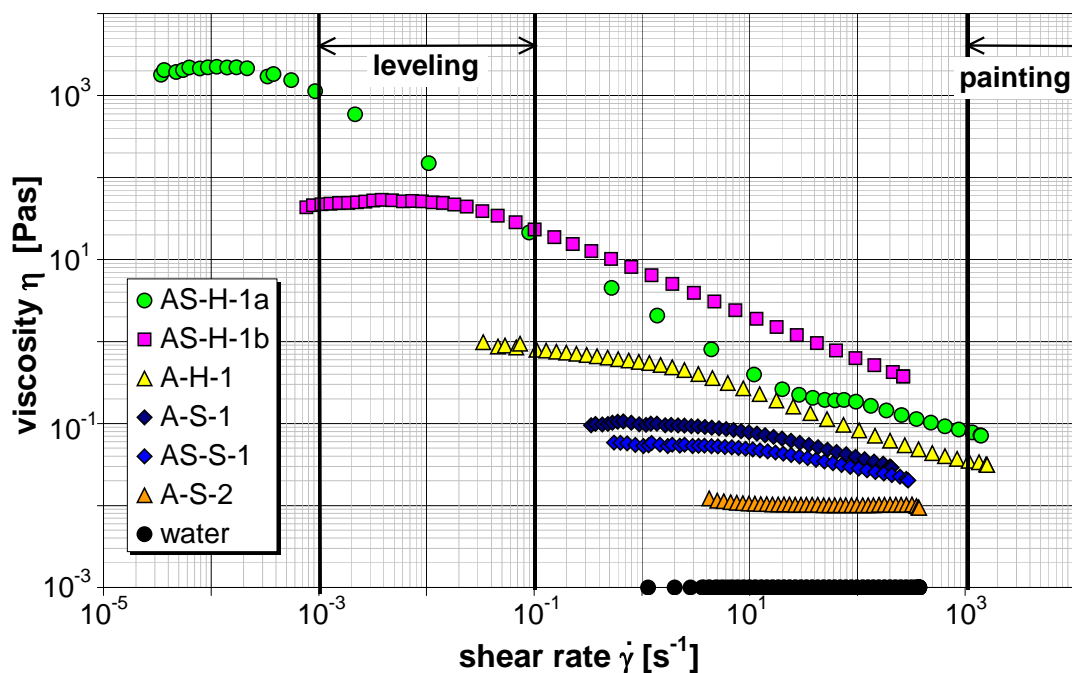


Figure 7-1: The viscosity over shear rate of different original dispersions, showing shear thinning behaviour. The zero-shear viscosity differs by several decades

The stress which must be exceeded in order to destroy an existing dispersion structure is called yield stress. Its appearance is related to the interaction between the polymer particles and to the elastic properties of the dispersion. AS-H-1a displays a yield stress (Figure 7-2), being the only dispersion where a network structure already exists in the original formulation, before the beginning of drying.

Colloidal dispersions that show a yield stress are termed gels. In this case, the gel-like behaviour can be explained by the fact, that AS-H-1a is the only formulation containing the water-soluble, cationic species amino-methyl-propanol which could be responsible for the existing network (compare also Chapter 2.1.2).

Based on this knowledge, the value and the shape of the viscosity curve of the gel AS-H-1a as presented in Figure 7-1 are questionable and not comparable to that of the other dispersions, because it displays the network destruction caused by simple shear and not the interplay between the repulsive interparticular forces and *Brownian* motion as for the other dispersions. For a gel, the experimental data are dependent on the experimental set-up.

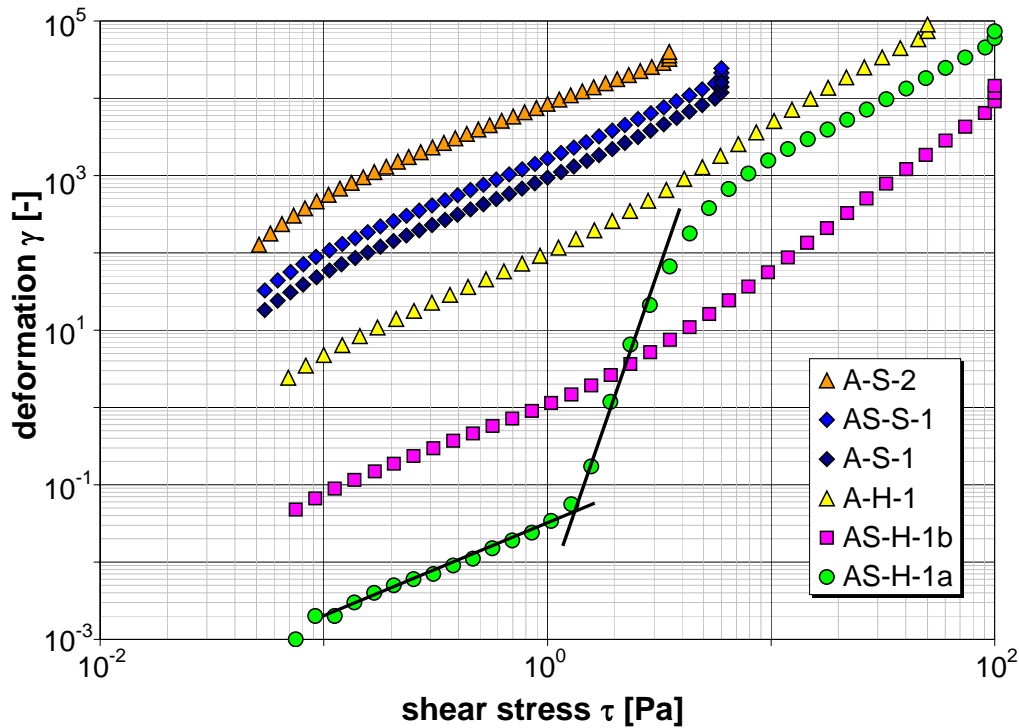


Figure 7-2: The deformation as a function of shear stress of the six investigated industrial dispersions

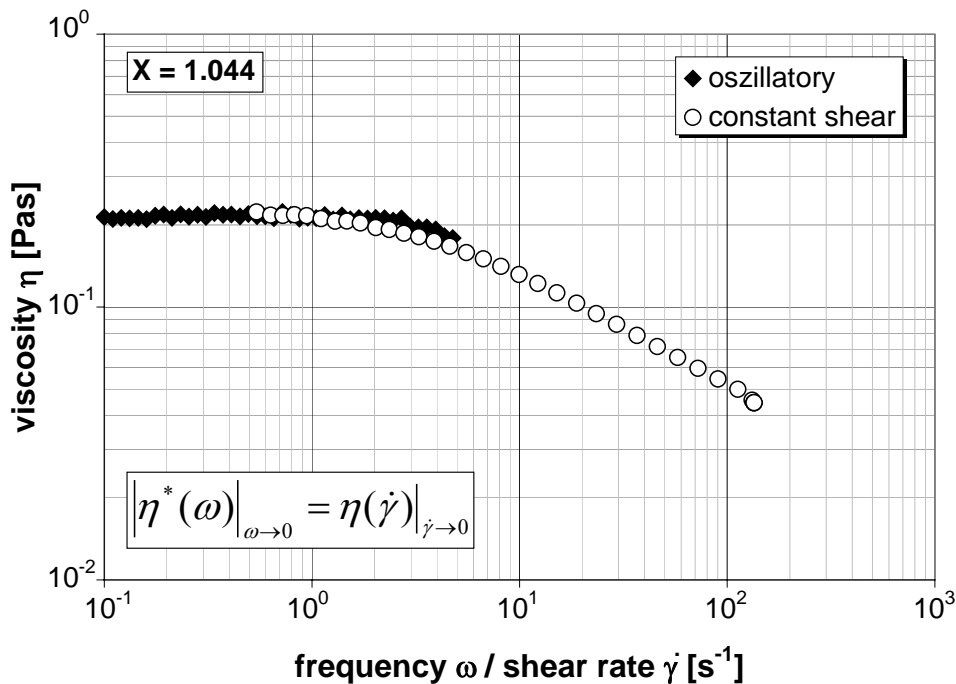


Figure 7-3: A comparison of the dynamic and the simple shear viscosity of A-S-1 ($X = 1.044$ g/g)

At low shear rates and low particle concentrations, aqueous polymer dispersions normally obey the *Cox-Merz* rule which states, that the dynamic and the steady shear viscosity display the same value, meaning that there is (I) no long-range order of particles in the dispersion or that (II) a rearrangement of distorted particles, induced by steady and dynamic shear is equally possible. The formulation of A-S-1 at its original

state is the only dispersion which obeys the *Cox-Merz* rule (Figure 7-3), which means that only for this formulation the distortion and rearrangement of the polymer particles is comparable in both, dynamic and steady shear flow. This can be due to a larger interparticle spacing in the original dispersion or a shorter range of the interparticular forces compared to the other investigated dispersions.

7.1.2 Rheological Properties as a Function of the Water Content X

Dealing with paints and varnishes, it is not enough to only characterize the original dispersion formulation, it is also necessary to discuss the rheological properties of the dispersion in connection with drying. The rheological properties are subject to considerable changes with decreasing water content X , since this brings the dispersion particles into contact and enhances particle interaction and structure formation.

At low shear rates, a decrease of the water content X by only $\sim 1/3$ of the initial value already results in an increase of the viscosity by several decades, being the result of colloidal interaction, structure formation and particle contact. Then, shear thinning displays the network destruction caused by simple shear and not the interplay between the repulsive interparticular forces and *Brownian* motion. With decreasing water contents X , the onset of shear thinning shifts to lower shear rates probably because the network that forms between the polymer particles becomes less flexible to shear.

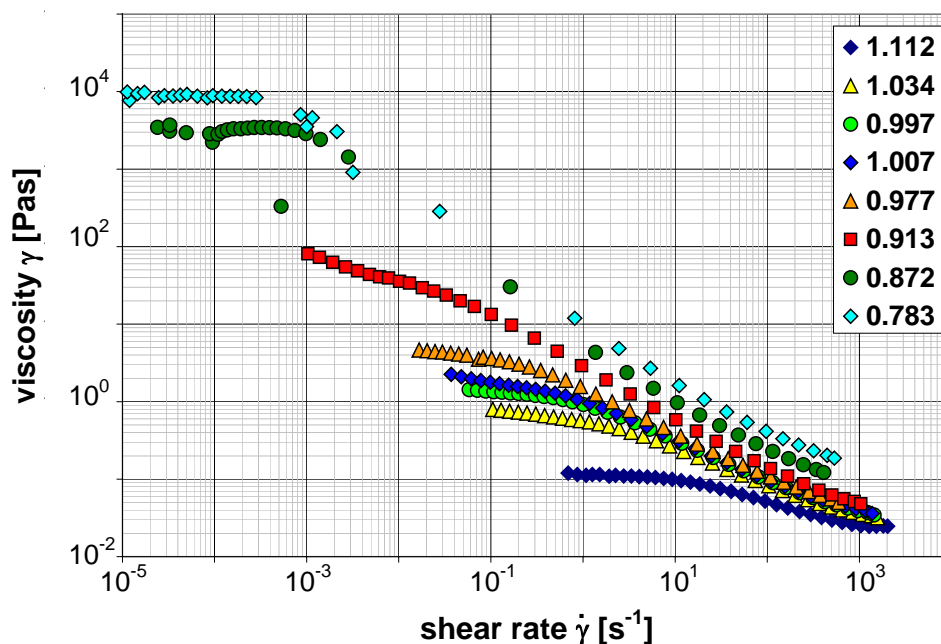


Figure 7-4: The viscosity over shear rate of A-H-1 for different water contents X

In Figure 7-4, this is illustrated for the hard particle dispersion A-H-1. The behaviour is representative for all dispersions (except for AS-H-1a) and displays the transformation from the aqueous latex dispersion to a gel.

Figure 7-5 shows that for AS-H-1a the change in viscosity in the comparable range of water content X is only two decades and that the onset of shear thinning is nearly

independent of X. It is explained by the fact, that the network structure of AS-H-1a already existed in the original formulation, which is why its destruction by simple shear is not influenced by the decrease in water content X.

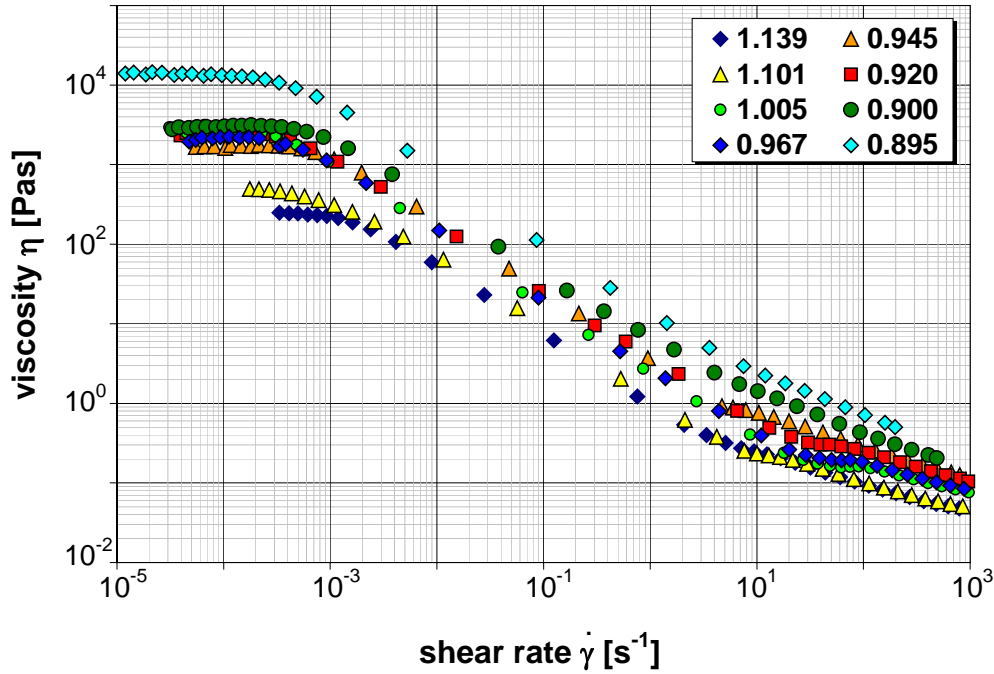


Figure 7-5: The viscosity over shear rate of AS-H-1a for different water contents X

All of the investigated dispersions form a yield stress at lower water content X as a result of particle contact and structure formation. This is exemplarily illustrated in Figure 7-6 for the dispersion A-H-1.

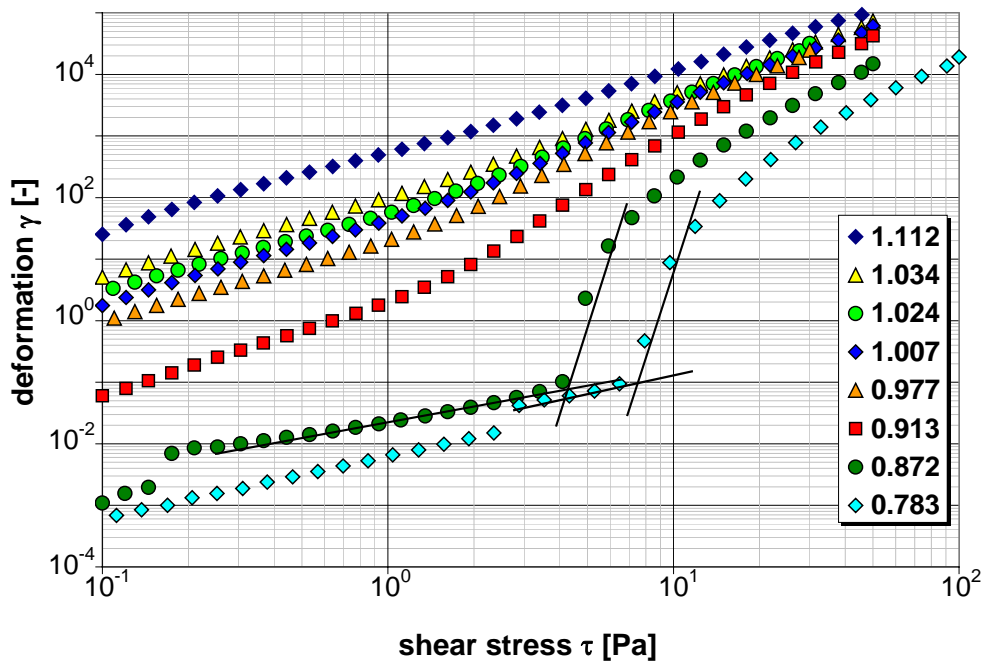


Figure 7-6: The deformation of A-H-1 as a function of the shear stress for different water contents X. With decreasing X, a yield stress is observed

As expected, in the case of AS-H-1a (Figure 7-7), the yield stress exists over the total range of investigated water contents X .

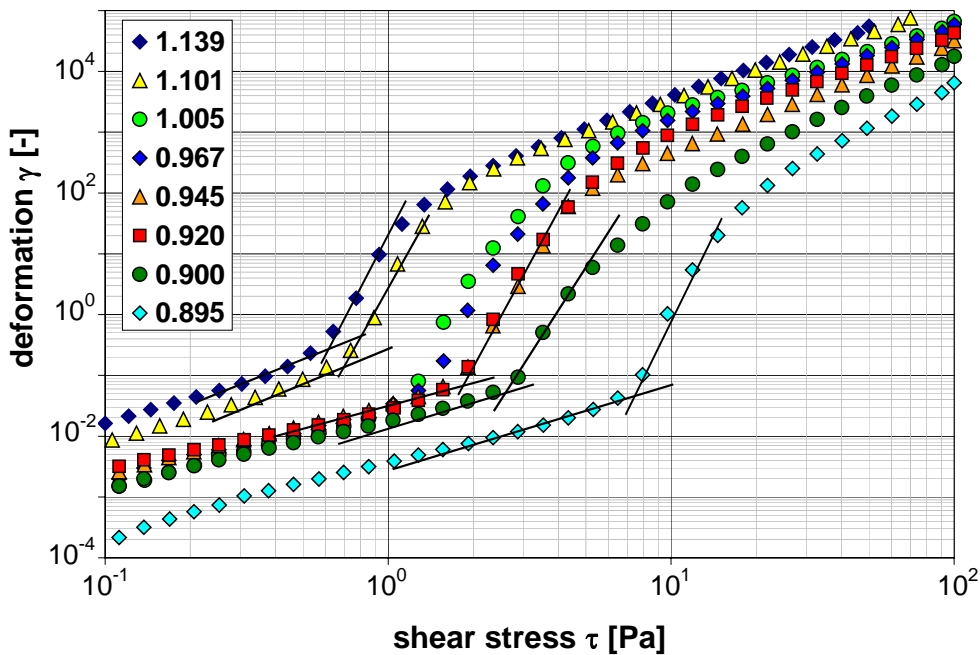


Figure 7-7: The deformation of AS-H-1a as a function of the shear stress for different water contents X . With decreasing X , no structure changes are observed

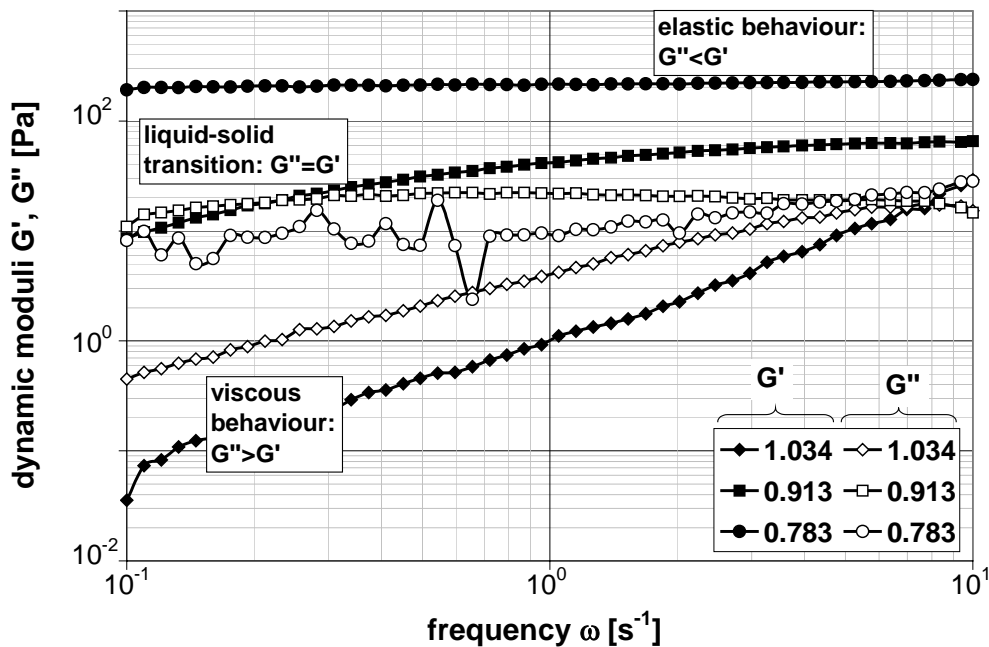


Figure 7-8: Liquid-solid transition of A-H-1. The elastic modulus G' crosses over the viscous modulus G''

In dynamic shear experiments, liquid-like behaviour of aqueous latex dispersions is characterized by a higher viscous dynamic modulus G'' compared to the elastic modulus G' . All investigated latex dispersions, except for AS-H-1a which has already

developed an internal structure, and also AS-H-1b show liquid-like behaviour in their original state. Oscillatory shear experiments at different water contents X show, that all dispersions - after a short drying time - undergo liquid-solid transition (Figure 7-8), indicated by the slope and position of the dynamic moduli G' and G'' . For increasing particle concentrations, the crossing of G' and G'' shifts to lower frequencies.

7.1.3 Viscosity Functions

As described in Chapter 7.1.2, for low shear rates, the latex dispersions show a strong increase of the viscosity with decreasing water content X (= increasing particle volume fraction ϕ). In drying technology, the water content X and in rheology the particle volume fraction ϕ is preferred to describe the ratio of water and polymer in the dispersion. A mathematical expression for the conversion of the two parameters is given in Appendix III 3).

A number of models are available to describe the viscosity function (Chapter 3.1.4). Some, like the ones of *Einstein* or *Doolittle*, are only able to properly describe the viscosity function of highly diluted dispersions. Other models use mostly empirical parameters to describe higher concentrated dispersions and also particle interaction.

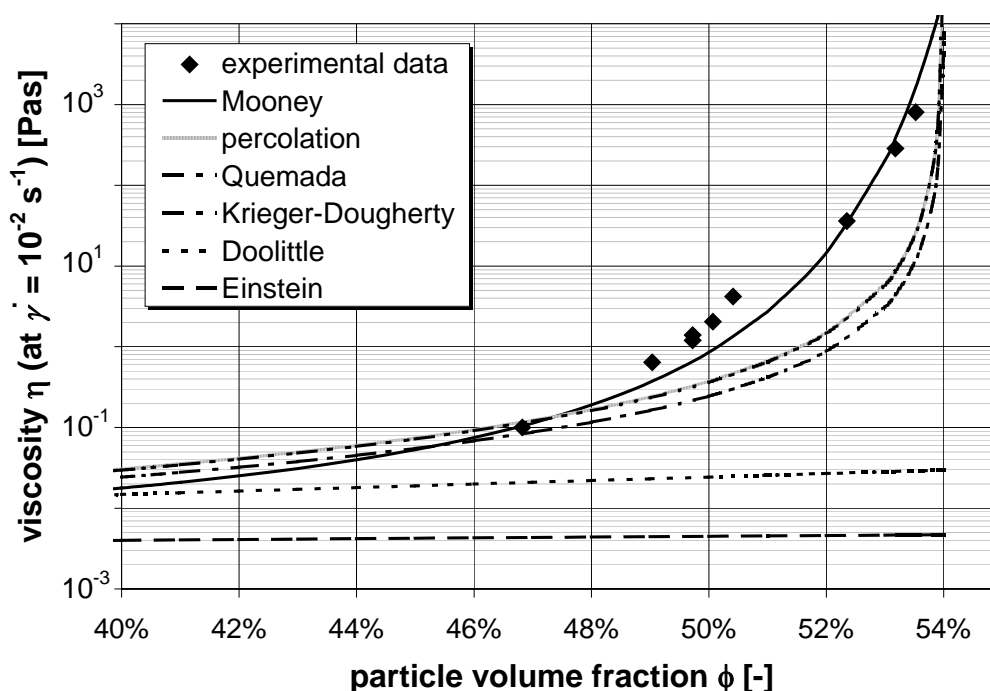


Figure 7-9: The viscosity of A-H-1 as a function of the particle volume fraction ϕ . The experimental data are compared with viscosity models

Exemplarily, Figure 7-9 shows the viscosity data at a typical shear rate for leveling ($\dot{\gamma} = 10^{-2} \text{ s}^{-1}$) of the hard-polymer dispersion A-H-1 and a comparison with the different model calculations. The early increase in the viscosity of A-H-1, indicating long-range repulsive forces between the particles, can be best described by the *Mooney* equation. The parameters and equations used to fit the experimental data are shown in Appendix XIII.

The differences in the viscosity of the aqueous medium (at low particle volume fractions ϕ) are the result of the presence of different amounts and kinds of high-molecular species in the serum. The increase in viscosity and the value of the maximum volume fraction are influenced by the kind of particle stabilization and by the change of the dimensions of the stabilizing layer around the particles (compare also Appendix III).

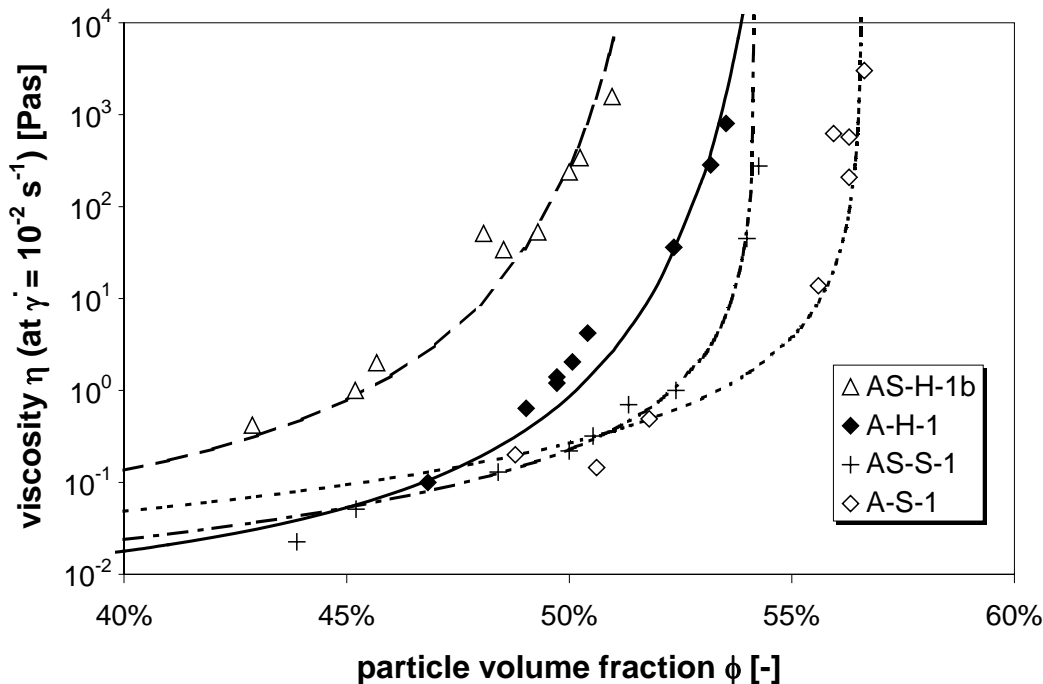


Figure 7-10: The viscosity as a function of the particle volume fraction ϕ of the different dispersions fitted by viscosity models

Above is a display of the viscosity data of the different latex dispersions and the best model fit of the data. AS-H-1b and A-H-1 can be fitted best by the *Mooney* equation, whereas the polymer latices AS-S-1 and A-S-1 are better described by the *Krieger-Dougherty* model. The formulation AS-H-1a (= gel) is not considered here, since the viscosity values are questionable in their meaning compared to the other dispersions (compare Chapter 7.1.1) and the model calculations are not applicable to a gel.

7.1.4 Liquid-Solid Transition

Figure 7-11 gives a representation of the phase angle δ as a function of the water content X , obtained from oscillatory shear experiments at $\omega = 10 \text{ s}^{-1}$ (= linear visco-elastic region). A phase angle near 90° displays mainly viscous behaviour and low values of δ indicate elastic behaviour. All highly concentrated dispersions - except for AS-H-1b - show highly elastic properties.

The dispersion AS-H-1b has very similar particle characteristics to AS-H-1a, e.g. particle size and particle surface characteristics. The two formulations differ by the existence of the high-molecular species amino-methyl-propanol in AS-H-1a, being responsible for its elastic behaviour and network formation in the original dispersion.

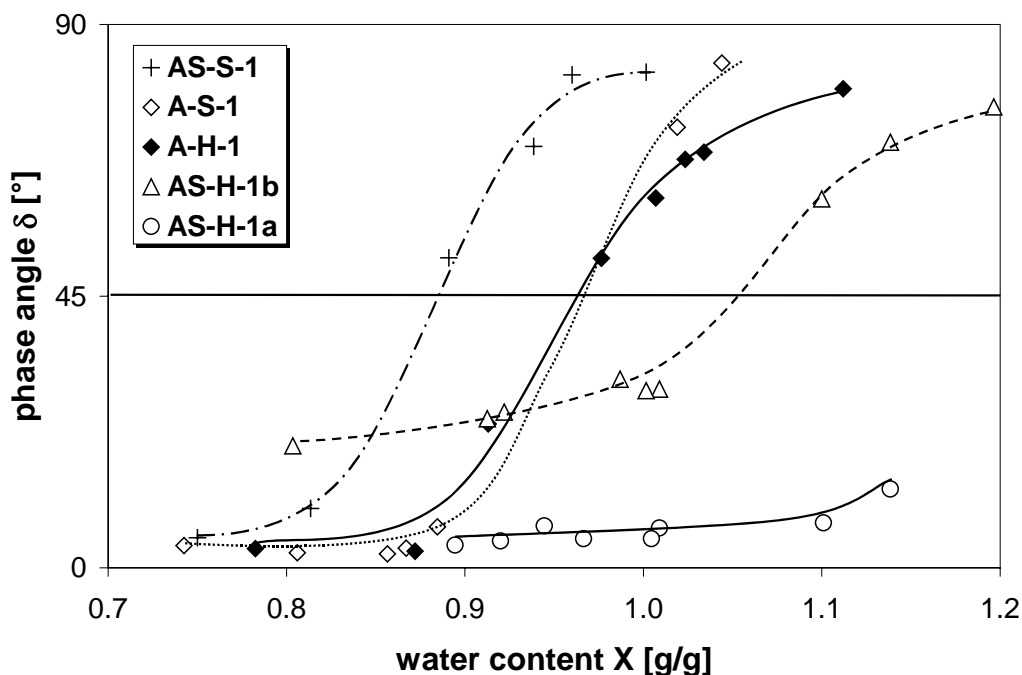


Figure 7-11: The phase angle δ as a function of the water content X

<i>dispersion name</i>	$X_{disp.} []$	$\phi_{disp.} [\%]$ (Appendix III 4)	$X_{max} []$ (Appendix III 4)	$\phi_{max} [\%]$ (Appendix III 4)	$X_{l-s} []$ (Figure 7-11)	$\phi_{l-s} [\%]$ (Appendix III 4)
A-S-1	1.04	48.8	0.87	56.5	0.97	52.5
A-H-1	1.03	49.0	0.85	53.5	0.96	51.0
AS-H-1a	0.97	-	-	-	-	-
AS-H-1b	0.99	49.3	0.93	51.0	1.05	46.5
AS-S-1	1.15	45.2	0.82	54.0	0.88	52.5
A-S-2	2.45	27.6	1.38	41.5	1.45	39.5

Table 7-1: The water content X and particle volume fraction ϕ of (I) the original dispersion, (II) at the maximum particle packing and (III) at the liquid-solid transition

The moment of liquid-solid transition depends on the interaction forces between the particles, that are also a function of the particle volume fraction ϕ . Table 7-1 gives the water content X and the polymer particle volume fraction ϕ of (I) the original dispersion, (II) the dispersion at the maximum particle fraction (compare Appendix III 3)) and (III) the dispersion at the point of liquid-solid transition as obtained from Figure 7-11. For all dispersions, the transition to merely elastic behaviour is reached before the maximum particle volume fraction ϕ_{max} . From Table 7.1 one can learn that not only AS-H-1a, but also AS-H-1b displays merely elastic properties at its original state X_{disp} , meaning that this formulation also has a certain network structure.

7.1.5 Influence of Additives on the Rheological Properties

Generally, the rheological properties of latex dispersions can be tuned in a desired way by changing one or more of the influencing factors like e.g. particle size and particle properties, particle interaction and stabilization. In this study, it was chosen to investigate the influence of additives on the rheological behaviour of the gel-like formulation AS-H-1a which doesn't display the typical rheological behaviour of polymer dispersions. Here, the influence of different amounts of (I) the surfactant sodium-dodecyl-sulfate (SDS) and (II) the plasticizer TexanolTM (= organic solvent) on the rheological behaviour of AS-H-1a is discussed.

(I) Influence of the Surfactant (SDS)

In the gel-like formulation AS-H-1a, different amounts of surfactant have an influence on the particle interactions. The addition of 2 *mass %* of sodium-dodecyl-sulfate (SDS) to the original formulation of AS-H-1a lowers the viscosity by 1-2 decades (Figure 7-12), probably because the existing interparticular network is destroyed or changed in a certain way. A further increase of the amount of surfactant above 2 *mass %* leads again to an increase of the viscosity which might be explained by a surplus of surfactant forming micelles in the aqueous medium, leading to stronger particle repulsion by depletion stabilization.

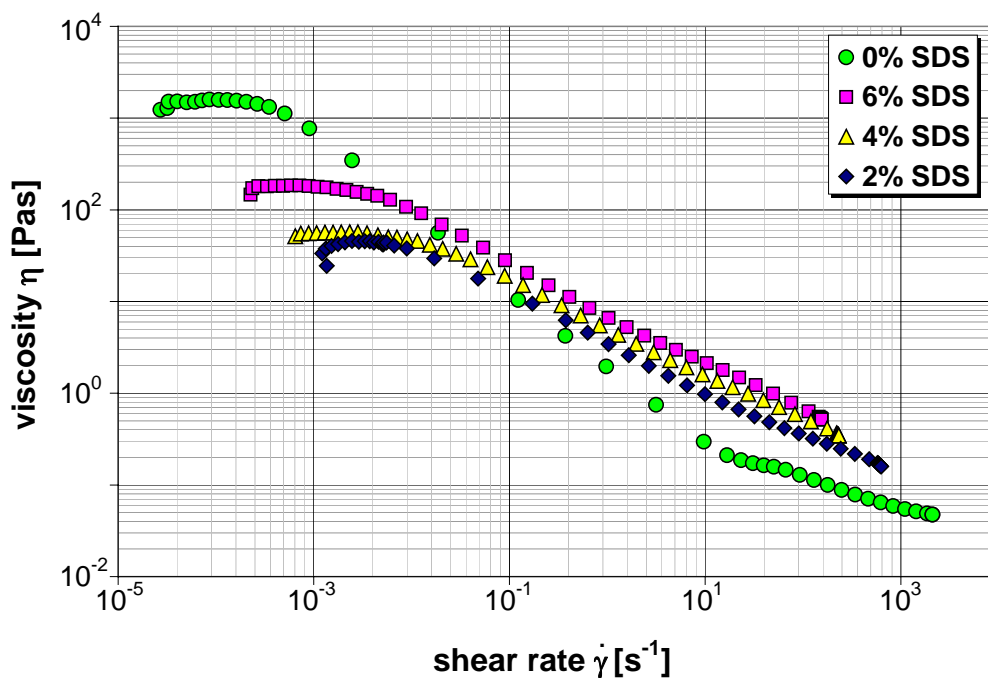


Figure 7-12: The viscosity as a function of shear rate for AS-H-1a, containing different amounts of the surfactant SDS

Compared to the original dispersion, the addition of 4 *mass %* of the surfactant SDS to AS-H-1a adds a strong viscous component to its rheological behaviour which is represented by a phase angle of 25° and higher. Such a behaviour was not observed for the original formulation of AS-H-1a, but for AS-H-1b (compare Figure 7-11), for

which it might be proof of a high surfactant level. Even with decreasing water contents X , the viscous elements in the investigated sample of AS-H-1a plus SDS persist (Figure 7-13).

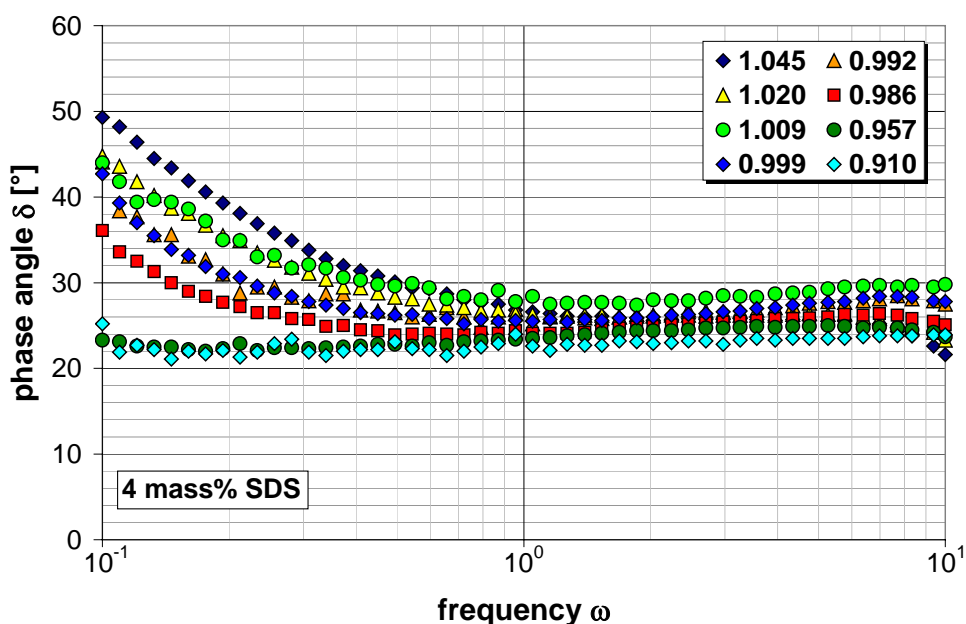


Figure 7-13: The phase angle for AS-H-1a containing an additional 4 mass % of surfactant (SDS) at different water contents X

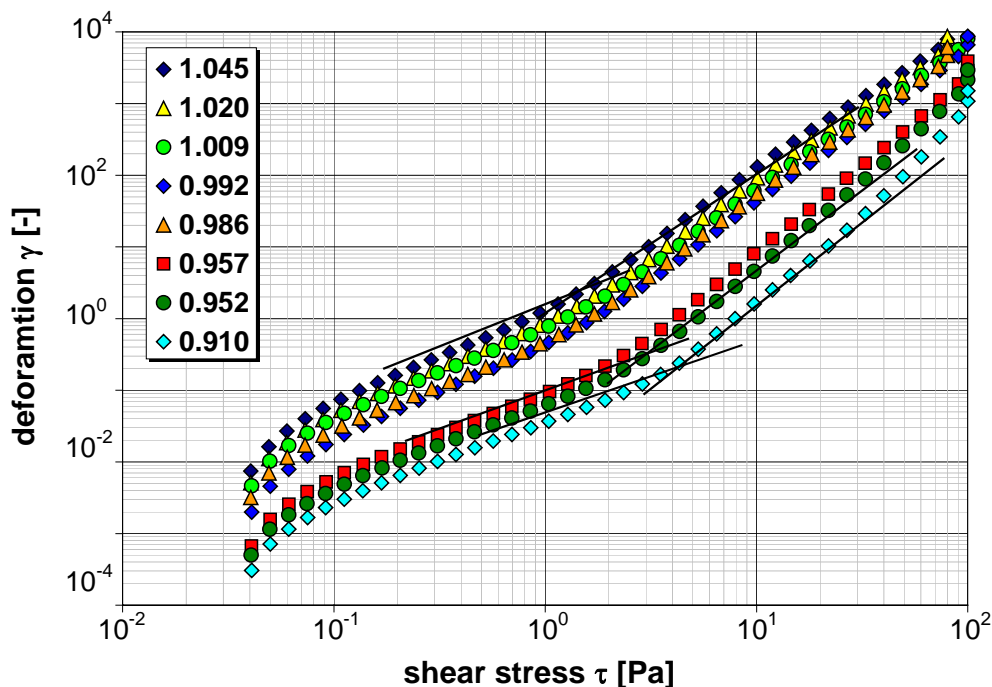


Figure 7-14: AS-H-1a with 4 mass %: The presence of the surfactant strongly influences the dispersion structure and considerably lowers the yield stress

The strong yield stress formerly encountered for AS-H-1a (see Figure 7-7) decreases considerably after the addition of 4 mass % sodium-dodecyl-sulfate (SDS) and is then comparable to that of AS-H-1b (see Figure 7-14 above and Figure 7-2).

(II) Influence of the Plasticizer Texanol™

Being low-volatile organic solvents, plasticizers like Texanol™ dissolve into the latex particles and lower the particle's glass transition temperature T_g . This helps particle deformation and polymer interdiffusion.

Here, the influence of different amounts of Texanol™ on the rheological behaviour of AS-H-1a is subject of investigation. Figure 7-15 shows, that higher amounts of Texanol™ increase the dispersion viscosity, possibly due to an increased polymer particle size, caused by the organic solvent that has diffused into the latex particles. At the same time, the shape of the viscosity curve which is simply shifted to higher values suggests that different amounts of Texanol™, - opposite to different amounts of surfactant -, do not change the particle interactions and the existing network structure. It means that Texanol™ must be mostly present within the polymer particles and not in the aqueous phase. Instead, as stated before, the rheological behaviour of the gel-like formulation AS-H-1a is mainly dictated by particle interaction.

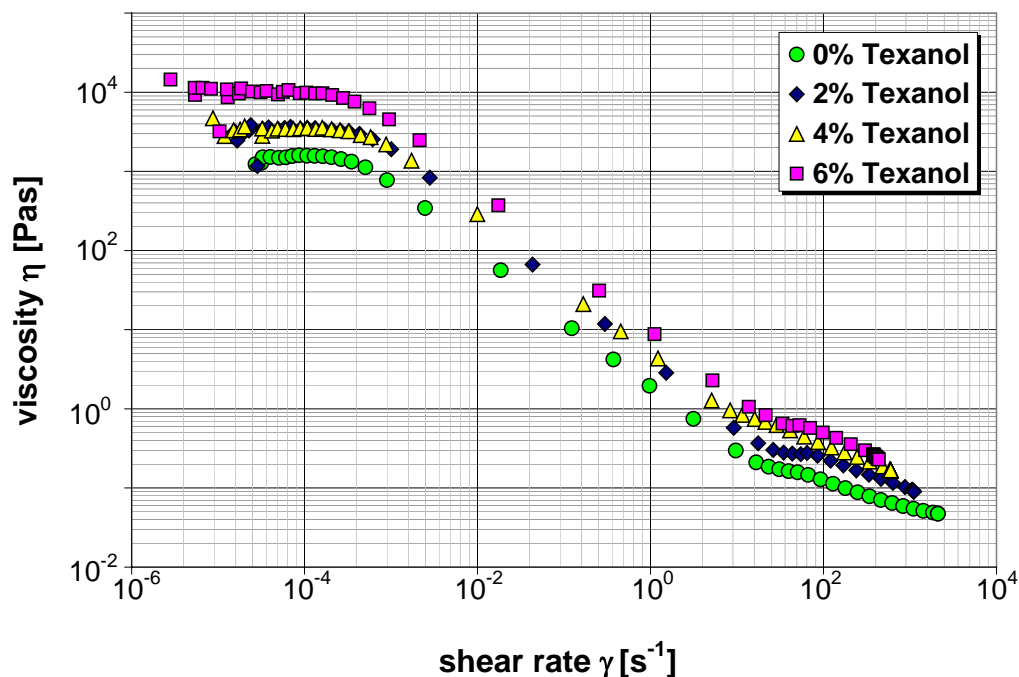


Figure 7-15: Viscosity over shear rate for AS-H-1a (different amounts of Texanol™)

Virtually no change of the phase angle compared to the original formulation without Texanol™ is proof of the largely unchanged rheological characteristics of the aqueous medium (Figure 7-16). The dispersion still shows largely elastic behaviour due to the existing network.

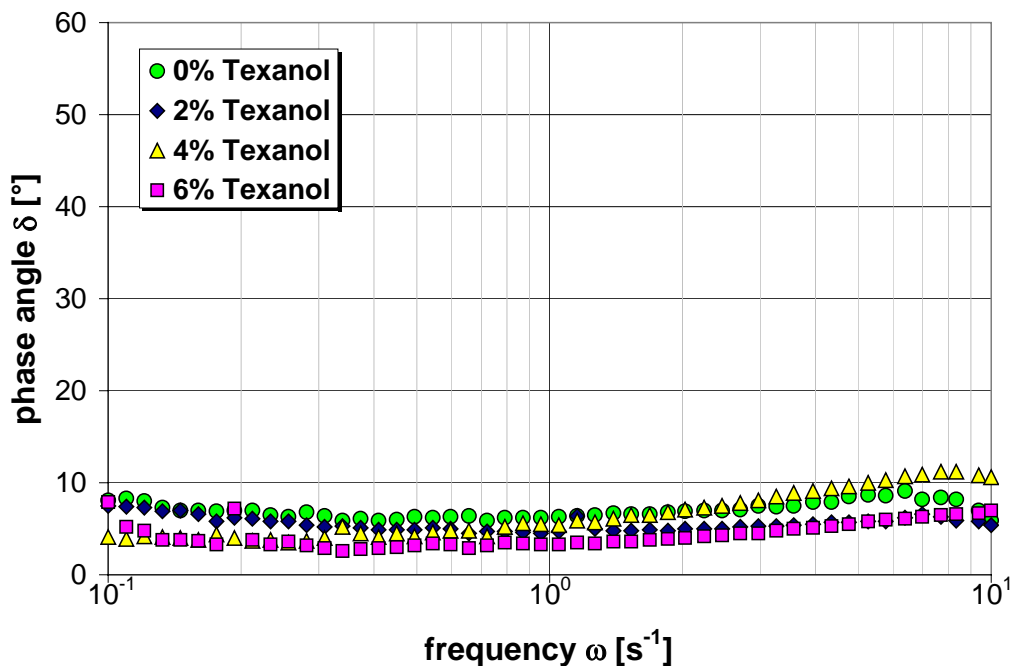


Figure 7-16: The phase angle δ of AS-H-1a with different amounts of TexanolTM

Since the rheological behaviour of AS-H-1a is dictated by the interparticular forces which are not influenced by TexanolTM, the strong yield stress at varying water contents X of the original dispersion AS-H-1a (Figure 7-7) is also observed for the dispersion containing 4 mass % TexanolTM.

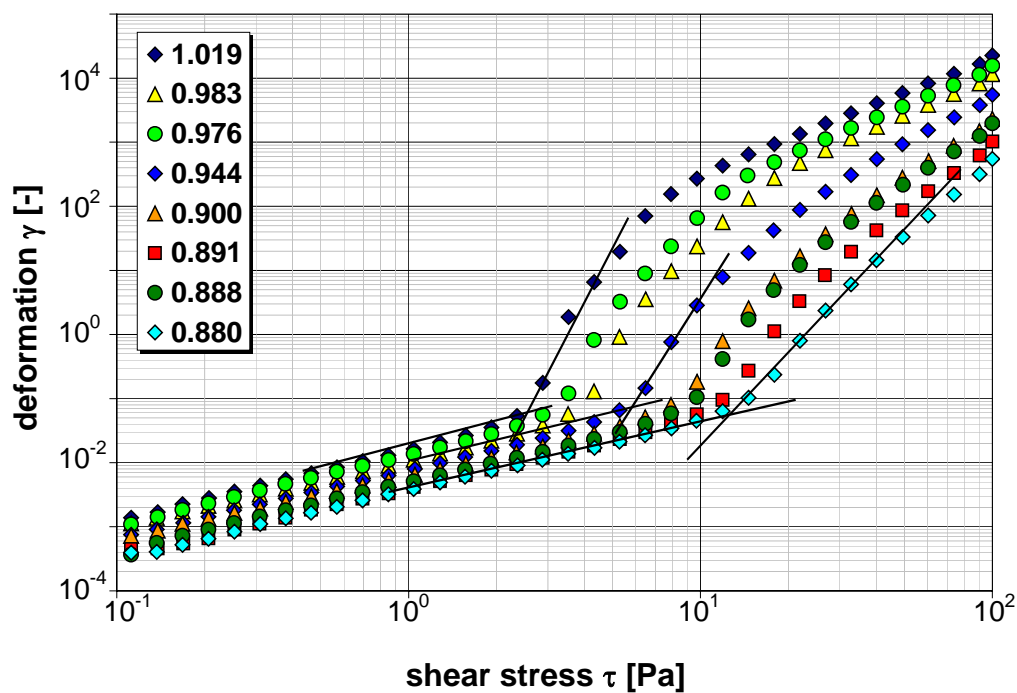


Figure 7-17: Yield stress of AS-H-1a (4 mass % TexanolTM; different water contents X)

7.1.6 Investigation of Film Leveling

In this chapter, film leveling of the different latex dispersions is modeled as described in Chapter 6.1 and is discussed concerning application properties and open time. For the model calculations, standard drying conditions for painting (temperature $T = 25\text{ }^\circ\text{C}$; relative air humidity $\varphi = 50\%$; air velocity $u = 0.05\text{ m/s}$) and typical application marks in thin films (film thickness $h_0 = 100\text{ }\mu\text{m}$; height of application marks $\delta = 10\text{ }\mu\text{m}$; spacing between brushmarks $\lambda = 0.1\text{ cm}$) are assumed.

The water content $X(t)$ in the film is calculated by the following expression:

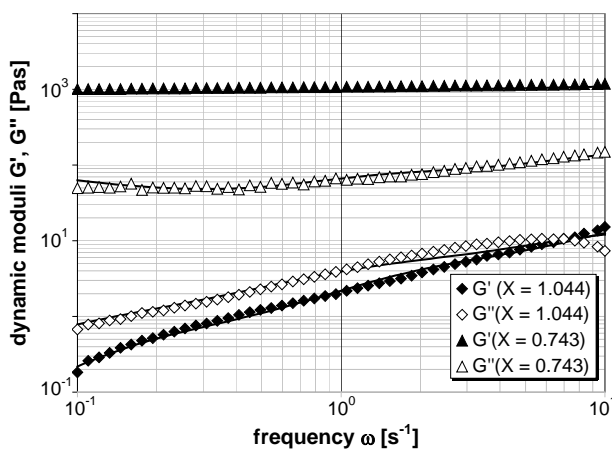
$$X(t) = X(t=0) - \frac{\dot{m} \cdot \Delta t}{x \cdot \rho_{disp} \cdot h_{start}} \quad \text{Equ. 7-1}$$

with:

\dot{m}	evaporation rate (Equ. AVII- 10)
x	mass content polymer
h_{start}	intitial film thickness

As introduced in Chapter 6.1, the mathematical description of leveling of surface disturbances depends on the leveling rate α . Here, for the mathematical description of leveling Equ. 6-1 is used in combination with a multi-mode *Maxwell* model with up to five relaxation times to describe the complex fluid-dynamic behaviour of the aqueous latex dispersions. Figure 7-18 shows that the dynamic shear data in the investigated range of low shear rates and at different water contents X are well fitted by the model.

The assumption of a constant value of the surface tension σ during drying is justified by the high surfactant level of the formulations which is close to or above the critical micelle concentration c_{cmc} (see Appendix III). Being in the range of $35\text{--}47\text{ mN/m}$, the surface tension of the investigated dispersions is considerably lower than the one of pure water ($\sigma = 73\text{ mN/m}$).



Coefficients and relaxation times:

X = 1.044		X = 0.743	
G_i	λ_i	G_i	λ_i
0	0.0001	270	0.01
0	0.001	90	0.1
25	0.01	30	1.0
5	0.1	200	10.0
0.7	1.0	700	100.0

Figure 7-18: A five-mode Maxwell fit of the dynamic shear data of A-S-1 at different water contents X (represented by the lines)

With the help of the relaxation times and weighting factors (compare Figure 7-18), obtained from a fit of Equ. AIV- 15 and Equ. AIV- 16 to the dynamic shear data, values of the the low-shear viscosity η for different water contents X can be calculated.

In Figure 7-19, the experimental data from constant shear experiments at different water contents X are compared with calculated viscosity curves, using (I) the *Krieger-Dougherty* model and (II) multi-mode *Maxwell* fits of the dynamic shear data. The experimental data are well-described by both equations. The decrease of brushmarks is calculated from Equ. 6-6.

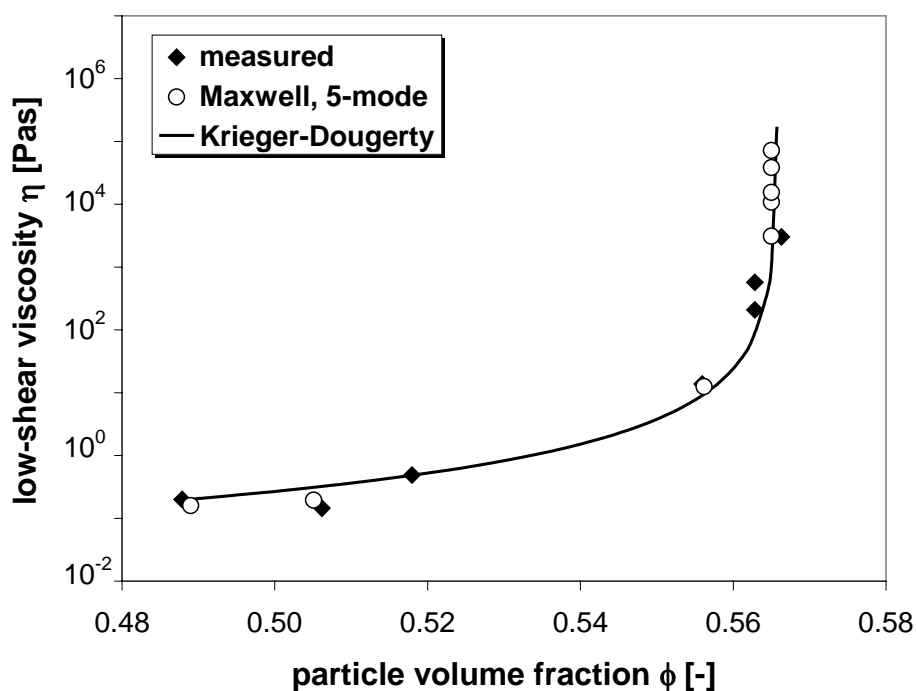


Figure 7-19: The viscosity function of A-S-1: a comparison of the experimental data and model calculations

For an evaluation of the application properties of a paint formulation, it is essential to investigate the leveling of application marks in films of different water contents X . This would correspond to the situation, where corrections on a freshly painted wall are made, a certain time after the application of a first paint layer, i.e. after a certain drying time.

For the model calculations, the criterium for sufficient leveling was chosen to be a decrease of the application marks to less than 5% of the initial height. As an example, Figure 7-20 shows the calculated leveling of application marks (I) of the original dispersion A-S-1 ($X = 1.044$ g water/g polymer) and (II) of A-S-1 at a lower initial water content of $X = 0.94$ g water/g polymer, using Equ. 6-6.

For the original dispersion of A-S-1, the leveling of application marks to less than 5% of the initial value takes about 0.25 seconds, but for the dispersion of lower initial water content ($X = 0.94$ g/g), the leveling of brushmarks to even less than 20% of the initial value is not possible (= end of open time). From Equ. 7-1 one can learn, that a

decrease of the water content from $X = 1.044$ to $X = 0.94$ g/g at ambient conditions corresponds to a drying time of ~ 70 s. Already after that time the increased viscosity of the dispersion prevents complete leveling of the application marks and doesn't allow further corrections on the film layer.

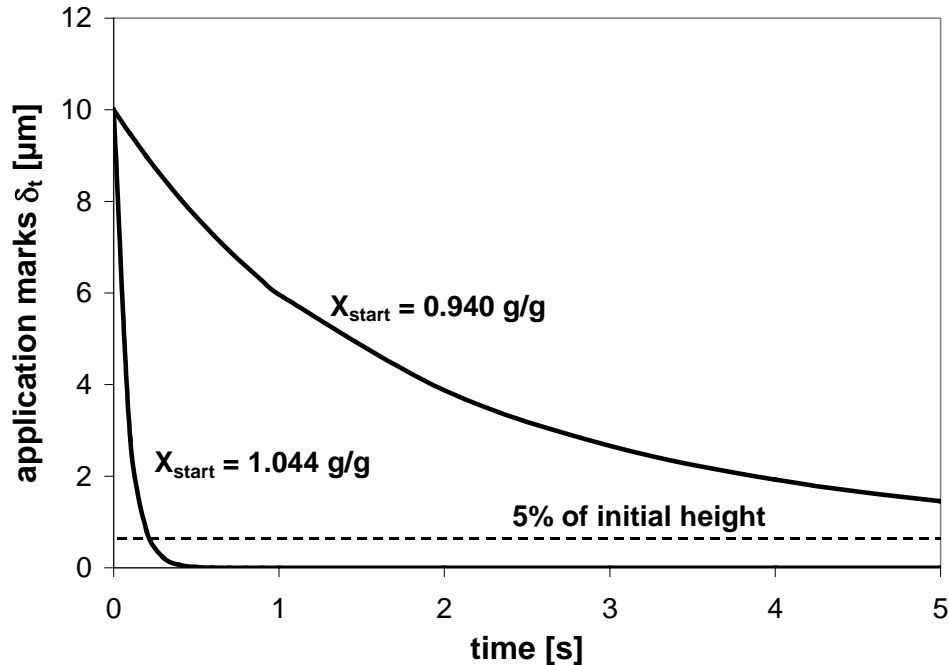


Figure 7-20: Leveling of brushmarks in a film of A-S-1 for two different initial water contents X

dispersion	(I) $t_{level}(X_{start})$	(II) $t_{level}(X_{I min})$	(III) $t_{open time}$
A-S-1	0.25 s ($X_{start} = 1.044$) $\eta = 0.20$ Pas	~ 7.5 s ($X_{I min} = 0.959$) $\eta = 2.54$ Pas	~ 61 s ($X = 0.957$) $\eta = 2.91$ Pas
A-H-1	2.40 s ($X_{start} = 1.034$) $\eta = 0.44$ Pas	~ 35 s ($X_{I min} = 0.949$) $\eta = 6.93$ Pas	~ 60 s ($X = 0.948$) $\eta = 14.65$ Pas
AS-H-1a	-	-	-
AS-H-1b	- ($X_{start} = 0.987$) $\eta = 58.24$ Pas	- ($X_{I min} = 0.902$) $\eta = 5538700.05$ Pas	-
AS-S-1	0.04 s ($X_{start} = 1.150$) $\eta = 0.06$ Pas	0.09 s ($X_{I min} = 1.065$) $\eta = 0.09$ Pas	~ 203 s ($X = 0.855$) $\eta = 2.15$ Pas
A-S-2	0.03 s ($X_{start} = 2.445$) $\eta = 0.008$ Pas	0.04 s ($X_{I min} = 2.360$) $\eta = 0.01$ Pas	~ 445 s ($X = 1.395$) $\eta = 369.71$ Pas

Table 7-2: The leveling times of all dispersions under investigation for different initial water contents X

For the different formulations, Table 7-2 gives an overview of the time, that a thin film of initial thickness $h_0 = 100 \mu\text{m}$ with application marks $\delta_0 = 10 \mu\text{m}$ in amplitude (spacing $\lambda = 0.1 \text{ cm}$) needs to level to less than 5% of its initial value (conditions: $T = 25^\circ\text{C}$, $\varphi = 50\%$, $u = 0.05 \text{ m/s}$).

The following information is presented:

- (I) The calculated leveling time after the application of a film of the original dispersion: $t_{\text{level}}(X_{\text{start}})$.
- (II) The calculated leveling time, when corrections to a one-minute-old film are made: $t_{\text{level}}(X_{1 \text{ min}})$.
- (III) The calculated open time $t_{\text{open time}}$ during which corrections can be done and complete leveling is still possible.

In addition, the corresponding low-shear viscosity η is indicated.

The model calculations indicate, that for AS-H-1a and AS-H-1b the viscosity of the original dispersions is already too high to allow extensive film leveling. According to the above definition, these formulations have no open time and application marks of geometric dimensions as employed here will therefore be permanently visible in the film. As long as the low initial viscosity of the soft-polymer dispersions A-S-1 and AS-S-1 doesn't cause sagging, these formulations should display a good open time behaviour. The considerable difference between the short open time of A-S-1 (*61 seconds*) and the good open time value of AS-S-1 (*203 seconds*) is caused by the initial water content X. AS-S-1 is more diluted and therefore, more water has to evaporate before the viscosity rises above the critical value which marks the end of complete film leveling. With *60 seconds*, the open time of the hard polymer dispersion A-H-1 is within the range of the one of A-S-1. A-S-2, being an aqueous dispersion of small and soft polymer particles, exhibits a very good open time of *445 seconds*. The good open time is achieved by a high dilution to only *~30 mass %* polymer compared to *~48 mass %* for the other dispersions. The small particles in A-S-2 help keeping the intrinsic viscosity sufficiently high to allow a higher dilution of the formulation without causing sagging. This again, is beneficial for the open time since water evaporation takes longer until the viscosity rises above the critical value. Apart from the viscoelastic behaviour of the individual formulations, thick films, small distances between the single brushmarks and a high surface tension would assist film leveling.

7.1.7 Influence of Additives on the Leveling of AS-H-1a

As stated above, the very high viscosity of AS-H-1a prevents extensive film leveling (compare Table 7-2).

The addition of 2% of surfactant to the gel-like formulation AS-H-1a (compare Chapter 7.1.5) decreases the viscosity and also surface tension, which is both, positive and negative for film leveling.

The addition of TexanolTM decreases the polymer's glass transition temperature. At the same time, in the high-viscosity dispersion AS-H-1a, the addition of TexanolTM further increases the viscosity of the dispersion which hinders film leveling from the moment of application (Figure 7-15).

In short words one can say, that in the case of AS-H-1a, none of the additives discussed here could change the dispersion properties in a way that would allow complete leveling of the freshly applied film of AS-H-1a.

7.1.8 Conclusions on Dispersion Rheology and Film Leveling

The following changes in the dispersion rheology during drying are negative for film leveling:

- the increased viscosity with decreasing water content X
- the formation of a yield stress and
- the early liquid-solid transition

Combined with film drying, it means that there is only a limited time available for the leveling of brushmarks in a freshly applied film, until the water content X of the film has decreased below a critical value. Even a small decrease of the water content X can make, that good application properties are lost and film leveling becomes impossible. A quantification of film leveling by model calculations and a discussion of the consequences for the different dispersions was presented in Chapter 7.1.6.

For the investigated dispersions, the model calculations give an open time between 60 and 445 seconds (compare Table 7-2). Two formulations (AS-H-1a, AS-H-1b) do not level at all. Here, a further elongation of the open time of aqueous dispersions could only be achieved by more diluted dispersions, in which the viscosity function was adjusted by adequate rheology modifiers (not investigated in this work).

7.2 Water Evaporation and Film Drying

A fundamental understanding of water evaporation and film drying of colloidal dispersions is pre-requisite to be able to further improve the application properties of waterborne latex formulations. So far, experimental data on drying are rare due to a lack of suitable experimental methods. Inverse-Micro-Raman-Spectroscopy (IMRS) is a powerful technique which allows measurements of local concentrations in thin coating layers, with a time and space resolution of about 1 s and 2-3 μm .

The chapter starts with a derivation of the parameters, necessary for the model calculations of film drying (i.e. the film temperature T_{film} , the gasside mass transfer coefficient $\beta_{w,g}$, water activity a_w and the diffusion coefficient of water in the film $\delta_{w,p}$). In Chapter 7.2.2, a film drying experiment using the IMRS technique is described. The evaluation of the original Raman data gives the water concentration in vertical direction of the film (Chapter 7.2.3).

Important for the understanding of film drying is the identification of the parameters, that influence drying and their systematic variation (Chapter 7.2.4). Defects like lap-lines or edge-effects are the result of horizontal inhomogeneous drying, which is investigated in Chapter 7.2.5. Drying of aqueous latex dispersions differs in many aspects from that of solvent-borne polymer solutions. To make this clear, a drying and a redissolution experiment (IMRS) of the polymer-solvent system PVAc-Toluene is presented (Chapter 7.2.6).

7.2.1 Parameters Necessary to Describe Drying

In the following chapter, the parameters required for the mathematical description of film drying (Chapter 6.2) are derived.

(I) The Wet Film Temperature and Isothermal Drying Conditions

For the evaporation of water from the surface of a wet latex film a large amount of energy is needed and is provided by the surrounding air and by the substrate. Depending on the heat transfer characteristics of the substrate, the temperature of the wet film will decrease until all energy fluxes to and from the film are balanced.

A lower film temperature will have a strong impact on drying and film formation. On the one hand it will slow down drying which is beneficial for the open time of the film, but on the other hand, it could be that the film temperature decreases below the polymer's glass transition temperature T_g , which hinders polymer deformation and slows down polymer interdiffusion. In the worst case, it will cause cracks, film defects and insufficient coalescence.

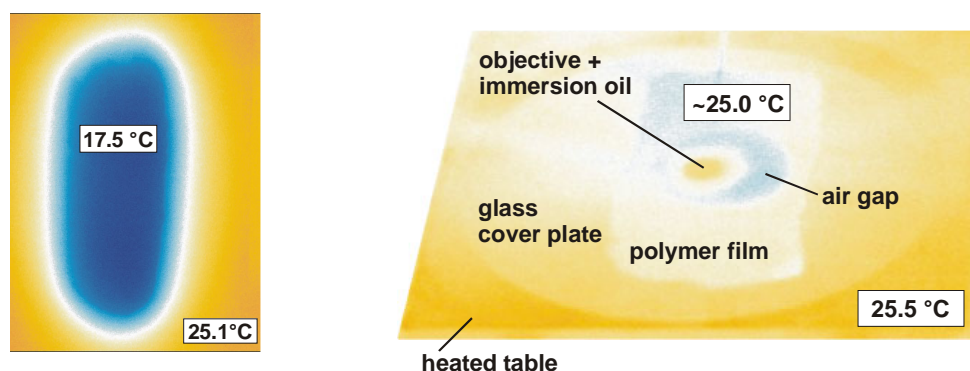


Figure 7-21: *Infrared-camera pictures of the surface of wet latex films. Left: a film on a substrate with a low heat transfer coefficient; right: a coating applied onto the heated table of the drying channel*

Figure 7-21 shows infrared-camera pictures (IR-M700 Mitsubishi Electronics; resolution: 801 x 512 pixels) of wet latex films coated onto substrates of different heat transfer characteristics. Due to the low heat transfer coefficient of insulation materials, the temperature of wet films coated onto such materials is very low ($\Delta T \sim 7\text{-}8\text{ }^\circ\text{C}$) (Figure 7-21 left). The good heat transfer characteristics of the brazen heatable table in

the drying channel make that the film is only slightly cooler ($\Delta T \sim 0.5 \text{ }^\circ\text{C}$) than its surroundings (Figure 7-21 right).

The data in Figure 7-21 justify the assumption of isothermal conditions in the drying channel, which is taken for the model calculations of drying (Chapter 6.2).

(II) The Mass Transfer Coefficient $\beta_{w,g}$

Mass transfer coefficients of water in the fully developed laminar flow of air can be obtained from evaporation experiments of the pure solvent: For different drying conditions, the evaporation rate of pure water is measured gravimetrically. Then, the mass transfer coefficient $\beta_{w,g}$ is calculated from Equ. AVII- 10, using the saturation pressure of water at the temperature of the wet film. Figure 7-22 shows measured and calculated values of $\beta_{w,g}$ as a function of the air velocity u . There is good agreement between the experimental data, represented by the symbols, and the calculated average values $\overline{\beta_{w,g}}$, obtained from the well-known *Sherwood*-correlation for plate-geometry (Equ. 6-8), represented by the curve.

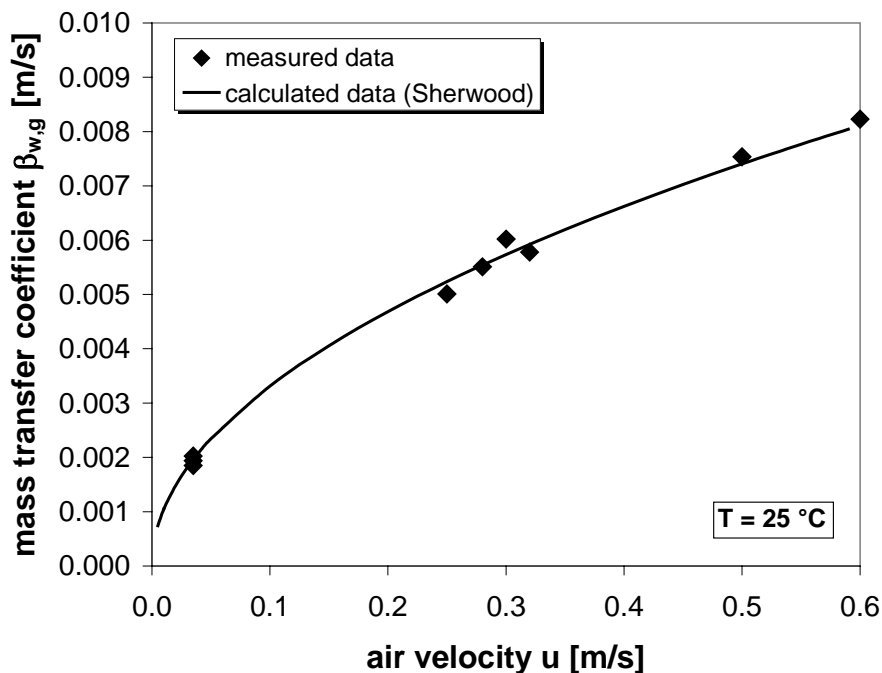


Figure 7-22: A comparison of experimental values of the mass transfer coefficient $\beta_{w,g}$ with the well-known *Sherwood* correlation (Equ. 6-8)

(III) The Phase Equilibrium and Sorption Isotherms

Phase equilibria can be measured by a gravimetric method, where dry latex films are placed into sealed boxes of defined water activity to reach sorptive equilibrium between the polymer film and the surrounding air. At regular times, the water uptake is recorded. It is assumed that the contact times are long enough to reach equilibrium. The defined water activity is caused by saturated solutions of different salts at the bottom of the different boxes. Appendix X gives a list of possible salt solutions and corresponding water activities. The experimental setup assures, that the polymer film

is in contact with the water vapor only and that the gas volume above the salt solution is kept as small as possible to assure the desired water activity. For isothermal conditions, the boxes are kept in an oven at a constant temperature.

As already mentioned before, fresh films of aqueous latex dispersions display a heterogeneous structure due to a network of surface-active material, hydrophilic particle interfaces or even pores in between the polymer particles. As long as the hydrophilic network is not destroyed by polymer interdiffusion, water transport and sorption are dominated by the nature of the network material.

Figure 7-23 and Figure 7-24 show the gravimetrically measured sorption isotherms of the two different latices A-S-1 and AS-H-1b. The one-day old films were kept in the boxes at a temperature of $T = 30\text{ }^{\circ}\text{C}$ for up to *15 days*. After *1, 3, 10* and *15 days* the water uptake of the films was measured gravimetrically. Since the latices under investigation are industrial products, it was not possible to compare the experimental data with literature values.

For the less hydrophilic latex A-S-1, a case III sorption isotherm, according to the BET classification was measured (compare Appendix IX). First experimental data, taken after $t = 1\text{ day}$, are represented by the black symbols. There is a gradual decrease in the sorptive capacity of the film with its age.

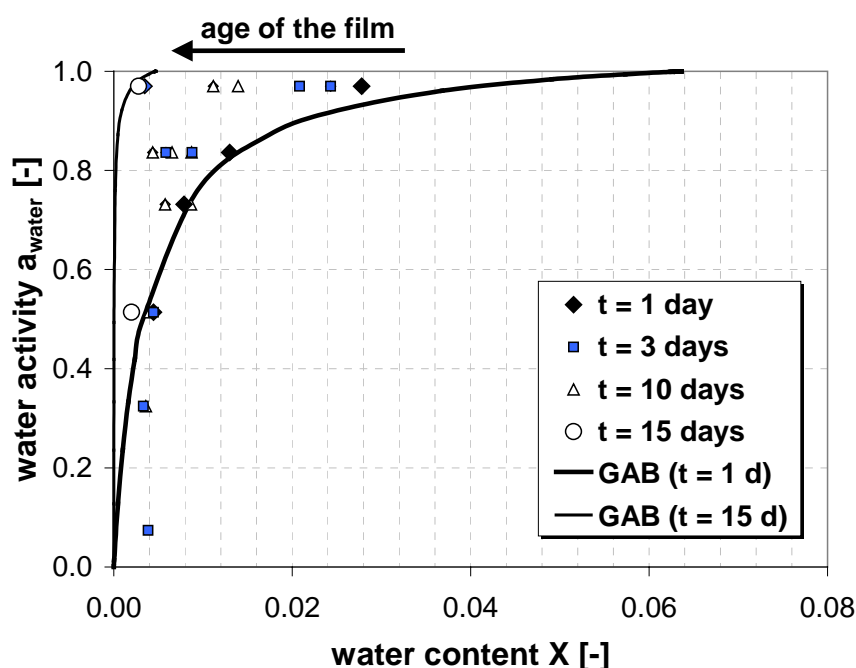


Figure 7-23: Dependence of the sorption isotherm at $T = 30\text{ }^{\circ}\text{C}$ on the age of a dried latex film (A-S-1; case III sorption behaviour (BET-classification))

Assuming that after *1 day* sorptive equilibrium has been reached, this would be the result of ongoing coalescence of the particles. It means that with film age, the hydrophilic layer at the particle interfaces, formed by functional groups and surfactant material, - the main path for water diffusion -, is destroyed by polymer interdiffusion. The experimental data after $t = 15\text{ days}$, represented by the circles, prove that the

sorptive capacity of the film has decreased by far, indicating that a hydrophilic network is no longer present.

For the more hydrophilic latex AS-H-1b, a case II sorption isotherm according to the BET classification (compare Appendix IX) was measured, showing stronger interactions between the water molecules and the polymer.

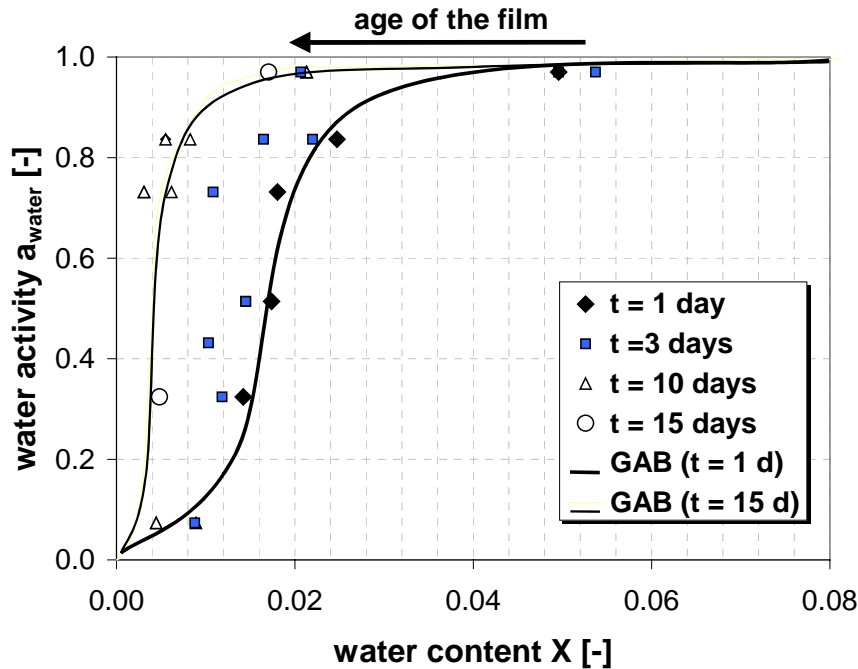


Figure 7-24: Dependence of the sorption isotherm at $T = 30\text{ }^{\circ}\text{C}$ on the age of a dried latex film (more hydrophilic latex AS-H-1b; case II and case III sorption behaviour (BET classification))

This is due to the large number of functional groups located at the particle surface and the higher glass transition temperature T_g of AS-H-1b. The higher T_g of the polymer is responsible for the still existing hydrophilic network or even pores in the dry film. Again, as observed for A-S-1, there is a gradual decrease in the sorptive capacity of the film, which indicates that the hydrophilic layer of functional groups and surfactant material between the polymer particles becomes thinner or is even interrupted due to polymer interdiffusion. With time, the shape of the isotherm changes from a case II to a case III type. This would indicate, that most of the pores formerly present in the film have been closed.

In Figure 7-23 and Figure 7-24, the data obtained from gravimetric sorption experiments are compared with GAB-model calculations. The three-parameter GAB-model (compare Appendix IX) is suited to fit the sorption isotherms of both latices not only for $t = 1\text{ day}$, but also for $t = 15\text{ days}$. Table 7-3 gives the parameters used to fit the experimental data: k represents the ratio of the heat of adsorption of water molecules to the heat of liquefaction and is required to be smaller than one and ϕ_m represents the volume fraction of a complete monolayer of water molecules. As expected, the more hydrophilic dispersion AS-H-1b, having more active sites for adsorption, shows a

higher value of φ_m than the less hydrophilic A-S-1. The parameter c_{GAB} is related to the partitioning of higher sorption layers with regard to the distribution of adsorbed water between the polymer surface and the first monolayer. For both latices, the value of c_{GAB} decreases with time, indicating that multi-layer adsorption continually decreases due to coalescence. For the less hydrophilic and low- T_g latex A-S-1, a value of $c_{GAB} = 0.005$ indicates that coalescence is almost completed after $t = 15$ days, whereas for the more hydrophilic and higher- T_g latex AS-H-1b, data fitting for $t = 15$ days gives a value of $c_{GAB,average} = 0.667$, indicating incomplete coalescence. For AS-H-1b, the water-polymer interactions are stronger and polymer interdiffusion is slower: two factors that are responsible for the incomplete coalescence and the higher permeability of this formulation.

	$t = 1$ day	$t = 15$ days
A-S-1	$c_{GAB} = 0.900$ $k = 0.940$ $\varphi_m = 0.004$	$c_{GAB} = 0.005$ $k = 0.940$ $\varphi_m = 0.004$
AS-H-1b	$c_{GAB} = 1.089$ $k = 0.940$ $\varphi_m = 0.100$	$c_{GAB} = 0.667$ $k = 0.940$ $\varphi_m = 0.100$

Table 7-3: Fitting parameters, used in the GAB-model for the two latices A-S-1 and AS-H-1b

In the mathematical model of film drying (Chapter 6.2), for reasons of simplicity, the phase equilibrium is expressed by simple exponential equations (Equ. 6-9 and Equ. 6-10) having been fitted to the experimental sorption data. Depending on the kind of experiment (= age of the investigated film), the equation obtained from data fitting at $t = 1$ day or $t = 15$ days is used. For the different dispersions, the values of the constants A, B, C, D are in Appendix IX.

(IV) Diffusion Coefficients $\delta_{w,p}$ of Water in the Polymer Film

As described in Chapter 6.2.3, the diffusion coefficient $\delta_{w,p}$ of water in the polymer film is a function of (I) the water content X and (II) the temperature T. Besides, water diffusion in a latex film strongly depends on (III) the age and structure of the film.

Values of the diffusion coefficient $\delta_{w,p}$ are obtained from a comparison of the theoretical model with the experimental data of film drying and redispersion using $\delta_{w,p}$ as a fitting parameter (described by the exponential equation in Chapter 6.2.3).

In the case of film drying experiments at ambient conditions, a typical value of the diffusion coefficient is $\delta_{w,p} = 1.95 \cdot 10^{-10} \text{ m}^2/\text{s}$.

In the case of redispersion and permeation experiments, the diffusion coefficient $\delta_{w,p}$ can have different values depending on the dispersion characteristics and the age and

pre-treatment of the film (e.g. drying at elevated temperatures). In the presence of a hydrophilic network, $\delta_{w,p}$ is relatively high (a typical value is $\delta_{w,p} = 4.2 \cdot 10^{-11} \text{ m}^2/\text{s}$), but as soon as it is destroyed by polymer interdiffusion, the diffusion coefficient of water in the film will decrease by about two decades.

Appendix XI gives a summary of the initial values of the diffusion coefficient $\delta_{w,p}$ for the different experiments where a comparison of the experimental data with model calculations is performed.

7.2.2 Film Drying Experiments using Inverse-Micro-Raman-Spectroscopy

The chapter illustrates a film drying experiment using Inverse-Micro-Raman-Spectroscopy (IMRS). This includes the film preparation and the description of a typical experiment. Raman data, as obtained from the measurement software, are presented.

For the investigation of drying and film formation, a thin film of aqueous polymer dispersion is applied onto a glass plate (= substrate), located in the Raman drying channel at defined drying conditions. For a sketch and a description of the IMRS-technique see Chapter 5.1.2. The dispersion's viscosity and the velocity of the roller coater have a strong influence on the initial film thickness. The film is prepared by a roller coater with a gap size of $d = 150 \mu\text{m}$ and different initial film thicknesses can be produced by roller coaters of different gap size. The drying experiment is started immediately after the film preparation: The laser is focused into the sample film from below the drying channel and is moved towards the film surface in constant steps (typical is a step size of $4\text{--}6 \mu\text{m}$). After each step upwards, a Raman spectrum is taken in the film. The time to obtain one Raman spectrum is $\sim 1.2 \text{ seconds}$. Figure 7-25 to Figure 7-27 show the measured Raman spectra obtained from a vertical scan through the film after different drying times ($t = 0, 10, 20 \text{ min}$). The sharp peak at $\sim 3000 \text{ cm}^{-1}$ represents the polymer component and the broad peak at $\sim 3500 \text{ cm}^{-1}$ the water in the wet film. At the beginning ($t = 0 \text{ min}$), the thickness of the wet film is about $60 \mu\text{m}$. The decrease of the peak intensity towards the film surface is the result of scattering effects in the wet dispersion (compare Chapter 5.3). After $t = 10 \text{ min}$ of drying, a decrease in the film thickness to about $40 \mu\text{m}$ is observed. At the same time, the intensity of the broad water peak decreases because of water evaporation. After a drying time of $t = 20 \text{ min}$, the polymer film is completely dry. This is indicated by the fact that the broad water peak has vanished and the thickness of the film has further decreased to little more than $20 \mu\text{m}$. The quantitative evaluation of the Raman raw data is described in Chapter 5.2.3. A center-of-gravity correction of the position of the laser focus in the film is done according to Appendix VI.

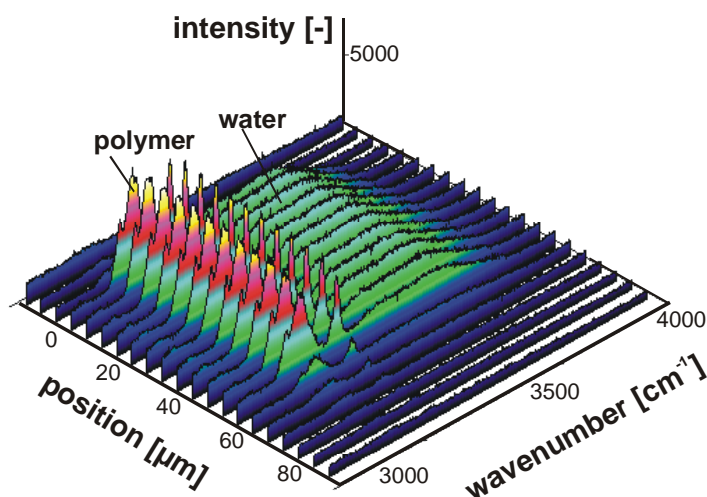


Figure 7-25:

A 3-dimensional plot of the Raman spectra of a 60- μm -thick film of AS-H-1b ($t = 0 \text{ min}$)

standard drying conditions:
 $T = 25 \text{ }^\circ\text{C}$; $\phi = 50\%$; $u = 0.05 \text{ m/s}$

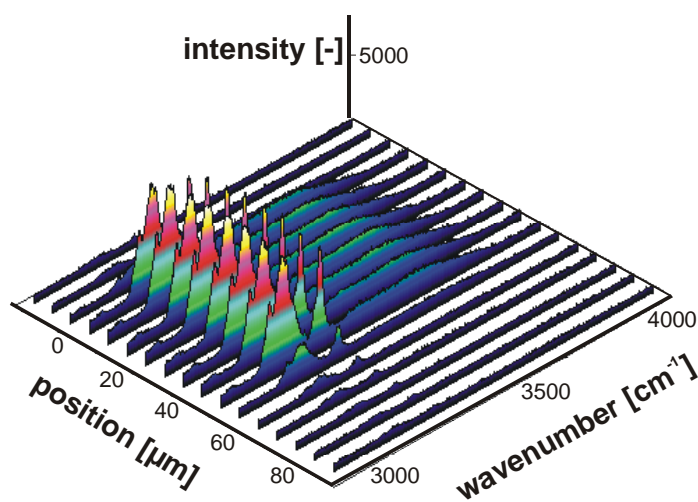


Figure 7-26:

A 3-dimensional plot of the Raman spectra after $t = 10 \text{ min}$ of drying ($d \sim 40 \text{ } \mu\text{m}$)

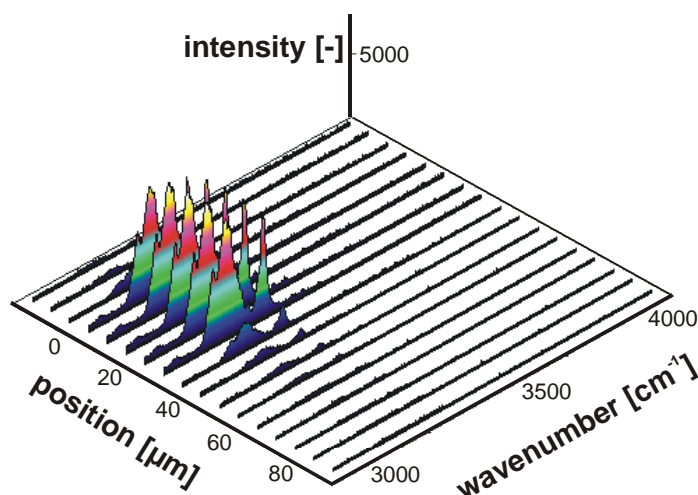


Figure 7-27:

A 3-dimensional plot of the Raman spectra after $t = 20 \text{ min}$ of drying ($d \sim 20 \text{ } \mu\text{m}$)

7.2.3 Homogeneous Drying in Vertical Direction of the Film

Generally, dealing with drying phenomena, one differentiates between the constant rate period and the falling rate period. In the period of constant evaporation rate, drying is limited by the gasside mass transfer, whereas, in the falling rate period, the transport resistance for the solvent in the bulk is dominant.

Figure 7-28 shows the water concentration profiles in a film of AS-H-1b during a drying experiment at $T = 25\text{ }^\circ\text{C}$, $u = 0.05\text{ m/s}$ and $\varphi = 50\%$ (also called “standard drying conditions”). Such conditions are typical for the application of interior and exterior wall paints. In this study, the hard polymer and more hydrophilic formulation AS-H-1b was chosen to serve as a model dispersion for the investigation of film drying. The initial water content of the dispersion is $X_0 = 1.0\text{ g water/g polymer}$ and the initial film thickness is $h_0 = 81.5\text{ }\mu\text{m}$. The lateral measurement position is in the middle of the sample film.

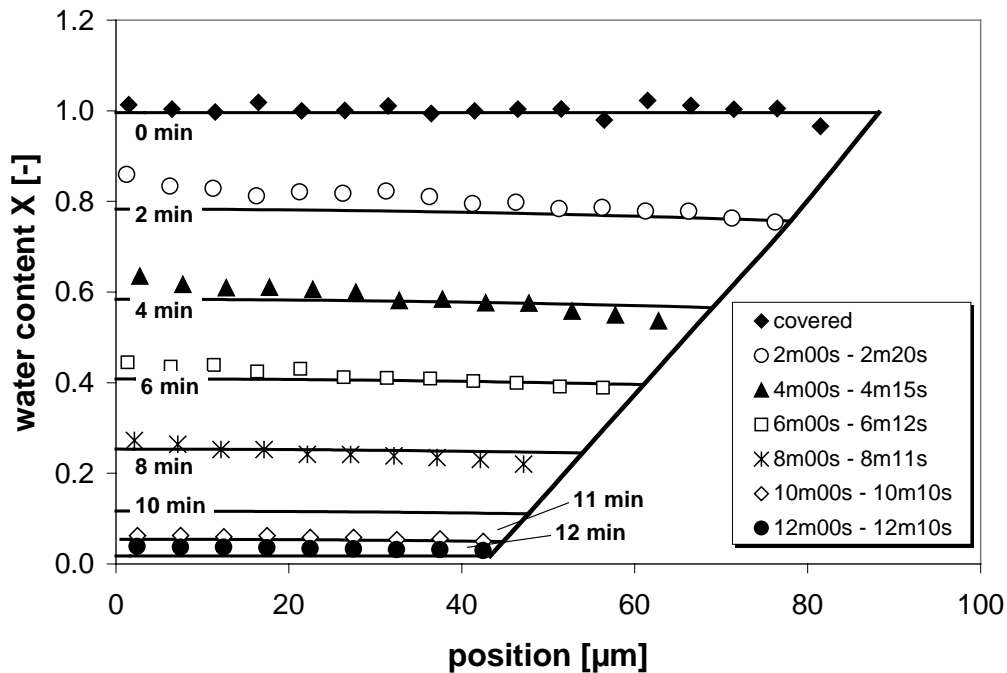


Figure 7-28: The water concentration profiles in a film of AS-H-1b (=water content X at different positions in vertical direction of the film)

The shape of the integral drying curve (Figure 7-29) is typical for aqueous polymer dispersions. It is characterized by a long constant rate period and it takes long time until a transport resistance for the small water molecules builds up in the film (= beginning of the falling rate period).

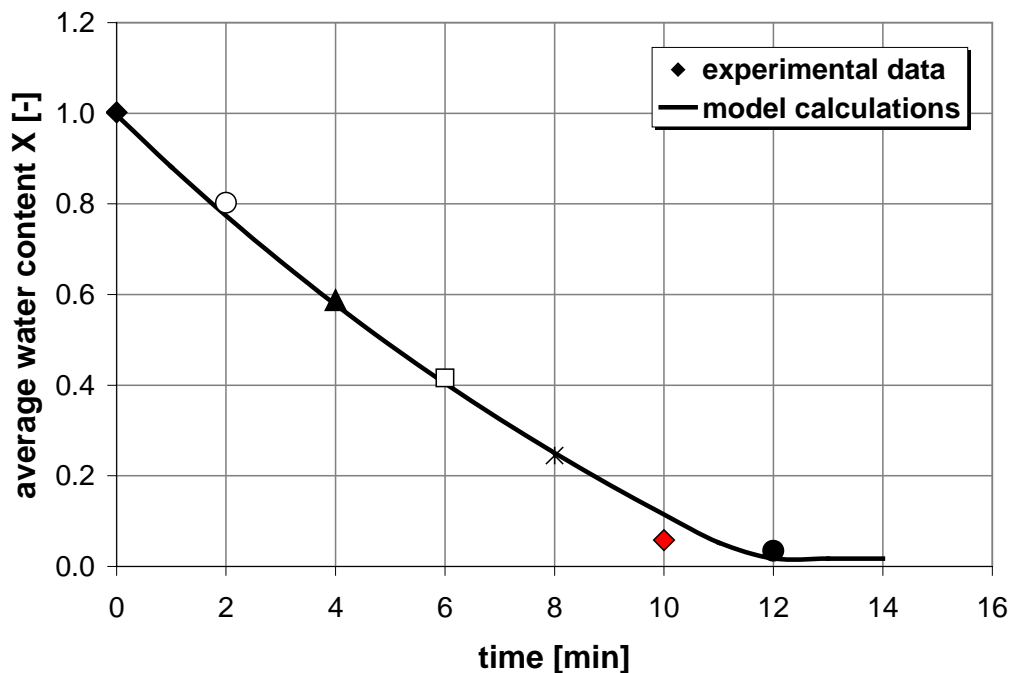


Figure 7-29: The drying curve of AS-H-1b, at standard drying conditions

Figure 7-28 proves that drying of aqueous latex dispersions is mainly gasphase controlled. Opposite to polymer solutions with organic solvents, no steep concentration gradients form during drying which would indicate a filmside diffusion resistance for water in the film. At a remaining water content of $X \sim 0.05$ g water/g polymer and lower, the drying rate is dominated by the transport of water along the hydrophilic layers at the particle interfaces.

An increased drying velocity towards the end of drying is often observed and is the result of horizontal inhomogeneous drying (see also Chapter 7.2.5).

During drying, a water front forms at the edge of the film and moves in horizontal direction towards the center of the film. In this case, the increased drying velocity at the measurement position is due to the water front that moves in horizontal direction and passes the measurement spot.

7.2.4 Influence of Different Drying Parameters on the Evaporation Rate

The evaporation rate of water during a film drying experiment strongly depends on the ambient conditions, like temperature, air humidity and air velocity. The drying time is also influenced by the initial film thickness and the initial water content X .

The table gives an overview of the different experiments that were performed to show the influence of the different drying parameters on the drying rate. The measurement position was always in the center of the sample film.

<i>dispersion</i>	<i>temperature</i> T [± 0.5 °C]	<i>relative humidity</i> φ [%]	<i>air velocity</i> u [m/s]	<i>initial film thickness</i> d [μm]
AS-H-1b ($X_0 = 1.0$ g/g)	25 °C	4% 50% 70%	0.05 m/s	52.5 ± 2 μm
A-H-1 ($X_0 = 1.0$ g/g)	25 °C 30 °C 40 °C	50%	0.05 m/s	40.3 ± 0.3 μm
AS-H-1b ($X_0 = 1.0$ g/g)	25 °C	50%	0.05 m/s 0.15 m/s 0.30 m/s	53.5 ± 0.5 μm
AS-H-1b ($X_0 = 1.0$ g/g)	25 °C	50%	0.05 m/s	32.0 μm 92.0 μm 123.0 μm

Table 7-4 An overview of the different experiments, performed to quantify the influence of the different drying parameters

Appendix XI gives basic considerations and a visualization about the influence of the different drying parameters as described in Table 74. Only one parameter is varied at a time whereas the other parameters are kept at standard conditions. The figures show the average water content of the film with time and a comparison with constant-rate model calculation.

7.2.5 Inhomogeneous Drying in Horizontal Direction of the Film

Horizontal inhomogeneous drying is responsible for a number of film defects expressed by lap lines that are visible in the dry coating or by edge effects. In this study, the lateral inhomogeneous drying and horizontal mass flow in thin films of aqueous polymer dispersions is observed and investigated by the different experimental methods of gravimetry and Inverse-Micro-Raman-Spectroscopy (IMRS). The local mass flow can be influenced by a special treatment of the film, e.g. (I) by covering parts of the film with a lid or (II) by applying locally higher temperatures, whereas (III) artificial borders around the film strongly reduce lateral mass flow. IMRS measurements at different positions in horizontal direction of the film give the concentration gradients in lateral direction and also the profile of the film.

(I) Gravimetric Drying Experiments

Gravimetry is a simple method, widely used to investigate the drying behaviour of thin polymer films. The disadvantage of this method is, that it is impossible to obtain local drying rates and to differentiate between the drying rates of different solvents in multi-component systems. Gravimetric drying experiments give the evaporated mass of solvent from a film with time (= average value).

In the case of aqueous polymer dispersions, the evaporation area of the film decreases throughout drying, being a fact which isn't necessarily obvious from the shape of the drying curve. Figure 7-30 shows the drying curve of AS-H-1b. The position of the drying front is illustrated by digital pictures of the sample film at $t = 5, 15$ and 25 minutes after application. The different zones, the transparent (= dry) border area and the milky (= wet) center of the film, can be distinguished.

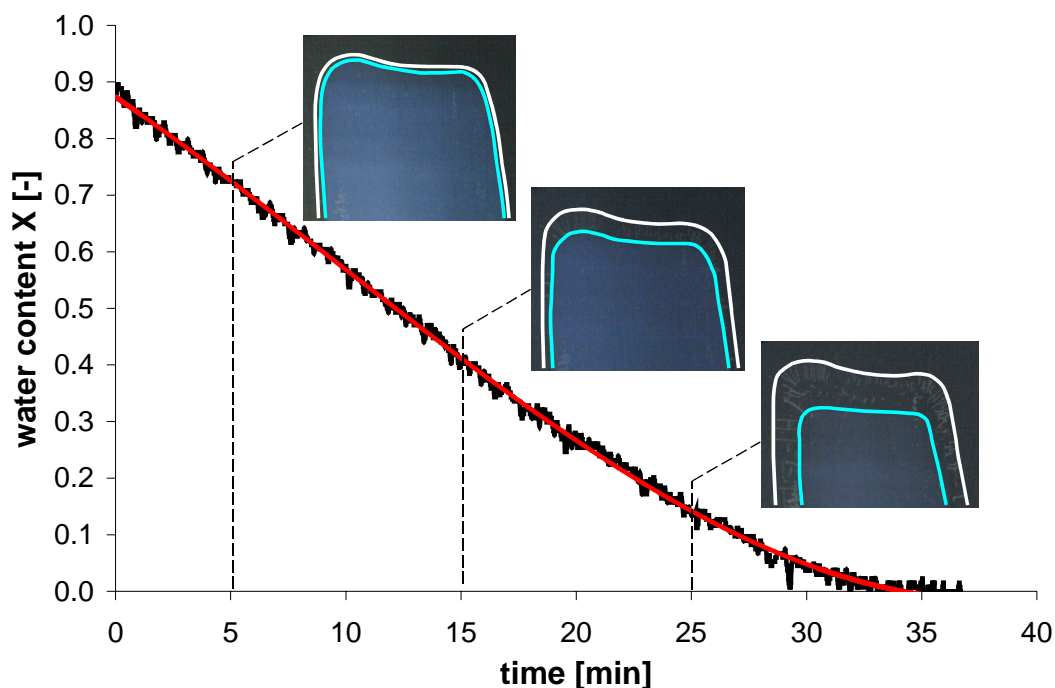


Figure 7-30: The gravimetric drying curve of AS-H-1b giving an illustration of horizontal inhomogeneous drying of aqueous latex dispersions. The pictures show parts of the wet latex

($T = 22$ °C; $u = 0.05$ m/s; $\varphi = 30\%$; $m_0 = 0.504$ g)

(II) The Time-Dependent Evaporation Area $A(t)$

The drying curves of AS-H-1b, obtained by the two experimental methods, (I) gravimetry and (II) IMRS, differ significantly in their shape: the average loss of water from the film, obtained from gravimetry, shows a constantly decreasing drying rate which is caused by a continually decreasing evaporation area A . The Raman experimental data, taken from one spot in the center of the sample film, give a constant evaporation rate which increases towards the end, when influenced by horizontal mass flow. Both curves end at the same time since the center position of the film is the last spot to dry (Figure 7-31 top). Assuming a uniform film thickness, the time-dependent evaporation area $A(t)$ can be calculated from a fit of the IMRS data (= film thickness) and gravimetric data (= water content).

$$X_{t,\text{gravimetric}} - \underbrace{\left(\frac{(h_{t,\text{Raman}} - h_{\text{end}}) \cdot A(t) \cdot \rho_{\text{water}}}{m_{\text{polymer}}} \right)}_{X_{t,\text{Raman}}} = 0 \quad \text{Equ. 7-2}$$

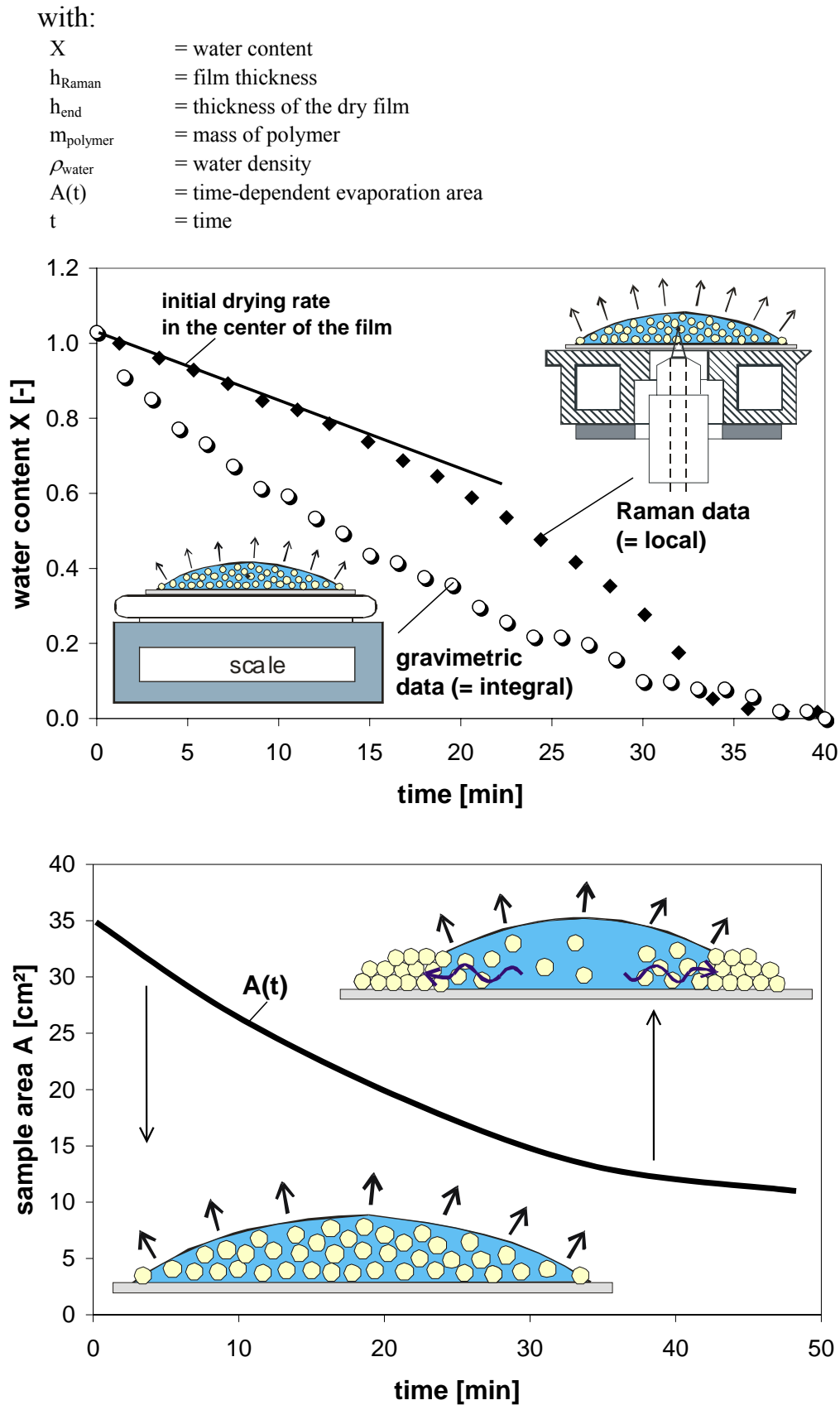


Figure 7-31: Top: A comparison of (I) the Raman and (II) the gravimetric drying curve of a sample film of AS-H-1b; bottom: The evaporation area $A(t)$

According to the calculation, the evaporation area $A(t)$ decreases by $\sim 57\%$ during drying (see Figure 7-31 bottom). $A(t)$ can be described by an exponentially decreasing function of time, which means that, - under the assumption of a uniform film thickness -, the drying front moves slower towards the end of drying.

(III) Enforced Horizontal Mass Flow (e.g. by Air Flow, Temperature)

According to Equ. 3-13, the average particle distance in the highly concentrated dispersion lies between 0 and 10 nm (see Appendix III). Compared to the latex particle diameter of $100\text{-}150\text{ nm}$, it means, that a drag flow of particles might only be possible at the very beginning of drying since the latex particles are already very much fixed in their position. Experiments, where drying is locally enhanced could show the existence of a drag flow of particles to the position of preferred evaporation. Such conditions can be provoked by, e.g. partly covered polymer films or by local heating of the film. In the case of a partly covered film, the air in the slit between the sample film and the cover plate is hardly exchanged and saturates with water vapour. Therefore, drying is considerably slowed down compared to the uncovered part of the film. Local heating of parts of the film increases the evaporation rate in these areas. Figure 7-32 shows the profile of a locally heated film and Figure 7-33 gives the dry film profile of a partly covered film obtained from IMRS experiments.

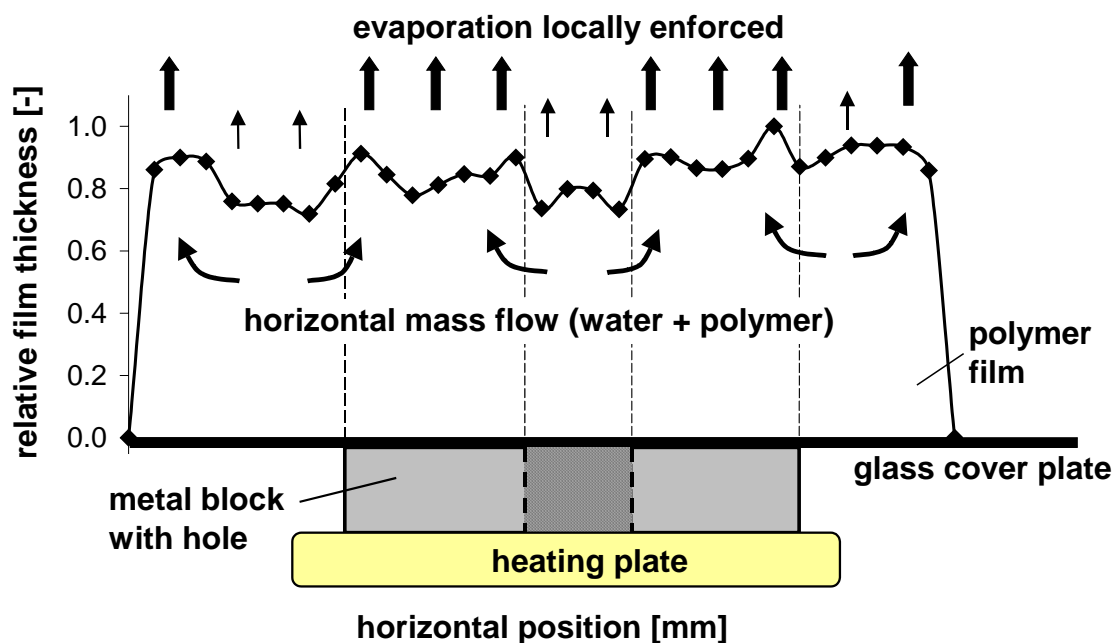


Figure 7-32: Experimental evidence for the drag flow of polymer particles in a locally heated film ($T = 50\text{ }^{\circ}\text{C}$) obtained by IMRS

The up to 10% increased film thickness at the positions of better drying conditions proves that, at the beginning of drying, a drag flow of water and particles has occurred. Since the dispersions display a low surface tension close to the minimum value observed for the critical micelle concentration of surfactant c_{cmc} , Marangoni-convection is believed not to be the main driving force. A further discussion and

investigation of the mechanism and the driving forces for horizontal drag flow of aqueous polymer dispersions would be suggested for future investigations.

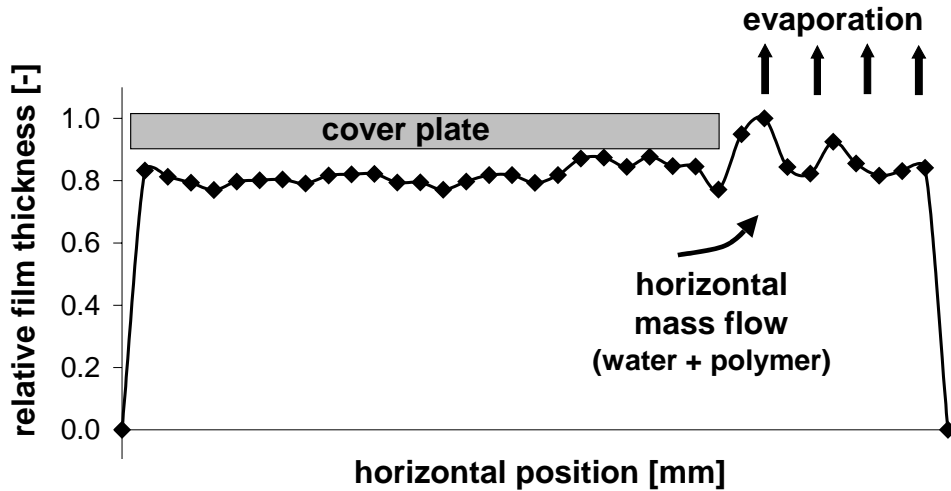


Figure 7-33: Experimental evidence for the drag flow of polymer particles in a partly covered film obtained by IMRS

(IV) Suppressed Horizontal Mass Flow (by Artificial Borders)

The convex shape of the drying curve of aqueous latex dispersions which is obtained by local measurements in the center of the film, is the result of horizontal flow of water to the edge of the film. Horizontal inhomogeneous drying can be considerably decreased by artificial borders around the measurement spot.

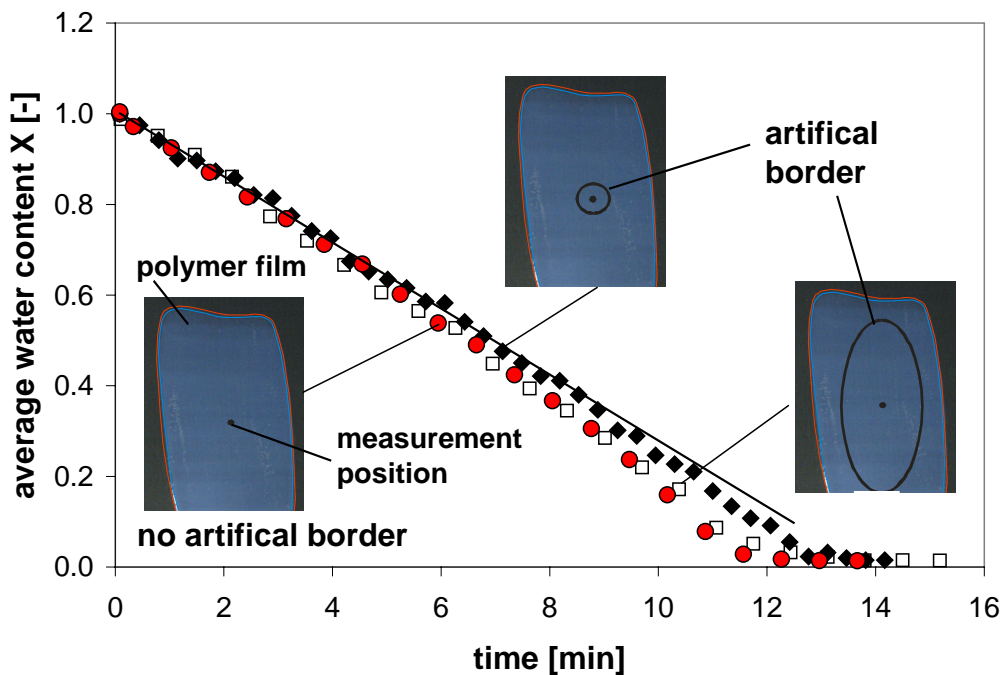


Figure 7-34: The horizontal mass flow can be largely prohibited by artificial borders

The dimensions of the artificial borders are indicated by the rings around the measurement position in Figure 7-34. A small plastic ring around the measurement spot gives a

nearly constant evaporation rate compared to the observed evaporation from films with no boundary or a large artificial border. The findings are explained by the fact that the large evaporation area at the edge of the film which causes inhomogeneous drying doesn't exist at the presence of an artificial border. By a ring of larger diameter, there is a higher risk of an inhomogeneous coating thickness within the borders where thin coating areas can also form starting points for faster drying and lateral flow.

(V) Measurements at Different Horizontal Positions of the Film

Figure 7-35 shows the drying curves, obtained from IMRS scanning experiments, at three different horizontal positions of a latex film (indicated by the sketch of the film). The first measurement position (drying curve 1) is located 3 mm away from the edge; drying curve 3 is obtained from the center position which is about 20 mm away from the border. The sample film dries three times faster at the edge (= position 1) than in the center (= position 3). The faster decrease of the water content is the result of a combination of (I) a reduced film thickness and (II) a larger evaporation area at the edge of the film. The initial slope of the drying curves corresponds well to constant-rate model calculations (Chapter 6.2.1), which are represented by the lines. The closer to the border of the film, the earlier an increase in the drying rate is observed, caused by horizontal flow. The same findings become clear from Figure 7-36 which shows the water flux described by:

$$\dot{m}_{\text{water}} = -\rho_{\text{polymer}} \cdot h_{\text{end}} \cdot \frac{dX}{dt} \quad \text{Equ. 7-3}$$

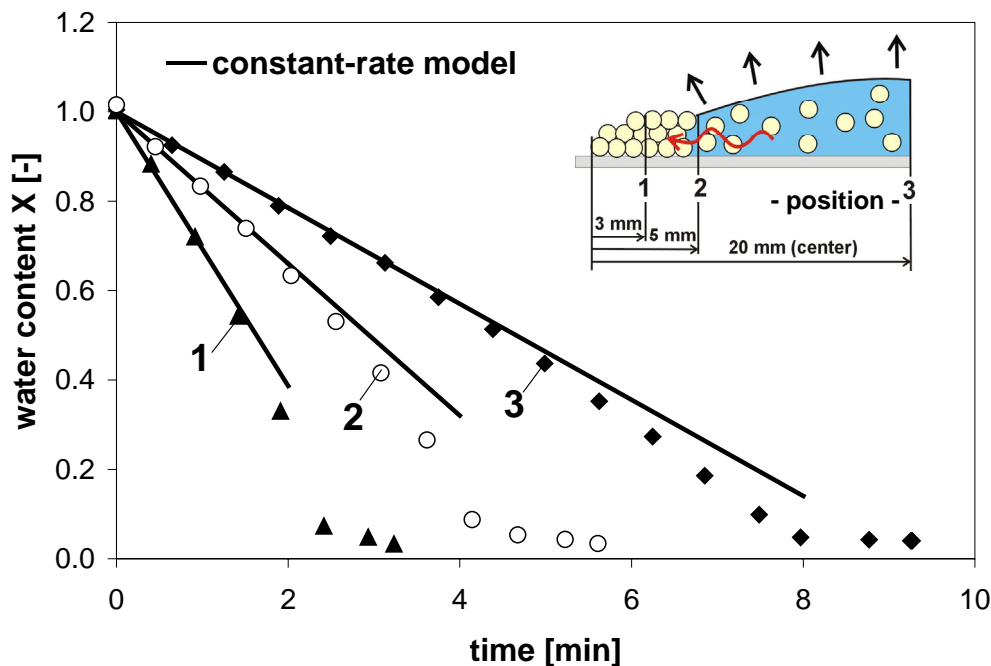


Figure 7-35: The drying curves at different horizontal positions of a film of AS-H-1b ($T = 25\text{ }^{\circ}\text{C}$; $u = 0.05\text{ m/s}$; $\varphi = 50\%$; $h_0 = 66.4 \pm 3.0\text{ }\mu\text{m}$)

The closer to the edge, the earlier and the steeper is the increase of the water flux. The straight lines represent the water flux that leaves the film by evaporation; the area above that line and below the respective curve gives the horizontal flux of water at the different measurement positions. At the two positions closer to the edge, the film is already dry before drying at the center (= position 3) is influenced by the horizontal water flux.

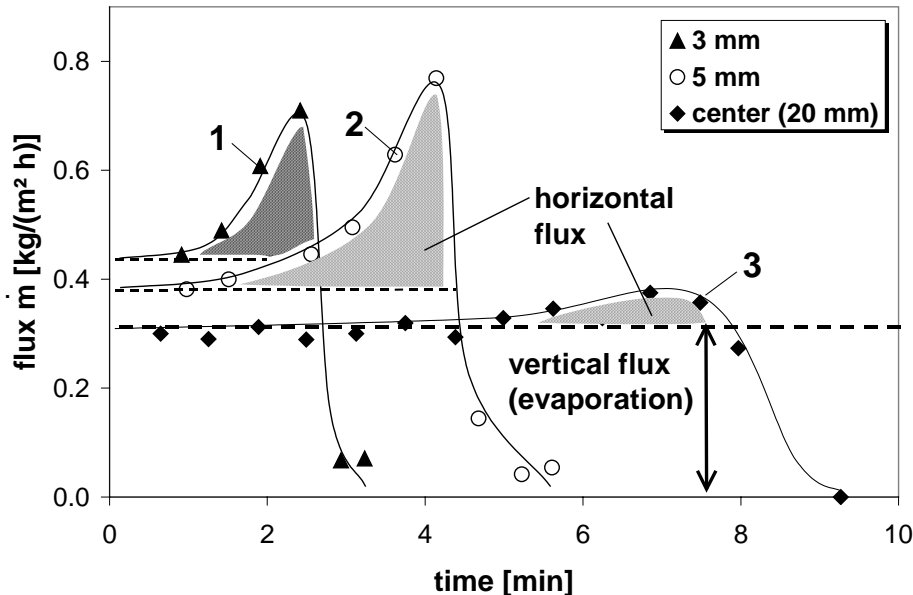


Figure 7-36: The water flux at the different positions (see Figure 7-35)

(VI) Horizontal Water Concentration Profiles in Thin Coatings

Horizontal water concentration profiles that form during drying can be visualized by IMRS measurements at different horizontal positions of the film.

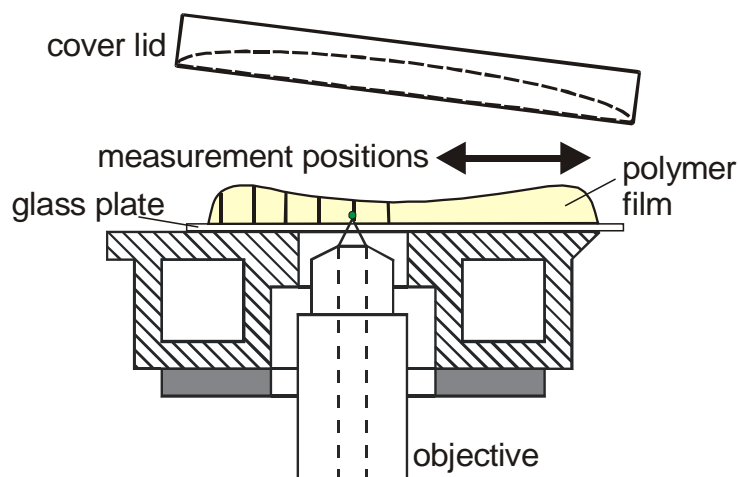


Figure 7-37: Experimental setup for IMRS measurements in horizontal direction

For the measurements, the wet film is covered by a lid which considerably slows down drying and allows taking data at the different horizontal positions while the concen-

tration profile is largely unchanged. Before the next line scan, the lid is removed for two minutes and the film is dried at standard drying conditions (see Figure 7-37).

In the hard polymer dispersion A-H-1 of $T_g = 25\text{ }^\circ\text{C}$, the water content at seven positions, being 3-4 mm apart from each other, was measured every two minutes. The water profiles and the corresponding film thickness are presented in Figure 7-38 and Figure 7-39. The edge of the film is at the left and the center of the film is at the right as indicated by the sketch of the film. At the moment of application, the water content in the film is homogeneous.

Due to the good wetting properties of the investigated dispersion on the substrate (= a larger evaporation area and a reduced film thickness at the edge), drying at the edge of the film is faster. This leads to the formation of strong lateral concentration gradients in the film. After 8 minutes of drying, the film at the edge is dry, whereas the water content in the center has decreased by little more than 30% of the initial value.

In hard-polymer dispersions like A-H-1, the particle deformation is incomplete leading to a porous film structure. Capillary forces in the large pores are not strong enough to completely deform the polymer particles and to keep the water at the edge of the film. Therefore a lateral drying front forms at the edge and moves towards the center. The minor importance of capillary forces for the drying of A-H-1 is proven by the good agreement between the experimental data (represented by the symbols) and the model calculations (obtained from the finite-element model (Chapter 6.2.5) where capillary forces are not taken into account. In the model, a typical value for the diffusion coefficient of water along the particle interfaces $\delta_{w,p} = 1.94 \cdot 10^{-10}\text{ m}^2/\text{s}$ was used. The model exclusively describes water diffusion in the film caused by concentration gradients. In the end, the distance of the observed edge-effects is $\sim 10\text{ mm}$ (compare Figure 7-38). Figure 7-39 gives a comparison of the measured and calculated thickness of the film.

In the case of the hard-polymer dispersion AS-H-1b of $T_g = 16\text{ }^\circ\text{C}$, basically the same observations are made as described above for the horizontal drying in a film of A-H-1. Due to the bad wetting properties, the larger evaporation area at the edge of the film is considered here. The thicker edge of the film seems to largely hinder the formation of a horizontal drying front. But as soon as the water content anywhere in the film has decreased below a value that allows the formation of pores, a faster decrease of the water content X as a result of horizontal flow is also measured in the center of the film.

The combination of a higher surface tension and a high viscosity of AS-H-1b makes, that the film has a concave shape and a thicker edge (Figure 7-41).

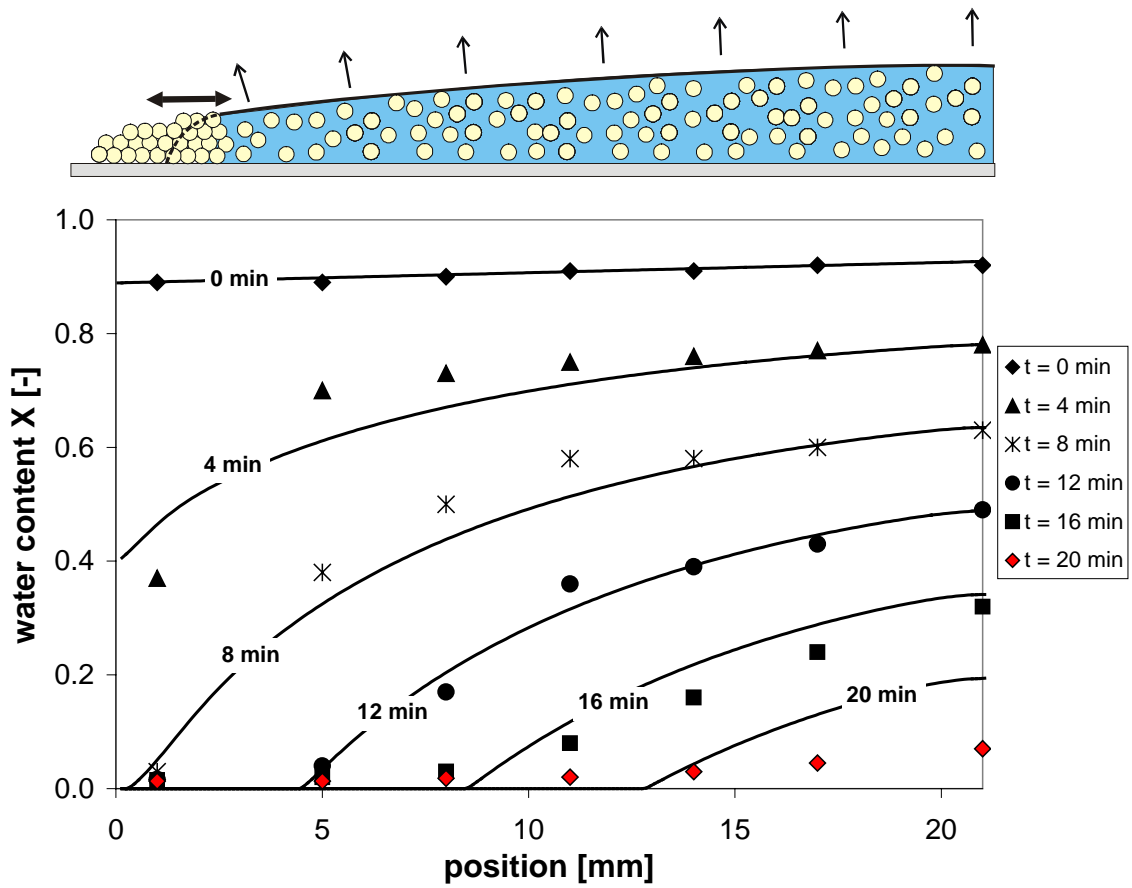


Figure 7-38: Water concentration profiles in horizontal direction of a film of A-H-1. The lines represent model calculations (see Chapter 6.2) ($T = 24\text{ }^{\circ}\text{C}$; $u = 0.05\text{ m/s}$; $\varphi = 50\%$; $h_0 = 105.5\text{ }\mu\text{m}$)

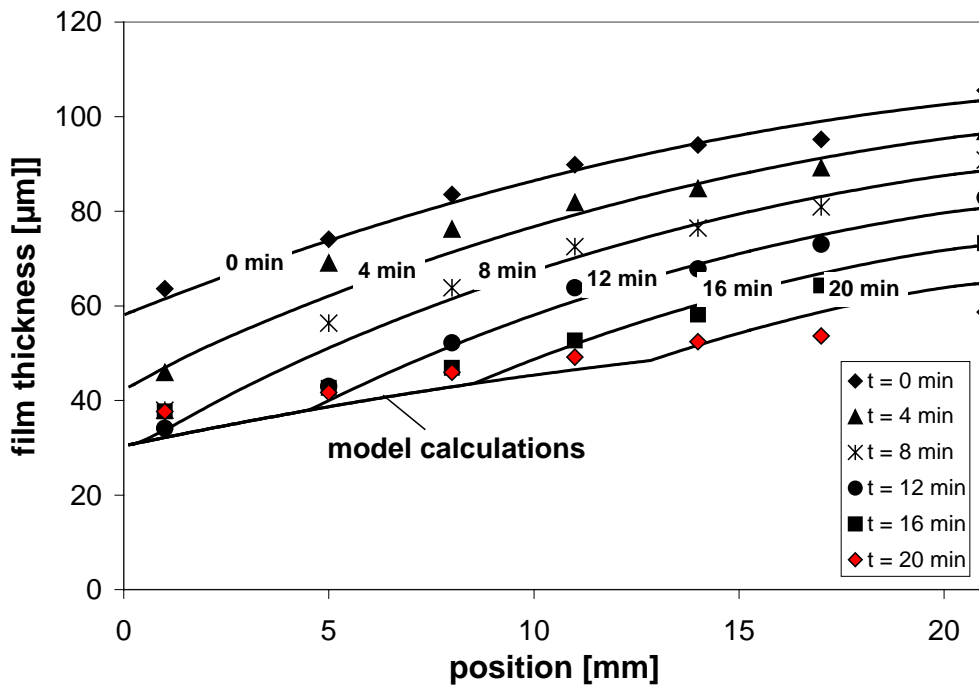


Figure 7-39: The corresponding film thickness of the layer of A-H-1 during drying

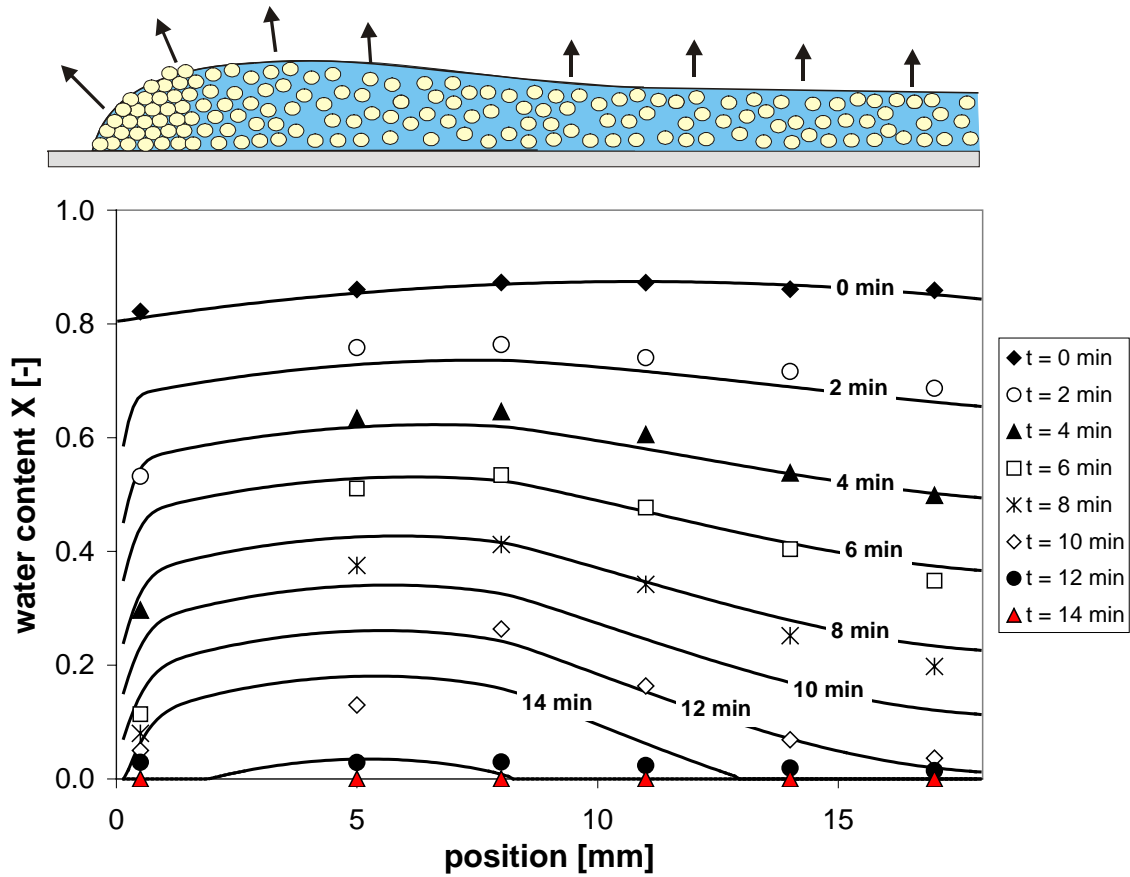


Figure 7-40: Water concentration profiles in horizontal direction of a film of AS-H-1b ($T = 24\text{ }^{\circ}\text{C}$; $u = 0.05\text{ m/s}$; $\varphi = 60\%$; $h_0 = 74.2\text{ }\mu\text{m}$ (center))

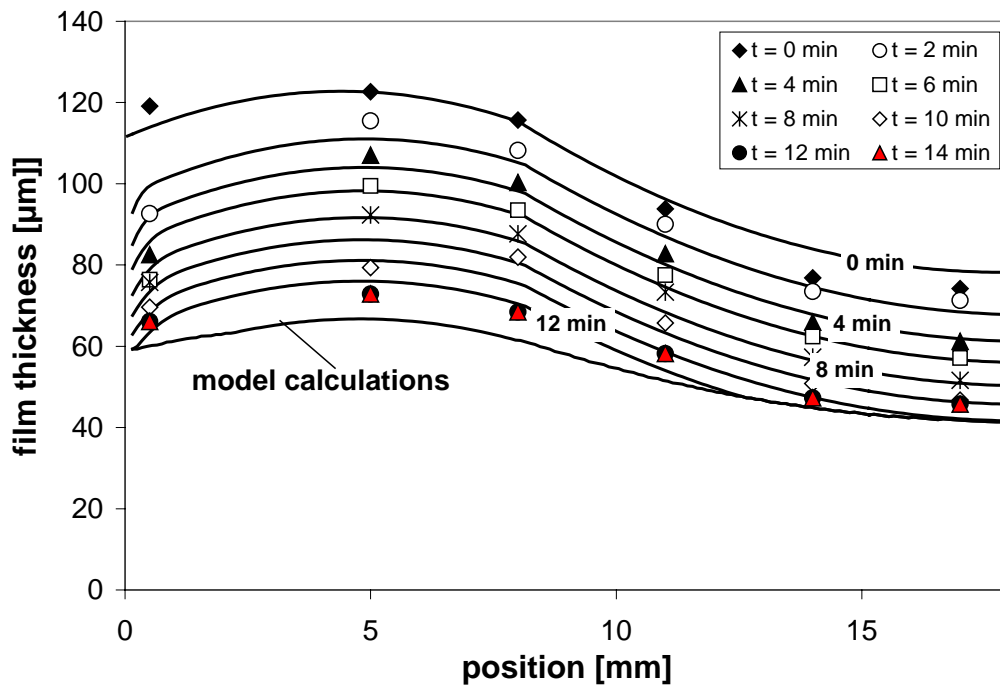


Figure 7-41: The corresponding film thickness of the layer of AS-H-1b during drying

Conclusion on Horizontal Inhomogeneous Drying

The combination of gravimetric drying experiments, digital pictures and IMRS measurements proves horizontal inhomogeneous drying and the existence of a drying front. Water evaporation is from the wet area of the film only. Horizontal inhomogeneous drying can be caused by locally changed drying conditions, i.e. air velocity or film temperature: the difference of up to 10% in the film thickness proves the existence of a drag flow of water and also particles. Due to the low surface tension of the dispersion, Maranghoni-convection is excluded as the main driving force, but a more detailed investigation of the phenomenon is left for the future. IMRS drying data show, that horizontal inhomogeneous drying can be largely suppressed by artificial borders. With the help of IMRS measurements at different horizontal positions of the film, water concentration gradients in the film can be obtained. For the investigated hard-polymer dispersions, capillary forces are not strong enough to allow complete particle deformation and to hinder horizontal inhomogeneous drying. This has been shown by the comparison of experimental data and model calculations. Edge-effects, i.e. the distance over which the lateral drying front moves into the film, strongly depend on the polymer's glass transition temperature T_g and the shape of the film.

7.2.6 Drying of Polymer Solutions

This is to illustrate the differences in drying and film formation of solvent-borne polymer solutions and aqueous latex dispersions.

Opposite to water-based polymer dispersions, solvent-based polymer solutions show steep concentration gradients in vertical direction of the film. Figure 7-42 and Figure 7-43 give the quantitative evaluation of a film drying experiment of the polymer-solvent system Toluene-PVAc, obtained from IMRS and the drying curve.

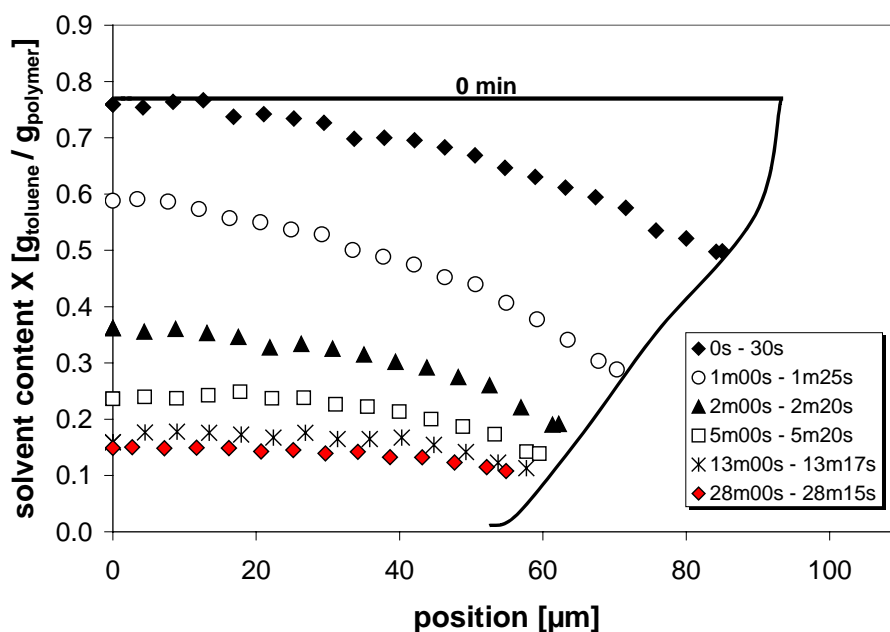


Figure 7-42: Concentration profiles in a film of Toluene-PVAc
($T = 25\text{ }^{\circ}\text{C}$; $u = 0.05\text{ m/s}$; $\phi = 30\%$; $h_0 = 87.1\text{ }\mu\text{m}$)

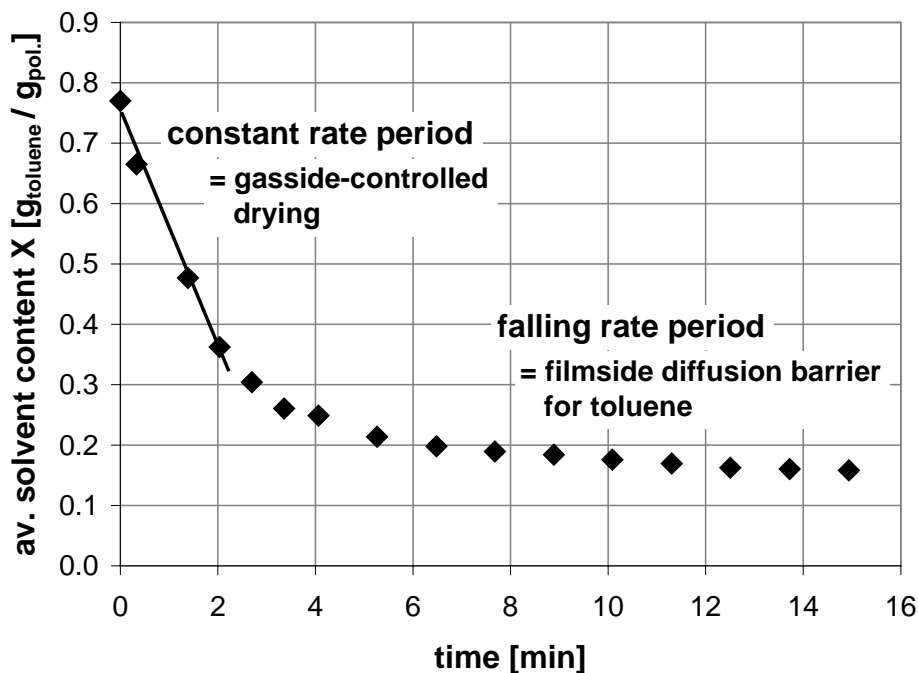


Figure 7-43: Drying curve of Toluene from a film of PVAc

The curve can be divided into a constant-rate period which is represented by a constant drying rate and into a falling-rate period where the drying rate becomes dominated by the diffusion of Toluene in the polymer film. The constant rate period where drying is mainly dependent on the gasside mass transfer coefficient ends at a solvent content of about $X = 0.3 \text{ g Toluene/g PVAc}$. This is where the activity of Toluene becomes less than one as a result of a very thin, dry film layer at the film surface that forms a very high diffusion resistance for the solvent. Due to this phenomenon, called “skin formation”, the organic solvent is still present in the film, even after a time of several days or longer.

In the case of water-based polymer dispersions, film formation is irreversible and below a critical water content X the complete redispersion of the film by water is no longer possible. A detailed discussion of the redispersion and 2-film-behaviour of aqueous polymer dispersions is in Chapter 7.3.2 below. Opposite to polymer dispersions, a redissolution of polymer solutions with the original solvent is always possible. This is demonstrated in Figure 7-44. Due to skin formation, the remaining solvent content in the 1-hour-old film is $X = 0.15 \text{ g Toluene/g PVAc}$. After the application of a large amount of the original polymer solution (= reservoir) onto the film, Toluene diffuses into the film which leads to the formation of steep concentration gradients. Within a few minutes, the film is completely redissolved and the solvent content in the film and in the reservoir on top of the film has become equal. In Figure 7-44, redissolution can be well described by model calculations, indicated by the lines (for the model compare Chapter 6.2.5). For a detailed investigation of the drying behaviour of solvent-based polymer solutions see *Schabel* (2004).

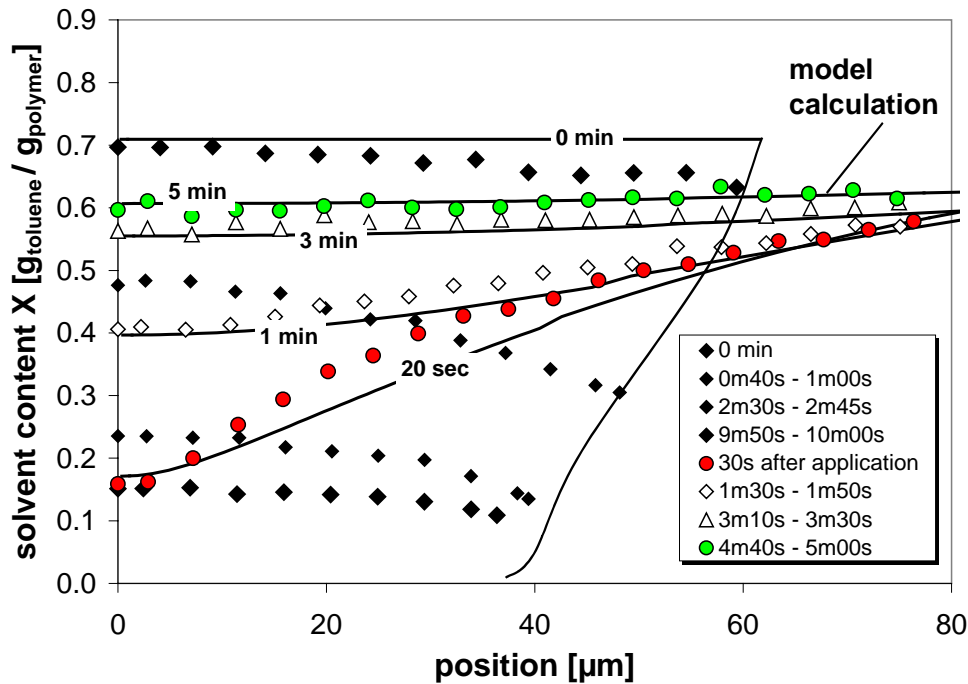


Figure 7-44: Complete redissolution of a 1-hour-old film of Toluene-PVAc

7.3 Irreversible Particle Contact and Particle Deformation

Opposite to within polymer solutions, an irreversible contact of the latex particles occurs in aqueous polymer dispersions during the drying process. As a consequence for the application properties of aqueous coatings, a first film layer can no longer be redispersed by a fresh film layer that is applied on top of it. The moment of irreversible particle contact is investigated below by so-called redispersion and 2-film experiments using the IMRS technique. In redispersion experiments, an infinite reservoir of the dispersion is applied on top of a film layer after different drying times. In 2-film experiments, one can learn about the water concentration in two film layers as a function of (I) the drying time of the first layer and (II) the film thickness of both layers. For the experimental setup see below Figure 7-45.

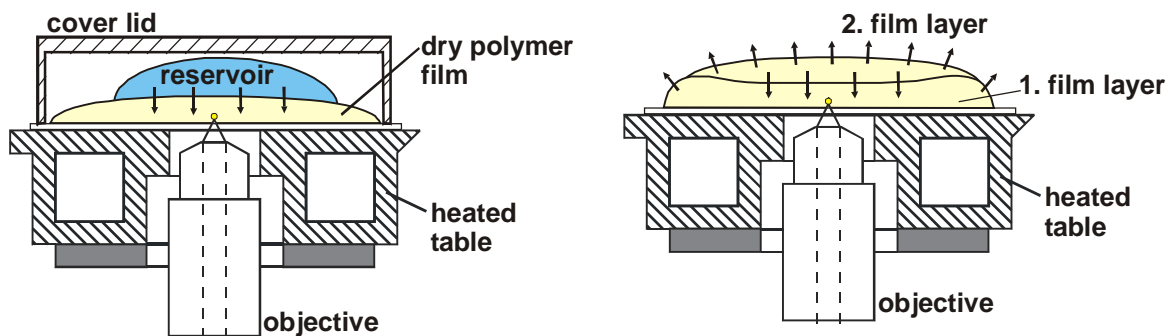


Figure 7-45: The experimental setup for a redispersion experiment (left) and a 2-film-experiment (right) using IMRS

7.3.1 Redispersion Experiments using IMRS

During drying of aqueous polymer dispersions, water evaporation leads to particle contact and beginning particle deformation. Depending on the drying conditions and the kind of dispersion stabilization, a more or less ordered structure forms within the dispersion. A strong particle contact takes place by particle-particle interactions such as van-der-Waals attraction and hydrogen-bonding and completely irreversible contact is the result of polymer chain interdiffusion. Depending on the polymer's glass transition temperature, either a porous structure of largely undeformed particles or a structure of completely deformed particles, - separated by a network of surface-active material -, forms. Depending on the strength of the particle interactions, there is one point during drying, where the water that invades between the latex particles is no longer able to redisperse the film.

The irreversible particle contact is investigated by so-called redispersion experiments, using Inverse-Micro-Raman-Spectroscopy (IMRS). A first film layer is prepared and is dried to a desired water content X , before a large reservoir of fresh dispersion is applied on top of this film layer (compare Figure 7-45 left for the experimental setup). Was the dispersion applied before the moment of irreversible particle contact, water fills the interstices between the particles and a complete redispersion of the film layer is possible. It is reached when the water content of the film layer becomes equal to that of the reservoir (Figure 7-47).

Was the dispersion applied after the moment of irreversible particle contact, water can fill the remaining interstices of the film and can diffuse along the particle-particle boundaries, but a complete redispersion is no longer possible and the water content of the film remains considerably lower than in the original dispersion (= step-profile, Figure 7-48). The increased water content X in the film causes swelling of the hydrophilic material between the particles, leading to an increase in film thickness. An increased water content towards the glass-film interface is sometimes observed, meaning that film formation and particle coalescence is faster near the film surface and is less complete near the substrate.

A comparison of the experimental data with model calculations shows, that complete redispersion before the irreversible particle contact is well described by the mathematical model (compare Chapter 6.2.4 and Figure 7-47). After the moment of irreversible particle contact, the data are not as well described (Figure 7-48). This is caused by the fact, that water diffusion preferably takes place along the network of hydrophilic, surface-active material at the particle interfaces which is limited in its volume. Therefore, the water content at any position of the film cannot be higher than a certain limiting value, which is not considered by the model.

The water content X during a redispersion experiment before and after irreversible particle contact is sketched in Figure 7-46.

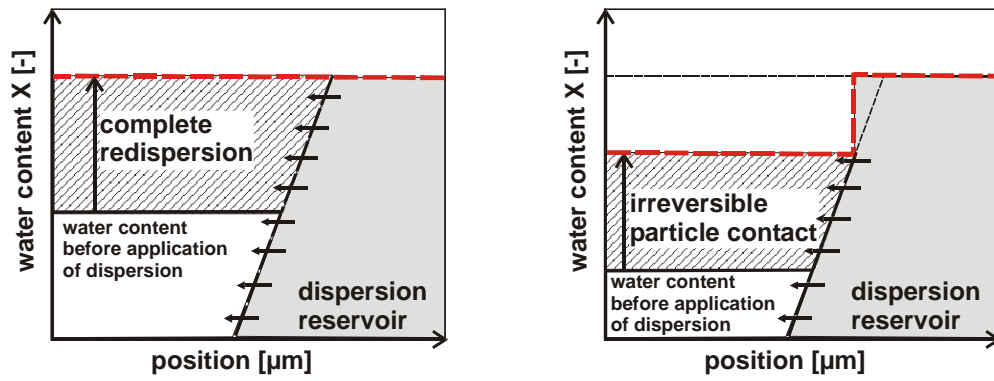


Figure 7-46: A sketch of the water content X in the film during a redispersion experiment before and after irreversible particle contact

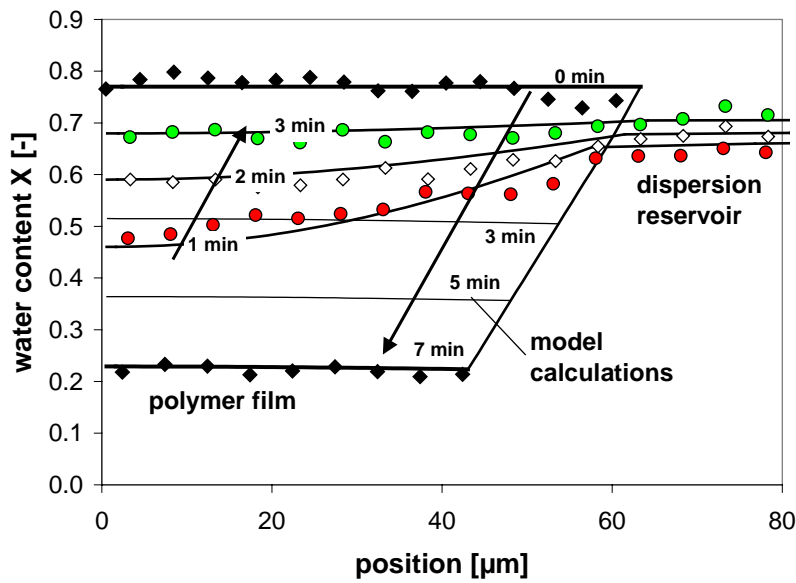


Figure 7-47: Redispersion experiment of AS-H-1b before the moment of irreversible particle contact

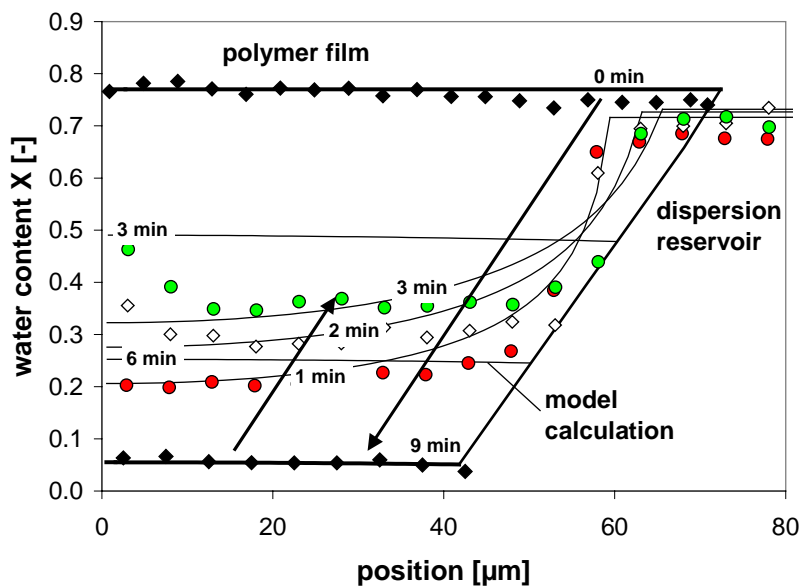


Figure 7-48: Redispersion experiment of AS-H-1b after the moment of irreversible particle contact

7.3.2 2-Film-Experiments using IMRS

In many applications it is necessary to apply more than one film layer or to make corrections on the surface of a fresh coating. To finally end up with a smooth surface showing no defects, it is important to know the interplay between the two film layers. Important is the thickness of both films and the drying time before the application of the second layer. A sketch of the experimental setup for 2-film experiments is given in Figure 7-45 (right). As in redispersion experiments, one differentiates between the application (I) before and (II) after irreversible particle contact. For a sketch of the water content X during a 2-film-experiment see Figure 7-49.

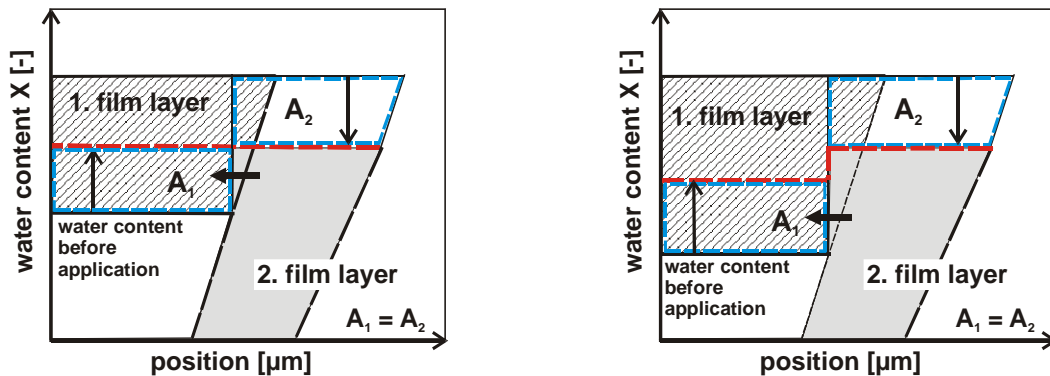


Figure 7-49: sketch of the water content in the film layers during the experiment; before (left) and after irreversible particle contact (right)

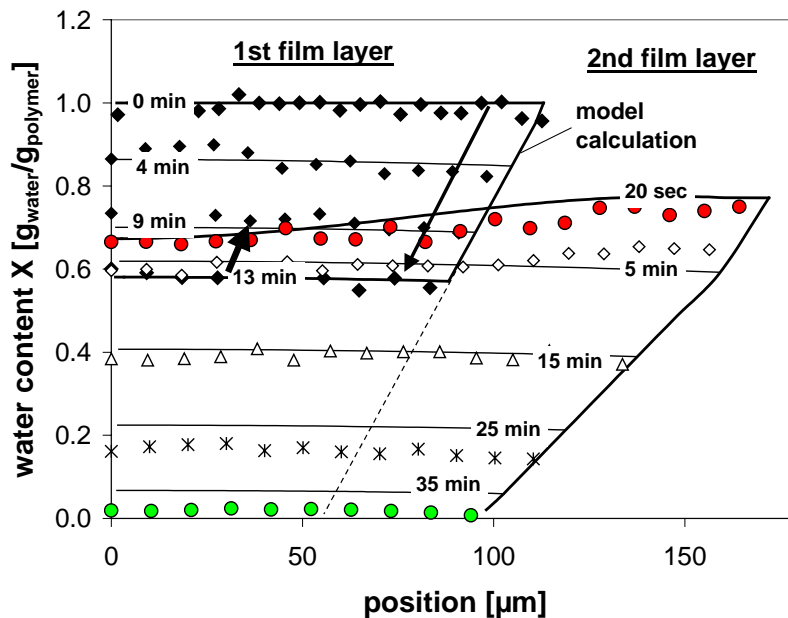


Figure 7-50: A 2-film-experiment of AS-H-1b before irreversible particle contact. Bottom layer: thick film, no irreversible particle contact; top layer: thin film, water diffuses into the bottom layer (standard drying conditions)

In the case of application before the irreversible particle contact, the water content in both film layers will equalize within a very short time, meaning that the water content of the bottom layer increases thanks to water diffusion from the top to the bottom layer (Figure 7-50). Depending on the film thickness of both layers, it can be, that, due to

the diffusion process, the water content of the top layer decreases to almost the critical value X_{crit} of irreversible particle contact. Then, further corrections on the top layer are not possible right from the moment of application and the coating will have no open time.

In the case of an application of the second layer after the moment of irreversible particle contact, water from the top layer quickly diffuses into the bottom layer, but cannot redisperse it. Except for the case, where the bottom layer is much thicker than the top layer (so that the volume that can invade is larger than what the top layer can provide), the solvent content in both film layers will not equalize but will display a step profile. Then, the top layer will dry independent from the bottom layer, until both layers have reached a uniform water content (Figure 7-51). From this moment on, both film layers behave like one single thick layer.

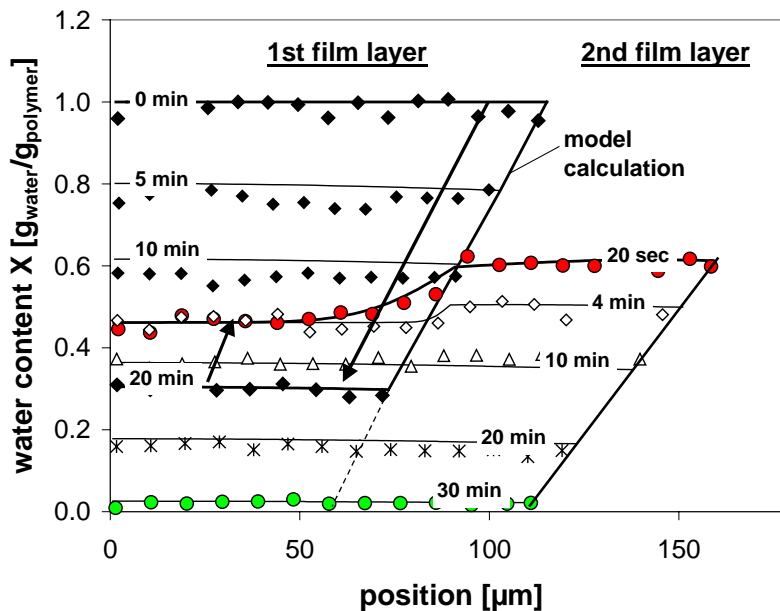


Figure 7-51: A 2-film-experiment of AS-H-1b after irreversible particle contact. The bottom layer cannot be redispersed by the 2nd film layer; the top layer dries independently until both films have the same water content X

7.3.3 Conclusions on Particle Contact and Deformation

Irreversible particle contact in concentrated polymer dispersions occurs during the drying process. Then, complete redispersion is no longer possible. For the application of a second film layer on top of a first coating, irreversible particle contact and water diffusion can have large consequences: Depending on (I) the moment of application of the second coating layer and (II) the thickness of both film layers, the water content will either equalize or will exhibit a step-profile. In the case of a thick bottom layer, it could be, that the water content of the top layer decreases in so far, that no corrections on the freshly applied layer can be done right after the application and complete film leveling is impossible. The above discussed facts would also apply for any porous substrate on which the dispersion is coated.

7.4 Particle Coalescence and Film Ageing

Essential for many applications are the protection properties of a coating, expressed by a low permeability for water and other harmful substances and a high mechanical strength. Both properties are only completely developed, when (I) the network of surface-active material, initially located at the particle interfaces has been fully destroyed by polymer interdiffusion and when (II) all pores in between the particles have vanished. The surfactant distribution in vertical direction of the film after different drying times is investigated in Chapter 7.4.1 and the water permeation in dry films of different dispersions is discussed in Chapter 7.4.2. Here, the permeability of the film is attributed to certain dispersion characteristics, e.g. the high/low- T_g polymer, the age of the film (1 day/1 week) and the treatment of the film (e.g. drying at elevated temperatures).

7.4.1 Surfactant Distribution in Vertical Direction of the Dry Film

Generally, a large amount of surface-active species or of functional groups, incorporated into the particle surface, is needed to prevent aqueous polymer dispersions from agglomeration. During film formation, the surfactant material, being located at the interfaces of the deformed latex particles, forms a network in between the particles. Depending on the thickness of the surfactant layer, its destruction by polymer chain interdiffusion can be the rate-limiting step of film formation. Important for the mechanical stability of the film is the location and distribution of the surfactant in the final film. Raman spectra, taken at different positions in vertical direction of the film, can give important information about the distribution of the surfactant in the film.

Among the investigated dispersions, A-H-1 is the one with the highest surfactant concentration. The surfactants used in this formulation belong to the group of sulfonated fatty acids. Figure 7-52 gives the distribution of the surfactant in a film of A-H-1 (I) after 1 day, (II) after 1 week and (III) after drying at elevated temperatures (curing at $T = 150\text{ }^\circ\text{C}$). The resolution of IMRS of $2\text{-}3\ \mu\text{m}$ cannot resolve the surfactant network structure itself, but can give tendencies of the surfactant distribution across the film. After one day, the film formation of the hard polymer dispersion A-H-1 is still incomplete (compare also Chapter 7.4.2). The surfactant forms a network and fills the interstices between the partially deformed particles. Its concentration is possibly higher in the remaining pores, which would explain the inhomogeneous surfactant distribution in the film. After one week, coalescence has further proceeded. The polymer chain interdiffusion and further deformation of the particles reduces the pores in the film which results in a more homogeneous surfactant distribution. Curing at elevated temperatures of $T = 150\text{ }^\circ\text{C}$ strongly increases particle coalescence and the diffusion rate of the surfactant in the film. After one hour at elevated temperatures, a gradient of the surfactant towards the film surface is observed with the highest surfactant concentration at the polymer-glass interface. Indicators for the formation of

separate areas of surfactant within the coalesced film (= phase separation) are not observed.

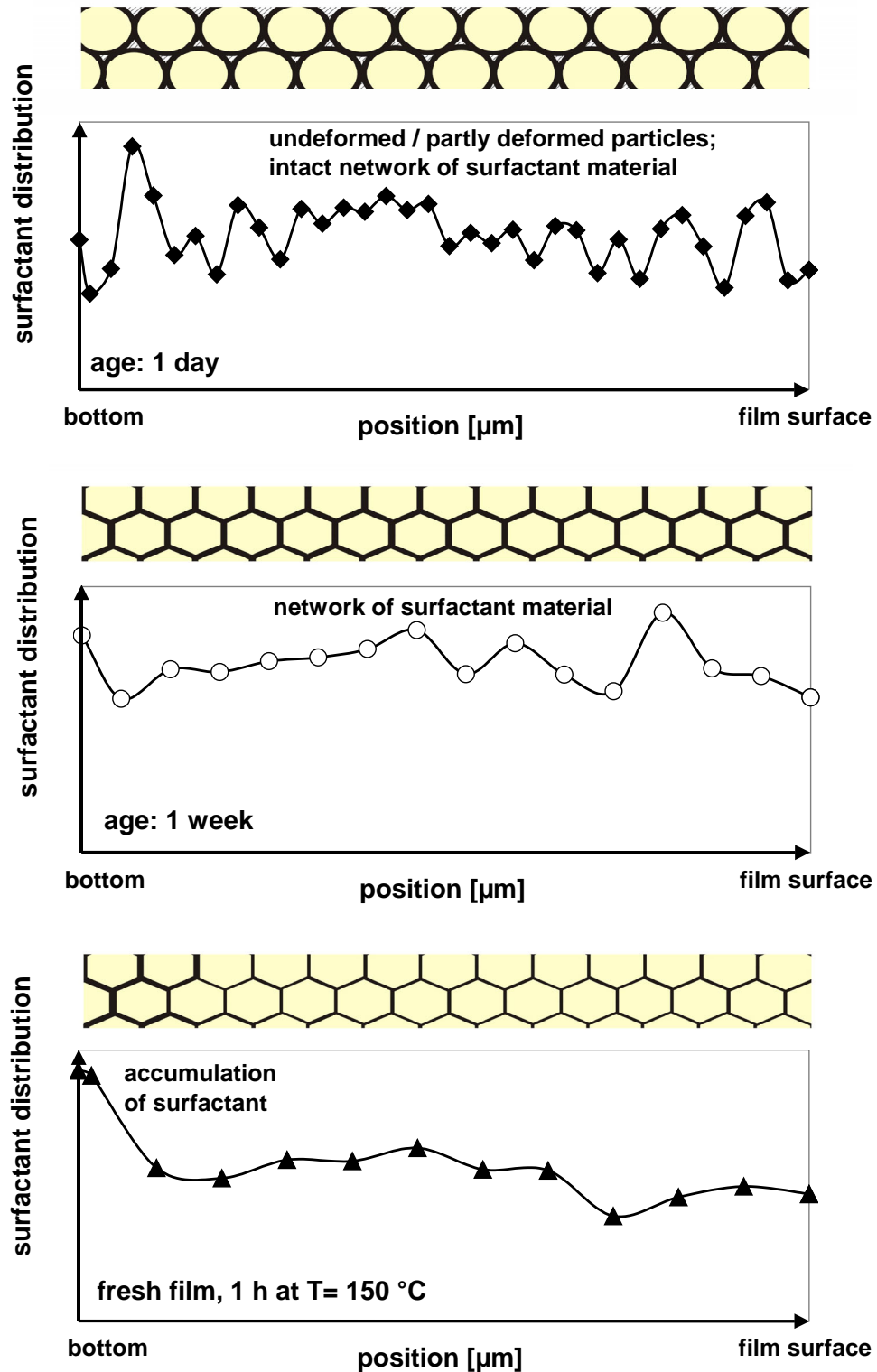


Figure 7-52: Surfactant distribution in a film of A-H-1 of different age: (I) top: 1 day; (II) middle: 1 week; (III) bottom: 1 h of curing at $T = 150\text{ }^{\circ}\text{C}$

7.4.2 Water Permeation in the Dry Film

The main function of a coating, apart from decorative aspects, is to protect an underlying substrate against humidity (corrosion) and other harmful substances. It is therefore important, that the final coating, - apart from mechanical stability -, shows low permeability for water.

Depending on the progress of film formation, the protection characteristics of the coating are developed. The degree of full polymer chain interdiffusion is a function of time, of particle characteristics, of the amount and kind of surfactant and of the external treatment like e.g. curing at elevated temperatures. In principle, one has to differentiate between three types of dispersion coatings:

- (I) coatings of soft polymer particles with thin surfactant membranes, where film formation is completed in a very short time. These coatings give an effective protection against water but are often not hard enough to also protect against mechanical destruction.
- (II) coatings of hard polymer particles and/or thick membranes, where complete film formation at ambient temperatures is hindered and can only be achieved by curing at elevated temperatures. Such coatings can only be used for applications where curing is possible. Then, the coating gives an effective protection against permeation and mechanical influences.
- (III) coatings of harder particles with thin surfactant membranes. Due to partial particle deformation, such coatings will have small pores in the fresh film where water can diffuse. Complete film formation of such coatings at ambient conditions is reached after a certain time. If one has the time to allow complete film formation, such formulations give an optimum of low permeation and high mechanical stability for applications at ambient conditions.

Figure 7-53 shows water diffusion into type (I) coatings of age *1 day* (left) and age *1 week* (right). In the 1-day-old film, film formation is almost completed and only a small amount of water can diffuse into the film along the last remaining particle interfaces. After one week, the surfactant network has been completely destroyed so that water has to diffuse through the polymer film. After one week, a type (I) coating, although very soft, forms an effective protection against water.

After 1 day, a type (II) coating (e.g. A-H-1) forms a partly irreversible structure of mostly non-deformed particles. As a consequence, water fills the pores of the coating, which leads to a maximum water content in the film of about *0.65 g water/g polymer* (Figure 7-54 left). Swelling of the hydrophilic surface-active material in between the particles leads to an increased film thickness. After *1 week*, progressed particle deformation and polymer diffusion have decreased the interstices between the particles, so that the maximum water uptake in the dry film is only *~0.25 g water/g polymer*. Here, an accumulation of water at the glass substrate-polymer interface is observed after *10 minutes*. Obviously, the contact between water and glass is - at least locally -

reversible. Curing at elevated temperatures of $T = 150\text{ }^{\circ}\text{C}$ allows complete particle deformation and increases the speed of polymer interdiffusion. Then, the water uptake is comparable to that of the 1-day-old film of the type (I) dispersion, where still a small amount of water can diffuse along the last remaining particle-particle interfaces.

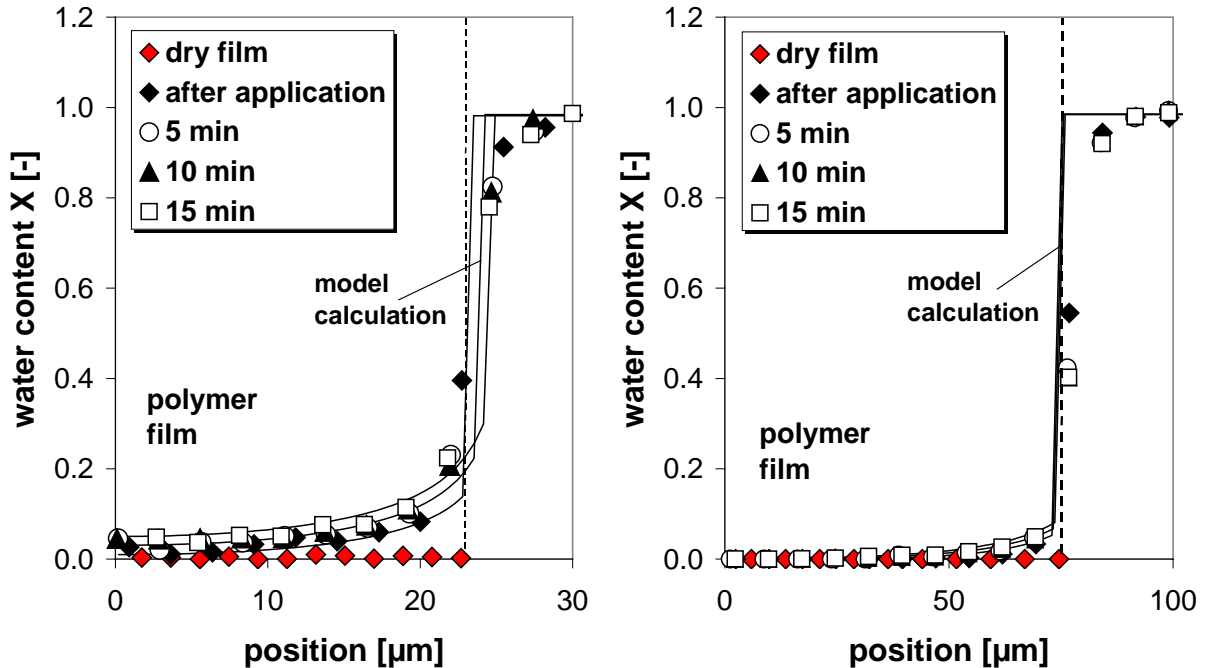


Figure 7-53: An example of complete film formation of A-S-1 (type (I) coating): left: 1-day-old film; right: 1-week-old film

Figure 7-54 (right) shows redispersion experiments of a type (III) film (e.g. AS-H-1b). In the 1-day-old film, water can diffuse into the porous film structure of partly deformed particles. Additional swelling of the surface-active material located at the particle-particle interfaces leads to an increased film thickness. The maximum water content in the film after one day is $\sim 0.3\text{ g water/g polymer}$. In this case, particle coalescence starts at the bottom of the film as shown in the 1-week-old film. Complete polymer interdiffusion has taken place and hinders water diffusion, but the structure at the film surface doesn't seem to be changed compared to the film of age 1 day. In the top layer, the maximum water uptake is still about $0.3\text{ g water/g polymer}$ but the diffusion network all of a sudden is blocked in the middle of the film.

Also for the type (III) coating, curing at elevated temperatures of $T = 150\text{ }^{\circ}\text{C}$ facilitates particle deformation and accelerates polymer interdiffusion. Then, only a small amount of water can diffuse into the coating, comparable to that of the hard polymer coating (type (II)) at elevated temperatures and the soft polymer coating (type (I)) at ambient conditions.

Wherever in Figure 7-53 and Figure 7-54 particle coalescence has formed a non-porous film, the experimental data of water diffusion into the film could be well described by model calculations, in which the diffusion coefficient $\delta_{w,p}$ was fitted to the data (compare Chapter 6.2.3 and Chapter 6.2.4).

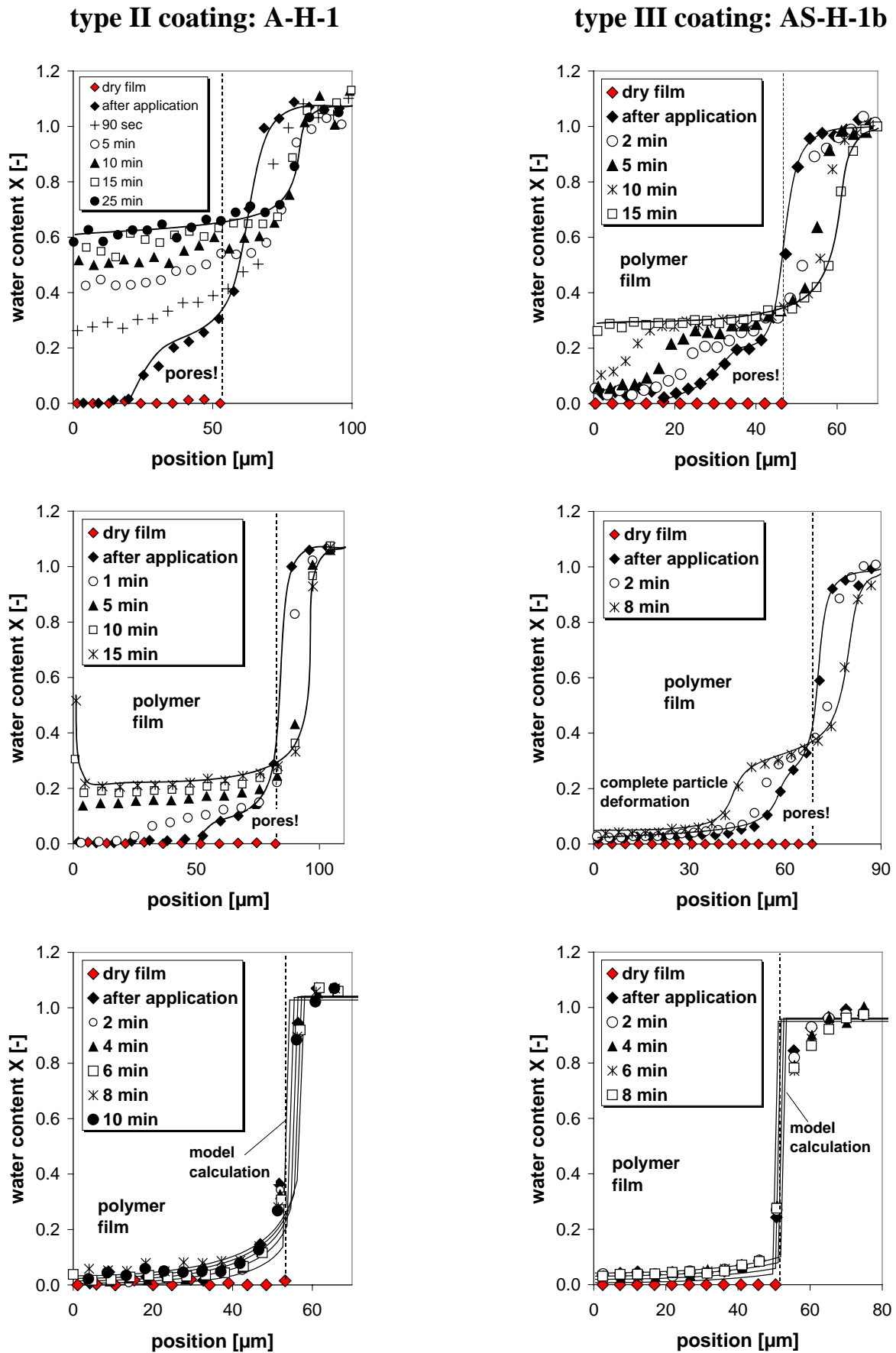


Figure 7-54: Example of a type II and a type III coating: top: 1-day old film; middle: 1-week-old film; bottom: after 1 hour at T = 150 °C

7.4.3 Conclusions on Particle Coalescence and Film Ageing

The surfactant distribution in the high- T_g latex A-H-1 becomes more homogeneous with time and accumulates at the film-substrate interface. Good coating properties (= low permeability of water in the film) strongly depend on the polymer's T_g and are often only achieved after several days or after curing at elevated temperatures. This has to be considered with regard to the desired application (e.g. where long curing is a problem/not a problem).

7.5 The Influence of Pigments on Drying and Film Formation

For colour and opacity, commercial paint formulations contain 20-30 mass % of pigments. It is expected, that the binder-pigment interactions are of great importance for the drying behaviour and film properties of the respective formulation. Pigments strongly limit the use of IMRS for the investigation of such formulations. Nevertheless, within these limits, IMRS experiments and also gravimetric drying experiments were performed to learn about the importance of pigments for the drying behaviour and the coating properties.

For the white colour in paints, typically titanium-dioxide (TiO_2) particles of an average size of 200 nm are used. By that, they are about twice the size of the round-shaped latex particles. At the presence of pigments in the formulation, a complete investigation of the water distribution in vertical direction of thin films by Inverse-Micro-Raman-Spectroscopy is impossible. The laser cannot penetrate the opaque film to more than 10 to 15 μm .

Within these limits, the drying behaviour of a full paint formulation, containing pigments, thickeners, plasticizers and AS-H-1b as the polymer component is investigated. Here, the water content a few microns into the film and close to the bottom is measured with time at standard drying conditions (see Figure 7-55). The initial water content of the formulation is 1.6 g water/g polymer, but with a pigment content of 21% of the total mass, the solid content of the paint is close to 50 mass %. From the experimental data it is impossible to draw conclusions about possible concentration gradients which might form during drying, but the experimental data can be well described by model calculations, showing no steep gradients. According to the data, a film-side diffusion resistance for water starts to build below a water content of $X = 0.6$ g water/g polymer. The diffusion resistance could be the result of the pigments which (I) hinder –or at least limitate- the formation of a diffusion network of surface-active material within the film and (II) reduce the evaporation area at the film surface, meaning, that water evaporation will be only possible from the pores in between the particles.

Figure 7-56 shows a comparison of the drying curves, obtained from (I) the measured water content at the bottom of the film by IMRS and (II) from a gravimetric drying experiment. Opposite to all investigated dispersions without pigments, the formulation

with pigments shows a different drying behaviour: A comparison of the drying curves (Figure 7-56) would suggest, that the presence of pigments hinders the formation of a lateral drying front. Evaporation from a constant film area would explain the long constant-rate period which was obtained from gravimetric measurements (= integral data); it would also explain the fast decrease of the locally measured water content X in the center of the film which would be the result of strong horizontal capillary flow in the pores formed by the pigments.

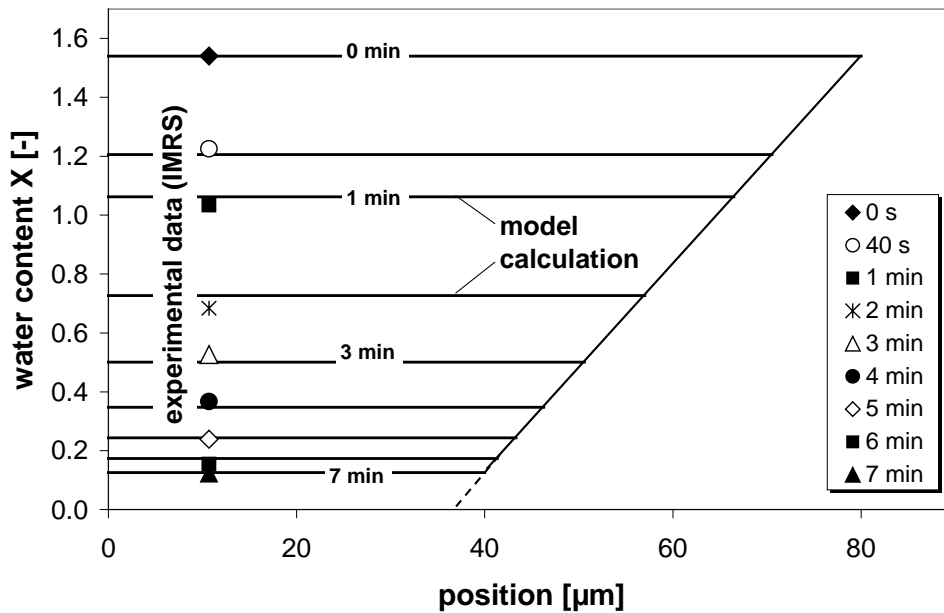


Figure 7-55: The water content in vertical direction of a film of AS-H-1b with plasticizers and pigments: experimental data and model calculation

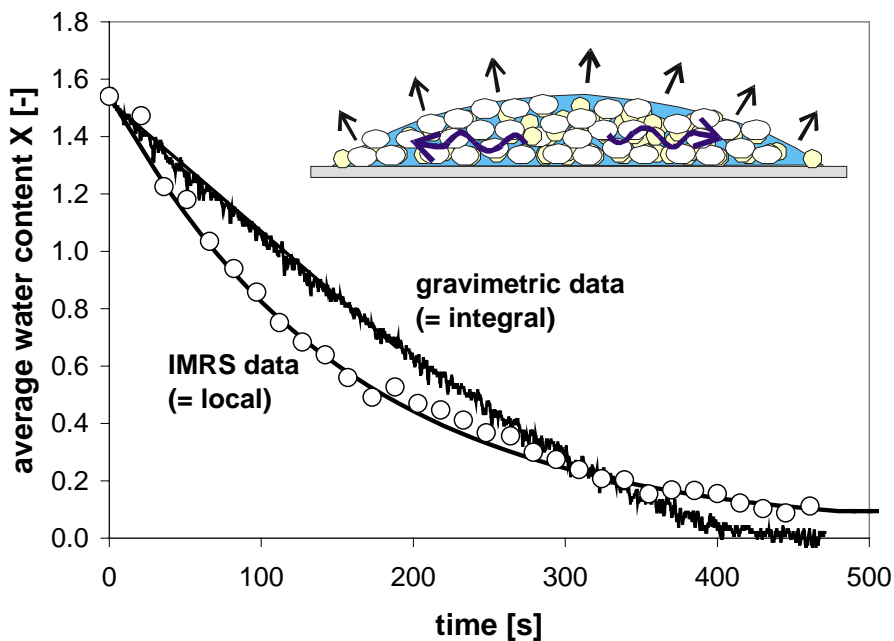


Figure 7-56: The drying curves of the complete paint formulation: comparison of IMRS and gravimetric data

A redispersion experiment of the 1-day-old, pigmented film of AS-H-1b (Figure 7-57) reveals, that within 3 minutes after the application of a large reservoir of water on top of the coating layer, the water content at the measurement position close to the bottom of the film increases to $X = 0.3 \text{ g water/g polymer}$ (Figure 7-57). This is about the same water content which was also observed for a 1-day-old film of pure AS-H-1b without pigments and plasticizers (Figure 7-54). The large water uptake shows that the protection properties of the pigmented coating formulation against water are as poor as they are for pure AS-H-1b. Although additives are included into the formulation to enforce particle deformation and polymer diffusion, one day is obviously not enough to assure complete particle coalescence. From the observations, the influence of the pigments on coalescence and on the formation of a diffusion network in the film is not clear and should be subject of future investigations.

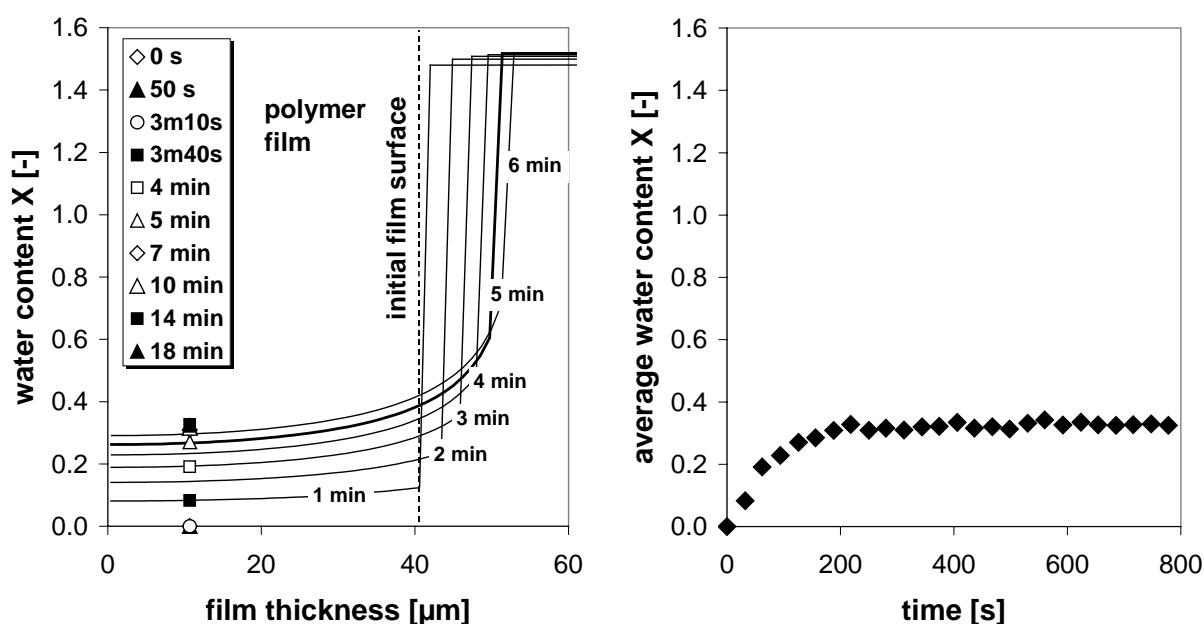


Figure 7-57: Water permeation in a 1-day-old film of a complete paint formulation, containing AS-H-1b and TiO_2 pigments: comparison between model calculations and experimental data

7.5.1 Conclusions on the Influence of Pigments

Drying of the pigmented formulation shows significant differences compared to that of the dispersions without pigments. The presence of the pigments largely hinders horizontal inhomogeneous drying as could be proven by the comparison of the drying curves obtained from local (IMRS) and integral (gravimetric) drying experiments. A 1-day-old film of the investigated formulation with pigments does exhibit the same high permeability for water as does the pure latex dispersion without pigments. From the experimental data, an explanation for this could not be found; the role of pigments during film formation needs further investigation.

7.6 Influence of Additives on Drying and Film Formation

Additives like surfactants, plasticizers, anti-foaming agents and rheology modifiers are given to dispersion formulations to improve the application and final film properties. Chapter 7.6.1 deals with the influence of the plasticizer Texanol™ on the drying behaviour and on the final film properties. In this work, the results of film drying experiments, redispersion experiments and 2-film-experiments at varying amounts of Texanol™ are discussed. In addition, the permeability of the final 1-day-old coating is tested.

Chapter 7.6.2 shows the influence of additional amounts of surfactant (SDS) on the permeability and mechanical strength of the dry film.

7.6.1 Plasticizer (Texanol™)

As indicated by the name, the plasticizer -being a hydrophobic, low-volatile, organic solvent- diffuses into the latex particles, lowers the polymer's glass transition temperature T_g and thus facilitates and accelerates particle deformation. Figure 7-58 shows the drying curves of the three-component-system water-polymer-Texanol™, containing different amounts of Texanol™. The data were measured at the same position in the center of a sample film and the experiments with films of uniform film thickness of $h_0 = 59 \pm 2 \mu\text{m}$ were performed at standard drying conditions. The content of Texanol™ ranges between zero and 18% per polymer. The more Texanol™ is given to the formulation, the faster is the decrease of the water content and the earlier a diffusion resistance for water forms in the film (Figure 7-58 (left)). During drying, the content of Texanol™ in the film is constant (Figure 7-58 (right)).

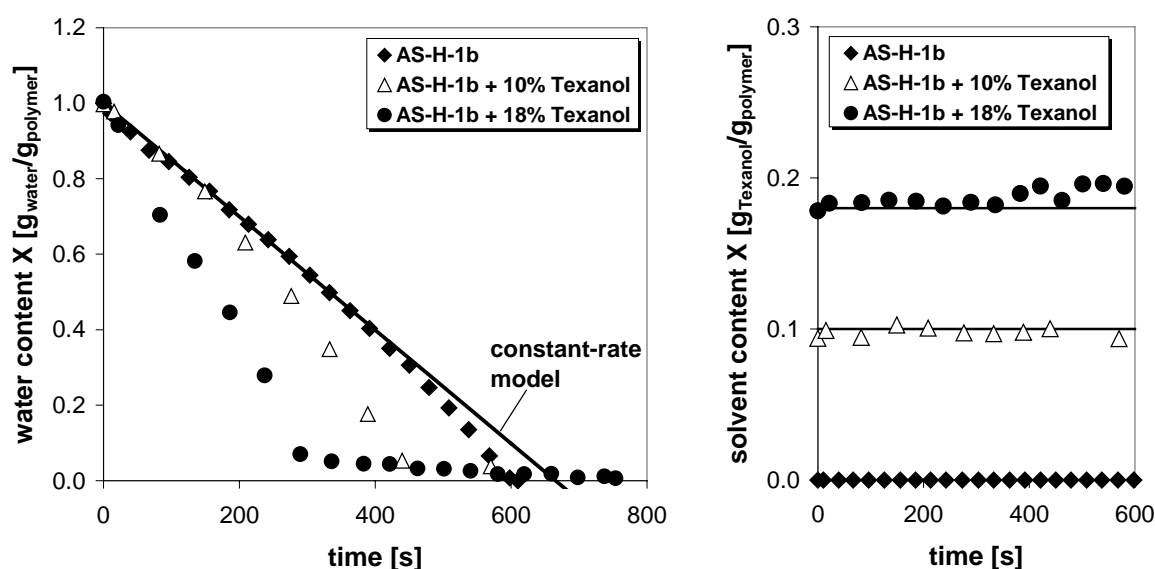


Figure 7-58: The drying curve of water (left) and Texanol™ (right) in a film of AS-H-1b containing different amounts of Texanol™
($T = 25 \text{ }^\circ\text{C}$; $\phi = 50\%$; $u = 0.05 \text{ m/s}$; $h_0 = 60.9 \pm 1 \mu\text{m}$).

Water evaporation from the film cannot be faster than in the gasside-controlled case (compare pure AS-H-1b). Obviously, higher amounts of Texanol™ in the formulation

lead to an increased horizontal flow of water away from the local measurement position in the center of the film. In this case, the lateral flow is possibly driven by a combination of (I) capillary forces and (II) a layer of deformed particles at the film surface. Such a layer exerts a pressure onto the underlying particles by which the water is pressed in horizontal direction to the edge of the film. This mechanism was propagated by *Sheetz* (see Appendix V). Once the pores at the particle surface are completely closed, the surface layer forms a diffusion barrier for water in the film indicated by the slow decrease of the water content X . Further proof of the existence of such a layer of deformed latex particles leading to a filmside diffusion resistance is given later in this chapter.

In Figure 7-59, one can differentiate between the constant water flux, caused by water evaporation and an additional flux caused by the horizontal transport of water.

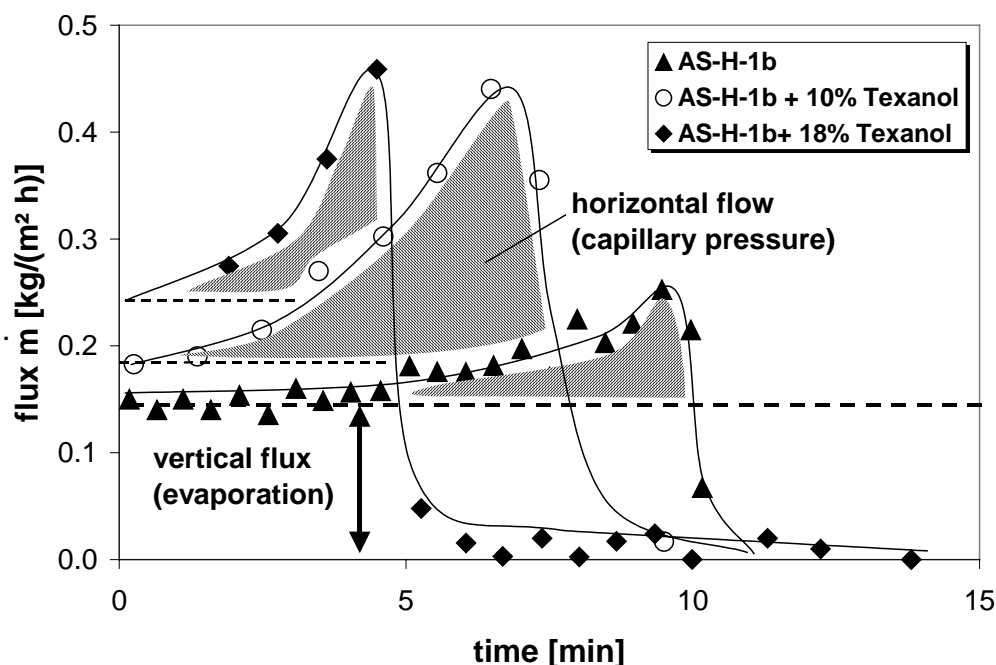


Figure 7-59: The water flux at the center position for AS-H-1b containing different amounts of TexanolTM

As discussed before in Chapter 7.4.2, the fast water diffusion in latex films is explained by the existence of a network of hydrophilic surface-active material in between the latex particles. Its presence strongly depends on the dispersion characteristics and the age of the coating. The presence of TexanolTM supports polymer interdiffusion and coalescence which destroys the hydrophilic diffusion network and leads to a strong and early decrease of the diffusion coefficient for water in the film.

Figure 7-60 and Figure 7-61 display permeation experiments in 1-day-old, dry films of AS-H-1b with and without 15 mass % TexanolTM per polymer. In a first experiment, a large reservoir of AS-H-1b containing 15 mass % TexanolTM is given on top of a dry film containing no TexanolTM; in a second experiment, the dry film layer contains TexanolTM, whereas the reservoir doesn't. Two aspects are investigated by these

experiments: (I) the diffusion of water into the dry film layer and the maximum final amount of water in the film and (II) the distribution of TexanolTM between the film layer and the reservoir during the experiment. In Figure 7-60, the dry film of AS-H-1b shows the typical redispersion characteristics of a hard-polymer dispersion (compare Chapter 7.4.2). Within a very short time, water fills the pores of the dry film and swelling is the result of the interaction of water with the hydrophilic surface-active material in between the particles and at the particle surface. The maximum water uptake in the film is $X = 0.2 \text{ g water/g polymer}$. Due to the weak contact of the latex film with the glass substrate, water accumulates at the interface and the film detaches from the substrate. Figure 7-60 (right) shows that the amount of TexanolTM in the reservoir keeps constant throughout the experiment and that no plasticizer has diffused into the polymer film. This proves that TexanolTM is dissolved in the latex particles and cannot be dragged away from the reservoir by water diffusion.

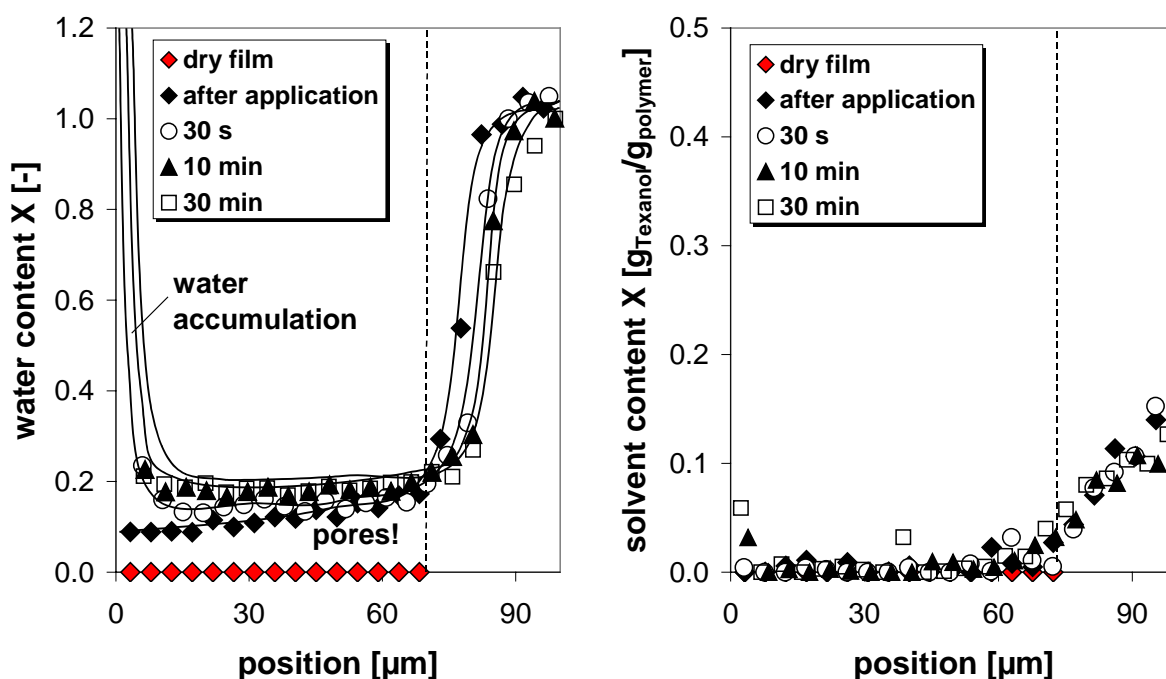


Figure 7-60: Water permeation in a 1-day-old film of AS-H-1b. The film does not contain TexanolTM, but the reservoir.
Left: the water content X ; right: the content of TexanolTM

Considerably less water can diffuse into a 1-day-old film of AS-H-1b containing TexanolTM (Figure 7-61). This is the result of the facilitated particle deformation and fast polymer interdiffusion which partly destroys the interparticular boundaries (= the diffusion path) and forms a non-porous film surface. The maximum water uptake after 24 minutes is $X = 0.08 \text{ g water/g polymer}$. The good adhesion at the glass substrate hinders an accumulation of water at the interface. After one day, the amount of TexanolTM in the dry film is still the same as at the moment of application and is constant in vertical direction of the film. As shown above, the low-volatile organic solvent is dissolved in the polymer particles and cannot diffuse into the reservoir of the pure AS-H-1b dispersion on top of the film (Figure 7-61 right).

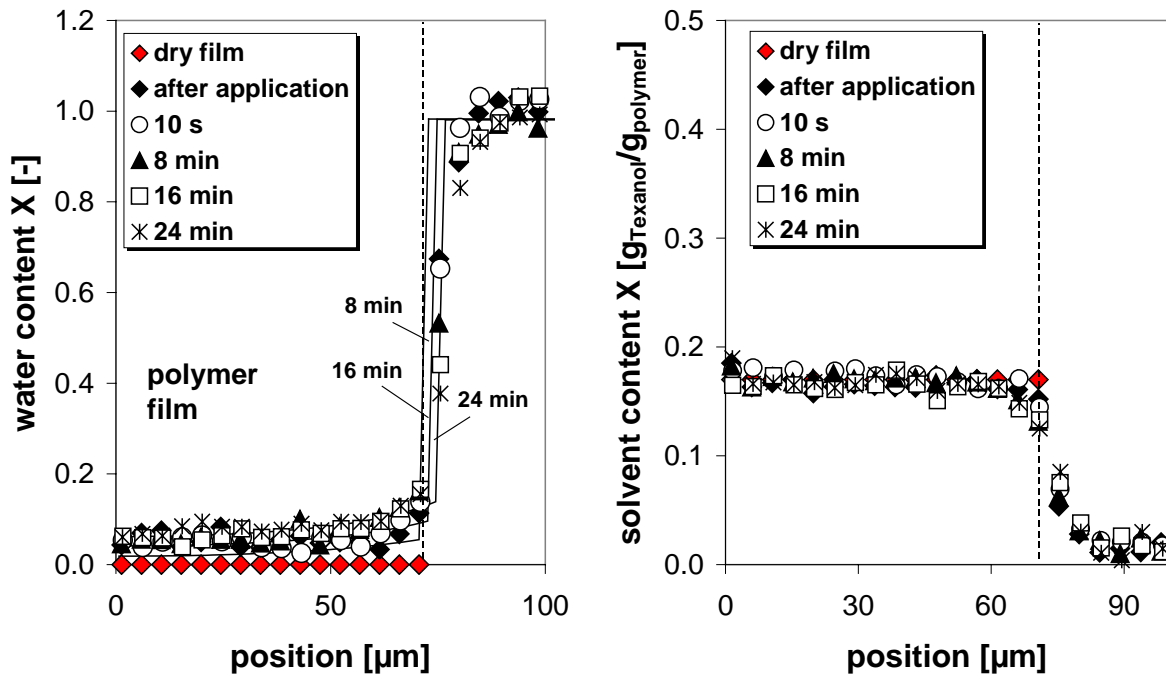


Figure 7-61: Water permeation in a 1-day-old film of AS-H-1b. The film does contain TexanolTM, but not the reservoir.
Left: the water content X ; right: the content of TexanolTM

In Figure 7-62 to Figure 7-65, all combinations of 2-film-experiments of AS-H-1b with and without TexanolTM are presented. The experiments were performed at standard drying conditions and the application of the top layer was after a drying time of 12-13 minutes. The initial thickness of the bottom layer is $h_0 = 60-75 \mu\text{m}$. After the application of a second film layer, the total film thickness $h_{total} = 110-150 \mu\text{m}$.

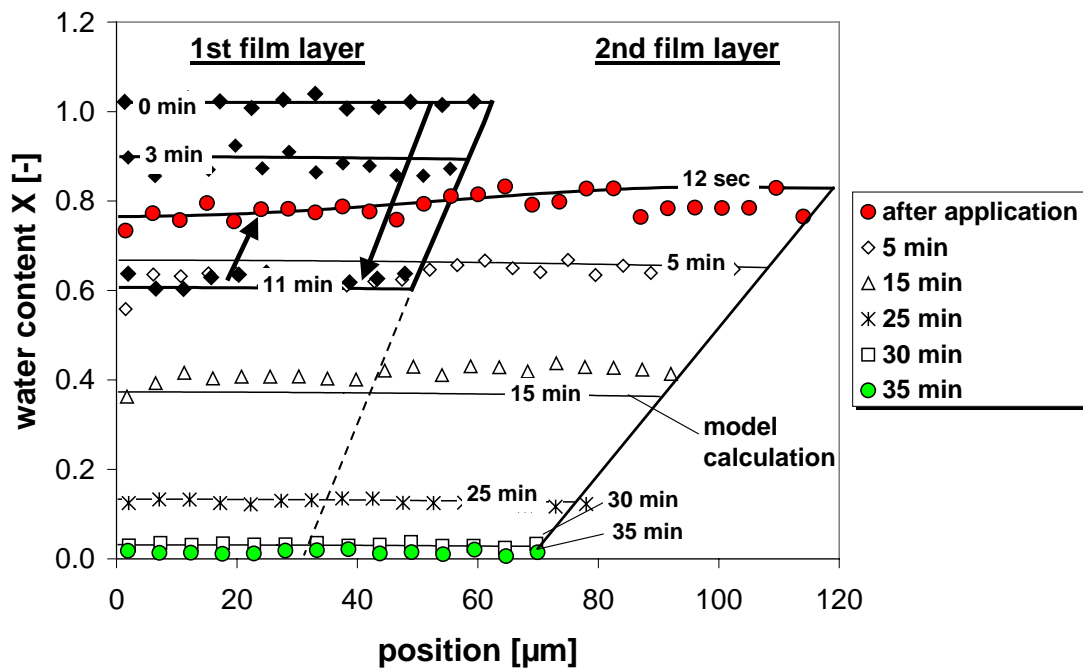


Figure 7-62: A 2-film-experiment with pure AS-H-1b. ($T = 25 \text{ }^\circ\text{C}$; $\varphi = 65\%$; $u = 0.05 \text{ m/s}$)

Two-film-experiments (I) give important insight into the degree of particle contact and coalescence in the bottom layer and (II) show how this has an influence on the water content of the top layer. Apart from the moment of application of the top layer, the thickness of the different layers is of crucial importance since this is responsible for the volume that can be filled with water.

A first experiment (Figure 7-62) shows the interaction of two films of pure AS-H-1b: Already the first Raman scan after the application of the second film layer shows an equal water content in both films. Obviously, a water content of $X \sim 0.6 \text{ g water/g polymer}$ in the bottom film layer allows complete redispersion. Both film layers together behave like they were one thick layer, showing an uniform water content.

In a second experiment (Figure 7-63), a film of AS-H-1b, containing TexanolTM, is applied onto a film of pure AS-H-1b. The water content of the bottom layer, before the application of layer two, is $X \sim 0.5 \text{ g water/g polymer}$. This is below the limit for complete redispersion as indicated by the step-profile of water that forms immediately after the application of the top film layer. The top layer dries independently of the bottom layer until the water content reaches that of the bottom layer.

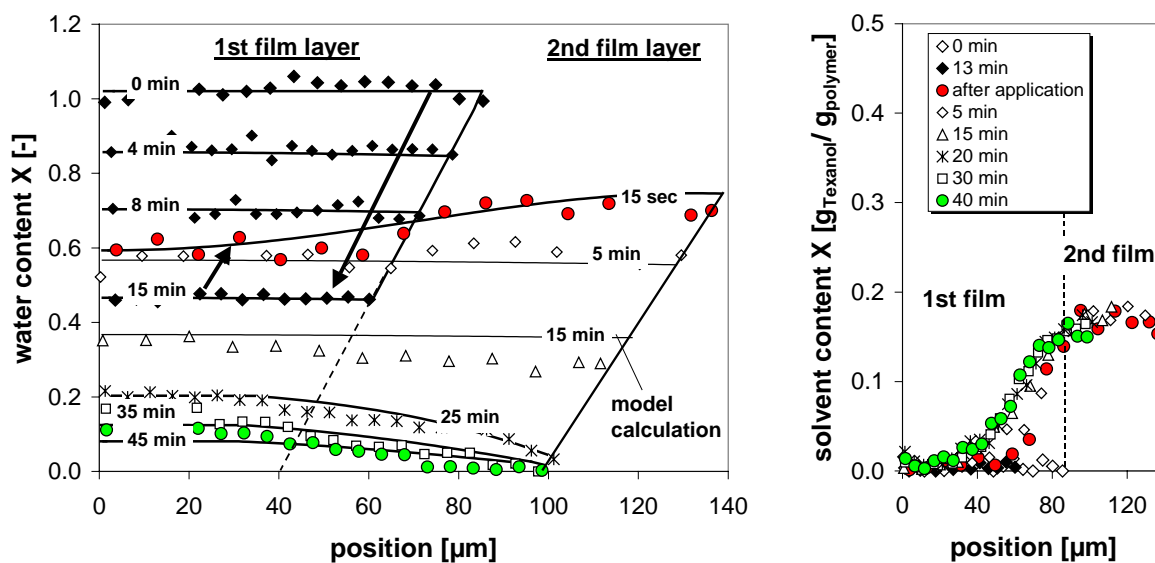


Figure 7-63: 2-film-experiment with films of AS-H-1b with/without 18 mass % TexanolTM per polymer (1st layer: no TexanolTM; 2nd layer: TexanolTM) ($T = 25 \text{ }^\circ\text{C}$; $\varphi = 65\%$; $u = 0.05 \text{ m/s}$)

Below a water content of $X \sim 0.2 \text{ g water/g polymer}$, it becomes obvious that the film consists of two layers having different characteristics: in the top layer, containing 18 mass % of TexanolTM per polymer, a filmside diffusion resistance for water forms, indicated by the concentration profiles that form towards the film surface. The formation of a diffusion resistance in the film is the consequence of complete particle deformation and fast polymer interdiffusion due to the presence of TexanolTM. The concentration gradients in Figure 7-63 show that the particle deformation is the strongest within the $20 \mu\text{m}$ below the film surface, driven by strong capillary forces (= skin layer formation). Remaining water in the bottom layer of pure AS-H-1b is

trapped and it takes long time until it leaves the film by diffusion. The content of TexanolTM in the top layer is constant throughout the experiment and no diffusion of TexanolTM into the bottom layer is observed.

In a third experiment (Figure 7-64), the bottom film is a layer of AS-H-1b, containing 18 mass % of TexanolTM per polymer, on which a second layer of pure AS-H-1b is applied.

The remaining water content of $X \sim 0.6 \text{ g water/g polymer}$ in the bottom layer after 12 minutes of drying is sufficient for complete redispersion indicated by the uniform water content in both film layers. Here, the top layer, which consists of the hard polymer dispersion AS-H-1b, doesn't show the formation of the filmside diffusion resistance like it was observed before for the same formulation containing TexanolTM. Opposite to the above experiment, here the capillary forces are not strong enough for the complete particle deformation of the hard polymer formulation AS-H-1b.

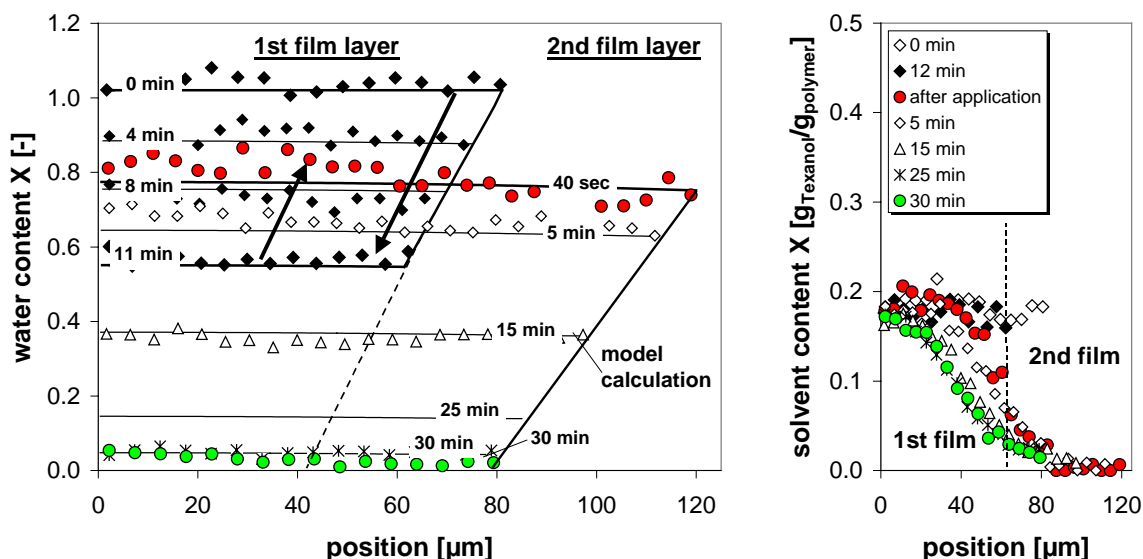


Figure 7-64: 2-film- experiment with films of AS-H-1b with/without 18 mass % TexanolTM per polymer (1st layer: TexanolTM; 2nd layer: no TexanolTM) ($T = 25 \text{ }^\circ\text{C}$; $\varphi = 65\%$; $u = 0.05 \text{ m/s}$)

The last possible combination of films with/without TexanolTM shows two films that contain 18 mass % of Texanol (Figure 7-65). In a film of soft particles, particle deformation takes place before the irreversible particle contact. Therefore, a lower water content (here: $X \sim 0.5 \text{ g water/g polymer}$) still allows the complete redispersion of the film. This is proven by an almost uniform water content in vertical direction of the two film layers. Towards the end of drying, whenever a formulation with TexanolTM is in contact with the drying air, a filmside diffusion resistance in the film forms, indicated by the water gradients and the decreased drying rate. The gradients indicate, that the diffusion resistance forms in a layer of about 20 microns in thickness located at the film surface (= skin). During the experiment, the content of TexanolTM in both film layers is constant.

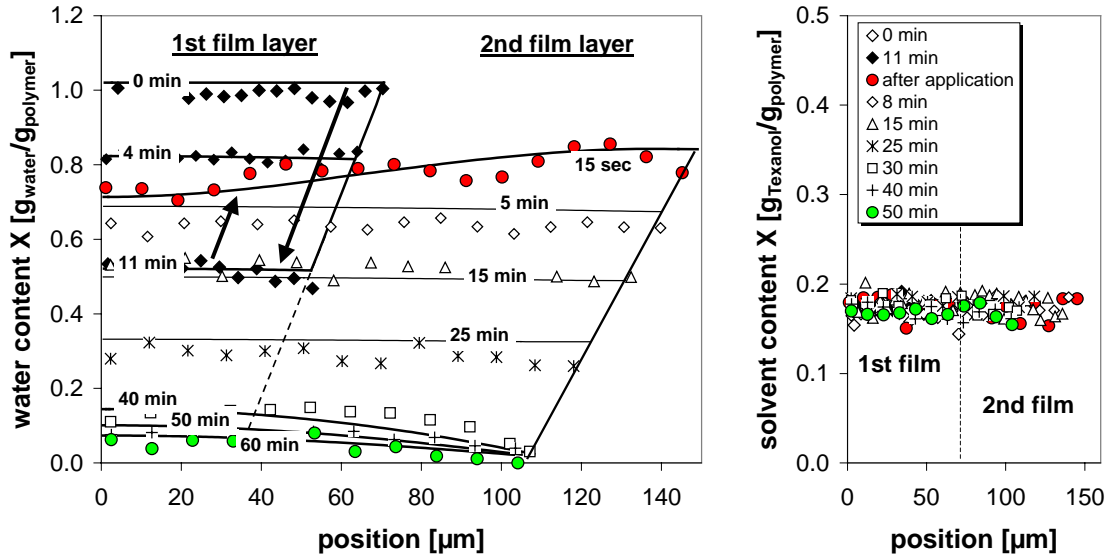


Figure 7-65: 2-film-experiment with films of AS-H-1b with 18 mass % Texanol™ per pol. ($T = 25\text{ }^{\circ}\text{C}$; $\varphi = 65\%$; $u = 0.05\text{ m/s}$)

The impact of Texanol™ on the redispersion properties of 1-day-old films of AS-H-1b is large. Figure 7-66 shows, that, after the application of water onto a dry film of pure AS-H-1b, it fills the porous film structure and causes an increase in film thickness due to the interaction with hydrophilic material. As discussed before, the contact between the polymer film and the glass substrate is not strong enough to hinder water accumulation below the film. By this, the complete film detaches from the substrate. Apart from the shape of the concentration gradients, the existence of a porous film structure is also proven by the atomic force microscopic (AFM) picture of the film surface, which shows single, undeformed latex particles.

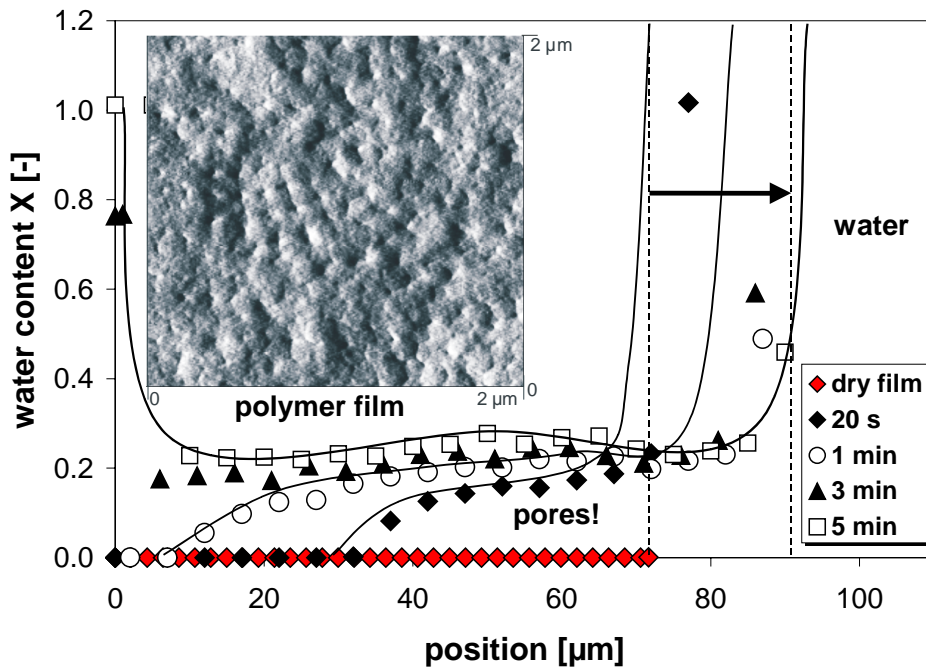


Figure 7-66: Water permeation in a 1-day-old film of AS-H-1b without Texanol™

Compared to the formulation without TexanolTM, the AFM picture of the surface of a film containing TexanolTM shows a smooth and non-porous coating surface, formed by a layer of sintered particles (Figure 7-67). The picture serves as a proof for the existence of the layer of completely deformed particles at the coating surface.

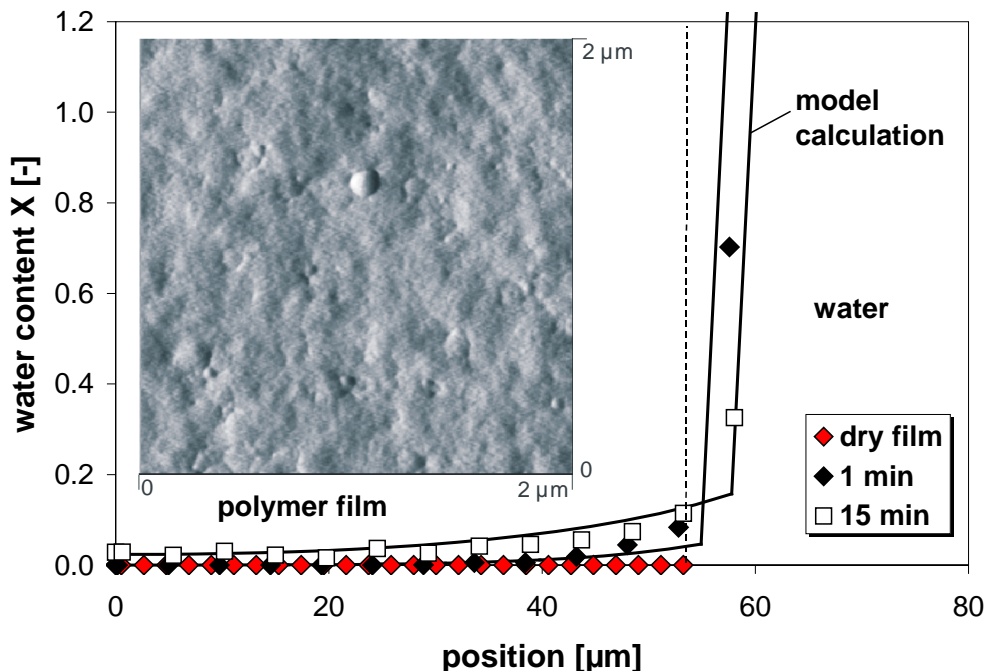


Figure 7-67: Water permeation in a 1-day-old film of AS-H-1b with TexanolTM

Conclusions on the Influence of Plasticizers

In several ways, the addition of a plasticizer is crucial for the film formation and coating properties. The plasticizer (TexanolTM) diffuses into the polymer particles and lowers the polymer glass transition temperature T_g . This has a great impact on film drying: A fast decreasing water content in the center of the film is found for high TexanolTM contents, which can only be caused by a stronger horizontal flow, as a result of capillary pressure and a layer of deformed particles at the film surface. The formation of such a skin layer, first propagated by Sheetz (1965), is proven here by AFM pictures of the coating surface and by the concentration gradients that form whenever a film, containing Texanol, is in contact with air during drying. Beneficial for the application properties is, that the moment of irreversible particle contact is slightly later during drying, due to the higher deformability of the particles. Besides, the addition of TexanolTM greatly improves the final coating properties because both, polymer interdiffusion and particle deformation, are increased. Despite the benefits, TexanolTM, being a low-volatile organic solvent, should generally be avoided in environmentally-friendly coating formulations.

7.6.2 Surfactant (Sodium-Dodecyl-Sulfate, SDS)

The redispersion experiments of a 1-day-old film of AS-H-1b with and without additional surfactant show, that a higher amount of surfactant will hinder, or at least slow down, the polymer interdiffusion. In the film without additional surfactant, water fills the pores and the interaction with the hydrophilic material causes an increase in film thickness. Due to a loose contact with the glass substrate, water accumulation below the film occurs, leading to the detachment of the film from the substrate. The maximum water content that is reached in the hard polymer film of AS-H-1b is $X \sim 0.2 \text{ g water/g polymer}$ (compare Chapter 7.4.2). Additional surfactant hinders polymer interdiffusion so that particle contact in the dry film remains reversible. After the application of a reservoir of the dispersion on top of the dry film, water diffuses into the film structure. Within minutes, the maximum water content in the former dry layer reaches a value ($X \sim 0.6 \text{ g water/g polymer}$) which is three times as high as that of a film without additional surfactant. As expected, a higher level of surfactant has no benefit on the adhesion properties of the film with its substrate.

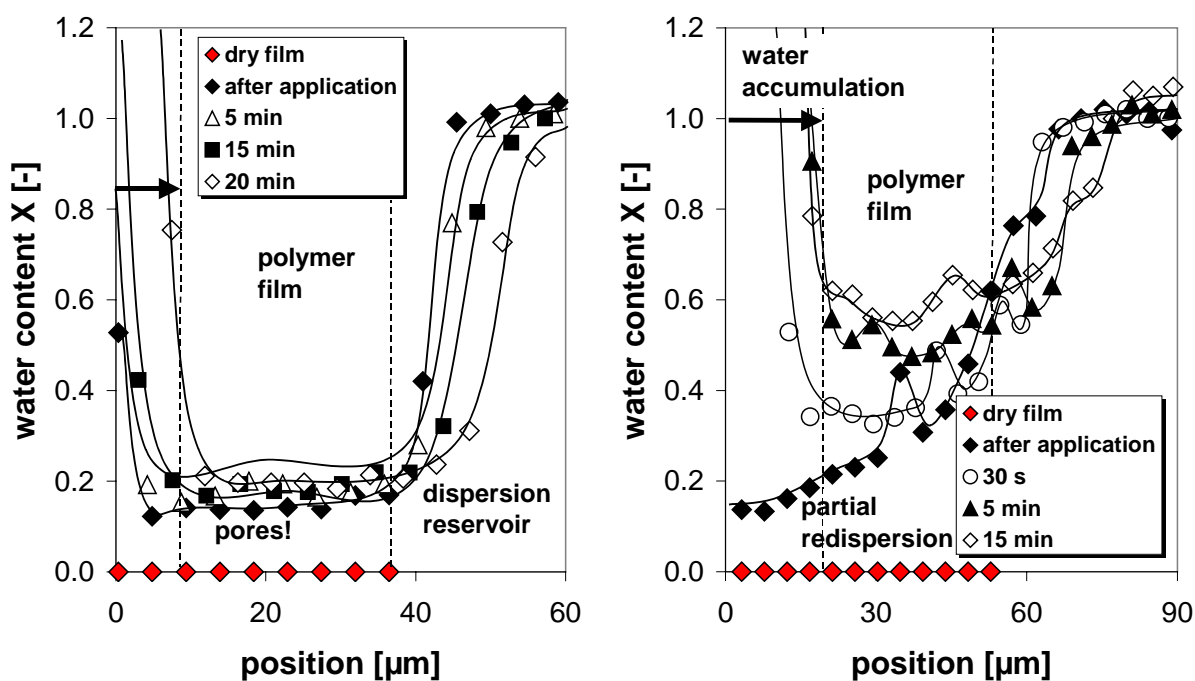


Figure 7-68: Redispersion of 1-day old films. Left: pure AS-H-1b; right: AS-H-1b with an additional amount of surfactant (SDS)

7.7 Aqueous Polyurethane (PU) Dispersions

In the coating business, aqueous 2-component PU dispersions become increasingly popular for many applications where they form excellent alternatives to aqueous latex dispersions. Therefore, this chapter gives some insight into the drying behaviour (Chapter 7.7.1) and the film properties (Chapter 7.7.2) of aqueous 2-component PU dispersions to show their commons and disparities compared to aqueous latex dispersions. The film formation of waterborne two-component polyurethanes is very complex due to the heterogeneous nature of the dispersion along with the simultaneous progression of several parallel physico-chemical processes which include water evaporation, chemical crosslinking reactions, phase separation, and droplet coalescence. Chemical crosslinking, which is responsible for the mechanical stability of the film is discussed in Chapter 7.7.3. Full crosslinking should largely hinder water permeation in the dry film and is investigated in Chapter 7.7.4.

7.7.1 Water Concentration in Vertical Direction of the Film during Drying

Typical for aqueous polymer dispersions is their gasside-controlled drying behaviour. Like aqueous latex dispersions, aqueous polyurethane (PU) dispersions show no concentration gradients of water towards the film surface, which would indicate a filmside diffusion resistance for water.

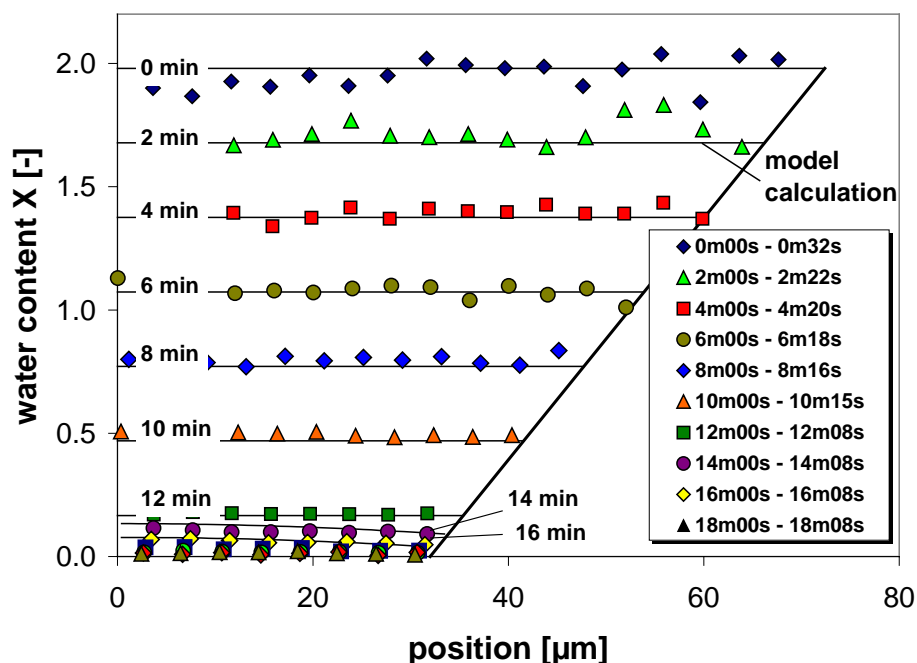


Figure 7-69: Concentration profiles in a thin film of PU dispersion during drying at standard conditions

Figure 7-69 shows the water concentration profiles in a thin film of PU dispersion during drying at standard drying conditions. The experimental data, obtained from IMRS measurements, can be well described by model calculations, indicated by the

lines. Below a water content of $X \sim 0.1 \text{ g water/g polyol}$, a decrease of the drying velocity is the result of a combination of the beginning chemical crosslinking and the formation of a filmside diffusion resistance for water (compare Figure 7-70). This is the moment when the film slowly turns transparent, meaning that the interstitials between the single particles become smaller than the wavelength of the incident light.

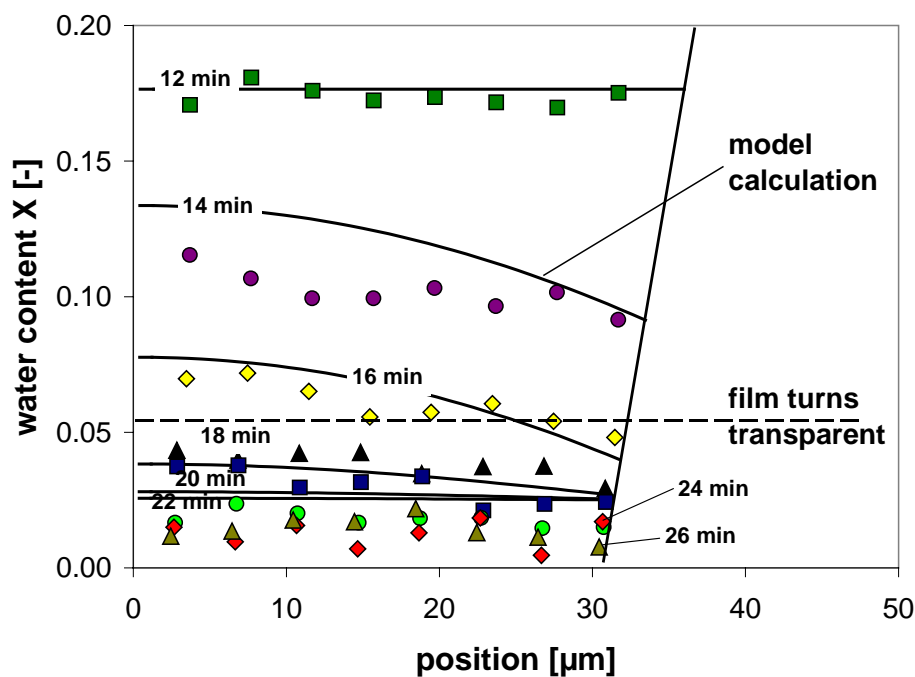


Figure 7-70: A magnified view of Figure 7-69 for low water contents

Chemical crosslinking starts with the contact of the reactive compounds and is slow compared to the velocity of film drying. A decrease of the Raman signal at 3500 cm^{-1} is the only measure for water evaporation from the film. Since also chemical crosslinking is exclusively characterized by changes of a weak Raman peak at 3500 cm^{-1} it is impossible to distinguish between the two effects in the Raman spectrum of the PU dispersion. The contribution of chemical crosslinking to the Raman signal is masked by the broad water peak. During drying, the peak intensity at 3500 cm^{-1} decreases due to water evaporation, but at the same time it should also slightly increase due to the bond formation by chemical crosslinking. Therefore, when both effects are parallel, beginning chemical crosslinking can also give the impression of a reduced evaporation rate.

7.7.2 Inhomogeneities in the Dry Film

Depending on the preparation route, the size distribution of the polyisocyanate droplets in the PU dispersion can be non-uniform (see Chapter 2.2.2). An inhomogeneous droplet size distribution leads to an inhomogeneous distribution of the reactive compounds (polyol and polyisocyanate) in the dry film. Figure 7-71 (bottom) shows the inhomogeneous distribution of polyisocyanate and polyol in a dry PU film, obtained from vertical IMRS scans at different horizontal positions of the film

(the distance between the measurement positions is 2 mm). The polyisocyanate-rich droplets can have a size of up to $\sim 8 \mu\text{m}$ in diameter (compare Figure 7-71). Within these droplets, the content of polyisocyanate is considerably higher than average and as a consequence, the content of polyisocyanate in the surrounding medium is lower than would be expected from the formulation. The surrounding medium is a homogeneous mixture of submicron droplets of polyol and polyisocyanate.

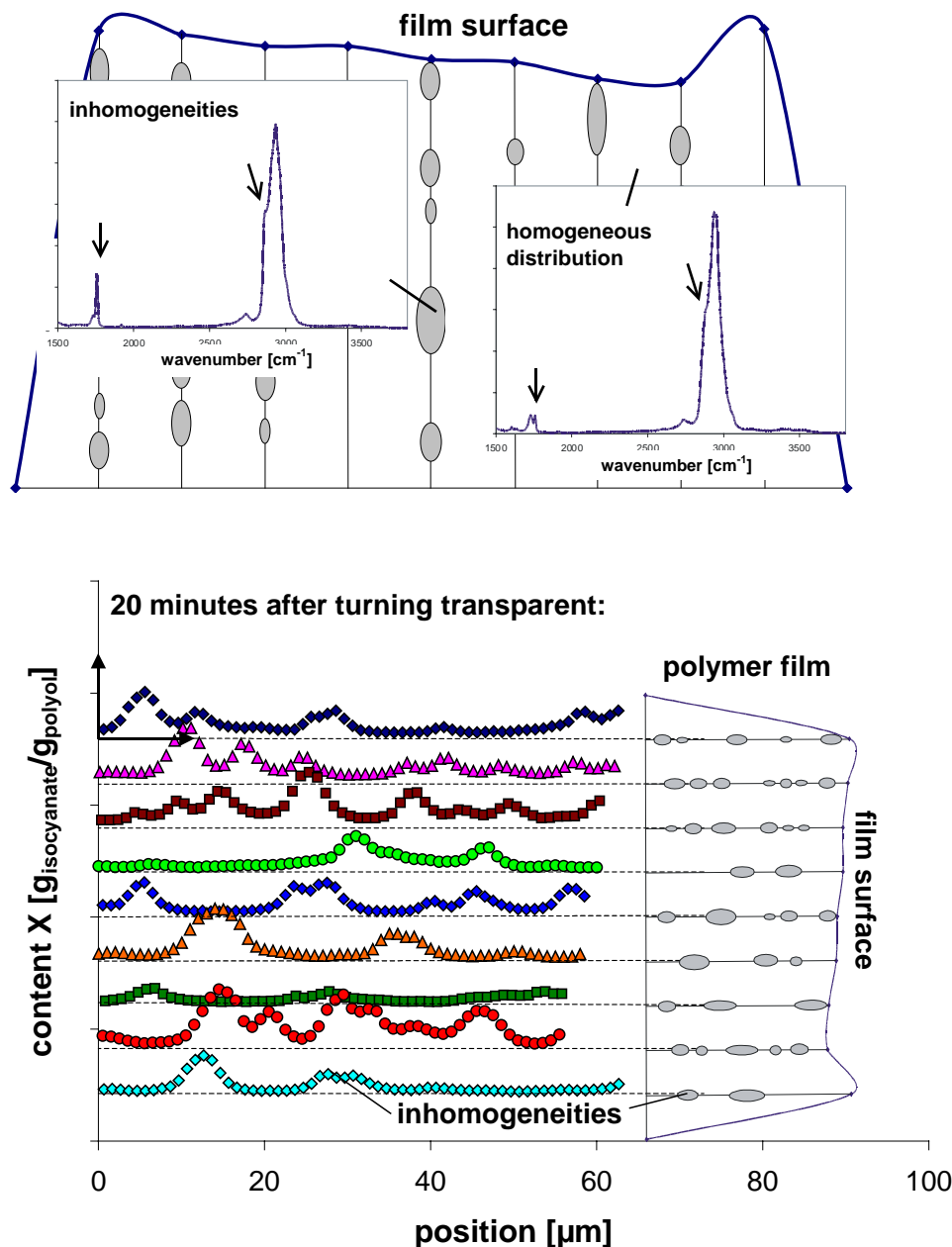


Figure 7-71: Top: the inhomogeneous distribution of the reactive compounds in the dry film, expressed by the different shapes of the Raman spectrum. Bottom: the ratio of polyisocyanate to polyol in a fresh, dry film, prepared by way 1 (= non-uniform droplet size)

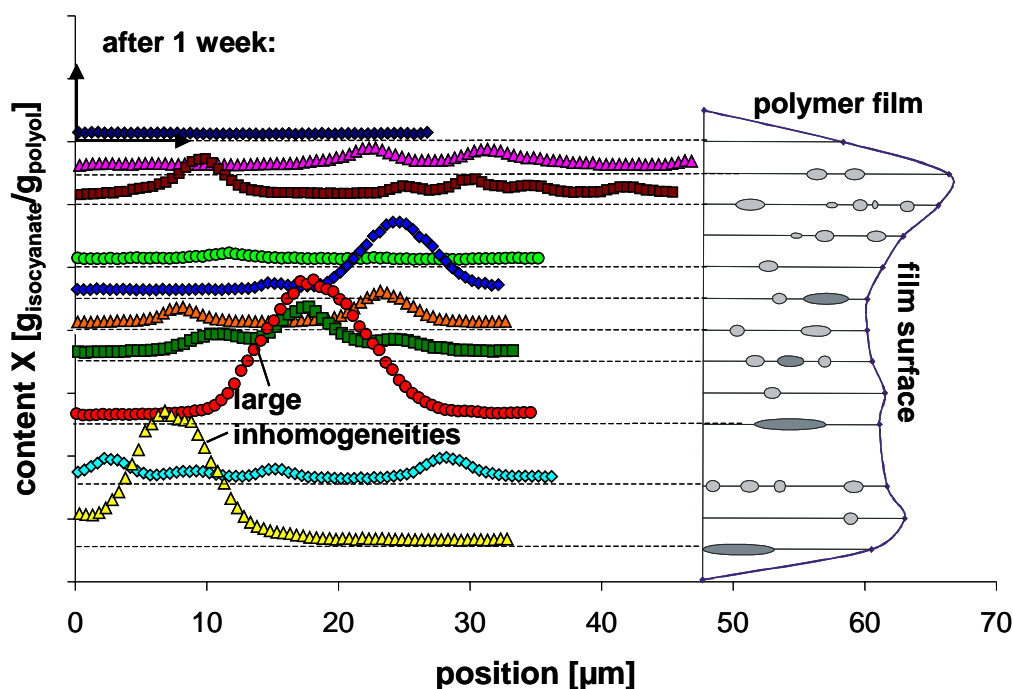


Figure 7-72: Inhomogeneities in the same dry PU film as above at the age of one week

With time, the inhomogeneities increase in size which might be ascribed to an internal separation process. This becomes clear from Figure 7-72 which shows the distribution of the polyisocyanate-rich inhomogeneities in the same sample film as in Figure 7-71 at the age of one week. After one week, the number of inhomogeneities has decreased due to droplet coalescence and their size has increased to up to $15\ \mu\text{m}$.

The inhomogeneous distribution of the two reactive compounds has an impact on the distribution of the other components, like surfactants or additional organic solvents. Polyisocyanate contains a large amount of surfactant. Its function is to stabilize the polyisocyanate droplets in the aqueous medium. Figure 7-73 shows the ratio of surfactant to polyisocyanate in the same sample film (I) *20 minutes* after turning transparent and (II) after one week. In the fresh film, the amount of surfactant per polyisocyanate is inhomogeneous, being higher outside the isocyanate-rich phase. This can be explained by the fact that small droplets have a higher specific surface than large droplets, meaning, that the surface and therefore the relative amount of surfactant per polyisocyanate of the small polyisocyanate droplets outside the inhomogeneities is higher. With time, the ratio of surfactant to polyisocyanate is influenced by crosslinking, interdiffusion and coagulation processes and becomes almost constant across the film, although the distribution of polyisocyanate per polyol is still inhomogeneous. This could be one proof for the existence of a network of polyisocyanate in the film, in which the surfactant preferably dissolves and where its content becomes homogeneous by diffusion processes. A slight increase of the surfactant level towards the glass substrate is observed in Figure 7-73.

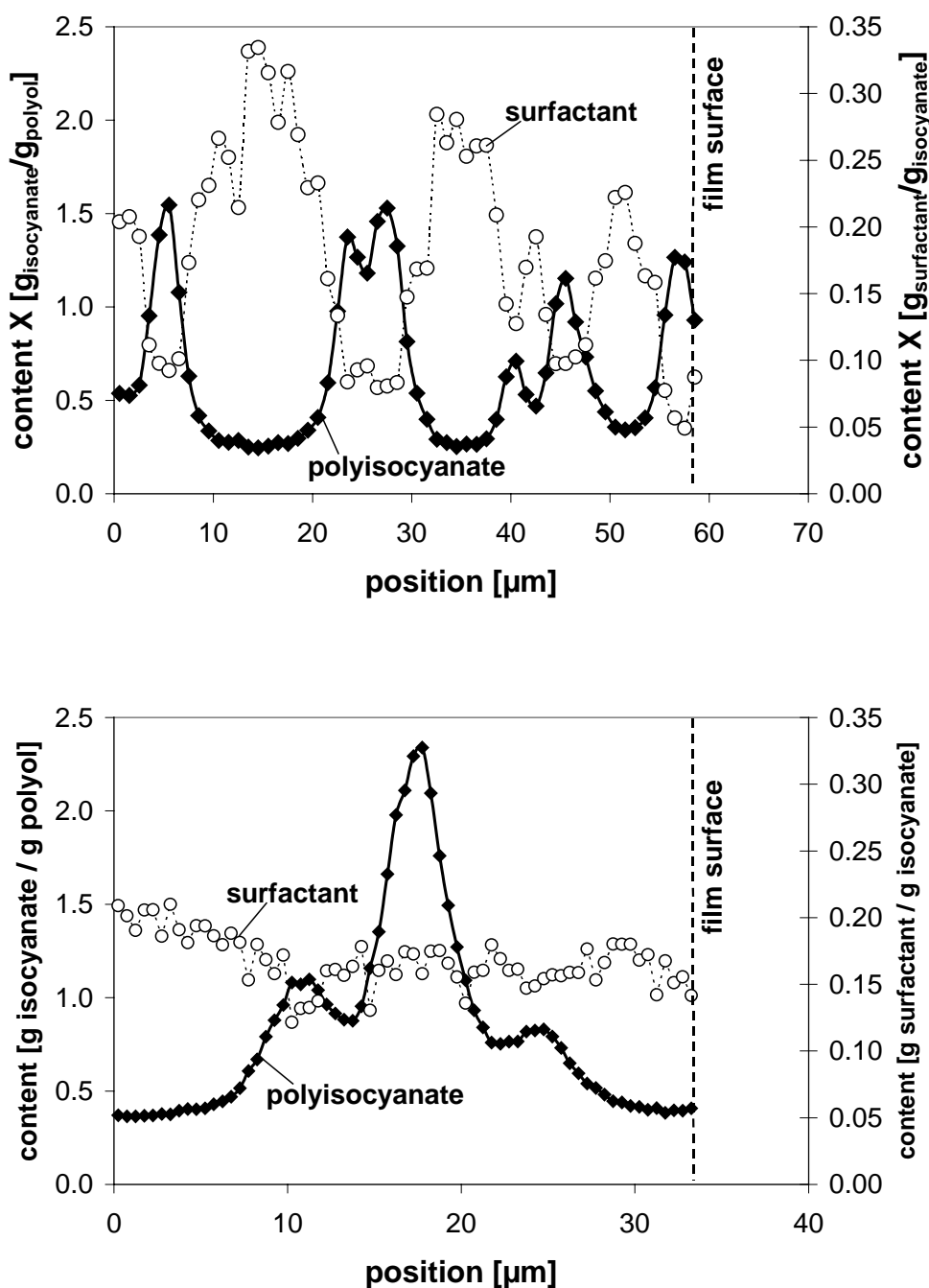


Figure 7-73: Surfactant distribution in the film. Top: 20 minutes after turning transparent; bottom: after one week

Small amounts of a low-volatile organic solvent are often added to the formulation to improve the film formation properties. Depending on the chemical structure, the solvent prefers to dissolve in either the isocyanate-rich or polyol-rich phase. Figure 7-74 shows the distribution of two different organic solvents in a sample film. The linear molecule of n-butyl acetate prefers the polyol-rich phase, but the cyclic molecule of propylen carbonate prefers to dissolve in the phase of higher polyisocyanate content. In addition, propylen carbonate is responsible for an even

more inhomogeneous distribution of the two reactive compounds in the freshly prepared film: here, small droplets are found that consist of almost pure polyol.

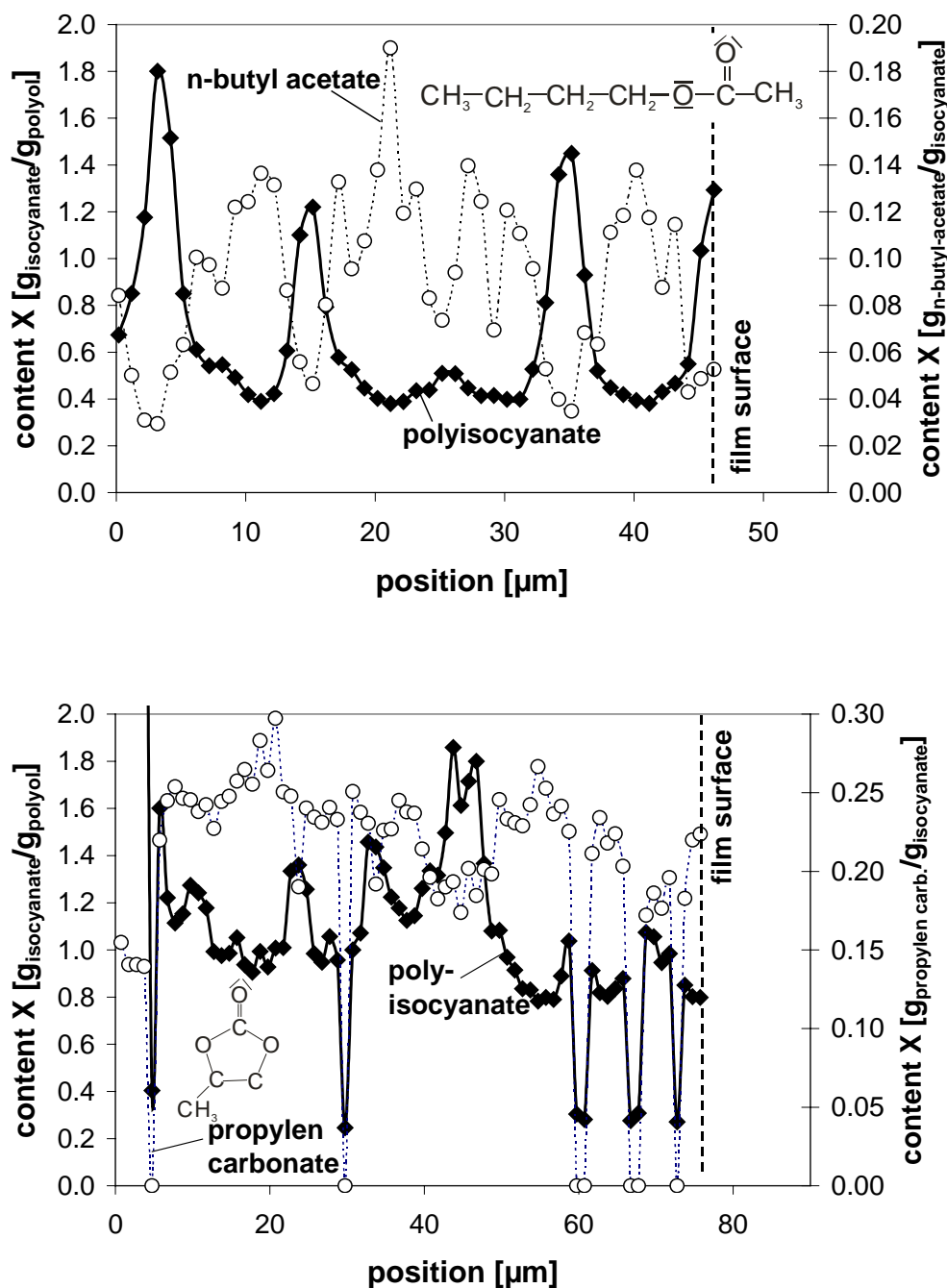


Figure 7-74: The distribution of an additional organic solvent in a fresh PU film. Top: linear n-butyl acetate; bottom: cyclic propylen carbonate

7.7.3 Chemical Crosslinking

Crosslinking of the film is mainly caused by the chemical reaction of polyol and polyisocyanate to form polyurethane. In addition, the presence of water in the film causes a side-reaction, which is the formation of polyurea. Crosslinking starts as soon as the

reactive compounds come into contact. The loss of isocyanate groups by the side reaction is taken into account by the ratio of hydroxy and isocyanate groups in the formulation. Figure 7-75 shows the distribution of the formed crosslinking-bonds per polyisocyanate in a sample film (I) 20 minutes after phase inversion and (II) after one week.

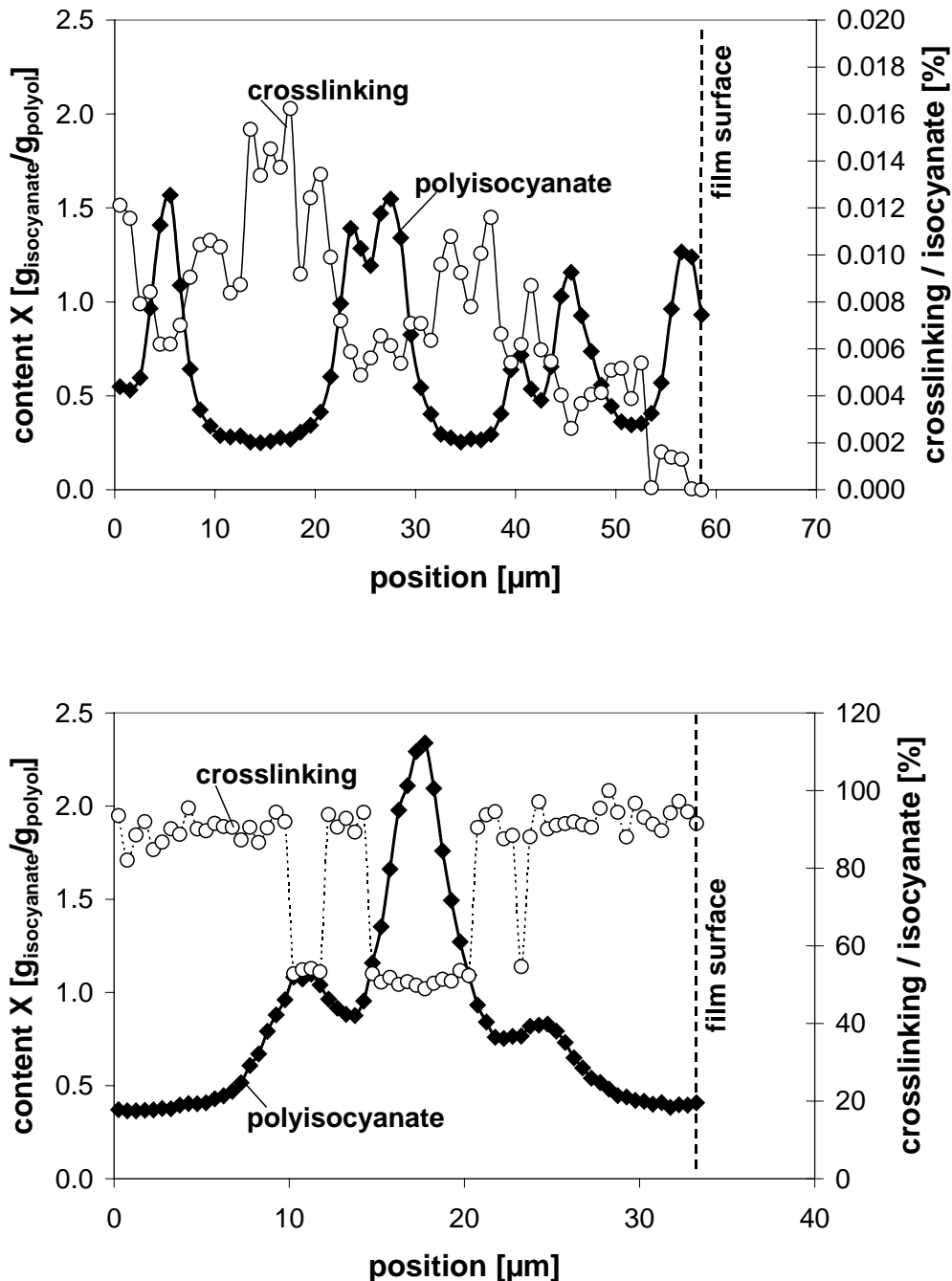


Figure 7-75: The crosslinking density per polyisocyanate. Top: 20 minutes after turning transparent; bottom: after one week

Attention has to be paid to the scale that indicates the degree of crosslinking per polyisocyanate: whereas, after one week, the film is fully crosslinked (= 100%), the

average crosslinking density in the fresh film is less than 0.01% of the amount, observed after one week. The comparison of crosslinking in fresh and older films gives the proof that crosslinking is slow compared to drying and that both processes can therefore be investigated separately. In the fresh film, the ratio of crosslinking to polyisocyanate is higher outside the inhomogeneities which can be explained by the fact that more reactive bonds of both components can come into contact which accelerates the beginning of crosslinking. After one week, the crosslinking of the film is mostly completed. Again, the crosslinking density is lower within the large, polyisocyanate-rich inhomogeneities: it is only around 60% of the total amount of crosslinking.

Obviously, the low content of polyol in the polyisocyanate-rich droplets doesn't provide enough active bounds for maximum crosslinking. This would mean that there are also non-reacted isocyanate groups present within the inhomogeneities. From the Raman data presented in Figure 7-75, it is impossible to differentiate between the formation of polyurethane (= main reaction), and the formation of polyurea (= side reaction).

7.7.4 Water Permeation in Fully Crosslinked PU Films

One main function of a coating is the protection of the underlying substrate against water (corrosion) or other harmful substances. In the case of water-based formulations, the challenge is to overcome the interparticular repulsion in the aqueous dispersion to form a strong polymer film which subsequently cannot be redispersed or penetrated by water. In the case of physical interactions, the mechanical stability of the dry polymer film is reached by the interdiffusion of polymer chains across the particle boundaries (\rightarrow aqueous latex dispersion). Redispersion experiments of different films, cast from aqueous latex dispersions, show that the formation of a mechanically stable film strongly depends on the minimum film formation temperature which also influences polymer interdiffusion. Complete coalescence takes time and can even be completely hindered by large amounts of surfactant (see Chapter 7.4.1). Therefore, the protection properties and the mechanical strength of the films from aqueous latex dispersions are often poor.

In the case of chemical crosslinking systems, e.g. aqueous polyurethane (PU) dispersions, the mechanical stability of the final coating is the result of the chemical reaction between polyol and polyisocyanate. Despite the inhomogeneous distribution of the two components in the investigated coating, the redispersion experiment in Figure 7-76 shows, that no water diffuses into the dry film. Obviously, compared to physical crosslinking formulations, the protective properties of the coating are greatly enhanced by chemical crosslinking.

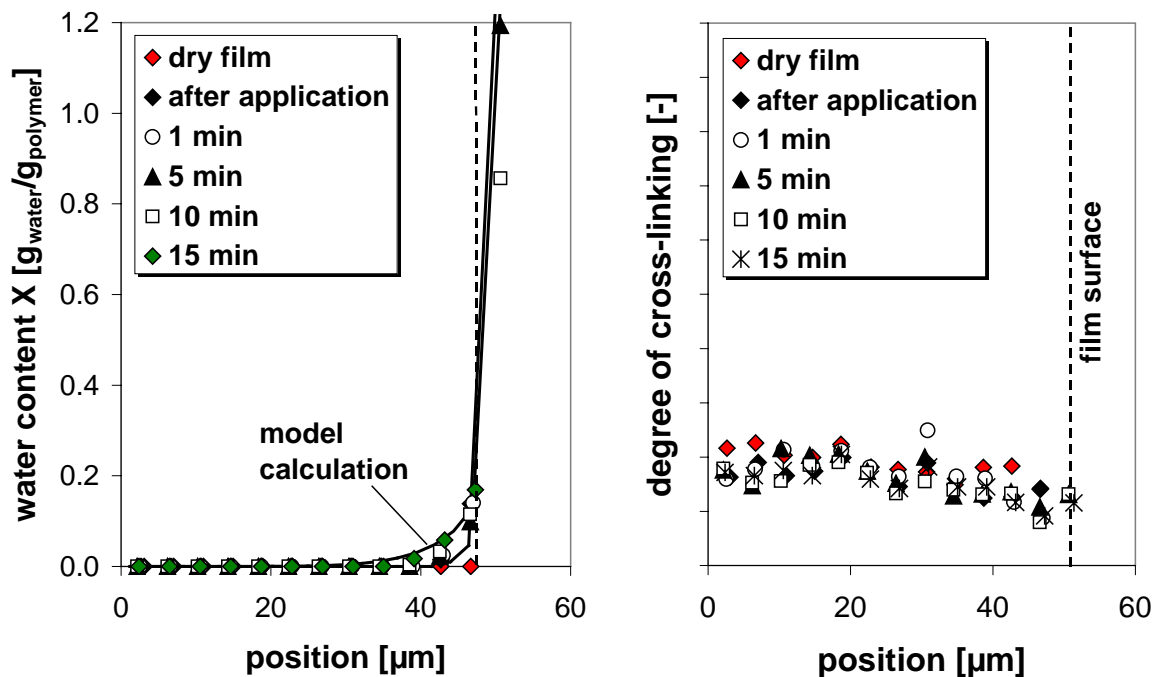


Figure 7-76: Water permeation into a fully crosslinked polyurethane film.
 Left: the water content X in the dry film; right: the degree of crosslinking per polyol

7.7.5 Conclusions on PU Dispersions

Aqueous PU dispersions show the typical gasside-controlled drying behaviour and horizontal inhomogeneous drying (not shown here). Depending on the dispersion preparation, the distribution of all components in the film (reactive compounds, surfactants, additives) can be inhomogeneous. In the final coating, the inhomogeneities can even have a size of 5-15 μm , depending on the age of the film and on internal separation processes. Investigations show, that film drying and crosslinking are largely separate processes and that full crosslinking of the coating generally takes several days. Once fully-crosslinked, the film shows excellent protection properties against water permeation despite the observed inhomogeneous distribution of the components. Compared to aqueous latex dispersions, such properties like film leveling, 2-film-experiments and the moment of irreversible particle contact were not investigated in this work, but could be interesting further steps. The big advantage, - compared to aqueous latex dispersions -, is that chemical crosslinking assures a desired low water permeability of the film and high mechanical stability without having to deal with film defects like pores or cracks, caused by insufficient particle deformation.

8 Conclusions

8.1 Summary

During the last decade, large efforts have been paid to the investigation of the drying and film formation properties of waterborne colloidal dispersions by both, academia and industry, but until today, the application and the final coating properties of waterborne polymer dispersions are poor compared to the ones of solventborne polymer solutions. This is expressed by visible lap lines, cracks, edge effects or strokes of the brush in the final dry coating, being not aesthetically pleasing to the customer, especially in gloss paints. The time during which corrections can be done on a freshly applied film layer without that striations or lap lines will be visible in the dry film is called open time. Horizontal inhomogeneous drying of aqueous polymer dispersions is responsible for edge-effects.

The poor coating properties of waterborne formulations are caused by one or more of the following factors:

- (I) the change of the rheological properties of the dispersion during drying
- (II) horizontal inhomogeneous drying
- (III) irreversible particle contact during drying
- (IV) incomplete particle deformation and polymer interdiffusion (=coalescence)
- (V) inhomogeneous distribution of components in the dry coating

The use of many different measurement techniques to investigate aspects of latex film formation, like e.g. surfactant distribution, particle ordering and deformation, is reported in the literature. Although there is fundamental interest in the role of water during drying, experimental data dealing with this aspect are rare. Apparently, this is due to a lack of experimental methods, which can detect water and which have a space and time resolution required to follow the local water concentration in the film.

In Karlsruhe a measurement technique, called Inverse-Micro-Raman-Spectroscopy (IMRS) has been developed by combining an inverse microscope with a confocal Raman spectrometer (*Schabel (2005); Schabel et al. (2005)*). It allows a quantitative evaluation of water concentration profiles in vertical and horizontal direction of thin polymer films online during drying. With an optical resolution of 2-3 μm and a time resolution of about 1 s the IMRS data possess a quality not yet presented by others.

Aim of this work is a discussion of the different aspects (rheology, horizontal inhomogeneous drying, irreversible particle contact, coalescence and component distribution) that are responsible for the poor application and coating properties of aqueous polymer dispersions by experimental data and model calculations. The industrial dispersion formulations used in this work were provided by RHODIA (France).

A dispersion paint is required to give a smooth (= glossy) coating on many substrates to be aesthetically pleasing to the customer. For good application properties (= easy application, good leveling, open time; no sagging,) a coating formulation has to display special rheological characteristics like e.g. shear thinning, a low yield stress and a well-designed viscosity function $\eta(\phi)$.

An investigation of the dispersion's rheological properties at different water contents X showed (I) a strongly increased low-shear viscosity with decreasing X, (II) the built-up of a yield stress and (III) an early liquid-solid transition. All of these findings are negative for the coating application and for film leveling. Concerning drying, it means that, depending on the drying conditions, there is only a limited time available for the leveling of brushmarks in the freshly applied film, until the viscosity reaches a critical value. The viscosity function $\eta(\phi)$ of the different dispersions can be well described by models from the literature.

Additives like surfactants change the particle-particle interactions and the dispersion structure; plasticizers change the polymer characteristics, but leave the particle interactions greatly unchanged.

Film leveling can be described by a mathematical model originally published by *Keunings and Bousfield* (1987), in which the viscoelastic behaviour of the dispersion is expressed by a multi-mode *Maxwell* fluid. For the investigated dispersions, the calculations give an open time (= time, available for corrections on a freshly applied layer) between 60 and 445 seconds. Two formulations, applied at their original state, do not level at all (\rightarrow AS-H-1a, AS-H-1b). For the investigated dispersions, this leads to the conclusion, that an elongation of the open time could only be achieved by more diluted dispersions, or by formulations in which the viscosity function is modified by adequate rheology modifiers (which is not investigated in this work).

The technique of Inverse-Micro-Raman-Spectroscopy (IMRS) was used for the investigation of film drying in vertical and horizontal direction of the film. The initial water content of the different latex dispersions was $X \sim 1.0$ g water/g polymer and the drying conditions were varied in a range that is typical for the application of paints and varnishes: temperature $T = 25-40$ °C; air velocity above the film $u = 0.05-0.3$ m/s; relative air humidity $\varphi = 4-70\%$; initial film thickness $h_0 = 32-123$ μm . Most experiments were performed at standard drying conditions ($T = 25$ °C; $\varphi = 50\%$; $u = 0.05$ m/s). Experimental results showed that, opposite to drying of polymer solutions, drying of aqueous polymer dispersions in vertical direction of the film (in the range of the experimental conditions used here) is largely gasside-controlled. No strong concentration gradients form in vertical direction of the film and water sorption becomes important only for very low water contents ($X < 0.05$ g water/g polymer).

The combination of gravimetric drying experiments, digital pictures and IMRS measurements proves horizontal inhomogeneous drying and the existence of a drying

front. Water evaporation is from the wet area of the film only. Horizontal inhomogeneous drying can be enforced by locally changed drying conditions (air velocity u , temperature T): the difference of up to 10% in the final film thickness proves the existence of a drag flow of water and also particles in the concentrated dispersion. Due to the low surface tension of the dispersion, *Maranghoni*-convection is excluded as the main driving force, but a more detailed investigation of the phenomenon is left for the future.

IMRS data show, that horizontal inhomogeneous drying can be largely suppressed by artificial borders. With the help of IMRS measurements at different horizontal positions of the film, water concentration gradients in the film can be measured. The data show, that horizontal mass flow is mainly driven by a water concentration gradient towards the edge. It seems that the formation of a drying front can be largely suppressed by low- T_g polymers.

Film drying experiments using IMRS showed that different amounts of additives like surfactants or plasticizers (TexanolTM) have an influence on film drying and film formation: a large amount of surfactant between the polymer particles hinders film formation, which is why very high levels of surfactant are not a means to improve the dispersion properties. Plasticizers (TexanolTM) diffuse into the polymer particles, which leads to a lower polymer glass transition temperature. An increase in the drying rate at the center of the film is found for increased TexanolTM contents, which is caused by a stronger horizontal flow, as the result of capillary pressure and a skin layer of deformed particles at the coating surface. The formation of such a non-porous layer of deformed particles is proven by AFM pictures of the coating surface and by the concentration gradients that form in 2-film-experiments. Also beneficial for the coating properties is, that the moment of irreversible particle contact occurs later during drying, due to the higher deformability of the particles.

Film formation from polymer dispersions includes the stages of (I) water evaporation, (II) particle deformation and particle contact and (III) polymer interdiffusion. Desired properties like full mechanical strength and low permeability of the coating for water are only reached if the individual particle interfaces that allow easy water diffusion are destroyed by the diffusion of polymer chains.

Redispersion and 2-film-experiments after different drying times showed that irreversible particle contact in the concentrated dispersion occurs already during drying. Then, a complete redispersion of the film is no longer possible. The experimental data (IMRS) revealed, that for the application of a second film layer on top of a first coating, the irreversible particle contact and water diffusion can have large consequences: Depending on (I) the moment of application of the second coating layer and (II) on the thickness of both film layers, the water content equalizes or exhibits a step-profile. In the case of a thick bottom layer, it could be, that the water content of

the top layer decreases in so far, that irreversible particle contact occurs immediately after application and no corrections on the freshly applied layer can be done. The above discussed facts would also apply for any porous substrate on which the dispersion is coated.

Permeation experiments in dry films of different age showed, that good coating properties (= a low permeability of water in the film) are often reached only after several days. This has to be considered with regard to the desired application (e.g. where long curing is a problem). Coalescence and polymer interdiffusion strongly depend on the polymer's glass transition temperature T_g . Therefore, complete film formation can be accelerated by low- T_g polymer dispersions or the addition of a plasticizer. On the other hand, this could be negative for the mechanical strength of the final coating. Low permeability and high mechanical strength could be reached by curing at elevated temperatures (where applicable) or by chemical crosslinking formulations.

The above described experimental data obtained from drying, redispersion and permeation experiments (IMRS) were compared to model calculations employing a finite-difference method as described by *Gutoff* (1994). In the model, the gasside mass transfer coefficient $\beta_{w,g}$ is obtained from a well-known *Sherwood*-correlation for laminar flow above a plate geometry. The sorption data to describe the phase equilibrium were obtained from gravimetric experiments, where the dry film is brought in contact with the gas phase of defined water activity a_w . In the model, the filmside diffusion coefficient $\delta_{w,p}$ is expressed by an exponential equation which is used to fit the experimental drying data. A typical diffusion coefficient for water in the wet film during drying is $\delta_{w,p} = 1.95 \cdot 10^{-10} \text{ m}^2/\text{s}$. Generally, the measured water concentration profiles in the film can be well described by the model. Compared to polymer solutions, the diffusion coefficient of water in the polymer film $\delta_{w,p}$ is larger and is a moderate function of the water content X .

In dry films with still existing particle interfaces (= diffusion network), $\delta_{w,p}$ describes water diffusion in the hydrophilic material that is located along the interfaces. Compared to the diffusion coefficient of water in the wet polymer film, the diffusion coefficient of water along the particle interfaces has a typical value of about $\delta_{w,p} = 2.0 \cdot 10^{-11} \text{ m}^2/\text{s}$ and as soon as polymer interdiffusion is completed (= destroyed diffusion network), a typical diffusion coefficient is $\delta_{w,p} = 4.0 \cdot 10^{-13} \text{ m}^2/\text{s}$.

Within the limitations, the drying and redispersion behaviour of a full paint formulation containing 20% pigments was investigated by IMRS. The data showed, that film drying of aqueous polymer dispersions is very different to paint formulations with pigments. A filmside diffusion resistance forms, possibly caused by the fact, that the pigments largely block the diffusion path for water in the film. A comparison of the

drying curves obtained from IMRS and gravimetric drying experiments shows that horizontal inhomogeneous drying is largely suppressed by the presence of the pigments which might be the result of stronger capillary forces. The investigated formulation with pigments and plasticizers does exhibit the same high permeability for water as the pure latex dispersion without pigments and plasticizers. From the experimental data, an explanation for this behaviour could not be found and needs further investigation. Obviously, it is not possible to fully transfer the results gained in this work from the investigation of aqueous latex dispersions to also full paint formulations containing pigments.

Chemical crosslinking waterborne systems, like e.g. PU dispersions, are one promising possibility to strongly improve the final coating properties of environmentally-friendly formulations, which is why their investigation is included in this work. PU dispersions show the typical gasside-controlled drying behaviour of aqueous dispersions and horizontal inhomogeneous drying. Depending on the dispersion preparation, (= emulsification) the distribution of all components in the film (reactive compounds, surfactants, additives) can be locally inhomogeneous. The inhomogeneities can even have a size of $5-15\ \mu\text{m}$, depending on the age of the film and on internal separation processes. Investigations showed, that film drying and crosslinking are merely separate processes and that full crosslinking of the coating generally takes several days. Once fully-crosslinked, the film shows excellent protection properties against water permeation despite the inhomogeneous distribution of the components. The big advantage, - compared to aqueous latex dispersions -, is that chemical crosslinking assures the desired low water permeability of the film and high mechanical stability without having to deal with film defects like pores or cracks, caused by the insufficient particle deformation of a high- T_g polymer latex.

8.2 Outlook

This work gives insight into many aspects that are responsible for the poor application and film formation properties of aqueous polymer dispersions. But to be able to further improve the application and coating properties of such formulations, a continuation of the experimental work is needed. Necessary future steps are described below:

Open time: An elongation of the open time of aqueous latex dispersions can only be reached if (I) the increase in viscosity as a function of the water content X is less severe and (II) the irreversible particle contact occurs later during drying. The investigations performed in this work revealed that both requirements could only be fulfilled by more diluted dispersions, in which the dispersion properties (viscosity, polymer T_g ...) would be adjusted by rheology modifiers and other additives.

Therefore, as next steps for the future, an investigation of the open time of a more diluted dispersion ($X_{start} = 1.5 \text{ g water/g polymer}$) by redispersion and 2-film-experiments using IMRS would be recommended. The diluted dispersion would require the use of rheology modifiers to adjust the dispersion viscosity and to assure good application properties of the coating. In a first step, suitable rheology modifiers would have to be identified by rheological measurements of the viscosity as a function of the water content X .

Edge effects: Based on the experimental results of this work, it seems that horizontal inhomogeneous drying can be avoided for low- T_g polymers. In such dispersions, a surface layer of completely deformed particles forms and exerts a pressure onto the underlying particles causing further particle deformation and horizontal flow of water. An investigation of this fact using a model dispersion of a high- T_g polymer and different amounts of a plasticizer (e.g. TexanolTM) would be of great importance to understand horizontal inhomogeneous drying and edge effects. Interesting would be a comparison of the dimensions of the surface layer with data obtained from cryo-SEM as presented by *Ma* (2005).

In connection with horizontal drying, (I) a different air flow above the sample or (II) a temperature gradient in the film would also cause horizontal mass flow of water and – at least at the beginning of drying - particles. An investigation of the respective area of the film by a 2-dimensional mapping using IMRS would give information about the driving forces causing horizontal flow and the impact of such effect on the final coating quality.

Alternative aqueous formulations: Chemical crosslinking systems like aqueous PU dispersions are superior in their final coating properties (= permeability and mechanical stability) compared to physical crosslinking systems like latex dispersions. Therefore, they seem to be the most promising alternatives for environmentally-

friendly coating formulations. Apart from the distribution and the degree of crosslinking, it would also be good to learn more about the application and final coating properties of such dispersions.

Horizontal inhomogeneous drying of PU dispersions was generally observed. Obviously, edge effects seem to also be a problem for these coatings. An investigation of the horizontal inhomogeneous drying and a comparison of the results with that of aqueous latex dispersion would be valuable. The change of the rheological properties with drying time and later during crosslinking could prove the onset of chemical crosslinking and could give a viscosity function of the dispersion. The investigation by redispersion experiments, 2-film experiments and water permeation in different films would give new insight in the film formation properties of such systems and the moment of irreversible contact between the two reactive components during drying. Water permeation as a function of the age of the film, the temperature treatment and the drying conditions could possibly be indication for the degree of crosslinking.

9 References

- Alexander KA**, Cebula DJ, Goodwin JW, Ottewill RH, Parentich A: Small-angle neutron scattering studies on an ion-exchanged polystyrene latex; *Colloids & Surfaces*; 7, 223-233, **1983**
- Anderson RB**: Modification of the Brunauer, Emmett and Teller equation; *Journal of the American Chemical Society*; 68, 686-691, **1946**
- Agarval UP**, Nancy K: "Self Absorption" Phenomenon in Near-Infrared Fourier Transform Raman Spectroscopy of Cellulosic and Lignocellulosic Materials; *Applied Spectroscopy*; 59, 385-388, **2005**
- Arce A**, Fornasiero F, Rodriguez O, Radke CJ, Prausnitz JM; Sorption and transport of water vapor in thin films at 35 °C; *Physical Chemistry - Chemical Physics*; 6, 103-108, **2004**
- Atkins W**: *Physikalische Chemie*; 3. korrigierte Auflage; Wiley-VCH, Weinheim, 1005, **2001**
- Belaroui F**, Grohens Y, Boyer H, Holl Y: Depth profiling of small molecules in dry latex films by confocal Raman spectroscopy; *Polymer*; 41, 7641-7645, **2000**
- Belaroui F**, Cabane B, Dorget M, Grohens Y, Marie P, Holl Y: Small-angle neutron scattering study of particle coalescence and SDS desorption during film formation from carboxylated acrylic latices; *Journal of Colloid and Interface Science*; 262, 409-417, **2003**
- Belaroui F**, Hirn MP, Grohens Y, Marie P, Holl Y: Distribution of water-soluble and surface-active low-molecular-weight species in acrylic latex films; *Journal of Colloid and Interface Science*; 261, 336-348, **2003**
- Bird RB**, Stuart WE, Lightfoot EN, *Transport Phenomena*, New York: John Wiley & Sons, 570, **1960**
- Bonnet-Gonnet C**, Belloni L, Cabane B; Osmotic pressure of Latex Dispersions; *Langmuir*; 10, 4012-4021, **1994**
- Brown GL**: Formation of Films from Polymer Dispersions; *Journal of Polymer Science*; 22, 423-434, **1956**
- Brown JC**, Pusey PN, Goodwin JW, Ottewill RH: Light scattering study of dynamic and time-averaged correlations in dispersions of charged particles; *Journal of Physics: A: Mathematical and General Volume*; 8, 664-683, **1975**
- Brunauer S**, Deming LS, Deming WE, Teller E: On a Theory of the van der Waals Adsorption of Gases; *Journal of the American Chemical Society*, 62, 1723-1732 **1940**
- Brunauer S, Emmett PH, Teller E**: Adsorption of Gases in Multimolecular Layers; *Journal of the American Chemical Society*; 60, 309-319, **1938**
- Buscall R**, Goodwin JW, Hawkins MW, Ottewill RH: Viscoelastic Properties of Concentrated Latices. Part 1 .- Methods of Examination; *Journal of the Chemical Society, Faraday Transactions I*; 78, 2873-2887, **1982**
- Carlsson K**: The Influence of Specimen Refractive Index, Detektor Signal Integration, and non-uniform Scan Speed on the Imaging Properties in Confocal Microscopy; *Journal of Microscopy*; 163, 167-178, **1991**
- Chevalier Y**: Small-angle neutron scattering for studying latex film structure; *Trends in Polymer Science*; 4, 197-203, **1996**
- Chevalier Y**, Hidalgo M, Cavaille JY, Cabane B: Structure of Waterborne Organic Composite Coatings; *Macromolecules*; 32, 7887-7896, **1999**
- Chu F**, Guillot J, Guyot A: Rheology of Concentrated Multi-Sized Poly(St/BA/MMA) Latices; *Colloid & Polymer Science*; 276, 305-312, **1998**
- Ciampi E**, Goerke U, Keddie JL, McDonald PJ: Lateral Transport of Water during Drying of Alkyd Emulsions; *Langmuir*; 16, 1057-1065, **2000**
- Conway BE, Dobry-Duclaux A**: in: *Rheology, Theory and Application*; Academic Press, New York, vol. 3, chapt. 3, **1960**
- Cox WP, Merz EH**: Correlation of Dynamic and Steady Flow Viscosities; *Journal of Polymer Science*; 28, 619-622, **1958**
- Daniel J-C**: *Les Latex Synthetiques*; Pour la Science; Rhone-Poulenc, company-internal, **unknown year**

- De Boer J.H.:** The Dynamical Character of Adsorption, 2nd edition, Clarendon Press, Oxford, **1968**
- Denkov ND, Velev OD, Kralchevsky PA, Ivanov IB, Yoshimura H, Nagayama K:** Mechanism of Formation of Two-Dimensional Crystals from Latex Particles on Substrates; *Langmuir*; 8, 3183-3190, **1992**
- Dillon RE, Matheson LA, Bradford EB:** Sintering of Synthetic Latex Particles; *Journal of Colloid Science*; 6, 108-117, **1951**
- Dobler F, Pith T, Lambla M, Holl Y:** Coalescence Mechanisms of Polymer Colloids I. Coalescence under the Influence of Particle-Water Interfacial Tension; *Journal of Colloid and Interface Science*; 152(1), 1-11, **1992**
- Doolittle AK:** Studies in Newtonian Flow. II. The Dependence of the Viscosity of Liquids on Free-Space; *Journal of Applied Physics*; 22, 1471-1475, **1951**
- Einstein A:** Über die von der molekularkinetischen Theorie der Wärme geforderte Bewegung von in ruhenden Flüssigkeiten suspendierten Teilchen; *Annalen der Physik*; 17, 549-560, **1905**
- Einstein A:** Eine neue Bestimmung der Moleküldimensionen; *Annalen der Physik*; 19, 289-305, **1906**
- Einstein A:** Berichtigung zu meiner Arbeit: Eine neue Bestimmung der Moleküldimensionen; *Annalen der Physik*; 34, 591-593, **1911**
- Everall NJ:** Confocal Raman Microscopy: Why the Depth Resolution and Spatial Accuracy Can Be Much Worse than You Think; *Applied Spectroscopy*; 54, 1515-1520, **2000**
- Everall NJ:** Modeling and Measuring the Effect of Refraction on the Depth Resolution of Confocal Raman Microscopy; *Applied Spectroscopy*; 54, 773-782, **2000**
- Fadini A, Schnepel FM:** Schwingungsspektroskopie: Methoden, Anwendungen; Stuttgart, Thieme-Verlag, **1985**
- Flickinger GL, Dairanieh IS, Zukoski CF:** The Rheology of Aqueous Polyurethane Dispersions; *Journal of Non-Newtonian Fluid Mechanics*; 87, 283-305, **1999**
- Flickinger GL, Zukoski CF:** Rheology of aqueous polyurethane dispersions: Links between flow and particle interaction; *Journal of Rheology*; 46, 455-480, **2002**
- Flory P.J.:** Thermodynamics of High Polymer Solutions, *Journal of Chemical Physics*, 9, 660-661, **1941**
- Fujita H:** Diffusion in Polymer - Diluent Systems; *Fortschritte der Hochpolymeren Forschung*; 3, 1-47, **1961**
- Fuller E.N., Schettler P.D., Giddings J.C.:** A new method of Prediction of binary Gas-Phase Diffusion Coefficients, *Industrial & Engineering Chemistry*, 58 (5), 18-27, **1966**
- Garg R, Prud'homme R.K, Aksay I.A, Liu F, Alfano R.R:** Optical Transmission in Highly Concentrated Dispersions; *Journal of the Optical Society of America*; 15, p. 932-935, **1997**
- Gleissle W, Hochstein B:** Validity of the Cox-Merz Rule for Concentrated Suspensions; *Journal of Rheology*, 47, 897-910, **2003**
- Goodwin JW, Smith RW:** General Discussion in Faraday Discussions of the Chemical Society; 57, 119-129, **1974**
- Goodwin JW, Gregory T, Stile JA:** A Study of some of the Rheological Properties of concentrated Polystyrene Latices; *Advances in Colloid and Interface Science*, 17, 185-195, **1982**
- Greenspan, L.:** Humidity fixed points of binary saturated aqueous solutions; *Journal of Research; National Bureau of Standards*, 81A, 89-96, **1977**
- Gorce JP, Bovey D, McDonald PJ, Palasz P, Taylor D, Keddie JL:** Vertical water distribution during the drying of polymer films cast from aqueous emulsions; *The European Physical Journal E*; 8, 421-429, **2002**
- Guggenheim E.A.:** Applications of Statistical Mechanics, Clarendon Press, Oxford, **1968**
- Guttoff EB:** Modeling the Drying of Solvent Coatings on Continuous Webs; *The Society for Imaging Science and Technology*; 38, 184-192, **1994**
- Hell S, Reiner G, Cremer C, Stelzer EHK:** Aberrations in Confocal Fluorescence Microscopy induced by Mismatches in refractive index; *Journal of Microscopy*; 169, 391-405, **1993**
- Hiller S:** Monomerverteilung in Latexsystemen; PhD-thesis (University of Erlangen-Nürnberg); 7-10, **2004**

- Hiltner PA**, Krieger IM: Diffraction of Light by Ordered Suspensions; *Journal of Physical Chemistry*; 73, 2386-2389, **1969**
- Hone JHE**, Howe AM, Whitesides TH: Rheology of Polystyrene Latexes with Adsorbed and Free Gelatin; *Colloids and Surfaces A: Physicochemical Engineering Aspects*; 161, 283-306, **2000**
- Horn FM**, Richtering W: Viscosity of Bimodal Charge-Stabilized Polymer Dispersions; *Journal of Rheology*; 44, 1279-1292, **2000**
- Huggins M.L.**: Solutions of Long Chain Compounds, *Journal of Chemical Physics*, 9, 440-441, **1941**
- Joanicot M**, Wong K, Maquet J, Chevalier Y, Pichot C, Graillet C, Lindner P, Rios L, Cabane B: Ordering of latex particles during film formation; *Progress in Colloid & Polymer Science*; 81, 175-183, **1990**
- Joanicot M**, Wong K, Richard J, Maquet J, Cabane B: Ripening of Cellular Latex Films; *Macromolecules*; 26, 3168-3175, **1993**
- Keddie JL**: Film formation of Latex (Review); *Material Science Engineering Reports*; 21, 101-170, **1997**
- Kendall K**, Padgett JC: Latex coalescence; *International Journal of Adhesion and Adhesives*; 2, 149-154, **1982**
- Keunings R**, Bousfield DW: Analysis of Surface Tension Driven Levelling in Viscoelastic Films; *Journal of Non-Newtonian Fluid Mechanics*; 22, 219-233, **1987**
- Kim HB**, Winnik MA: Factors Affecting Interdiffusion Rates in Films Prepared from Latex Particles with a Surface Rich in Acid Groups and Their Salts; *Macromolecules*; 28, 2033-2041, **1995**
- Krieger IM**: Rheology of Monodisperse Latices; *Advances in Colloid and Interface Science*; 3, 111-136, **1972**
- Krieger IM**, Dougherty TJ: A Mechanism for Non-Newtonian Flow in Suspensions of Rigid Spheres; *Transactions of the Society of Rheology*; 3, 137-152, **1959**
- Lagaly G**: Colloids; in: *Ullmann's Encyclopedia of Industrial Chemistry*; Wiley-VCH; Weinheim; A7, 341-367; **2000**
- Lamprecht J**: Ein neues Filmbildungskriterium für wässrige Polymerdispersionen; *Colloid and Polymer Science*; 258, 960-967; 1980
- Laun HM**: Rheological Properties of Aqueous Polymer Dispersions; *Angewandte Makromolekulare Chemie*; 123, 335-359, **1984**
- Ma Y**, Davis HT, Scriven LE: Microstructure development in drying latex coatings; *Progress in Organic Coatings*; 52, 46-62, **2005**
- Mallegol J**, Dupont O, Keddie JL: Obtaining and Interpreting Images of Waterborne Acrylic Pressure-Sensitive Adhesives by Tapping-Mode Atomic Force Microscopy; *Langmuir*; 17, 7022-7031, **2001**
- Mason G**: Formation of Films from Latices: A Theoretical Treatment; *British Polymer Journal*; 5, 101-108, 1973
- Mayinger F**: Optical measurements, techniques and applications, Springer-Verlag, **1994**
- Meeten G**, North AN: Refractive Index Measurements of Absorbing and Turbid Fluids by Reflection near the Critical Angle; *Measurements Science Technology*; 6, 214-221, **1995**
- Mewis J**, Frith WJ, Strivens TA, Russel WB: The Rheology of Suspensions Containing Polymerically Stabilized Particles; *AIChE Journal*; 35, 415-422, **1989**
- Mie, G**: Beiträge zur Optik trüber Medien, speziell kolloidaler Metallösungen; *Annalen der Physik*; 25(3), p 377-445, **1908**
- Milkie T**, Lok K, Croucher MD: Viscoelastic Properties of Sterically Stabilized Nonaqueous Dispersions; *Colloid & Polymer Science*; 260, 531-535, **1982**
- Mohammadi, M**: Colloidal Refractometry: Meaning and Measurement of Refractive Index for Dispersions; the Science that Time Forgot; *Advances in Colloid and Interface Science*; 62, 17-29, **1995**
- Molenaar F**, Svanholm T, Toussaint A: Rheological Behaviour of Latexes in-can during Film Drying; *Progress in Organic Coatings*; 30, 141-158, **1997**
- Mooney M**: The Viscosity of a Concentrated Suspension of Spherical Particles; *Journal of Colloid Science*; 6, 162-170, **1951**

- Moritz H:** Messungen des Konzentrationsfeldes verdunstender binärer Mikropartikel mittels linearer Raman-Spektroskopie, Fortschritt-Berichte VDI, Düsseldorf, **1999**
- Mulder M.H.V.:** Pervaporation Membrane Separation Processes, Elsevier Science Publishers, Amsterdam, 4, 225-252, **1991**
- Napper DH:** Polymeric Stabilization of Colloidal Dispersions; 1st edition, Academic Press, London, **1983**
- Nashima T, Furusawa K:** The Rheological Behaviour of a Latex Dispersion including a non-ionic Polymer; Colloids and Surfaces A; 55, 149-161, **1991**
- Niu M, Urban MW:** Recent Advances in Stratification and Film Formation of Latex Films; Attenuated Total Reflection and Step-Scan Photoacoustic FTIR Spectroscopic Studies; Journal of Applied Polymer Science; 70, 1321-1348, **1998**
- Orchard SE:** On Surface Leveling in Viscous Liquids and Gels; Applied Scientific Research, Section A; 11, 451-464, **1962**
- Overbeek JThG:** Recent Developments in the Understanding of Colloidal Stability; Journal of Colloid and Interface Science; 58, 408-421, **1977**
- Overbeek JThG:** The Rule of Schulze and Hardy; Pure Applied Chemistry; 52, 1151-1161, **1980**
- Patton TC:** A New Method for the Viscosity Measurement of Paint in the Settling, Sagging, Leveling and Penetration Shear Rate Range of 0.001 to 1. Reciprocal Seconds Using a Cone/Spring Relaxation Technique; Journal of Paint Technology; 38, 656, **1966**
- Pecul M, Rizzo A:** Linear Response Coupled Cluster Calculation of Raman Scattering Cross Sections; Journal of Chemical Physics; 116, 1259-1268, **2002**
- Pishvaei M, Graillat C, McKenna TF, Cassagnau P:** Rheological Behaviour of Polystyrene Latex near the Maximum Packing Fraction of Particles; Polymer; 46, 1235-1244, **2005**
- Quach A:** Polymer Coatings. Physics and Mechanics of Levelling; Industrial & Engineering Chemistry, Product Research and Development; 12, 110-116, **1973**
- Quemada D:** An Overview of Recent Results on Rheology of Concentrated Colloidal Dispersions; Progress in Colloid and Polymer Science; 79, 112-119, **1989**
- Raynaud L, Ernst B, Verge C, Mewis J:** Rheology of Aqueous Latices. with Adsorbed Stabilizer Layers; Journal of Colloid and Interface Science; 181, 11-19, **1996**
- Richard J, Maquet J:** Dynamic micromechanical investigations into particle / particle interfaces in latex films; Polymer; 33(19), 4164-4173, **1992**
- Riebel U:** An Estimate of Some Statistical Properties of Extinction Signals in Dilute and Concentrated Suspensions of Monosized Spherical Particles; Particle & Particle Systems Characterization; 8, 95-99, **1991**
- Rottstegge J, Traub B, Wilhelm M, Landfester K, Heldmann C, Spiess HW:** Investigations on the Film-Formation Process of Latex Dispersions by Solid-State NMR Spectroscopy; Macromolecular Chemistry and Physics; 204, 787-802, **2003**
- Routh A, Russel W:** Horizontal drying fronts during solvent evaporation from latex films; AIChE Journal; 44 (9), 2088-2098, **1998**
- Routh AF, Russel WB:** A Process Model for Latex Film Formation: Limiting Regimes for Individual Driving Forces; Langmuir; 15, 7762-7773, **1999**
- Routh A, Russel W:** Process Model for latex film formation: optical clarity fronts; Journal of Coatings Technology; 73(916), 41-48, **2001**
- Salamanca JM, Ciampi E, Faux DA, Glover PM, McDonald PJ, Routh AF, Peters ACIA, Satguru R, Keddie JL:** Lateral drying in thick films of waterborne colloidal particles; Langmuir; 17, 3202-3207, **2001**
- Schabel W, Scharfer P, Müller M, Ludwig I, Kind M:** Messung und Simulation von Konzentrationsprofilen bei der Trocknung binärer Polymerlösungen; Chemie Ingenieur Technik; 75, 1336-1344, **2003**
- Schabel W:** Trocknung von Polymerfilmen – Messung von Konzentrationsprofilen mit der Inversen-Mikro-Raman-Spektroskopie; PhD Thesis; Shaker Verlag; **2004**

- Schabel W**, Scharfer P, Müller M, Ludwig I, Kind M: Concentration Profile Measurements in Polymeric Coatings during Drying by Means of Inverse-Micro-Raman-Spectroscopy (IMRS); Raman Update Autumn 2005: Horiba Jobin Yvon; 3, 1-3, **2005**
- Schabel W**: Inverse Mikro Raman Spektroskopie - eine neue Messmethode zur Untersuchung lokaler Stofftransportvorgänge in dünnen Filmen, Folien und Membranen; Chemie Ingenieur Technik; 77, 1915-1926, **2005**
- Scharfer P**: algorithm, realized in VBA; personal communication, **2006**
- Schrader B**: Infrared and Raman Spectroscopy: Methods and Applications; VCH, Weinheim, **1995**
- Schlünder E.U.**: Einführung in die Stoffübertragung, Braunschweig: Friedrich Vieweg & Sohn, 49-58, **1984**
- Schmidt W**: Optische Spektroskopie – Eine Einführung; 2. Auflage, Wiley-VCH, Kapitel 7; **1994**
- Sheetz DP**: Formation of Films by Drying of Latex; Journal of Applied Polymer Science; 9, 3759-3773, **1965**
- Smith NDP**, Orchard SE, Rhind-Tutt AJ: The Physics of Brushmarks; Journal of the Oil and Colour Chemists Association, 44, 618-633, **1961**
- Steward PA, Hearn J, Wilkinson MC**: An overview of polymer latex film formation and properties; Advances in Colloid and Interface Science; 86, 195-267, **2000**
- Tadros ThF**, Zsednai A: A Collection of Invited Papers Dedicated to the Memory of Professor F. Szántó (1925-1989); Colloids and Surfaces A: Physicochemical Engineering Aspects; 49, 103-119, **1990**
- Theodoor J, Overbeek JThG**: Strong and Weak Points in the Interpretation of Colloid Stability; Advances in Colloid and Interface Science, 16, 17-30, **1982**
- Tirumkudulu MS**, Russel W: Role of capillary stresses in film formation; Langmuir; 20, 2947-2961, **2004**
- Toussaint A**, De Wilde M: A Comprehensive Model of Sintering and Coalescence of Unpigmented Latexes; Progress in Organic Coatings; 30, 113-126, **1997**
- Van den Brink M**, Pepers M, van Herk AM: Raman Spectroscopy of Polymer Latexes; Journal of Raman Spectroscopy; 33, 264-272, **2002**
- van Tent A, te Nijenhuis K**: The Film Formation of Polymer Particles in Drying Thin Films of Aqueous Acrylic Latices II. Coalescence, Studied with Transmission Spectrophotometry; Journal of Colloid and Interface Science; 232, 350-363, **2000**
- VDI-Wärmeatlas**: Wärmeübertragung bei der Strömung längs einer ebenen Wand, 10th edition, Berlin: Springer-Verlag, Gd1, **2005**
- Verwey EJW, Overbeek JThG**: Theory of the Stability of Lyophobic Colloids; Elsevier; Amsterdam; **1948**
- Visschers M**, Laven J, German AL: Current understanding of the deformation of latex particles during film formation; Progress in Organic Coatings; 30, 39-49, **1997**
- Visser J**: On the Hamaker Constant: A Comparison between Hamaker Constants and Lifshitz – van der Waals Constants; Advances in Colloid & Interface Science; 3, 331-363, **1972**.
- Visser TD**, Oud JL, Brankenhoff GJ: Refractive Index and Axial Distance Measurements in 3-D Microscopy; Optik, 90, 17-19, **1992**
- Von Smoluchowski M**: Theoretical observations on the viscosity of colloides; Kolloid-Zeitschrift; 18, 190-195, **1916**
- Vortisch H**: Observation of phase transitions in single levitated sulfuric acid solution droplets using Raman spectroscopy and elastic light scattering; Dissertation; chapter 2, **2002**
- Vrentas JS**, Duda JL: Diffusion in Polymer-Solvent Systems: I. Re-examination of the Free-Volume Theory; Journal of Polymer Science; Polymer Physics Edition; 15, 403-416, **1977**
- Waring RK**: An Analytical Study of Leveling; Rheology; 2, 307-314, **1931**
- Weitz DA**, Pine DJ, Pusey PN, Tough RJA: Nondiffusive Brownian Motion Studied by Diffusing-Wave Spectroscopy; Physical Review Letters; 63, 1747-1750, **1989**
- Wilson SK**: The Leveling of Paint Films; Journal of Applied Mathematics; 50, 149-166, **1993**

- Winnik MA**: Latex film formation; Current Opinion in Colloid & Interface Science; 192-199, **1997**
- Winter HH**, Mours M: Rheology of Polymers near Liquid-Solid Transitions; Advances in Polymer Science; 134, 165-234, **1997**
- Woodcock LV**: Developments in the Non-Newtonian Rheology of Glass Forming Systems; Lecture Notes in Physics; 277;113-124, **1985**
- Zhang J.T., Wang B.X.**: Study on the interfacial evaporation of aqueous solution of SDS surfactant self-assembly monolayer; Journal of Heat and Mass Transfer; 46, 5059 – 5064; **2003**
- Zhao CL**, Holl Y, Pith T, Lambla M: FTIR-ATR spectroscopic determination of the distribution of surfactants in latex films; Colloid and Polymer Science; 265, 823-829, **1987**
- Zhu JX**, Durian DJ, Müller J, Weitz DA, Pine DJ: Scaling of Transient Hydrodynamic Interactions in Concentrated Suspensions; Physical Review Letters; 68, 2559-2562, **1992**

9.1 Publications in Connection with this Work

- Schabel W**, Scharfer P, Müller M, Ludwig I, Kind M: Messung und Simulation von Konzentrationsprofilen bei der Trocknung binärer Polymerlösungen; Chemie Ingenieur Technik; 75(9), 1336-1344, **2003**
- Schabel W**, Ludwig I, Kind M: Measurements of Concentration Profiles in Polymeric Solvent Coatings by Means of an Inverse-Confocal-Micro-Raman-Spectrometer – Initial results; Drying Technology; 22 (1&2), 285-294, **2004**
- Ludwig I**, Schabel W Castaing J-C, Ferlin P, Kind. M: Drying of Industrial Waterborne Latices; AIChE Journal; 53(3), 549-560, **2007**
- Ludwig I**, Schabel W, Ferlin P, Castaing J-C and Kind M: Drying, Film Formation and Open Time of Aqueous Polymer Dispersions; European Physical Journal; **accepted**

9.2 Proceedings

- Schabel W**, Ludwig I, Kind M: Measurements of concentration profiles in polymeric solvent coatings by means of confocal-micro-Raman-spectroscopy; Proceedings of the 13th International Drying Symposium (IDS), Beijing, China; vol. B, 1161/1168, **2002**
- Ludwig I**, Castaing J-C, Ferlin P, Kind M: About the Film Formation from Industrial Waterborne Latices; Proceedings of the AFSIA conference, Paris, France; 114/115, **2005**
- Ludwig I**, Schabel W, Castaing J-C, Ferlin P, Kind M: Drying of aqueous latex dispersions, investigated by Inverse-Micro-Raman-Spectroscopy; Bayreuth Polymer Symposium (BPS), poster PII 03, **2005**
- Ludwig I**, Schabel W, Castaing J-C, Ferlin P, Kind M: Film Formation from Industrial Waterborne Latices; Proceedings of the 6th European Coating Symposium (ECS), Bradford, UK; **2005**
- Ludwig I**, Schabel W, Castaing J-C, Ferlin P, Kind M: Film Formation from Industrial Waterborne Latices; Proceedings of the 15th International Drying Symposium (IDS), Budapest, Hungary; vol. C, 1825/1830, **2006**
- Ludwig I**, Schabel W, Castaing J-C, Ferlin P, Kind M: Investigation of inhomogeneous drying of aqueous latex dispersions; Proceedings of the 13th ISCST Symposium (International Society for Coating Science & Technology), Denver, USA; **2006**
- Ludwig I**, Schabel W, Castaing J-C, Ferlin P, Kind M: Untersuchungen zur inhomogenen Trocknung wässriger Latex-Dispersionen; Chemie Ingenieur Technik; 78(9), 1355, **2006**
- Olier P**, Ludwig I, Kind M, Schabel W, Meeker S: Investigation of Drying of 2K Waterborne Polyurethane Composition by Inverse Micro Raman Spectroscopy; Proceedings of the European Coatings Show 2007, Nuremberg, **2007**
- Ludwig I**, Schabel W, Castaing J-C, Ferlin P, Kind M: Drying, Film Formation and Open Time of Aqueous Polymer Dispersions; Proceedings of the 7th European Coating Symposium (ECS), Paris, France; **2007**
- Ludwig I**, Kind M, Schabel W, Meeker S, Olier P: Monitoring of film formation and curing of waterborne 2K polyurethane coatings using Inverse-Micro-Raman-Spectroscopy; Proceedings of the European Coatings Conference (ECC), Berlin, **2007**

9.3 Student's Theses

Demarez P: Beeinflussung der Open Time bei Wasserbasislacken; Diploma Thesis, University of Karlsruhe (TH), **2005**

Chan J: Untersuchungen zum Einfluss der Viskosität auf die Open Time wässriger Latex-Dispersionen; Diploma Thesis, University of Karlsruhe (TH), **2006**

Gedikli Ö: Investigation of the inhomogeneous drying of latex films; Seminar Thesis, University of Karlsruhe (TH), **2006**

Appendix

Appendix I Emulsion Polymerization

The latex particles used in this work are either copolymers of different acrylic esters or co-polymers of acrylic esters and styrene. They are made by so-called emulsion polymerization.

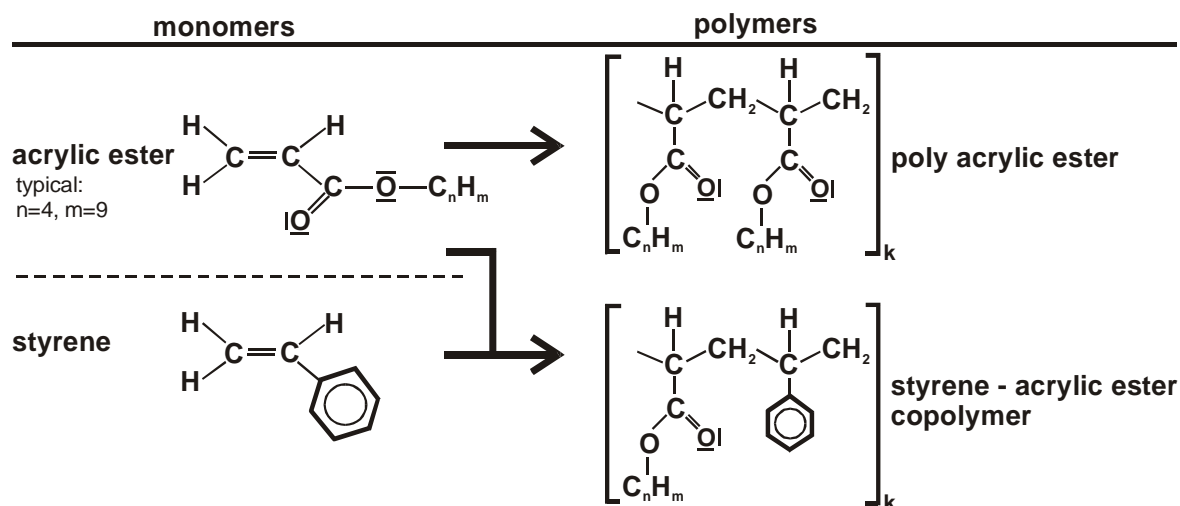


Figure AI- 1: Copolymers made from acrylic esters and styrene

The general process is a radical polymerization of monomers in the aqueous medium. The reaction starter is a water-soluble substance, e.g. a persulfate. Surface-active material is added to stabilize the particles in the aqueous phase (= serum). Depending on the solubility of the respective monomer in water, two different mechanisms of emulsion polymerization are distinguished (Hiller (2004); Daniel (unknown)):

- (I) Monomers that are hardly soluble in water, like e.g. styrene, are dissolved to only a low extent, whereas the largest part of the monomer is dispersed in water and is stabilized by surfactants (Figure AI- 2). The radical polymerization reaction starts outside the monomer droplets, where the starter radical forms a short chain by reaction with the dissolved monomer. Since the new chain is less soluble than the single monomer, it diffuses into the stabilized monomer droplets where the reaction continues until a new radical enters and the reaction is stopped by recombination. In each monomer droplet, there is only one growing chain at a time.
- (II) Due to their functional groups, monomers like e.g. acrylic esters are more hydrophilic and therefore more soluble in water (Figure AI- 3). Again, polymerization starts in the aqueous phase. This time, the radical reaction continues until the polymer chain has reached a critical chain length. At this moment, the chain is surrounded by surfactant molecules and forms the final latex particle. Often, a certain amount of ionic co-monomer, e.g. pure acrylic acid, is present to further improve the water-solubility of the latex molecules.

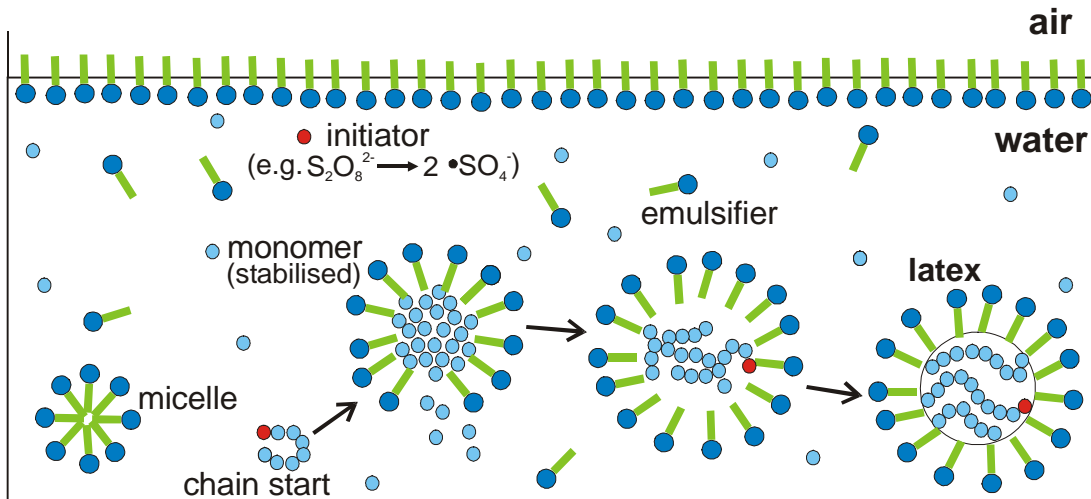


Figure AI- 2: Emulsion polymerization of a hardly soluble monomer, e.g. styrene

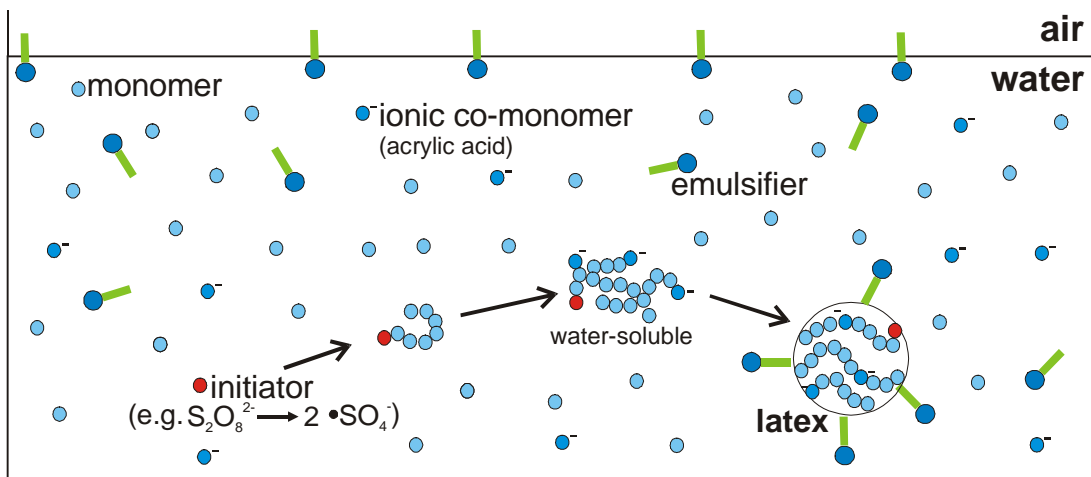


Figure AI- 3: Emulsion polymerization of a well-soluble monomer, e.g. acrylic monomers

A narrow particle size distribution and other desired particle characteristics can be obtained from a variation of the reaction parameters like reaction temperature, concentration of monomer, starter radicals, surfactants and from a variation of the serum characteristics like pH or ionic strength. After cleaning and reconditioning, the latex dispersion is ready to use in many applications.

Appendix II Dispersion Stabilization

Polymer particles in water are two-phase systems which are thermodynamically unstable (*Napper* (1983)). During long-term storage, thermodynamics and gravity would cause unstabilized particles to undergo agglomeration and sedimentation.

In aqueous latex dispersions, particle stabilization is often achieved by a combination of (I) different kinds of surfactants and (II) co-monomers with functional groups (COOH-, SO₄H-, SO₃H-...) incorporated into the latex particle surface. Also beneficial for the dispersion stabilization is a similar density of the particles and the surrounding medium.

Widely-used are anionic surfactants which are salts of organic molecules like e.g. fatty acids, consisting of an anionic organic ion and its counter-ion. In the aqueous medium, the surfactant dissociates and the charged part of the organic molecule shows an affinity to the polar water molecules, whereas the unpolar carbon backbone prefers the less polar particle surface. The arrangement of the surfactant molecules around the particles is responsible for the dispersion stabilization. The use of long-chained non-ionic surfactants, adsorbed at the particle surface, generates steric repulsion of the latex particles and hinders agglomeration. Another benefit of the high level of surfactants next to dispersion stabilization is the reduction of the high surface tension of water which considerably improves the wetting properties of aqueous coating formulations. A disadvantage of the high surfactant level is that during film formation the surfactant material, located at the particle surface, will form membranes in between the deformed latex particles and will therefore delay or even hinder polymer interdiffusion. As long as polymer interdiffusion is incomplete, the dry polymer film will be susceptible for water permeation.

Surface functionalities can be produced by small amounts of co-monomers with functional groups, e.g. pure acrylic acid. In the case of acrylic acid, the carboxylic functional groups located at the latex particle surface create a negative, pH-dependent surface charge.

Ionic surfactants and surface functionalities at the particle surface create an electrical double layer around the latex particles, causing particle repulsion. In this case, the particle repulsion depends on the pH and ionic strength of the serum, whereas in the case of steric stabilization (by non-ionic surfactants) it is independent of the pH and ionic strength.

Electrostatic stabilization is caused by the interparticular repulsion of the electrical double layers around the particles which works against the long-range attractive *van-der-Waals* forces. Based on a summation of all attractive and repulsive forces, the DLVO-theory (*Verwey and Overbeek* (1948); *Overbeek* (1977); *Theodoor and Overbeek* (1982)) is commonly used to describe the interaction between the polymer particles that are dispersed in the aqueous medium. The stabilizing effect can be

illustrated by a potential diagram (e.g. Figure AII- 1), in which the summation of all repulsive and attractive potentials yields the total potential. The total potential curve shows a maximum which explains why particle agglomeration is hindered. Once the particles are forced close enough to reach the primary potential minimum, agglomeration will take place and, - depending on the height of the potential barrier -, will be irreversible.

The repulsive potential $V_R(r)$ at the distance r from the particle surface depends on the thickness of the diffuse electrical double layer, described by the characteristic *Debye* length κ^{-1} :

$$V_R(r) = V_0 \cdot e^{-\kappa \cdot r} \quad \text{Equ. AII- 1}$$

with:

V_0	= surface potential
r	= distance from particle surface

The *Debye* length is influenced by the relative dielectric constant ε , ionic strength I and temperature T of the surrounding medium. From the *Debye-Hückel* theory, κ^{-1} can be calculated by the following equation (*Atkins* (2001)):

$$\frac{1}{\kappa} = \sqrt{\frac{\varepsilon \cdot \varepsilon_0 \cdot R \cdot T}{F^2 \cdot \sum_i c_i \cdot z_i^2}} \quad \text{Equ. AII- 2}$$

with:

ε	= relative dielectric constant
ε_0	= electrical field constant
R	= universal gas constant
T	= temperature
F	= <i>Farady</i> constant
c_i	= concentration of ions i
z_i	= charge number of ions i

The attractive *van-der-Waals* potential V_A is nearly independent of the salt concentration. A good approximation for spherical particles is given by *Overbeek* (1980):

$$V_A = -\frac{A_H}{12} \left(\frac{L}{H} + 2 \ln \frac{H}{L} \right) \quad \text{where } L = a + 0.75 \cdot H \quad \text{Equ. AII- 3}$$

with:

A_H	= <i>Hamaker</i> constant
H	= nearest distance between two spheres
a	= particle radius

The *Hamaker* constant A_H depends on the polarizability of the particle surface, the concentration of the particles and the first ionization potential of the polymer particles (*Visser* (1972)).

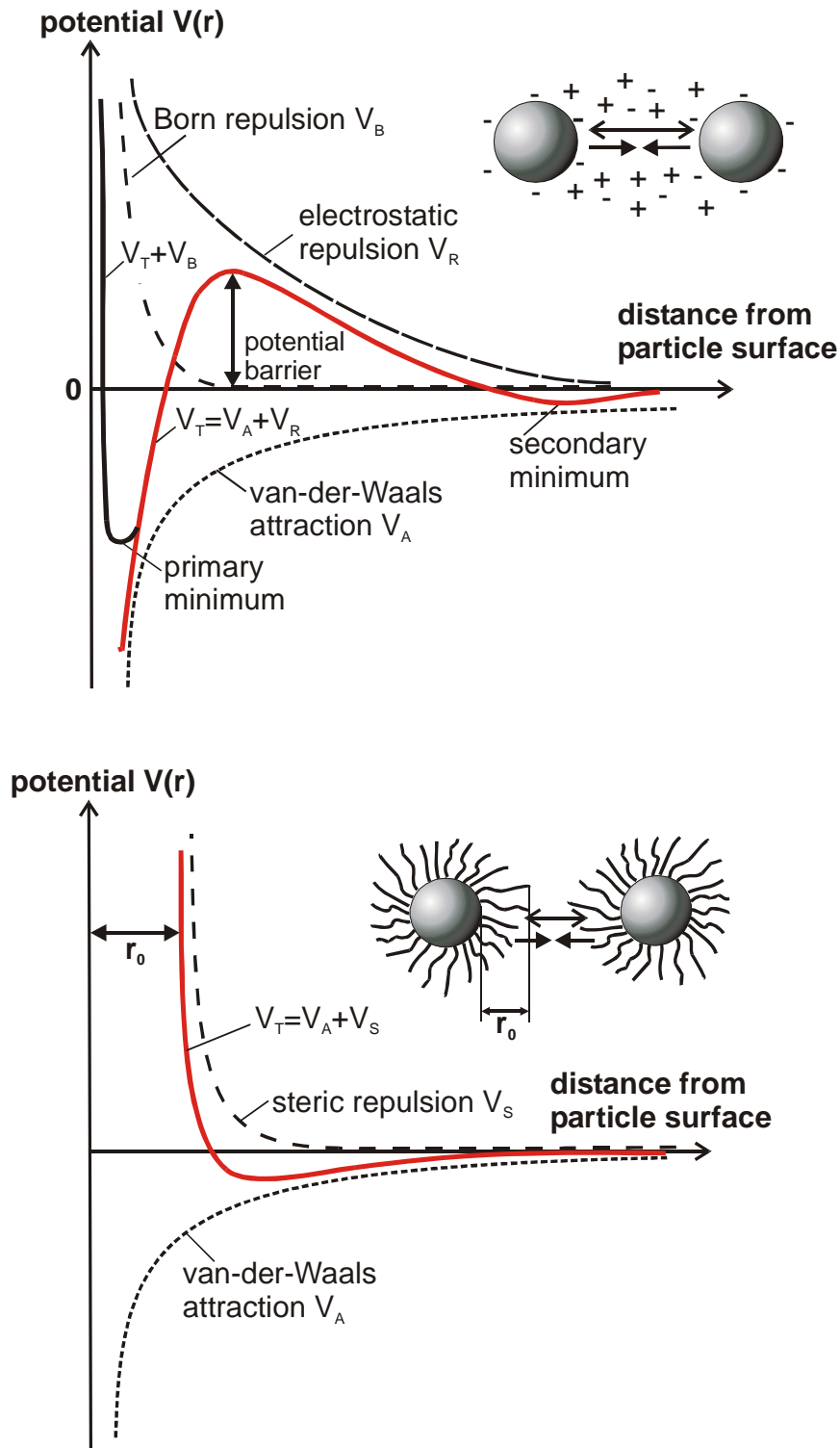


Figure AII- 1: Top: potential diagram of electrostatic stabilization. The potential barrier prevents agglomeration; bottom: potential diagram of steric stabilization

In the case of steric stabilization, the latex particles are kept apart by means of long-chained macromolecules adsorbed at the particle surface. The concentration of surfactant in the medium is very important for their stabilizing effect. Below a threshold concentration of surfactant, the stabilizer can adhere to multiple particles and cause a bridging effect that makes the particles flocculate (= sensibilization) (Lagaly (2000)). Above the threshold concentration, the mutual approach of the

particles is hindered by a reduction of entropy in the system caused by a compression or interpenetration of the adsorbed and free polymer chains. In addition, the local increase in concentration of the organic material between the particles causes an osmotic effect and exerts a repulsive force between the particles (Napper (1983)).

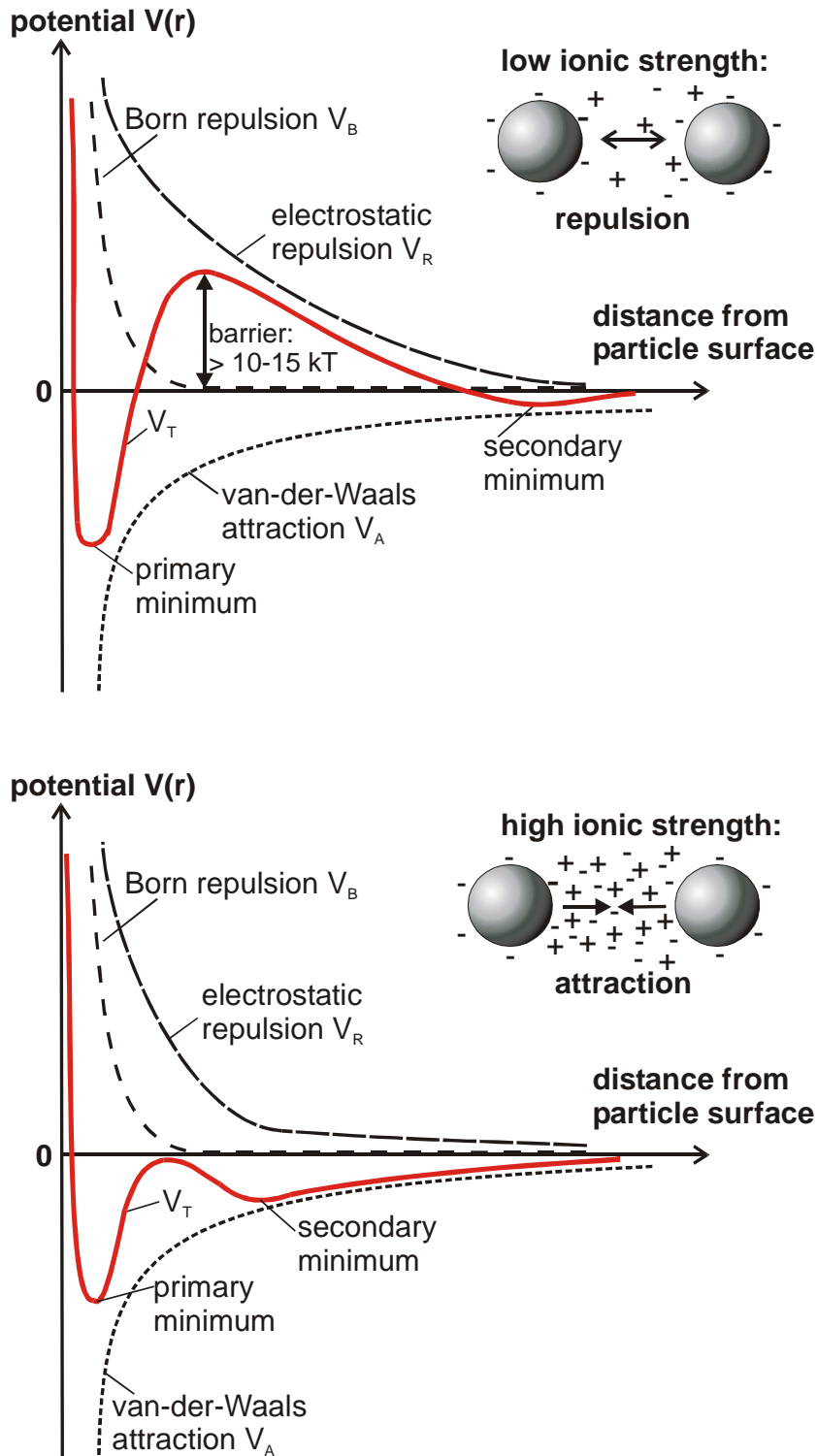


Figure AII- 2: Potential curves of latex dispersions with low (top) and high (bottom) ionic strength of the serum

Steric interactions have a shorter effective range than electrostatic interactions and are therefore often referred to as “hard” interactions. Depletion stabilization differs from

steric stabilization in that stability is imparted not by adsorbed macromolecules, but by macromolecules that are free in solution (Napper (1983)).

The equilibrium distance between the colloidal particles is influenced by (I) the type of surfactant used, affecting the surface potential V_0 and (II) the ionic strength I of the salt that is dissolved in the surrounding medium. A change of the ionic strength alters the repulsive component of the potential curve, but leaves the attractive component unaffected. High ionic strength of the medium reduces the *Debye* length. As a consequence, the range of electrostatic repulsion is reduced, leading to a more compact potential curve (Figure AII- 2). As soon as the potential barrier sinks below a value of about $10-15 kT$ ($k = \text{Boltzmann constant}$), *Brownian* motion of the latex particles allows spontaneous irreversible particle agglomeration (Verwey, Overbeek (1948)).

The incorporation of pH-dependent ionizable groups into the polymer particle surface (e.g. acid groups) causes so-called electrosteric stabilization: Above a certain pH, the surface functional groups will dissociate and by this, the surface layer of the polymer particles will become more hydrophilic. This will lead to an increase in thickness of the outer particle layer due to the interaction of the functional groups with the water molecules.

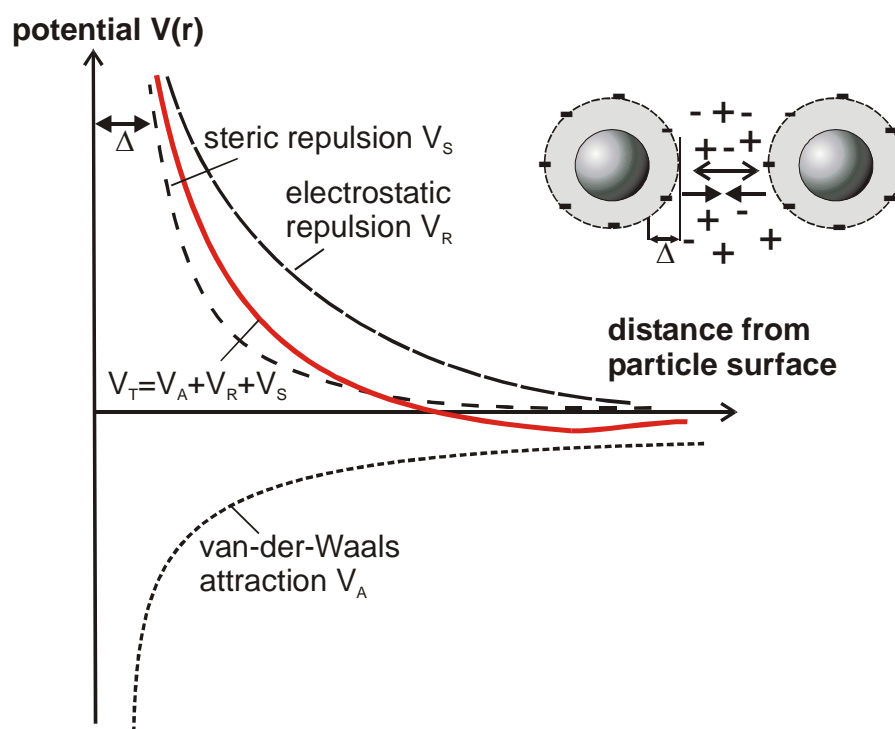


Figure AII- 3 Potential curve of electrosteric stabilization. The potential barrier prevents agglomeration

Appendix III Latex Dispersion Characteristics

Below are some dispersion characteristics of the different formulations under investigation. Characteristic parameters like the polymer particle size, glass transition temperature T_g , the polymer volume fraction and the average particle distance in the original dispersion are investigated. Finally, the surface tension of the dispersion and the contact angle of the dispersion on the substrate are measured. The tables at the end of this chapter summarize all important dispersion parameters.

1) Particle Size

The size of the latex particles is in the nanometer to micrometer range and can be obtained from photon correlation spectroscopy (PCS): Using PCS, the interaction of an incident laser light with the particles in the dispersion causes light fluctuations which are the result of the diffusion process of the latex particles (*Brownian* motion). The frequency shift of the incident laser light depends on the particle size. This is used to obtain the particle size from a fit of the fourier-transformed frequency spectrum.

In the case of pH-dependent ionizable groups at the particle surface, the latex particle size is a function of pH. Typical ionizable groups are acid groups COOH, sulfate groups SO₄H and sulfonate groups SO₃H. Above a pH of 4 the acid groups start to dissociate, which makes the particle surface more hydrophilic. As a consequence, the outer particle layer swells due to water hydration, which leads to an increase in the particle size. Figure AIII- 1 shows the pH-dependence of the particles size obtained from PCS measurements.

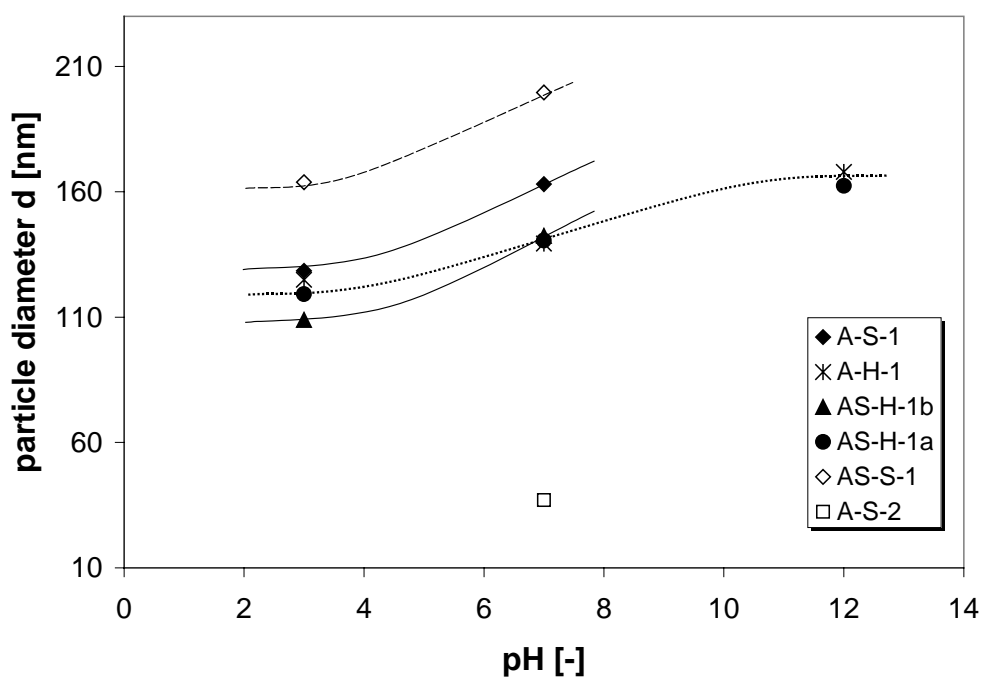


Figure AIII- 1: pH-dependence of the particle size for the different latex dispersions under investigation

The experimental data show considerable changes of the particle size, but differences in the degree of change of the particles size with pH, resulting from different amounts of ionizable groups, can hardly be observed. Based on what is described in Appendix II, the strong pH-dependence of the particle diameter is proof for a strong electrosteric stabilization of all investigated latex dispersions.

2) Glass Transition Temperature T_g

The glass transition temperature of a polymer is the temperature at which its behaviour changes from primarily viscous to primarily elastic. Normally, the T_g is obtained from differential scanning calorimetry (DSC).

Either (I) water at the functionalized particle surface or (II) organic solvents that diffuse into the polymer particles can plasticize the latices, leading to a lower glass transition temperature. In drying technology, the lower glass transition temperature of the wet latex caused by plasticization is called minimum film formation temperature T_{mff} . It is defined by the temperature above which film drying leads to the formation of a transparent, clear and non-porous film. The glass transition temperature T_g and the minimum film formation temperature T_{mff} for the different latices are obtained from the dispersion's chemical data sheet, as provided by RHODIA.

The data show, that water is a plasticizer for the dispersions under investigation. Depending on the hydrophilic character of the polymer, their minimum film formation temperature lays about 10-20 °C below the dry polymer's glass transition temperature.

Knowing the T_g of the dry latex film, the *Gordon-Taylor* equation allows the calculation of the mass fractions of the different polymer compounds, e.g. for a binary formulation it is:

$$\frac{1}{T_g} = \frac{x_1}{T_{g1}} + \frac{(1-x_1)}{T_{g2}} \quad \text{Equ. AIII- 1}$$

3) Particle Volume Fraction ϕ

Rheological properties are normally expressed as a function of the particle volume fraction ϕ . It refers to the occupancy of space by the particles. Mainly the presence of electrical charges and surfactants at the particle surface, but also the characteristics of the polymer and the medium, expressed by the glass transition temperature and the pH, have a strong influence on the perceived particle volume fraction. For example, latex particles may be plasticized by water or may be covered by a layer of surfactant.

One way to measure the particle volume fraction of dispersions in their original state may be by refractive index measurements: *Mohammadi* (1995) describes the use of light scattering to measure the refractive index n of latex dispersions in their native, undiluted state. The method allows the investigation of processes like particle size changes, flocculation, structure formation and concentration changes. *Meeten et al.* (1995) found semi-empirically that the following volume additive

expression is valid for latices in the size range of $100 - 500 \mu m$ and up to a concentration of $50 \text{ vol}\%$.

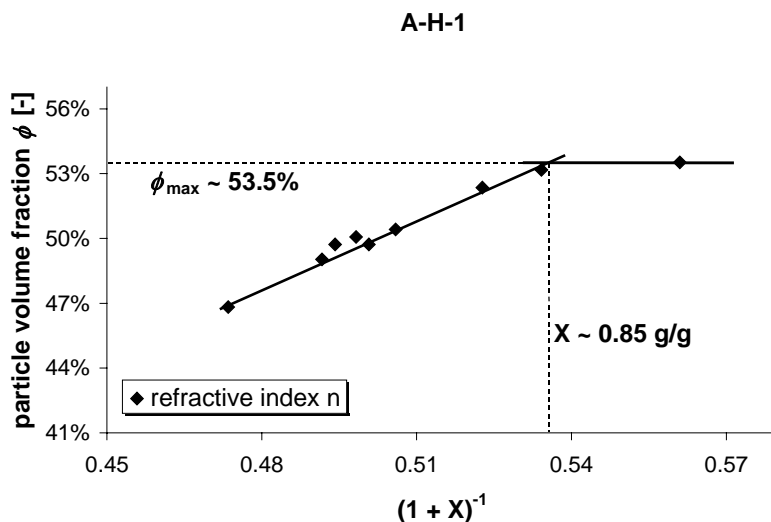
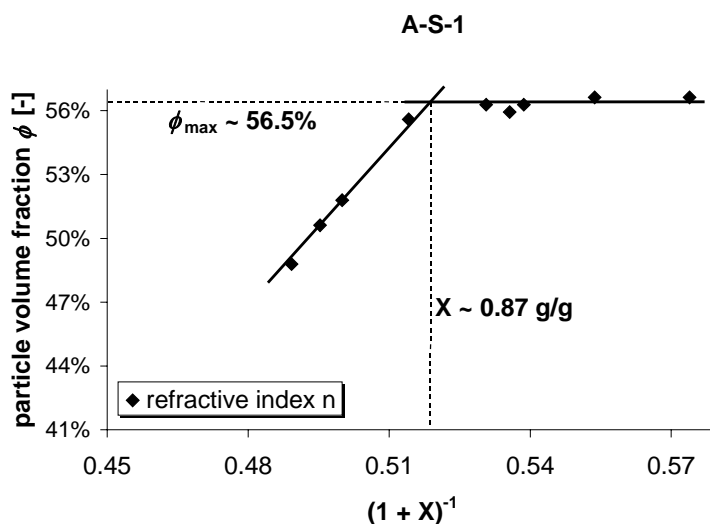
$$n_{\text{dispersion}} = n_{\text{water}} + \phi(n_{\text{polymer}} - n_{\text{water}}) \quad \text{Equ. AIII- 2}$$

with:

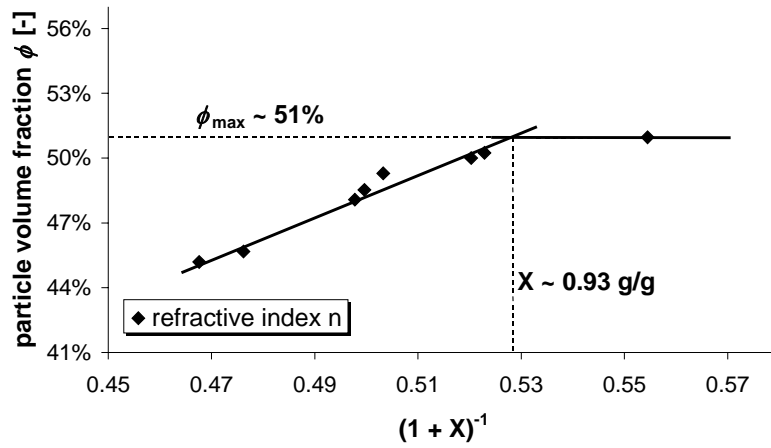
$$n_i = \text{refractive index (i = dispersion, water, polymer)}$$

Here, the refractive index n is measured with an automatic refractometer (type: Abbemat), having a light source of $\lambda = 589 \text{ nm}$ and working on the total-internal-reflection principle. Light scattering at the particle surface should give the volume fraction ϕ of the particles in their original, plasticized state. Interparticle repulsion by electrostatic forces is not considered by this method, which is why the measured maximum particle volume fractions are low.

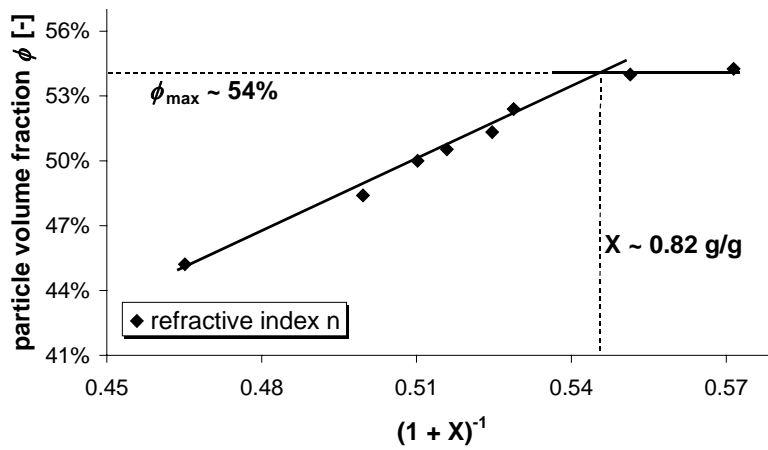
The following figures show the particle volume fraction as a function of the water content X , obtained from refractive index measurements. For a gel (AS-H-1a), having no separated particles, a particle volume fraction cannot be calculated.



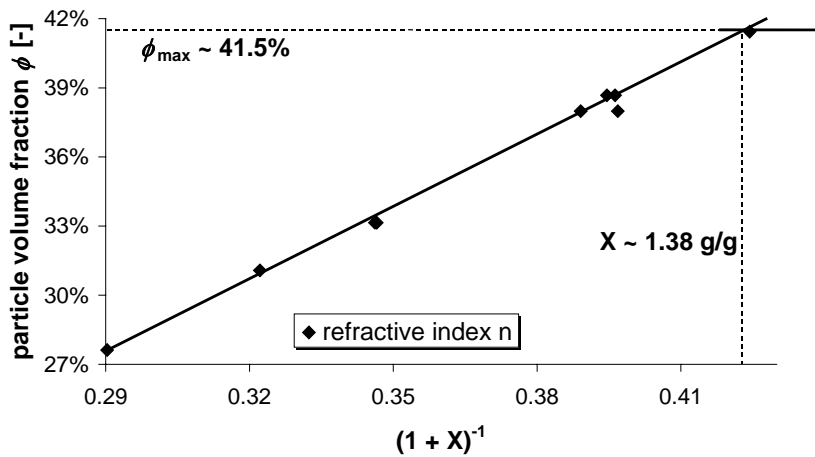
AS-H-1b



AS-S-1



AS-S-2



4) Average Particle Separation in the Original Dispersion

With the help of the maximum particle volume fraction ϕ_{\max} and the latex particle diameter d obtained from light scattering experiments, an average interparticle distance \bar{h} can be calculated by Equ. 3-13. In Equ. 3-13, the mean particle distance is calculated from geometrical considerations, assuming hard particle behaviour and incorporating the measured particle volume fractions $\phi_{\text{disp.}}$ and ϕ_{\max} .

As mentioned before, this doesn't take into account the repulsive electrostatic forces between the particles. They can be accounted for by an effective particle volume fraction ϕ_{eff} , calculated from Equ. 3-16 and an additional repulsive layer Δ obtained from Equ. 3-15.

Table AIII-1 gives very short interparticle distances of a few nanometers in all original dispersions. This leads to the conclusion, that there is a high degree of particle ordering already in the original dispersion and that single particles are not free to move in the dispersion without influencing neighbouring particles.

<i>dispersion name</i>	<i>d [nm]</i> (particle diameter)	$\phi_{\text{disp.}}$ [%] (from refr. Index)	ϕ_{\max} [%] (from refr. Index)	ϕ_{eff} [%]* (Equ. 3-16)	Δ [nm] (Equ. 3-15)	\bar{h} [nm] (Equ. 3-13)
A-S-1	163	48.8	56.5	54.4	3.0	8.2
A-H-1	139	49.0	53.5	57.0	3.6	4.6
AS-H-1a	140	-	-	-	-	contact
AS-H-1b	142	48.3	51.0	59.6	5.2	1.6
AS-S-1	199	45.2	54.0	52.7	5.2	12.2
A-S-2	37	27.6	41.5	41.9	2.8	5.4

* with $\phi_{\max,hs} = 63\%$

Table AIII- 1: Average interparticle distance in the original dispersion

5) Surface Tension of the Dispersion

In aqueous latex dispersions, the high amount of surface-active species adsorbed at the particle surface and present in the aqueous medium is responsible for a considerably lower surface tension and improved wetting properties compared with pure water.

The surface tension of a latex dispersion depends on the kind and amount of surfactant present. An increase of the amount of surfactant will decrease the surface tension, but only until all possible sites at the interfaces are occupied. Then, a further increase of the level of surfactant will lead to the formation of micelles in the dispersion serum. The moment of micelle formation is marked by the so-called critical micelle concentration c_{cmc} . The c_{cmc} is illustrated in Figure AIII- 2 for a model system of water and sodium-dodecyl-sulfate (SDS).

The surface tension of all dispersions is investigated by the *Du-Noüy* ring method, where a platinum ring is submerged into the dispersion and the force that is necessary

to pull out the ring is measured. All dispersions show a surface tension that is considerably lower than the one of pure water. The surface tension of the high surfactant formulations A-H-1, AS-S-1 and A-S-2 is close to that of the aqueous dispersion of SDS at its critical micelle concentration c_{cmc} (see Figure AIII- 2 bottom). This indicates, that the level of surfactant in the latex dispersions is very high and close to, or even above, the critical micelle concentration. Therefore, it is expected that during drying and film formation the surface tension is not subject to changes.

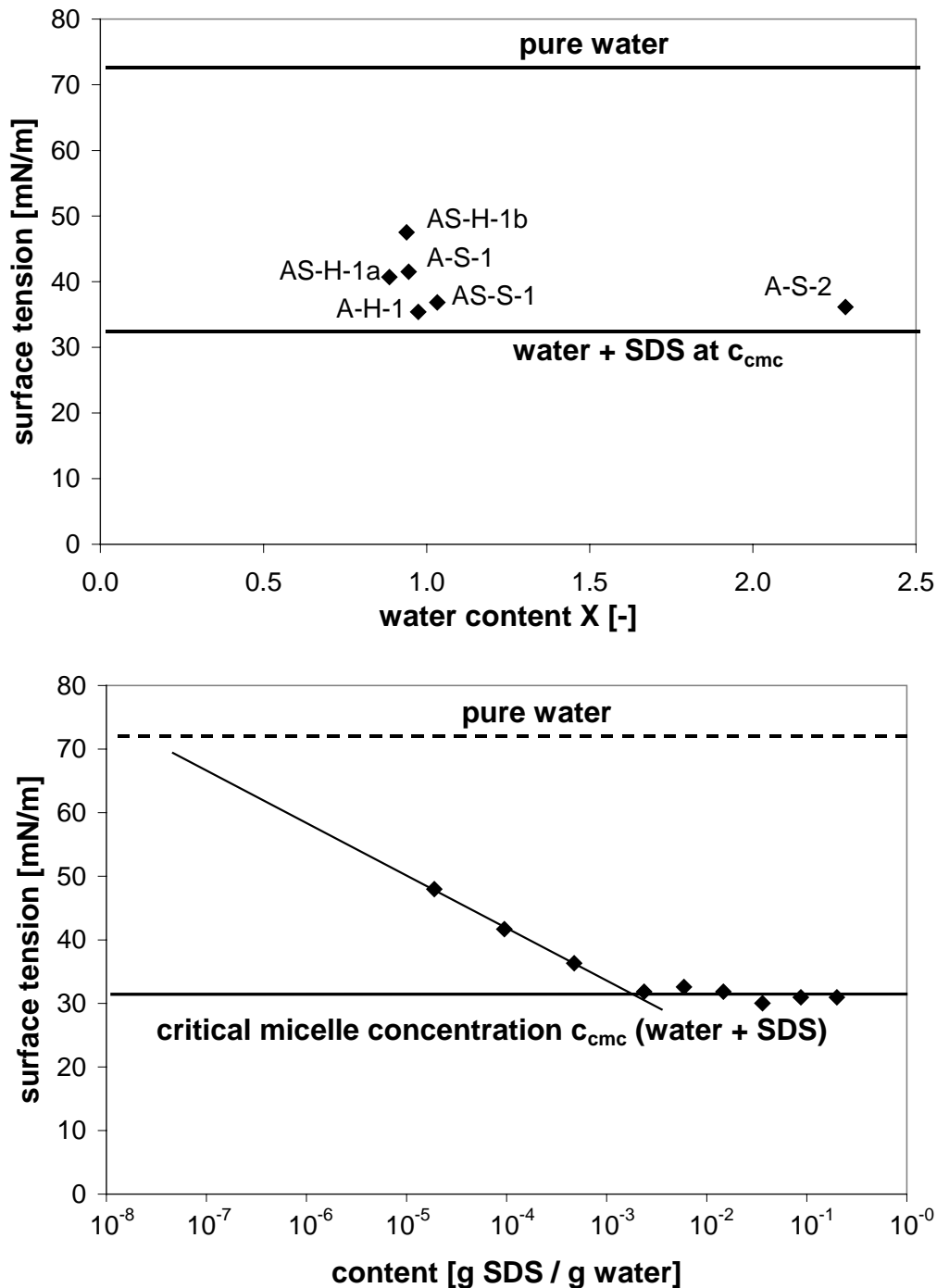


Figure AIII- 2: Top: the surface tension of the different latex dispersions; bottom: the surface tension as a function of surfactant concentration for the model system of water and sodium-dodecyl-sulfate (SDS)

6) Static Contact Angle

The static contact angle is the angle which forms between the dispersion-air and the dispersion-substrate interface of thin coating layers on a substrate. It is used to characterize the wettability of a dispersion. Depending on the surface energy of the substrate and the surface tension of the dispersion, the static contact angle of a thin film of latex dispersion on the respective substrate will be different. This becomes very important if one tries to understand and minimize such film defects like edge-effects and lap lines, visible in the dry film. Here, the static contact angle of uniform-size droplets of all dispersions on (I) a glass substrate and (II) a dry polymer film was measured (see Appendix III 7)). Wet films of lower surface tension show a smaller contact angle α with the glass substrate and a convex shape, whereas wet films of higher surface tension and pure water films show a concave shape (Figure AIII- 3).

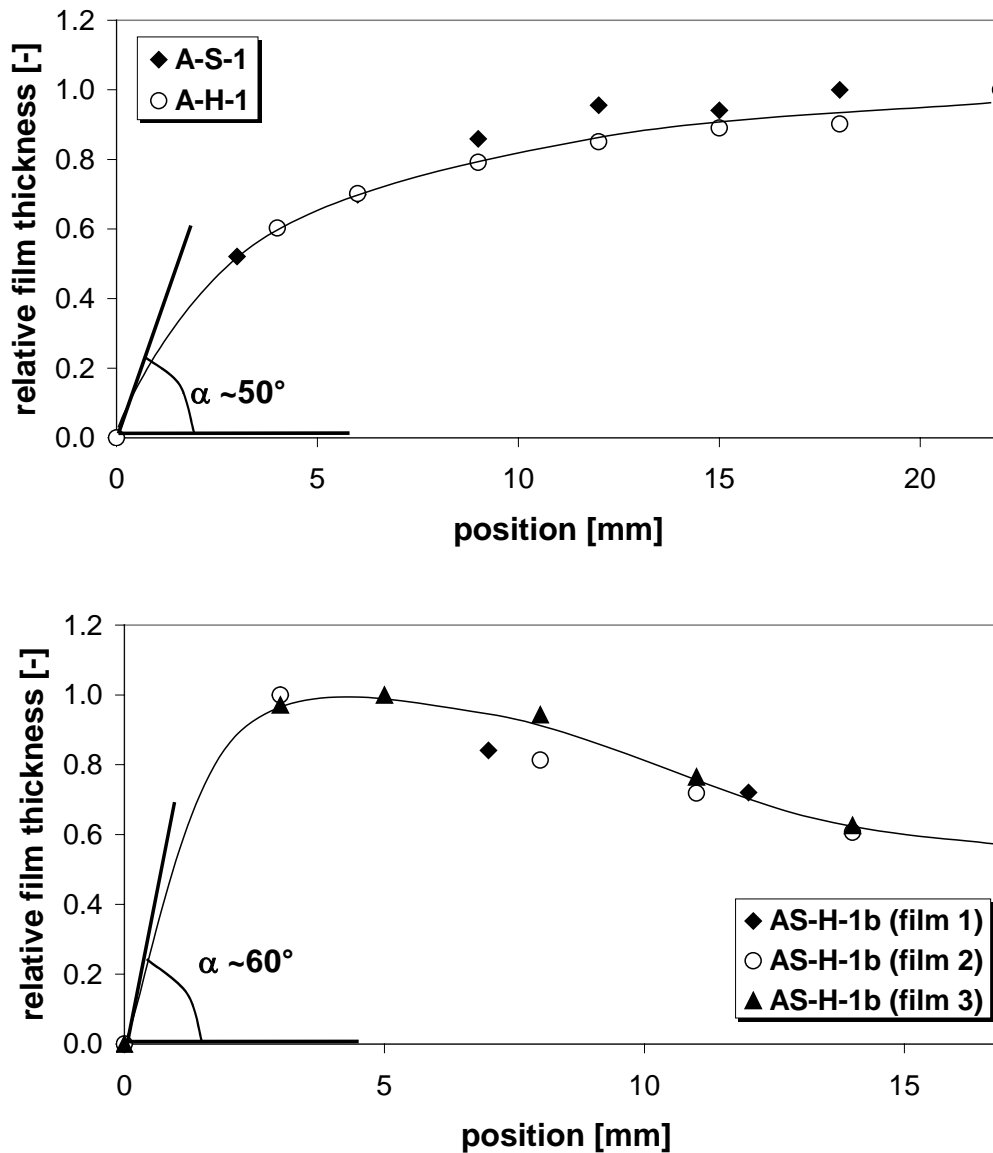


Figure AIII- 3: Top: wet films of lower surface tension (A-S-1, A-H-1);
Bottom: wet films of higher surface tension (AS-H-1b)

7) Summary of the Characteristic Dispersion Parameters

A-S-1 (at $T = 25\text{ °C}$):

polymer:	monomers:		composition:
polyacrylate	- methyl methacrylate - ethyl-hexyl-acrylate	($T_g = 105\text{ °C}$) ($T_g = -70\text{ °C}$)	-
stabilization:		[mmol /100g dry polymer]	level:
<i>surfactants</i>	- anionic ethoxylated C10-surfactant	1.6	medium
<i>anions</i>	- anions of sulfur (monovalent, divalent)	0.8	low
<i>cations</i>		9.4	low
<i>ionizable groups</i>	- covalently-bonded at the particle surface (acid groups \rightarrow pH-dependent)	14.0	low
<i>ionic groups</i>	- covalently bonded at the particle surface (\rightarrow non-pH-dependent)	2.3	

parameter:		experiment:	
<i>mass fraction polymer</i>	x []	gravimetric	0.494
<i>initial water content</i>	X [g water/g polymer]	gravimetric	1.020
<i>density</i>	ρ [g/cm ³]		
	- dispersion	data sheet	1.040
	- polymer	calculation (by x)	1.080
<i>hydrodynamic particle diameter (pH = 7)</i>	d [nm]	photon correlation spectroscopy (PCS)	163
<i>refractive index</i>	n []	refractometer (Abbemat)	
	- water		1.3333
	- dispersion		1.4058
	- polymer		1.4698
<i>pH</i>	pH []	data sheet	7-9
<i>surface tension</i>	γ [mN/m]	Du-Noüy ring	41.5
<i>contact angle</i>	α [°]		
	- on glass		41
	- on polymer		66
<i>zero-shear viscosity</i>	η_0 [mPas]	rheometer (cone-plate geometry)	~100
<i>glass transition temperature (polymer)</i>	T_g [°C]		-
<i>minimum film formation temperature</i>	T_{mff} [°C]	data sheet	0-2

G.-T. = Gordon-Taylor

A-H-1 (at T = 25 °C):

polymer:	monomers:		composition: *
polyacrylate	- methyl methacrylate - butyl-acrylate	(T _g = 105 °C) (T _g = -54 °C)	~66% ~34%
stabilization:		[mmol /100g dry polymer]	level:
<i>surfactants</i>	- ethoxylated, sulfated C13-fatty acid - anionic C14-C16 sulfonated surfactant - anionic surfactant	0.3 4.0 1.1	high
<i>anions</i>	- monovalent, divalent	4.0	medium
<i>cations</i>	- sodium, ammonium	18.1 + 4.0	medium
<i>ionizable groups</i>	- covalently-bonded at the particle surface (acid groups → pH-dependent)	32.0	medium
<i>carboxylic acid</i>		0.3	

parameter:		experiment:	
<i>mass fraction polymer</i>	x []	gravimetric	0.487
<i>initial water content</i>	X [g water/g polymer]	gravimetric	1.060
<i>density</i>	ρ [g/cm ³]		
	- dispersion	data sheet	1.040
	- polymer	calculation (by x)	1.080
<i>hydrodynamic particle diameter (pH = 7)</i>	d [nm]	photon correlation spectroscopy (PCS)	139
<i>refractive index</i>	n []	refractometer (Abbemat)	
	- water		1.3333
	- dispersion		1.4030
	- polymer		1.4768
<i>pH</i>	pH []	data sheet	7-8
<i>surface tension</i>	γ [mN/m]	Du-Noüy ring	35.4
<i>contact angle</i>	α [°]		
	- on glass		48
	- on polymer		34
<i>zero-shear viscosity</i>	η ₀ [mPas]	rheometer (cone-plate geometry)	~890
<i>glass transition temperature (polymer)</i>	T _g [°C]	G.-T.	~30
<i>minimum film formation temperature</i>	T _{mff} [°C]	data sheet	23

G.-T. = Gordon-Taylor

* obtained from the evaluation of Raman spectra

AS-H-1a (at T = 25 °C):

polymer:	monomers:		composition:*
polystyrene	- styrene	(T _g = 100 °C)	~70%
polyacrylate	- butyl-acrylate	(T _g = -54 °C)	~30%
stabilization:		[mmol /100g dry polymer]	level:
<i>surfactants</i>	- alkylsulfonate C15 surfactant	0.4	low
<i>anions</i>	- monovalent, divalent	7.0	high
<i>cations</i>	- sodium	48.0	high
<i>ionizable groups</i>	- covalently-bonded at the particle surface (acid groups → pH-dependent)	61.0	high
<i>hydrophilic non-ionic groups</i>	- covalently bonded at the particle surface	6.2	
<i>amino-methyl-propanol</i>	= emulsifier, gelling agent		

parameter:		experiment:	
<i>mass fraction polymer</i>	x []	gravimetric	0.503
<i>initial water content</i>	X [g water/g polymer]	gravimetric	0.990
<i>density</i>	ρ [g/cm ³]		
	- dispersion	data sheet	1.020
	- polymer	calculation (by x)	1.040
<i>hydrodynamic particle diameter (pH = 7)</i>	d [nm]	photon correlation spectroscopy (PCS)	140
<i>refractive index</i>	n []	refractometer (Abbemat)	
	- water		1.3333
	- dispersion		1.4293
	- polymer		1.5411
<i>pH</i>	pH []	data sheet	8
<i>surface tension</i>	γ [mN/m]	Du-Noüy ring	47.5
<i>contact angle</i>	α [°]		
	- on glass		50
	- on polymer		44
<i>zero-shear viscosity</i>	η ₀ [mPas]	rheometer (cone-plate geometry)	~220 000
<i>glass transition temperature (polymer)</i>	T _g [°C]	G.-T.	~35
<i>minimum film formation temperature</i>	T _{mff} [°C]	data sheet	18

G.-T. = Gordon-Taylor

* obtained from the evaluation of Raman spectra

AS-H-1b (at T = 25 °C):

polymer:	monomers:		composition: *
polystyrene	- styrene	(T _g = 100 °C)	~70%
polyacrylate	- butyl-acrylate	(T _g = -54 °C)	~30%
stabilization:	- similar to AS-H-1a -	[mmol /100g dry polymer]	level:
<i>surfactants</i>		-	low
<i>anions</i>	- monovalent, divalent	-	high
<i>cations</i>	- sodium	-	high
<i>ionizable groups</i>	- covalently-bonded at the particle surface (acid groups → pH-dependent)	-	high
<i>hydrophilic non-ionic groups</i>	- covalently bonded at the particle surface	-	

parameter:		experiment:	
<i>mass fraction polymer</i>	x []	gravimetric	0.501
<i>initial water content</i>	X [g water/g polymer]	gravimetric	1.000
<i>density</i>	ρ [g/cm ³]		
	- dispersion	data sheet	1.040
	- polymer	calculation (by x)	1.080
<i>hydrodynamic particle diameter (pH = 7)</i>	d [nm]	photon correlation spectroscopy (PCS)	142
<i>refractive index</i>	n []	refractometer (Abbemat)	
	- water		1.3333
	- dispersion		1.4328
	- polymer		1.5459
<i>pH</i>	pH []	data sheet	7.5-8.5
<i>surface tension</i>	γ [mN/m]	Du-Noüy ring	40.7
<i>contact angle</i>	α [°]		
	- on glass		57
	- on polymer		50
<i>zero-shear viscosity</i>	η ₀ [mPas]	rheometer (cone-plate geometry)	~52 000
<i>glass transition temperature (polymer)</i>	T _g [°C]	DSC	~35
<i>minimum film formation temperature</i>	T _{mfft} [°C]	data sheet	16

AS-S-1 (at T = 25 °C):

polymer:	monomers:		composition: *
polystyrene	- styrene	(T _g = 100 °C)	~60%
polyacrylate	- butyl-acrylate	(T _g = -54 °C)	~40%
stabilization:		[mmol /100g dry polymer]	level:
<i>surfactants</i>	- ethoxylated, sulfated fatty acid - C8-C10 phosphated surfactant - cyclic anionic surfactant	0.26 1.0 0.7	medium
<i>anions</i>	- monovalent, divalent	4.8	medium
<i>cations</i>	- sodium	29.5	medium
<i>ionizable groups</i>	- covalently-bonded at the particle surface (acid groups → pH-dependent)	28.1	medium

parameter:		experiment:	
<i>mass fraction polymer</i>	x []	gravimetric	0.480
<i>initial water content</i>	X [g water/g polymer]	gravimetric	1.080
<i>density</i>	ρ [g/cm ³]		
	- dispersion	data sheet	1.040
	- polymer	calculation (by x)	1.080
<i>hydrodynamic particle diameter (pH = 7)</i>	d [nm]	photon correlation spectroscopy (PCS)	199
<i>refractive index</i>	n []	refractometer (Abbemat)	
	- water		1.3333
	- dispersion		1.4200
	- polymer		1.5209
<i>pH</i>	pH []	data sheet	8.5-9.5
<i>surface tension</i>	γ [mN/m]	Du-Noüy ring	36.8
<i>contact angle</i>	α [°]		
	- on glass		38
	- on polymer		41
<i>zero-shear viscosity</i>	η ₀ [mPas]	rheometer (cone-plate geometry)	~55
<i>glass transition temperature (polymer)</i>	T _g [°C]	G.-T.	~18
<i>minimum film formation temperature</i>	T _{mfft} [°C]	data sheet	0-2

G.-T. = Gordon-Taylor

* obtained from the evaluation of Raman spectra

A-S-2 (at T = 25 °C):

polymer:	monomers:		composition:
polyacrylate	- methyl methacrylate - butyl-acrylate	(T _g = 105 °C) (T _g = -54 °C)	~58% ~42%
stabilization:		[mmol /100g dry polymer]	level:
<i>surfactants</i>	- anionic ethoxylated C12 surfactant	4.8	high
<i>anions</i>	- sulfur; monovalent, divalent; grafted at the particle surface	1.4	low
<i>cations</i>		22.4	medium
<i>ionizable groups</i>	- covalently-bonded at the particle surface (acid groups → pH-dependent)	62.0	high

parameter:		experiment:	
<i>mass fraction polymer</i>	x []	gravimetric	0.293
<i>initial water content</i>	X [g water/g polymer]	gravimetric	2.420
<i>density</i>	ρ [g/cm ³]		
	- dispersion	data sheet	1.030
	- polymer	calculation (by x)	1.100
<i>hydrodynamic particle diameter (pH = 7)</i>	d [nm]	photon correlation spectroscopy (PCS)	37
<i>refractive index</i>	n []	refractometer (Abbemat)	
	- water		1.3333
	- dispersion		1.3731
	- polymer		1.4552
<i>pH</i>	pH []	data sheet	7
<i>surface tension</i>	γ [mN/m]	Du-Noüy ring	36.1
<i>contact angle</i>	α [°]		
	- on glass		32
	- on polymer		18
<i>zero-shear viscosity</i>	η ₀ [mPas]	rheometer (cone-plate geometry)	~10
<i>glass transition temperature (polymer)</i>	T _g [°C]	G.-T.	~16
<i>minimum film formation temperature</i>	T _{mfft} [°C]	data sheet	0

G.-T. = Gordon-Taylor

Appendix IV Theoretical Basics of Rheology

1) Elastic Solids

Elastic solids, when subjected to a normal force that produces a small deformation, will return to its original length upon release of the force. The ideal elastic solid obeys *Hook's law*, which relates the normal stress σ to the strain ε . The constant of proportionality is known as the elastic modulus E .

$$\sigma = \frac{F}{A} = E \cdot \varepsilon \quad (\text{Hook's Law}) \quad \text{with: } \varepsilon = \frac{\Delta L}{L_0} \quad \text{Equ. AIV- 1}$$

with:

σ	= normal stress
F	= normal force
A	= cross-sectional area
E	= elastic modulus
ε	= strain
ΔL	= change in length
L_0	= initial length

When subjected to a shear stress τ , a *Hookean* solid will produce a shear strain γ . The constant of proportionality relating stress and strain is known as the shear modulus G .

$$\tau = \frac{F}{A} = G \cdot \gamma \quad \text{with: } \gamma = \frac{\Delta x}{\Delta y} \quad \text{Equ. AIV- 2}$$

with:

τ	= shear stress
F	= force
A	= area, tangent to the force
G	= shear modulus
γ	= shear strain
Δx	= deformation
Δy	= thickness of the solid

An illustration of uni-axial extension and simple shear of a solid is given in Figure AIV- 1. In rheological models, an elastic element is depicted as a spring, signifying reversible deformation.

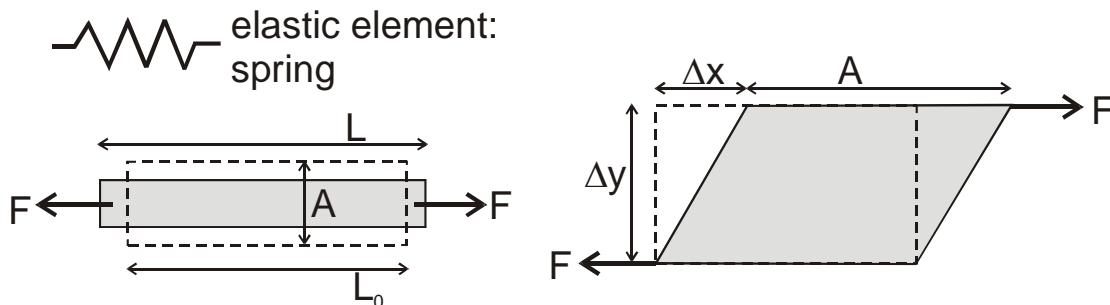


Figure AIV- 1: Left: Uni-axial extension; right: Simple shear of a solid

2) Viscous Fluids

Viscous fluids, when subjected to a force, become irreversibly deformed. For an ideal-viscous fluid (*Newtonian* fluid) the shear stress τ is directly proportional to the rate of deformation $\dot{\gamma}$ (= shear rate). For the *Newtonian* fluid, the constant of proportionality is independent of $\dot{\gamma}$ and is known as the dynamic viscosity η .

$$\tau = \frac{F}{A} = \eta \cdot \dot{\gamma} \quad \text{with: } \dot{\gamma} = \frac{v}{h} \quad \text{Equ. AIV- 3}$$

with:

τ	= shear stress
F	= force
A	= area tangent to the force
η	= dynamic viscosity
$\dot{\gamma}$	= shear rate
v	= velocity of top plate
h	= vertical dimension of the fluid film

In Figure AIV- 2, viscous fluid behaviour is illustrated by laminar shear flow between two parallel plates.

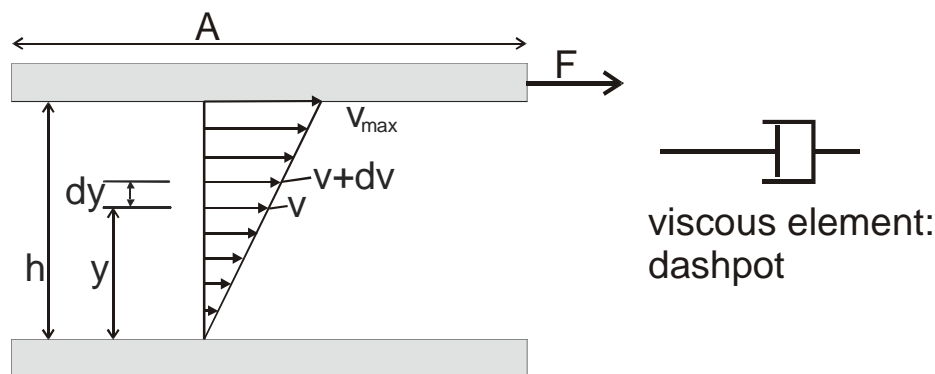


Figure AIV- 2: Left: Laminar shear of a fluid between two parallel plates; right: Representation of a viscous element (= dashpot)

The *Newtonian* fluid, having a shear rate-independent viscosity η , is an idealized case that is rarely satisfied in nature. The most popular example of a *Newtonian* fluid is water. Most fluids display a viscosity that is dependent on the shear rate:

$$\tau(\dot{\gamma}) = \eta(\dot{\gamma}) \cdot \dot{\gamma} \quad \text{Equ. AIV- 4}$$

Material behaviour, that displays a decreasing viscosity η with increasing shear rate $\dot{\gamma}$ is called shear thinning; an increase of the viscosity with shear rate is referred to as shear thickening. In rheological models, a viscous element is represented by a dashpot.

3) Linear Viscoelasticity

Materials normally display both, elastic and viscous properties at a time. In addition, the material often shows a time-dependent response to deformation. This is referred to as viscoelasticity and is typical for all polymeric materials.

For a viscoelastic fluid, when subjected to a step-increase in strain, the stress relaxes to zero in an exponential fashion, while for a viscoelastic solid the stress asymptotically approaches an equilibrium state. Figure AIV- 3 shows the four possible combinations of one spring and one dashpot representing viscous, viscoelastic and elastic material response.

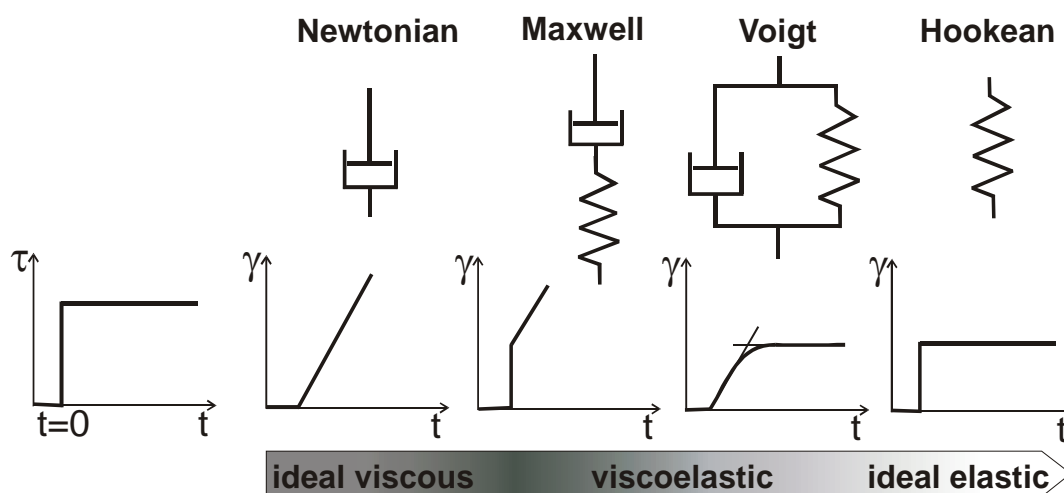


Figure AIV- 3: A representation of the four rheological models, consisting of not more than one spring and one dashpot, describing the material's strain response for suddenly applied stress

As mentioned above, the rheological behaviour of the ideal-viscous fluid is represented by a dashpot; the ideal-elastic solid obeys *Hook's* law and its rheological behaviour is expressed by a spring. The rheological model of a viscoelastic fluid, the *Maxwell* model, is a combination of a spring and a dashpot in a row. For the *Maxwell* model, the stresses of spring and dashpot are the same and the strains of the two elements are additive. Viscoelastic solids are described by the so-called *Voigt* model, which is a parallel setup of spring and dashpot. In the *Voigt* model the stresses are additive:

$$\tau = \eta \cdot \dot{\gamma} + G \cdot \gamma$$

Equ. AIV- 5

Also shown in Figure AIV- 3 is the deformation response of the different materials when subjected to a step-increase in stress. In reality, often more complex models involving many springs and dashpots are necessary to describe the viscoelastic properties of a material.

The viscoelastic behaviour of a material can be described by a time-dependent shear modulus $G(\gamma, t)$, also known as relaxation modulus. One simplification to obtain the relaxation modulus G is to focus on the material response in the linear viscoelastic

region, which is normally restricted to small material strains. As long as linear viscoelasticity applies, the time-dependent shear modulus $G(t)$ is independent of strain.

$$G(t) = \frac{\tau(t)}{\gamma} \quad \text{and } G \neq G(\gamma) \quad \text{Equ. AIV- 6}$$

In this case, all relaxation moduli $G(t)$ fall on the same curve when plotted as $\log G$ against $\log t$.

Latex dispersions of high particle volume fractions demonstrate viscoelastic properties (*Pishvaei et al. (2005)*). This is due to the presence of the polymer particles in the dispersion. During flow the interparticle distance will be distorted, but will regain their original state when the fluid is at rest. The simplest model to describe the rheological behaviour of a viscoelastic fluid is that of a *Maxwell* fluid. The typical shape of the stress response of a *Maxwell* fluid represented by $G(t)$ shows an exponential decay (Figure AIV- 3) expressed by:

$$G(t) = G_0 \cdot e^{-t/\lambda} \quad \text{Equ. AIV- 7}$$

with:

G	= relaxation modulus
G_0	= weighting constant
t	= time
λ	= relaxation time

However, one single relaxation time is often not enough to describe the complex material behaviour. Therefore, often multiple relaxation times λ_i and weighting constants G_i are needed. This approach is also known as the general linear viscoelastic model and is expressed by:

$$G(t) = \sum_{i=1}^N G_i \cdot e^{-t/\lambda_i} \quad \text{Equ. AIV- 8}$$

4) Theoretical Basics of Rheometry

Viscoelastic materials are commonly studied by small strain experiments in the gap between a fixed and a rotating plate. Simple shear experiments measure the viscosity for uni-directional rotation of the upper plate. For oscillatory shear experiments, a sinusoidal oscillating strain is applied:

$$\gamma = \gamma_0 \cdot \sin(\omega t) \quad \text{Equ. AIV- 9}$$

with:

γ	= strain
γ_0	= strain amplitude
ω	= rotational speed

Within a few cycles, the stress required to induce the strain function will also oscillate sinusoidal at the same frequency but is shifted by a phase angle δ .

$$\tau = \tau_0 \cdot \sin(\omega t + \delta)$$

Equ. AIV- 10

For an analysis, the time-dependent measured stress τ , causing the sinusoidal deformation is split into two components τ' and τ'' .

$$\begin{aligned} \tau &= \tau_0 \cdot \sin(\omega t + \delta) = (\tau_0 \cdot \cos \delta) \cdot \sin(\omega t) + (\tau_0 \cdot \sin \delta) \cdot \cos(\omega t) \\ &= \tau'_0 \cdot \sin(\omega t) + \tau''_0 \cdot \cos \omega t = \tau' + \tau'' \end{aligned}$$

Equ. AIV- 11

with τ' being in-phase with the strain γ and τ'' being 90 degrees out-of-phase with γ (Figure AIV- 4).

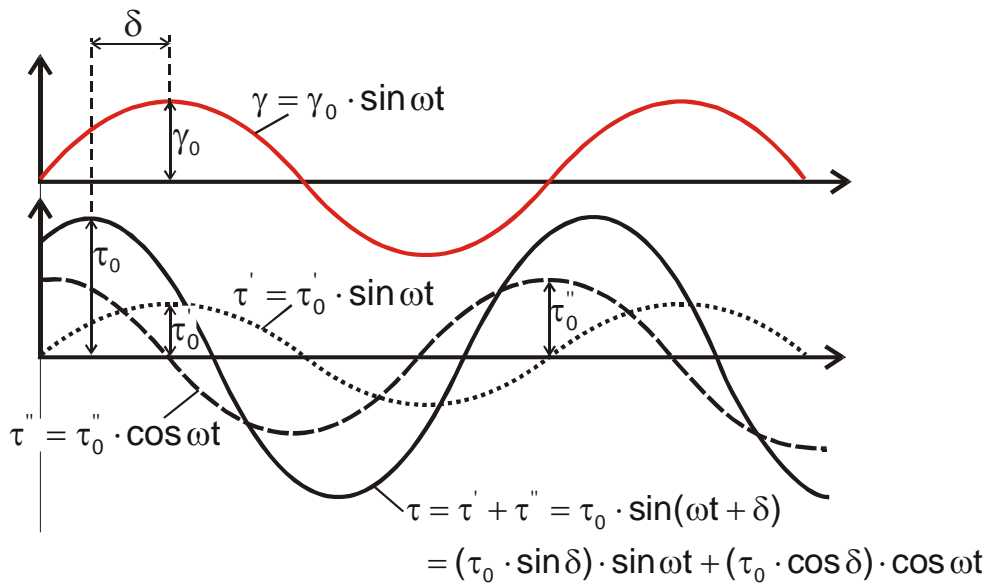


Figure AIV- 4: A sinusoidal oscillating shear strain γ produces a sinusoidal deformation τ , shifted by a phase angle δ

The decomposition of τ allows the formation of two dynamic moduli G' , G'' :

$$G' = \frac{\tau'_0}{\gamma_0} \quad (\text{in-phase or storage modulus}) \quad \text{Equ. AIV- 12}$$

$$G'' = \frac{\tau''_0}{\gamma_0} \quad (\text{out-of-phase or loss modulus}) \quad \text{Equ. AIV- 13}$$

G' is a measure for the elastic material behaviour and G'' expresses the viscous component of the material's response to deformation. The ratio of the two moduli yields:

$$\tan \delta = \frac{\tau''_0}{\tau'_0} = \frac{G''}{G'} \quad (\delta = \text{phase angle}) \quad \text{Equ. AIV- 14}$$

Based on the general linear viscoelastic model (see Equ. AIV- 8), trigonometric considerations give the following expressions of the dynamic moduli G' and G'' for sinusoidal oscillating deformation:

$$G'(\omega) = \sum_k G_k \frac{\lambda_k^2 \cdot \omega^2}{(1 + \lambda_k^2 \cdot \omega^2)} \quad \text{Equ. AIV- 15}$$

$$G''(\omega) = \sum_k G_k \frac{\lambda_k \cdot \omega}{(1 + \lambda_k^2 \cdot \omega^2)} \quad \text{Equ. AIV- 16}$$

with:

G_k = weighting constants
 λ_k = relaxation times
 ω = rotational speed

As an example, plots of G' , G'' and of δ of an ideal *Maxwell* fluid, characterized by one single relaxation time (compare Equ. AIV- 7), are shown in Figure AIV- 5.

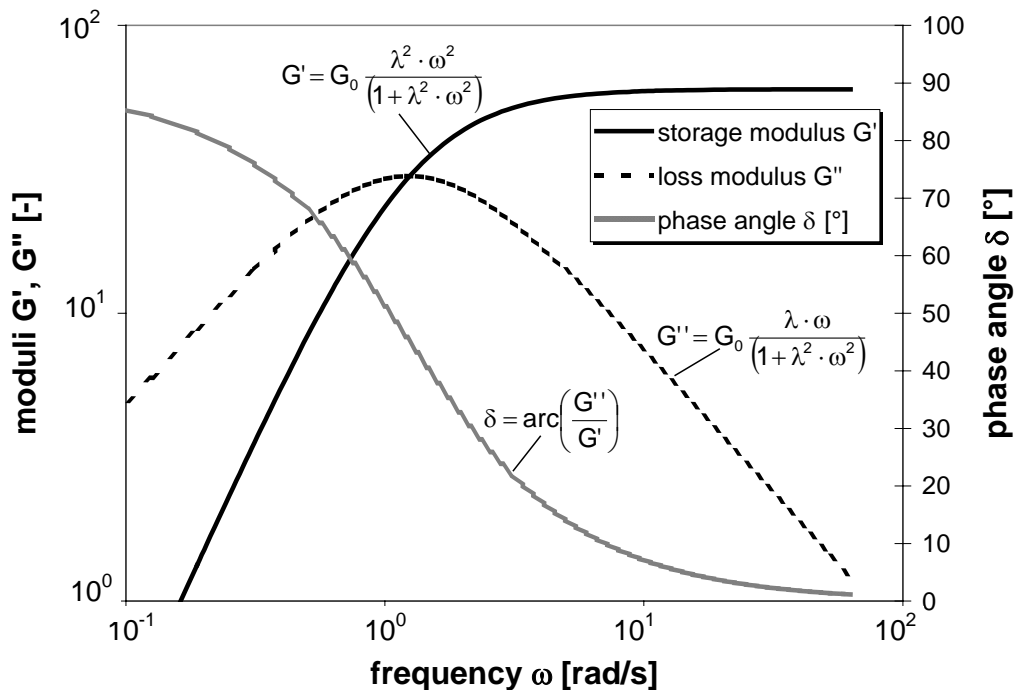


Figure AIV- 5: A representation of G' , G'' and δ of an ideal *Maxwell* fluid with one single relaxation time λ

5) Experimental Setup for the Rheological Measurements

According to the definition of the shear viscosity of a *Newtonian* fluid the plates must possess an infinite length to assure constant motion of the fluid. Therefore, the use of a rotational rheometer is a solution to provide high quality viscosity measurements. For rheological experiments, three geometries are commonly used: (I) coaxial cylinders, (II) plate-plate and (III) cone-plate geometry. The cone-plate geometry is often preferred, because it assures a shear stress within the gap which is independent of the cone radius r , as explained by the following mathematical relations:

- the tangential velocity of the cone at distance r from the center is:

$$v(r) = r \cdot \omega \quad \text{Equ. AIV- 17}$$

- the height of the gap between plate and cone at radius r is:

$$h(r) = r \cdot \tan \alpha \quad \text{Equ. AIV- 18}$$

With Equ. AIV- 17 and Equ. AIV- 18 the shear rate is:

$$\dot{\gamma} = \frac{dv(r)}{dh(r)} = \frac{\omega \cdot dr}{\tan \alpha \cdot dr} = \frac{\omega}{\tan \alpha} \neq f(r) \quad \text{Equ. AIV- 19}$$

The shear stress τ applied to the sample can be obtained from the torque M at the shaft of the cone. A small torque element dM acting on a small area dA is expressed by:

$$dM = r \cdot dF = r \cdot \tau \cdot dA = r \cdot \tau \cdot 2\pi \cdot r \cdot dr = \tau \cdot 2\pi \cdot r^2 \cdot dr \quad \text{Equ. AIV- 20}$$

With the valid assumption of $A_{\text{cone}} \approx A_{\text{plate}}$ the integration of Equ. AIV- 20 yields:

$$M = \tau \cdot 2\pi \cdot \frac{r_0^3}{3} \quad \text{or: } \tau = \frac{3}{2\pi \cdot r_0^3} \cdot M \quad \text{Equ. AIV- 21}$$

Then, the dynamic viscosity η can be obtained from Equ. AIV- 4 and Equ. AIV- 21:

$$\eta = \frac{\tau}{\dot{\gamma}} = \frac{3 \cdot M \cdot \tan \alpha}{2\pi \cdot r_0^3 \cdot \omega} \approx \frac{3 \cdot M \cdot \alpha}{2\pi \cdot r_0^3 \cdot \omega} \quad \text{Equ. AIV- 22}$$

Below is a sketch of the cone-plate experimental setup as used in this work.

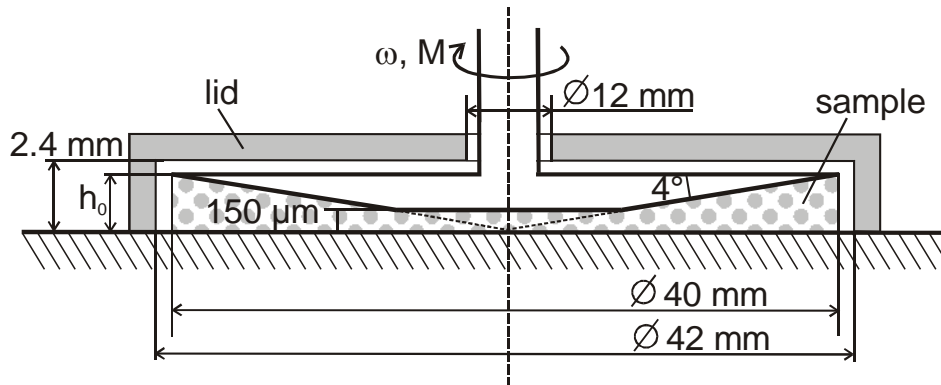


Figure AIV- 6: Experimental setup for the rheological investigation of latex dispersions

The rheological investigations were performed with a Bohlin CVO rheometer, equipped with a 40 mm diameter/4° cone. Before starting the measurements, each sample in the gap was equilibrated to $T = 25 \text{ }^\circ\text{C}$.

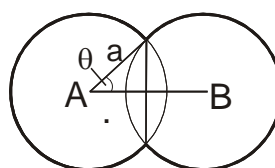
Due to the fast drying of the concentrated polymer dispersion, special precautions had to be taken to suppress the evaporation of water during the measurement. Therefore, a lid made from poly-methyl-methacrylate was used to create a small volume around the sample (Figure AIV- 6) which would saturate with water vapour and hinder further drying. A fast and accurate filling of the gap between the cone and the plate was realized by the injection of a defined volume of dispersion into the gap using a syringe.

Appendix V Driving Forces of Film Formation

1) “Dry Sintering” (*Dillon, Matheson, Bradford (1951)*)

Dillon et al. (1951) state that drying and particle coalescence occur separately and that dry sintering of the latex particles is due to the polymer/air interfacial tension. Based on *Frenkel’s* investigations about the viscous creep of bodies, the polymer particles are modeled as viscous spheres where the surface tension provides the main driving force for particle deformation. Here, particle deformation occurs, because a reduction of the overall surface area is energetically favourable. The sketch below presents two bodies in contact with each other. Starting from here, *Frenkel* derived the following relationship between the angle of deformation, the particle radius and the time.

$$\theta^2 = \frac{3}{2\pi} \frac{\sigma}{a \cdot \eta} t$$



Equ. AV- 1

with:

θ	= angle of deformation
σ	= polymer surface tension
η	= polymer viscosity
a	= particle radius
t	= time

In their model, *Dillon et al.* do not consider any other forces to be important for the film formation process of latex films. Besides, the particles are assumed to be viscous spheres, rather than viscoelastic bodies.

2) “Wet Sintering“ and Capillary Forces (*Brown (1956)*)

Brown experienced that water evaporation from latex films finishes at the same time as does film formation. Therefore, according to *Brown*, both, the polymer/water interface and the water/air interface must be of importance for the film forming process. Based on this finding, *Brown* developed a model where water evaporates from the interstices between the closest-packed polymer particles, forming a water/air interface that recedes from the film surface.

The main objective of his approach was to identify the parameters which promote particle deformation and the ones which oppose it. There is a large number of forces supporting particle deformation like surface and interfacial forces (F_S), capillary forces (F_C), electrostatic double-layers (F_V) and gravitational forces (F_g). Coulombic forces (F_e) and the resistance of the polymer particles to deformation (F_G) oppose the film formation process. *Brown* states, that for particle deformation, the forces that promote deformation have to always be larger than the ones that oppose it.

$$F_S + F_C + F_V + F_g > F_G + F_e$$

Equ. AV- 2

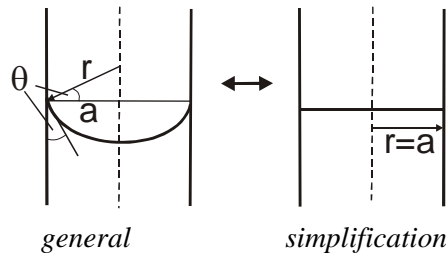
Since some of these forces are relatively small, *Brown* only considers capillary and deformation forces in his model:

$$F_c > F_G \quad \text{Equ. AV- 3}$$

The pressure in a capillary between contiguous latex particles is described by the *Laplace* equation. For reasons of simplification *Brown* assumes that the contact angle between water and polymer is always equal to 90° .

$$\Delta p_c = \frac{2 \cdot \sigma}{r}$$

$$\cos \theta = \frac{a}{r}$$



Equ. AV- 4

with:

σ	= water/air interfacial tension
r	= radius of surface curvature
a	= radius of the capillary
θ	= polymer-water contact angle

The resulting contact pressure causes viscoelastic deformation of the particles. In order to model the response of the particles to deformation, *Brown* assumes the particles to be smooth, elastic spheres rather than viscoelastic bodies. He applied the theory of *Hertz* for elastic bodies, which describes the dependence of the contact area between two smooth, elastic bodies on the applied force.

There are two important assumptions in *Brown's* model that are questionable: (I) in this model, capillary and deformation forces act on the same area and (II) the polymer particles are assumed to be purely elastic. The first assumption was corrected by *Mason* who compared the forces instead of their associated pressures (*Mason* (1973)). He took into account that the cross-section of a latex particle changes from circular to hexagonal during deformation using a correction parameter f . *Mason* still applied the *Hertz* model to obtain an expression for the deformation force. *Lamprecht* developed an alternative model, in which he applied *Yang's* theory of two linear viscoelastic spheres to be pressed together to describe the deformation (*Lamprecht* (1980)). In reality though, the extent of deformation is of such a degree, that the particles show non-linear viscoelastic behaviour. The second shortcome of *Brown's* model was further developed by *Kendall* and *Padget* who used the *Johnson-Kendall-Roberts* (JKR) theory as an alternative to describe deformation (*Kendall* and *Padget* (1982)). Their contact model also takes into account attractive forces between the particles. It describes a combination of body and surface forces acting onto two elastic spheres.

3) „Skin Formation“ (*Sheetz (1965)*)

Sheetz developed a model of capillary forces and osmotic pressure-driven film formation. As the latex dispersion becomes concentrated by evaporation of water, flocculation occurs. Particles at the latex-air interface are then subject to capillary forces and subsequently coalesce, leading to a compaction and deformation of the particles that are close to the surface. At a polymer volume fraction of $\phi = 30-40\%$, a surface layer of completely deformed particles develops which acts as an osmotic membrane (*Winnik (1997)*). The water in the film's interior must then diffuse through the upper layer and this generates a further compressive force acting normal to the film's surface. The mechanism is therefore seen to be based on *Brown's* wet sintering mechanism and on water diffusion.

Opposite to *Brown*, *Sheetz* considers, that the contact angle between water and the polymer is generally not equal to 90° , but smaller. He therefore calculates the compressive contribution of the water/air interface in each capillary of the surface particle layer in terms of the respective forces normal and parallel to the surface.

$$F_n = 2\pi \cdot r \cdot \sigma_{1/a} \cdot \cos \theta \quad (\text{compressive force}) \quad \text{Equ. AV- 5}$$

$$F_p = 2\pi \cdot r \cdot \sigma_{1/a} \cdot \sin \theta \quad (\text{pulls together the walls of the capillary}) \quad \text{Equ. AV- 6}$$

with:

$$\begin{aligned} \sigma_{1/a} &= \text{water/air surface tension} \\ \theta &= \text{contact angle between water and polymer} \end{aligned}$$

$$\sigma_{1/a} \cos \theta = \sigma_{p/a} - \sigma_{p/l} \quad (\text{Young equation}) \quad \text{Equ. AV- 7}$$

F_p is generally larger than F_n , because the contact angle at the polymer/air/water interface is often larger than 45° . Therefore, instead of Equ. AV- 4, the pressure, exerted on the cross-sectional area of the capillary, is:

$$p_n = \frac{2\pi \sigma_{1/a} \cos \theta}{\pi r^2} = 2 \frac{\sigma_{p/a} - \sigma_{p/l}}{r} \quad \text{Equ. AV- 8}$$

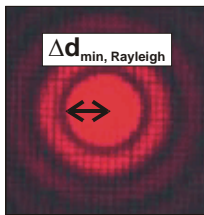
Fundamental data on measurements of the osmotic pressure in latex dispersions as a function of the polymer volume fraction exist in the literature (*Bonnet-Gonnet (1994)*). According to the *Sheetz* model, a uniform drying rate is experienced as long as the evaporation area is constant. Evaporation is slowed down as soon as areas of coalesced particles decrease the water/air interface. Then, according to *Sheetz*, water escapes from the film by diffusion at a decreased rate.

Appendix VI Microscopy and Spectroscopy

The chapter gives a summary of the basics of microscopy, i.e. diffraction-limited resolution in the plane of focus and refraction-limited resolution in vertical direction. The equations that describe the deviation of the real position and volume of the laser focus from the nominal focus position are derived. The chapter ends with the theoretical basics of elastic and inelastic (Raman) light-scattering.

1) Light Diffraction and Optical Resolution

Optical lenses magnify by bending light. They are restricted in their ability to resolve features by a phenomenon called diffraction, which sets a definite limit to the optical resolution. A measure for the resolution of optical lenses in lateral direction is the distance d , up to which punctual light sources can be recognized as separated. The minimum distance is obtained from the diffraction pattern of a plane wave on a circular hole (so-called *Fraunhofer* diffraction), which gives a centered, bright spot, surrounded by diffraction rings, also known as the *Airy* disc. The radius of the first diffraction ring was chosen by *Rayleigh* to be that minimum distance and is expressed by:



Airy ring;
(picture: R.C: Nave)

$$d_{\min, \text{Rayleigh}} = 1.22 \frac{\lambda}{2NA} \quad \text{Equ. AVI- 1}$$

The minimum optical resolution depends on the numerical aperture NA of the optical system and on the wavelength of light. According to this, a better resolution is obtained with light sources of shorter wavelength or optical lenses of high numerical aperture NA. The numerical aperture NA is a measure for the resolving power of a lens and is defined by:

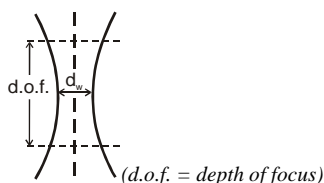
$$NA = n_{\text{medium}} \cdot \sin \theta_{\max} \quad \text{Equ. AVI- 2}$$

with:

$$\begin{aligned} n_{\text{medium}} &= \text{refractive index of the medium in which the lens is working} \\ \theta_{\max} &= \text{half-angle of the maximum cone described by the light} \end{aligned}$$

The definition of NA takes into account, that in other media than air, e.g. immersion oil, the wavelength of light is changed according to λ/n . The numerical aperture can have values larger than one.

For the investigation of thin films, the spatial resolution defined by the dimensions of the so-called focal tube is of importance. Its dimensions, being the result of diffraction phenomena, are defined by (e.g. *Everall* (2000)):



$$d_w = 1.22 \frac{\lambda}{NA} \text{ and}$$

$$\text{d.o.f.} = 4 \frac{\lambda}{NA^2} n_{\text{medium}}$$

Equ. AVI- 3

Here, d_w is the diameter (= waist) of the focal tube and d.o.f. is its length. Both are functions of the wavelength of light in the working medium and of the numerical aperture NA. Compared to *Rayleigh's* definition, d_w is formed with the diameter of the *Airy* disc, which is responsible for a difference of factor 2 in both expressions.

For the immersion oil objective used in this work ($n_{oil} = 1.51$; $NA = 1.3$) and the Ar-laser of wavelength $\lambda = 514 \text{ nm}$ Equ. AVI- 3 would give a d.o.f. of $1.84 \mu\text{m}$ in the case of light diffraction.

2) Light Refraction and Depth Resolution

For the depth resolution in thin films, the influence of light refraction is much more important than the above discussed diffraction. Spherical aberration by light refraction occurs at the phase boundary between any two media of different refractive index (e.g. *Carlsson* (1991); *Visser et al.* (1992); *Hell et al.* (1993)). There is not only a change in the position of the focus, depending on whether the refractive index at the phase boundary increases or decreases, but also an increase of the focal tube in axial direction, because light is refracted differently at the edge of the optical lens than in the center.

An illustration of the position and volume of the true focal tube in a polymer film by use of an immersion oil objective is given in Figure AVI- 1. The position of the focus of non-refracted light is named P_1 and is located at a distance z_1 above the interface. The position of the refracted light, leaving the optical lens at the distance r_{max} away from the center axis, is indicated by P_2 . In the wet latex film, the focal tube lies below the nominal focus position and is shifted to above that position due to refractive index changes during drying (Figure AVI- 1 bottom).

The true position and the dimensions of the focal tube under consideration of spherical aberration can be calculated (*Everall* (2000)). However, the effect of light diffraction is not taken into account in this calculation. Therefore, one simplifying assumption is, that the focus doesn't have any volume, but is treated as a geometrical spot. In reality, the dimensions of the focus are limited by diffraction effects (see above: Light Diffraction and Optical Resolution). Depending on the incident angle (= position r away from the center axis of the optical lens), the light is refracted differently, which is the reason why it is no longer bundled in one focus point. This is expressed by *Snellius's* refraction law:

$$n = \frac{n_2}{n_1} = \frac{\sin \Theta_1}{\sin \Theta_2}$$

Equ. AVI- 4

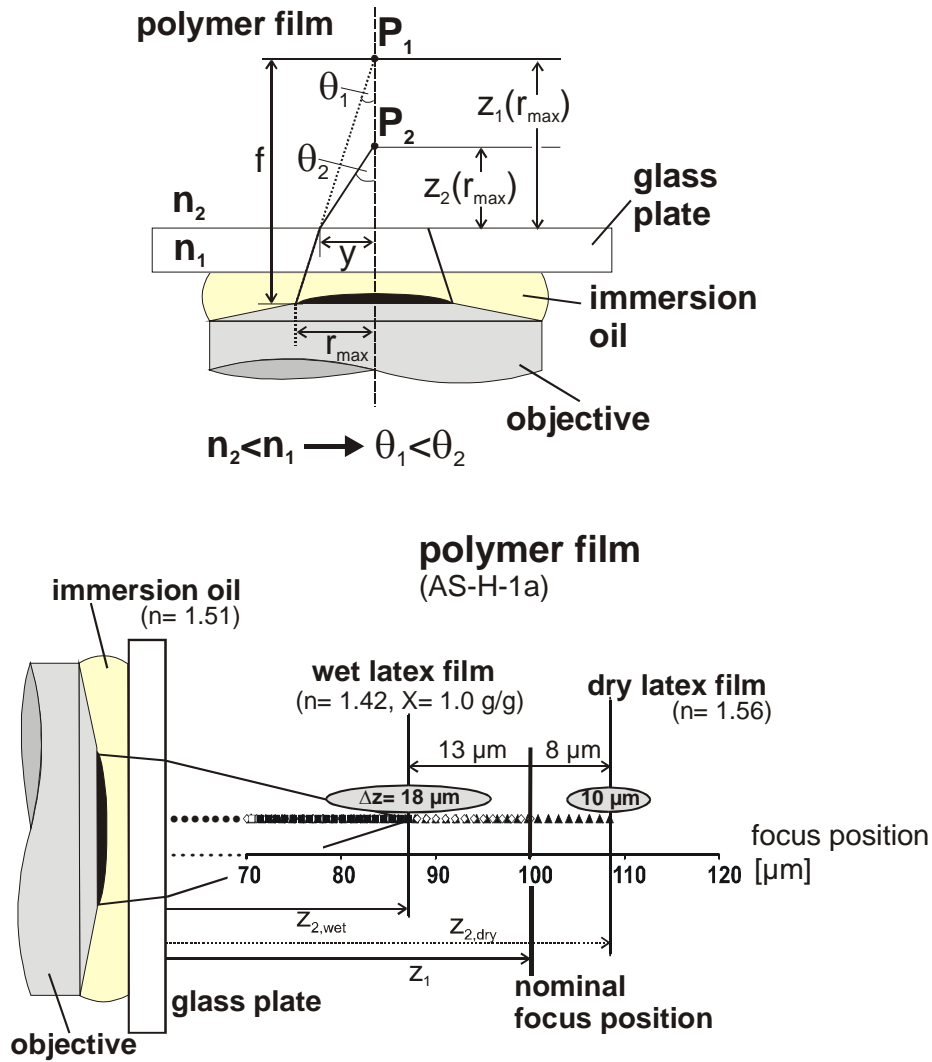


Figure AVI- 1: Top: the focus position of refracted and non-refracted light at a distance r_{max} away from the center axis. Bottom: an illustration of the position and volume of the focal tube in a film of AS-H-1a during a drying experiment (by use of an immersion oil objective)

The numbers 1 and 2 indicate the different media in direction of the refracted beam. If $n_2 < n_1$, the light is refracted away from the perpendicular axis ($\theta_2 > \theta_1$). The position of the focus $z_2(r)$ of a beam which leaves the optical lens at a distance r away from the center axis is obtained from trigonometric considerations:

$$\sin \theta_1 = \frac{r}{\sqrt{r^2 + f^2}}, \quad \cos \theta_1 = \sqrt{1 - \sin^2 \theta_1} \quad \text{Equ. AVI- 5}$$

$$\sin \theta_2 = \frac{r}{n \cdot \sqrt{r^2 + f^2}}, \quad \cos \theta_2 = \sqrt{1 - \frac{\sin^2 \theta_1}{n^2}} \quad \text{Equ. AVI- 6}$$

$$z_2(r) = \frac{y}{\tan \theta_2} = \frac{z_1 \cdot \tan \theta_1}{\tan \theta_2} \quad \text{Equ. AVI- 7}$$

Rearrangement of Equ. AVI- 1 to Equ. AVI- 7 gives the following expression for $z_2(r)$:

$$z_2(r) = \frac{z_1}{f} \cdot \sqrt{n^2 \cdot (r^2 + f^2) - r^2} \quad \text{with: } r \leq r_{\max} \quad \text{Equ. AVI- 8}$$

The focal distance depends on the optical lense of the objective. It can be calculated from geometrical considerations and the definition of the numerical aperture NA (Equ. AVI- 2).

$$f = r_{\max} \cdot \frac{\sqrt{1 - \frac{NA^2}{n_{\text{medium}}^2}}}{NA} \quad \text{Equ. AVI- 9}$$

with:

r_{\max} = maximum distance away from the center axis of the optical lense

Substitution of f in Equ. AVI- 8 leads to:

$$z_2(m) = z_1 \cdot \left(m^2 \cdot \frac{\frac{NA^2}{n_{\text{medium}}^2} \cdot (n^2 - 1)}{1 - \frac{NA^2}{n_{\text{medium}}^2}} + n^2 \right)^{1/2} \quad \text{Equ. AVI- 10}$$

with:

m = dimensionless radius

An expression of the maximum expansion Δz of the focal tube can be derived from the distance of the so-called refraction-limited foci of the light leaving the lense at r_{\max} ($m = 1$) and perpendicular to the lense ($m = 0$):

$$\Delta z = |z_2(m = 1) - z_2(m = 0)| = z_1 \cdot \left| \left(\frac{\frac{NA^2}{n_{\text{medium}}^2} \cdot (n^2 - 1)}{1 - \frac{NA^2}{n_{\text{medium}}^2}} + n^2 \right)^{1/2} - n \right|$$

Equ. AVI- 11

with:

z_1 = nominal focal depth

NA = numerical aperture

$n = n_{\text{sample}}/n_{\text{medium}}$ = ratio of refractive indices

n_{medium} = refractive index of immersion oil

The expansion of the focal tube increases with the nominal position of focus z_1 , the numerical aperture NA and the ratio of refractive indices of the sample and the

penetrated medium (compare also Figure AVI- 1). If the refractive index would be the same in all penetrated media, the sperical abberation would be zero.

The distribution of the laser light intensity within the focal tube is obtained from the following considerations: All light that is focused onto the spot $z_2(m)$ was emitted by the optical lense from a circle of radius m away from the center. The perimeter of a circle U increases proportional to its radius ($U=2\pi r$), which can be transferred to the laser light intensity, being also a function of m . Therefore, the distribution of laser light intensity along the center axis is:

$$L(z_m) = m \cdot I(m) \quad \text{Equ. AVI- 12}$$

In other words, it is a weighting factor for the laser intensity distribution of the lense, expressed in axial direction. Assuming a *Gaussian* distribution of the laser light intensity across the lense of the objective,

$$I(r) = I_0 \exp\left[\frac{-2r^2}{(r_{\max} \cdot \Phi)^2}\right] \quad \text{Equ. AVI- 13}$$

with:

- I_0 = laser light intensity in the center
- Φ = filling factor, expressing the degree of illumination of the optical lense

Equ. AVI- 13 can be written as:

$$I(m) = I_0 \exp\left[\frac{-2m^2}{\Phi^2}\right] \quad \text{Equ. AVI- 14}$$

With the help of $I(m)$, a center of gravity (c.o.g.) of the laser light intensity distribution in axial direction can be calculated, which is the same as an average point of focus of the incident laser light:

$$\text{c.o.g.}_{(\text{laser})} = \frac{\int_0^1 m z_2(m) I(m) dm}{\int_0^1 m I(m) dm} = \frac{\int_0^1 m z_2(m) \exp\left[\frac{-2m^2}{\Phi^2}\right] dm}{\int_0^1 m \exp\left[\frac{-2m^2}{\Phi^2}\right] dm}$$

Equ. AVI- 15

At any position within the illuminated focal tube, the scattered Raman signal is proportional to the intensity of the incident laser light. The probability that a scattered photon will be collected by the optical lense depends on $z_2(m)$. Equ. AVI- 15 gives the geometrical correlation between (I) the position $z_2(m)$ where scattering takes place, (II) the dimensionless radius m and (III) the angle Θ_1 of light emission, under which also the backscattered Raman light will hit the lense. This shows, that the probability of collection by the lense also depends on m . Here, m is a weighting factor for the scattering signal. Analogous to Equ. AVI- 14 a center of gravity of the intensity

distribution of Raman scattering within the illuminated focal tube can be obtained by replacing the intensity distribution of the laser light $m I(m)$ by an intensity distribution of the Raman light which is:

$$R(z_m) = m^2 I(m) \quad \text{Equ. AVI- 16}$$

This results in:

$$\text{c.o.g.}_{(\text{Raman})} = \frac{\int_0^1 m^2 z_2(m) I(m) dm}{\int_0^1 m^2 I(m) dm} = \frac{\int_0^1 m^2 z_2(m) \exp\left[\frac{-2m^2}{\Phi^2}\right] dm}{\int_0^1 m^2 \exp\left[\frac{-2m^2}{\Phi^2}\right] dm}$$

Equ. AVI- 17

And replacing $z_2(m)$ by Equ. AVI- 10 finally gives the following expression:

$$\text{c.o.g.}_{(\text{Raman})} = \frac{\int_0^1 \left(m^2 \cdot \frac{\frac{NA^2}{n_{\text{medium}}^2} \cdot (n^2 - 1)}{1 - \frac{NA^2}{n_{\text{medium}}^2}} + n^2 \right)^{1/2} \cdot m^2 \cdot \exp\left[\frac{-2m^2}{\Phi^2}\right] dm}{\int_0^1 m^2 \cdot \exp\left[\frac{-2m^2}{\Phi^2}\right] dm}$$

Equ. AVI- 18

With the help of this equation, the signal obtained at different positions in the polymer film can be corrected for its true position which depends on the refractive indices of the sample and the immersion medium. The graveness of correction depends on the ratio of the refractive indices of the penetrated media. The refractive index of the immersion medium should therefore be selected as close as possible to the one of the sample. During drying of latex dispersions, the refractive index changes from ~ 1.42 to 1.56 (Figure AVI- 1). This means, that during drying, the vertical resolution increases continuously.

Nevertheless, in the example given in Figure AVI- 1, the spectral information is from a volume with $\Delta z = 18 \mu\text{m}$ ($n = 1.42$) and $\Delta z = 10 \mu\text{m}$ ($n = 1.56$) which is by far larger than the high vertical resolution of $2\text{-}3 \mu\text{m}$, propagated for the IMRS setup. The high optical resolution can only be reached by the use of a confocal pinhole. It is optically coupled with the objective's focus and allows only backscattered light from the plane of focus to pass to be detected by the spectrometer. The confocal pinhole can be continuously adjusted between 0 and $1000 \mu\text{m}$. For an open pinhole, the depth resolution corresponds to that of a conventional microscope, but approaches a value comparable to that of Equ. AVI- 3 for smaller pinholes. Unfortunately, the better optical resolution is achieved only by a decrease in signal intensity. For a good space

and time resolution one has to make a compromise between high signal intensity (= large pinhole) and good depth resolution (= small pinhole). Therefore, for the drying experiments in this work, a pinhole diameter of $200\ \mu\text{m}$ was chosen at a laser light intensity of $100\ \text{mW}$ and an integration time of $1\ \text{s}$.

3) Spectroscopy

The vibrational energy of molecules can be measured by either infrared (IR) or Raman spectroscopy. Both methods rely on different physical principles:

In the case of infrared spectroscopy, a chemical species can be identified from certain absorbed frequency bands in the spectrum of light in the NIR-IR region. The characterisation of a chemical species using Raman spectroscopy is from light scattering in the UV-NIR region. Since Raman scattering is not very efficient, a high power excitation source such as a laser is necessary. Also, the excitation source has to be monochromatic to measure the energy (wavenumber) difference between the excitation and the Raman lines.

For a vibrational motion to be IR-active, the dipole moment of the molecule must change, whereas for a vibration to be Raman-active, there must be a change in the polarizability of the molecule. For example, homonuclear, diatomic molecules do not have an infrared absorption spectrum, because they have no dipole moment, but do have a Raman spectrum, because stretching and contraction of the bond changes the interactions between the electrons and nuclei, thereby changing the molecular polarizability. With both spectroscopic techniques, different spectral information about the molecules is obtained, depending on the symmetry of vibration. Thus, infrared and Raman spectroscopy are complementary techniques.

Talking about Raman spectroscopy, one differentiates between elastic and inelastic light scattering. Elastic scattering of light in the range between ultraviolet ($\lambda = 400\ \text{nm}$) and near-infrared ($\lambda = 700\ \text{nm}$) is named Rayleigh-scattering. In the case of Rayleigh scattering, only the momentum but not the energy of the photons is changed. Light is inelastically scattered when both, the momentum and also the photon energy change. Raman scattering is the most important representative of inelastic light scattering and is characterized by a change in energy that depends on the frequency of the excited molecules. A large number of books has been published about the theory of spectroscopy and Raman spectroscopy in special, e.g. *Fadini* (1985); *Schmidt* (1994); *Schrader* (1995).

(I) Elastic Scattering Theory

Elastic scattering can be described by a sinusoidal deformation of the electron cloud around the scattering molecule, being induced by the oscillating electric field of light. *Maxwell's* theory, which states that light has the character of an electromagnetic wave, can be used to describe particle-light interaction. In his model, *Maxwell* reveals that a

sinusoidal oscillating wave consists of a magnetic and an electric field which are orientated orthogonal, but oscillate in-phase to each other.

The electric field E of linear polarised light can be expressed by:

$$E = E_0 \cdot \cos(2\pi\nu t) \quad \text{Equ. AVI- 19}$$

with:

ν	= frequency of oscillation
E_0	= amplitude of the oscillating electric field
E	= electric field

The degree of displacement of charges or, in other words, the degree of the deformation of the molecule's electron cloud by an external electric field can be quantified by the polarizability α of the molecule. It is caused by the affinity of the positive nuclei of each atom to the negative pole and the affinity of the electrons to the positive pole. The polarizability of the molecule, caused by the external electric field, can induce a dipole moment μ . As a consequence, the dipole moment not only depends on the strength of the electric field, but also on the polarizability of the molecule and can be expressed by:

$$\mu = \alpha \cdot E \quad \text{Equ. AVI- 20}$$

with:

μ	= dipole moment
α	= polarization

Taking together Equ. AVI- 19 and Equ. AVI- 20, the induced dipole moment μ is modulated by the frequency of the oscillating electric field:

$$\mu = \alpha \cdot E_0 \cdot \cos(2\pi\nu t) \quad \text{Equ. AVI- 21}$$

The equation expresses the periodical displacement of charges. It is electrodynamic law, that moving charges emit electromagnetic radiation, which is why the oscillating molecules can be regarded as *Hertz* dipoles. Isotropic molecules emit electromagnetic radiation of the same oscillation frequency ν as was used for excitation. According to *Maxwell's* theory, the electric field at any point at a distance r away from the *Hertz* dipole and oriented by an angle θ can be expressed by:

$$E = \left(\frac{\alpha E_0 4\pi^2 \sin \theta}{r\lambda^2} \right) \cos(2\pi\nu t) \quad \text{with: } \lambda = \frac{c}{\nu} \quad \text{Equ. AVI- 22}$$

with:

r	= distance away from the <i>Hertz</i> dipole
λ	= wavelength
c	= velocity of light
ν	= frequency

In Equ. AVI- 22, the expression in parenthesis represents the amplitude of the electric field. The intensity of electromagnetic radiation is defined by the amplitude of the

electric field to the square. An impression of the ratio of scattered radiation to the intensity of incident light is therefore given by the well-known *Rayleigh* equation:

$$\frac{I_{\text{scatter}}}{I_0} = \frac{\left(\frac{\alpha E_0 4\pi^2}{r\lambda^2} \sin \theta \right)^2}{E_0^2} = \frac{16\pi^4 \alpha^2 \sin^2 \theta}{r^2 \lambda^4} \quad \text{Equ. AVI- 23}$$

It shows that (I) the intensity of scattered radiation decreases with the distance to the scattering center by the power of two ($I \sim r^{-2}$) and that (II) the intensity inversely depends on the wavelength of light to the power of four ($I \sim \lambda^{-4}$). For a high signal intensity, it is therefore important to collect the light as close as possible to the scattering center and to use light of short wavelength (= blue light).

Rayleigh's theory of elastic light scattering describes the scattering behaviour of molecules that are by far smaller than the wavelength of the incident light. For larger particles of $d > 0.1\lambda$ - like in colloidal dispersions -, such parameters as the difference of the refractive index of the polymer particles, the solvent medium ($m_p - m_m$) and the particle diameter d have to also be taken into account. In 1908, *Mie* found a solution of *Maxwell's* equations for the elastic scattering of electromagnetic waves at spherical particles. According to the *Mie theory*, the scattering intensity I_{scatter} is a complicated function of the scattering angle θ , of the ratio of wavelength and particle diameter λ/d , of the direction of light polarization and of the complex refractive indices of particles and medium. The calculation of scattering intensities and scattering coefficients, according to the *Mie theory*, requires numerical computation. A good description of the *Mie theory* can be found in *Vortisch* (2002). In short terms, the *Mie theory* considers spherical, homogeneous, isotropic particles and the classical *Maxwell* scattering theory of electromagnetic waves. The particles are characterized by the parameters x , y :

$$x = \frac{2\pi d}{\lambda} \quad \text{and } y = m \cdot x \quad \text{Equ. AVI- 24}$$

with:

d	= particle diameter
λ	= wavelength
m	= complex index of refraction

The solutions of *Maxwell's* equations are expressed in terms of spherical *Bessel* functions $j_n(x)$ and $h_n^{(2)}(x)$:

$$\psi_n(x) = x \cdot j_n(x) \quad \text{Equ. AVI- 25}$$

$$\zeta_n(x) = x \cdot h_n^{(2)}(x) \quad \text{Equ. AVI- 26}$$

Then, the scattering amplitudes a_n , b_n for an incident wave with polarisation perpendicular and parallel to the scattering plane can be written by the following complex expressions:

$$a_n = \frac{\psi'_n(y)\psi_n(x) - m\psi_n(y)\psi'_n(x)}{\psi'_n(y)\zeta_n(x) - m\psi_n(y)\zeta'_n(x)} \quad \text{Equ. AVI- 27}$$

$$b_n = \frac{m\psi'_n(y)\psi_n(x) - \psi_n(y)\psi'_n(x)}{m\psi'_n(y)\zeta_n(x) - \psi_n(y)\zeta'_n(x)} \quad \text{Equ. AVI- 28}$$

This results in the following efficiencies for extinction Q_{ext} , scattering Q_{scatter} and absorption Q_{abs} :

$$Q_{\text{ext}} = \frac{I_{\text{ext}}}{I_0} = \frac{2}{x^2} \left[\sum_{n=1}^{\infty} (2n+1) \text{Re}(a_n + b_n) \right] \quad \text{Equ. AVI- 29}$$

$$Q_{\text{scatter}} = \frac{I_{\text{scatter}}}{I_0} = \frac{2}{x^2} \sum_{n=1}^{\infty} (2n+1) (|a_n|^2 + |b_n|^2) \quad \text{Equ. AVI- 30}$$

The laser light extinction is the sum of the intensity loss due to absorption and scattering:

$$Q_{\text{ext}} = Q_{\text{abs}} + Q_{\text{scatter}} \quad \text{Equ. AVI- 31}$$

For non-absorbing media, which is the case for aqueous polymer dispersions, the extinction efficiency Q_{ext} is equal to Q_{scatter} . According to the *Mie* theory, the scattering intensity I_{scatter} strongly increases with increasing particle diameter and the distribution of scattering directions becomes asymmetric. *Rayleigh* and *Mie* scattering always coexist. With increasing particle diameter d , *Mie* scattering becomes more and more important, which means that the part of forward scattered light increases.

(II) Raman Scattering

When light is scattered at a molecule, most photons are scattered elastically (= Rayleigh scattering). The scattered photons have the same energy (frequency) and therefore wavelength as the incident photons. However, a small fraction of light is scattered at optical frequencies that are different from and usually lower than the frequency of the incident photons, which is also expressed by a different wavelength. The process, leading to inelastic scattering, is termed the Raman effect. Raman scattering can occur with a change in vibrational, rotational or electronic energy of the molecule, but one is often primarily concerned with the vibrational Raman effect. The energy of a vibrational mode depends on the molecular structure and the environment. Atomic mass, bond order, molecular substituents, molecular geometry and hydrogen bonding all affect the vibrational force constant, which in turn dictates the vibrational energy.

The Raman effect was first reported by *C.V. Raman* and *K. S. Krishnan*, and independently by *L. J. Mandelstam* and *G. S. Landsberg* in 1928. In 1930, *Raman* received the Nobel Prize for his work on the scattering of light. As stated above, the Raman effect arises when a photon is incident on a molecule and interacts with the electric dipole of the molecule. This results in a difference in energy between the incident photon and the Raman scattered photon which is equal to the energy of vibration of the scattering molecule. This interaction will change the polarizability α of the molecule, as can be illustrated by the following simple example of linear vibration: As stated above, the polarizability is a measure for the deformation of the electron cloud around a molecule, provoked by an external electric field. If now, the distance between two atoms is increased due to linear vibration of the bonding, this will also increase the average distance between the atomic nuclei and the electrons of the chemical bonding. Then, the electrostatic attraction between the nuclei and the electrons is decreased and the electrons are therefore more prone to a displacement, caused by an external electric field. At this moment, the polarizability is increased, whereas for a decrease in distance between atoms and electrons, the polarizability is also decreased. In the case of elastic Rayleigh scattering, the polarizability has a constant specific value. As a consequence, for the linear vibration of a diatomic molecule at frequency ν_M the polarizability α can be expressed by:

$$\alpha = \alpha_0 + \alpha_M \cos(2\pi\nu_M t) \quad \text{Equ. AVI- 32}$$

with:

α_0 = polarizability at rest

α_M = amplitude of the change of polarizability

With this expression, the dipole moment μ can be formed in analogy to Equ. AVI- 19 with E_0 being the amplitude of the electric field and ν_0 being the frequency of the incident light:

$$\mu = \underbrace{\alpha_0 E_0 \cos(2\pi\nu_0 t)}_{\text{elastic}} + \frac{1}{2} \alpha_M E_0 \left\{ \underbrace{\cos[2\pi(\nu_0 + \nu_M)t]}_{\text{Antistokes-Raman}} + \underbrace{\cos[2\pi(\nu_0 - \nu_M)t]}_{\text{Stokes-Raman}} \right\}$$

Equ. AVI- 33

The dipole moment contains three different frequencies which implies that the molecule (= *Hertz* dipole) can emit electromagnetic radiation at these frequencies. The first term represents elastic scattering at the frequency of the incident light ν_0 . In the other terms of Equ. AVI- 33, the frequency of the incident light has been modulated by ν_M . The change to higher frequencies (= shorter wavelength) is termed anti-Stokes Raman scattering and the change to lower frequencies is the so-called Raman scattering.

In quantum mechanics, scattering can be described as an excitation to a virtual state lower in energy than a real electronic transition with a nearly coincident de-excitation and a change in vibrational energy. The virtual state description of scattering is shown in Figure AVI- 2.

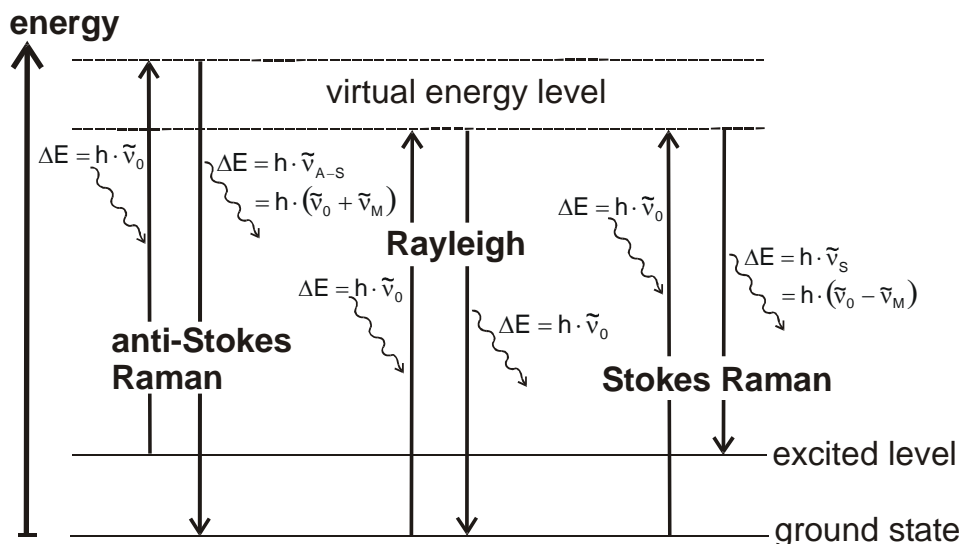


Figure AVI- 2: An illustration of the virtual energy levels of Raman scattering

At room temperatures, the thermal population of vibrational excited states is low, although not zero. Therefore, the initial state is normally the ground state, and the scattered photon will have a lower energy (= longer wavelength) than the exciting photon. Such a Stokes-shifted scatter is what is usually observed in Raman spectroscopy. A small fraction of the molecules is in a vibrationally excited state. Raman scattering from vibrationally excited molecules transfers the molecule to the ground state. The scattered photon appears at higher energy. Such an anti-Stokes-shifted Raman spectrum is always weaker than the Stokes-shifted spectrum. The ratio of anti-Stokes to Stokes intensity at any vibrational frequency is temperature-dependent. Therefore, Anti-Stokes Raman scattering can be used for contactless thermometry. The intensity ratio of the incident laser light to the scattered light is around:

$$I_{\text{laser}} : I_{\text{Rayleigh}} : I_{\text{Stokes-Raman}} : I_{\text{anti-Stokes-Raman}} \approx 1 : 10^{-4} : 10^{-7} : 10^{-10} \quad \text{Equ. AVI- 34}$$

In other words, about one out of 10^4 photons is scattered elastically, but only one out of 10^7 photons is scattered inelastically. This is why only during the last decade, driven by the development of new lasers, filters and detectors, Raman spectroscopy has become a powerful measurement technique for many applications. The Stokes and anti-Stokes spectra contain the same frequency information. Their frequency shift only depends on the frequency ν_M of the scattering molecule, but not on the frequency of the incident light. Therefore, the Raman spectrum is normally a plot of the intensity of scattered light versus energy difference (= shift in wavenumber $\Delta\tilde{\nu}$), also called Raman shift. The relation between wavenumber $\tilde{\nu}$, wavelength λ and frequency ν is given by $\tilde{\nu} = 1/\lambda = \nu/c$ and is illustrated in Figure AVI- 3, which shows the Raman

spectrum of an acrylic-styrene polymer film (AS-H-1a). The Raman shift is plotted positive in direction of longer wavelength (Stokes-Raman lines).

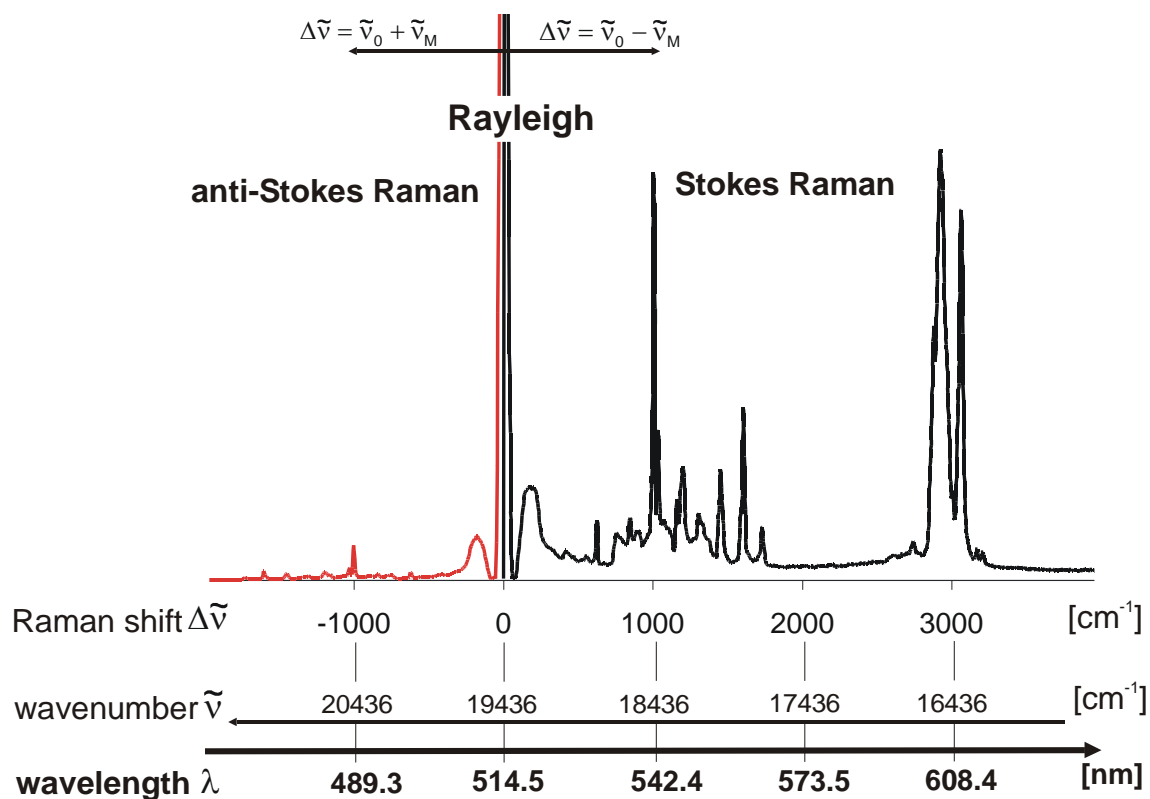


Figure AVI- 3: The Raman spectrum of AS-H-1a with the Stokes and anti-Stokes Raman region, obtained by an Argon laser of $\lambda_0 = 514 \text{ nm}$

Appendix VII Mass Transfer: Gasphase

Generally, mass transfer in the gas phase is described by the *Stefan-Maxwell* equation which can be derived from a theory of molecular interaction and friction. For a multi-component ideal gas, this is (see, e.g. *Bird et al.* (1960)):

$$\frac{\partial \tilde{y}_i}{\partial z} = \sum_{j=1}^{i=k} \frac{1}{\tilde{\rho}_g \cdot \delta_{ji}} (\tilde{y}_j \cdot \dot{n}_i - \tilde{y}_i \cdot \dot{n}_j) \quad \text{Equ. AVII- 1}$$

with:

\tilde{y}_i	= molar fraction of component i in the gas phase
z	= direction
$\tilde{\rho}_g$	= molar density of the gas phase
δ_{ji}	= <i>Stefan-Maxwell</i> diffusion coefficient
\dot{n}_i	= specific molar flow of component i

In the case of uni-directional diffusion of water in air (= binary system, semi-permeable interface, diffusion of one component), the *Stefan-Maxwell* equation can be solved explicitly (e.g. *Schlünder* (1984)), because the following assumptions hold:

$$\delta_{w,g} = \delta_{g,w} = \delta \quad \text{Equ. AVII- 2}$$

$$\dot{n} = \dot{n}_w \quad \text{Equ. AVII- 3}$$

Then, the expression for the specific molar flow of water (w) in air (g) is:

$$\dot{n}_w = -\tilde{\rho}_g \cdot \delta \cdot \frac{\partial \tilde{y}_w}{\partial z} + \tilde{y}_w \cdot \dot{n}_w \quad \text{Equ. AVII- 4}$$

And the integration of Equ. AVII- 4 gives the following expression for the specific molar flow:

$$\dot{n}_w = \tilde{\rho}_g \cdot \beta_{w,g} \cdot \ln \frac{1 - \tilde{y}_w^\infty}{1 - \tilde{y}_w^{\text{ph}}} \quad \text{or: } \dot{m}_w = \tilde{M}_w \cdot \tilde{\rho}_g \cdot \beta_{w,g} \cdot \ln \frac{1 - \tilde{y}_w^\infty}{1 - \tilde{y}_w^{\text{ph}}} \quad \text{Equ. AVII- 5}$$

with:

\dot{n}_w	= specific molar flow of water
\dot{m}_w	= specific mass flow of water
$\beta_{w,g}$	= binary mass transfer coefficient
\tilde{M}_w	= molar mass of water
\tilde{y}_w^∞	= molar fraction of water in the bulk at T_{air}
\tilde{y}_w^{ph}	= molar fraction of water at the interface at T_{film}

The vapour pressure reduction due to sorptive effects is taken into account by:

$$\tilde{y}_w^{\text{ph}}(T_{\text{film}}) = \frac{p_w^{\text{ph}}(T_{\text{film}})}{p} = a_w(T_{\text{film}}, X) \cdot \tilde{y}_w^*(T_{\text{film}}) \quad \text{Equ. AVII- 6}$$

with:

a_w	= water activity
p_w	= partial pressure of water vapour
\tilde{y}_w^*	= molar fraction of water corresponding to the saturation pressure p_w^*
p	= total pressure

The molar fraction of water in the bulk phase is obtained from:

$$\tilde{y}_w^\infty(T_{\text{air}}) = \frac{p_w^*(T_{\text{air}})}{p} \cdot \varphi \quad \text{Equ. AVII- 7}$$

with:

φ	= relative humidity of process air
-----------	------------------------------------

In Equ. AVII- 6 and Equ. AVII- 7, the saturation pressure p_w^* at T_{film} and T_{air} is calculated from *Antoine's* equation (see Appendix VIII).

Equ. AVII- 5 can also be written in the linear form using a so-called *Stefan* correction term K_S .

$$\dot{n}_w = \tilde{\rho}_g \cdot \beta_{w,g} \cdot (\tilde{y}_w^{\text{ph}} - \tilde{y}_w^\infty) \cdot K_S \quad \text{Equ. AVII- 8}$$

From a comparison of Equ. AVII- 5 and Equ. AVII- 8, the *Stefan* correction term can be defined by (*Schlünder* (1984)):

$$K_S = \frac{\ln \frac{1 - \tilde{y}_w^\infty}{1 - \tilde{y}_w^{\text{ph}}}}{\tilde{y}_w^{\text{ph}} - \tilde{y}_w^\infty} \quad \text{Equ. AVII- 9}$$

This term represents the influence of the overall convective flux \dot{n} and the mutual interaction of the different component fluxes \dot{n}_i on mass transfer. The *Stefan* correction term can have any value between $-\infty$ and $+\infty$, but is for many practical cases close to one.

For ambient drying conditions, the *Stefan* correction term for water evaporation in air is close to unity, e.g. $K_S = 1.01$ for $T = 20$ °C. In this study, it is therefore allowed to use the linear approach instead of the *Stefan-Maxwell* equation to describe the diffusion of water in air:

$$\dot{m}_w = \tilde{M}_w \cdot \tilde{\rho}_g \cdot \beta_{w,g} (\tilde{y}_w^{\text{ph}} - \tilde{y}_w^\infty) \quad \text{Equ. AVII- 10}$$

Or expressed in terms of concentration:

$$\dot{m}_w = \beta_{w,g} (c_w^{\text{ph}} - c_w^\infty) \quad \text{Equ. AVII- 11}$$

Appendix VIII Parameter Equations

1) Antoine Equation for Water

$$p_i^*(T) = \exp\left(A - \frac{B}{C + T}\right) \quad T \text{ [}^\circ\text{C]}; p \text{ [mbar]} \quad \text{Equ. AVIII- 1}$$

$$A = 19.016$$

$$B = 4064.95$$

$$C = 236.25$$

2) Fuller Equation

$$\delta_{i,j} = \frac{1.013 \cdot 10^{-7} \cdot T^{1.75} \cdot (1/\tilde{M}_i + 1/\tilde{M}_j)^{0.5}}{p \cdot [(\sum \nu_i)^{1/3} + (\sum \nu_j)^{1/3}]^2} \quad \text{Equ. AVIII- 2}$$

with:

$\delta_{i,j}$	= binary diffusion coefficient in the gas phase [m ² /s]
T	= temperature [K]
\tilde{M}_i	= molar mass [g/mol]
p	= pressure [bar]
$\sum \nu_i$	= diffusion volumina

		<i>air</i>	<i>water</i>	
molar mass	\tilde{M}_i	28.98	18.02	g/mol
diffusion volume	$\sum \nu_i$	20.1	12.7	-

Appendix IX Sorption Theories

1) Localized Sorption Theories

(I) Brunauer, Emmet, Teller (BET)-model

The shape of the sorption isotherm depends on the adsorption characteristics of the penetrant to specific sites in the polymer. According to the classification of *Brunauer, Emmet* and *Teller* (BET), five different types exist. The type I isotherm is the so-called *Langmuir* isotherm. Its shape represents the formation of a mono-molecular layer of adsorbed species. A type II isotherm represents the formation of more than one sorptive layer. Besides, a compatibility between the penetrant and the polymer must exist. The shape of the isotherm of type III is the result of low compatibility between the penetrant and the polymer, but also the formation of multi-layers at higher water activities. Isotherms of type IV and V are the result of penetrant condensation in meso-porous materials. Figure IX- 1 shows the different isotherms according to the BET-classification.

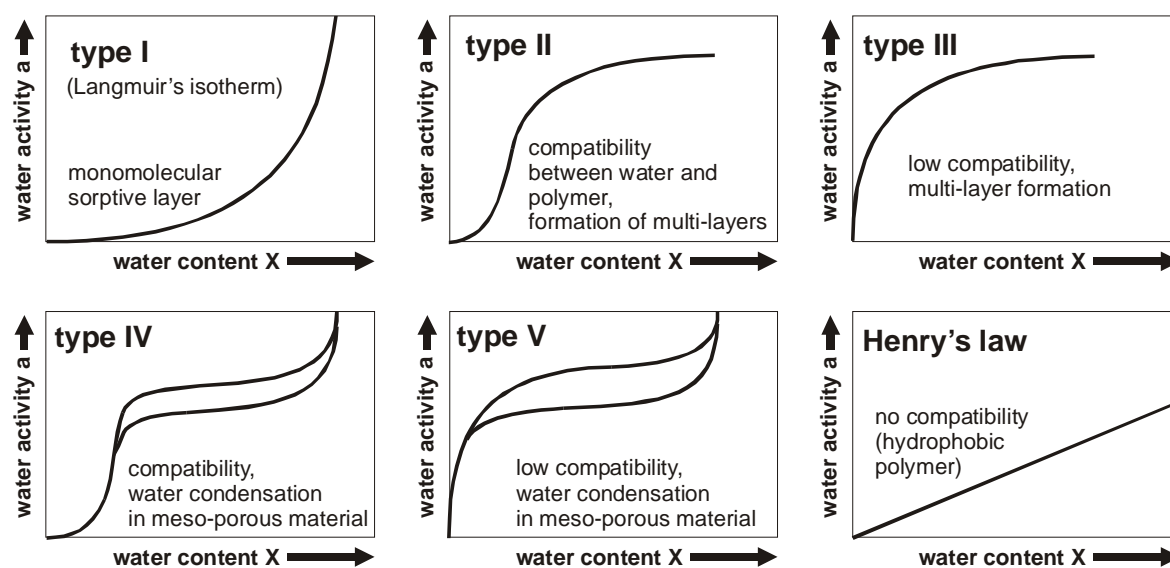


Figure IX- 1: BET-classification of sorption isotherms

In less hydrophilic polymers, the isotherm normally shows class III behaviour according to the BET classification and transport of water at low water activities is by single water molecules. Clustering of water molecules is the result of a high affinity to other water molecules, combined with a lower affinity of water molecules for the polymer matrix. Therefore, for high water activities clustering is expected.

In more hydrophilic polymers, the sorption isotherm at low water activities shows a class II behaviour according to the BET classification. For more hydrophilic polymers, there is interaction of water molecules with the functional groups of the polymer. Clustering is also expected when the amount of water molecules in the polymer is higher than the quantity that can be bound to the polymer.

Starting point for the mathematical derivation of the BET-isotherm are the following assumptions:

- There exists a limited number of energetically equal adsorption sites.
- No interaction between adsorbed molecules occurs, which means that the adsorption enthalpy is independent of the number of adsorbed molecules.
- There exists a dynamic equilibrium between adsorption and desorption.
- Multi-layer adsorption (physisorption) is possible.

This means, that for each layer the number of occupied sites must be constant and therefore, the rate of evaporation must be equal to the rate of condensation:

$$k_{-i} \cdot \theta_i = k_i \cdot p \cdot \theta_{i-1} \quad \text{Equ. IX- 1}$$

with:

$$\begin{aligned} k_i, k_{-i} &= \text{rate constant for adsorption and desorption} \\ \theta_i &= \text{fraction of occupied sites} \\ p &= \text{pressure} \end{aligned}$$

The ratio of the total volume fraction of adsorbed species to the volume fraction of one complete monolayer can be expressed by:

$$\frac{\varphi}{\varphi_m} = \frac{\sum_{i=0}^{\infty} i \cdot \theta_i}{\sum_{i=0}^{\infty} \theta_i} \quad \text{Equ. IX- 2}$$

with:

$$\begin{aligned} \varphi &= \text{volume fraction of adsorbed species} \\ \varphi_m &= \text{volume fraction of a complete monolayer} \end{aligned}$$

With Equ. IX- 1, the fraction of occupied sites of layer i can be expressed as:

$$\theta_i = \frac{k_i}{k_{-i}} \cdot p \cdot \theta_{i-1} \quad \text{Equ. IX- 3}$$

Assuming, that for all layers the ratio of desorption and adsorption is the same and can be expressed by a constant g ,

$$\frac{k_{-i}}{k_i} = g \quad \text{Equ. IX- 4}$$

this will lead to the following, general expression for the occupied sites θ_i of layer i :

$$\theta_i = \underbrace{\left(\frac{p}{g} \right)}_x \cdot \theta_{i-1} = x^{i-1} \cdot \theta_1 \quad \text{Equ. IX- 5}$$

θ_1 can be expressed by the fraction of occupied sites at the polymer surface θ_0 :

$$\theta_1 = \underbrace{\frac{k_1}{k_{-1}}}_y \cdot p \cdot \theta_0 \quad \text{Equ. IX- 6}$$

With $c_{\text{BET}} = x/y$, the general equation for θ_i is:

$$\theta_i = c_{\text{BET}} \cdot x^i \cdot \theta_0 \quad \text{Equ. IX- 7}$$

with:

c_{BET} = parameter related to the partitioning of higher sorption layers.

Substitution in Equ. IX- 2 gives:

$$\frac{\varphi}{\varphi_m} = \frac{c_{\text{BET}} \cdot \theta_0 \sum_{i=1}^{\infty} i \cdot x^i}{(\theta_0 + \theta_1 + \theta_2 + \dots)} = \frac{c_{\text{BET}} \cdot \theta_0 \sum_{i=1}^{\infty} i \cdot x^i}{\theta_0 \left(1 + c_{\text{BET}} \sum_{i=1}^{\infty} x^i\right)} = \frac{c_{\text{BET}} \sum_{i=1}^{\infty} i \cdot x^i}{\left(1 + c_{\text{BET}} \sum_{i=1}^{\infty} x^i\right)} \quad \text{Equ. IX- 8}$$

The sum of an infinite geometric progression is:

$$\sum_{i=1}^{\infty} x^i = \frac{x}{1-x} \quad \text{Equ. IX- 9}$$

and

$$\begin{aligned} \sum_{i=1}^{\infty} i \cdot x^i &= x^1 + 2x^2 + 3x^3 + \dots \\ &= x \frac{d}{dx} \sum_{i=1}^{\infty} x^i = x \frac{d}{dx} \left(\frac{x}{1-x} \right) = \frac{x}{(1-x)^2} \end{aligned} \quad \text{Equ. IX- 10}$$

Again, substitution of Equ. IX- 9 and Equ. IX- 10 in Equ. IX- 8 gives:

$$\frac{\varphi}{\varphi_m} = \frac{c_{\text{BET}} \cdot x}{(1-x) \cdot (1-x + c_{\text{BET}} \cdot x)} \quad \text{Equ. IX- 11}$$

To arrive at the well-known expression for the BET-isotherm, the following consideration is necessary: At the saturation pressure p^* of the gas, an infinite number of adsorbed layers must build. Mathematically, this means that for $p = p^*$ the expression in Equ. IX- 11 must go to infinity, which is the case for $x = 1$.

From the definition of x it becomes clear that g equals p_0 and therefore:

$$x = \frac{p}{p^*} = a \quad \text{Equ. IX- 12}$$

with:

a = activity

Resubstitution in Equ. IX- 11 gives the equation for the BET-isotherm:

$$\varphi = \frac{\varphi_m \cdot c_{\text{BET}} \cdot a}{(1-a) \cdot (1 + (c_{\text{BET}} - 1)a)} \quad \text{Equ. IX- 13}$$

(II) Guggenheim, Anderson, de Boer (GAB)-model

A modification of the BET-model is the so-called *Guggenheim, Anderson, de Boer* (GAB)-model which assumes that the heat of adsorption of water on localized sites in the film is less than the heat of liquefaction of water. This is expressed by an additional parameter k , being smaller than one. The GAB equation can be used for the fitting of non-ideal water sorption in polymers over a large range of water activities, which is not the case for the classical BET-model. According to the GAB-model, the sorption isotherm can be expressed by the following equation:

$$\varphi = \frac{\varphi_m \cdot c_{\text{GAB}} \cdot k \cdot a}{(1 - k \cdot a) \cdot (1 + (c_{\text{GAB}} - 1)k \cdot a)} \quad \text{Equ. IX- 14}$$

with:

- c_{GAB} = fitting parameter, related to the partitioning of higher sorptive layers
 k = ratio of the heat of adsorption and the heat of liquefaction

(III) GAB-Fitting Parameters (Water Sorption)

	$t = 18 h$	$t = 336 h$
A-S-1	$c_{\text{GAB}} = 0.900$ $k = 0.940$ $\varphi_m = 0.004$	$c_{\text{GAB}} = 0.005$ $k = 0.940$ $\varphi_m = 0.004$
A-H-1	$c_{\text{GAB,average}} = 0.900$ $k = 0.992$ $\varphi_m = 0.001$	$c_{\text{GAB,average}} = 0.900$ $k = 0.992$ $\varphi_m = 0.0002$
AS-H-1a	$c_{\text{GAB,average}} = 0.900$ $k = 0.920$ $\varphi_m = 0.0268$	$c_{\text{GAB,average}} = 0.900$ $k = 0.920$ $\varphi_m = 0.002$
AS-H-1b	$c_{\text{GAB,average}} = 0.900$ $k = 0.940$ $\varphi_m = 0.0030$	$c_{\text{GAB,average}} = 0.005$ $k = 0.940$ $\varphi_m = 0.030$
AS-S-1	$c_{\text{GAB,average}} = 0.01$ $k = 0.993$ $\varphi_m = 0.01$	$c_{\text{GAB,average}} = 0.900$ $k = 0.993$ $\varphi_m = 0.0002$
A-S-2	$c_{\text{GAB,average}} = 0.900$ $k = 0.920$ $\varphi_m = 0.0253$	$c_{\text{GAB,average}} = 0.900$ $k = 0.920$ $\varphi_m = 0.0015$

Table IX- 1: Fitting parameters, used in the GAB-model for the description of water sorption of the different dispersions ($T = 30 \text{ }^\circ\text{C}$)

2) Dissolution Theories

(I) Flory-Huggins Model

According to *Flory*, the theory is limited to relatively apolar systems with weak interactions. For water sorption, the model can prove useful to fit isotherms of relatively hydrophobic polymers at high water activities. In this model, a polymer solution is represented by a three-dimensional lattice of rigid spheres, in which the solvent molecules are defined by single spheres and the polymer is compared to a chain of spheres. For a system, where the gas phase shows ideal behaviour, the thermodynamic equilibrium at the phase boundary can be described by:

$$\tilde{y}_i = \frac{p_i}{p} = \underbrace{\gamma_i \cdot \tilde{x}_i}_{a_i} \cdot \frac{p_i^*(T)}{p} \quad \text{Equ. IX- 15}$$

with:

\tilde{y}_i	= molar fraction of component i in the gas phase
\tilde{x}_i	= molar fraction of component i in the liquid phase
$p_i, p_i^*(T)$	= partial pressure, saturation pressure of component i in the gas phase
p	= total pressure of the gas phase
γ_i	= activity coefficient of component i

The saturation pressure at temperature T, $p_i^*(T)$, is obtained from *Antoine's* equation (compare Appendix VIII). The activity coefficient γ_i can be expressed with the help of *Gibb's* excess enthalpie G^E :

$$\ln \gamma_i = \frac{1}{\tilde{R}T} \left(\frac{\partial G^E}{\partial n_i} \right)_{T,p,n_{j \neq i}} \quad \text{Equ. IX- 16}$$

with:

\tilde{R}	= ideal gas constant
T	= temperature in Kelvin
G^E	= <i>Gibb's</i> excess enthalpy
n_i	= moles of component i

The *Gibb's* excess enthalpy is derived from:

$$G^E = H^E - T \cdot S^E \quad \text{Equ. IX- 17}$$

with:

H^E	= excess enthalpy
S^E	= excess entropy

From statistical considerations, *Flory* (1941) derived an expression for the excess entropy S^E and gives an equation for the excess enthalpy H^E of multi-component systems (*Flory* (1953)). Intermolecular forces are taken into account by binary interaction parameters χ_{ij} :

$$S^E = -\tilde{R} \sum n_i \ln \frac{\phi_i}{\tilde{x}_i} \quad \text{Equ. IX- 18}$$

$$H^E = \tilde{R}T \sum_{i < j} n_i \varphi_i \chi_{ij} \quad \text{Equ. IX- 19}$$

with:

$$\begin{aligned} \varphi_i &= \text{volume fraction of component } i \\ \tilde{x}_i &= \text{molar fraction of component } i \\ \chi_{ij} &= \text{Flory-Huggins interaction parameter, which expresses the compatibility of} \\ &\quad \text{penetrant and polymer} \end{aligned}$$

The binary interaction parameter can be expressed by:

$$\chi_{ij} = \chi_{ji} \frac{\tilde{V}_i}{\tilde{V}_p} \quad \text{Equ. IX- 20}$$

with:

$$\tilde{V}_i, \tilde{V}_p = \text{partial molar volume of component } i, \text{ polymer } p$$

For the binary system water (1) – polymer (p), Equ. IX- 17 to Equ. IX- 19 give:

$$\frac{G^E}{\tilde{R}T} = n_1 \varphi_p \chi_{1p} + n_1 \ln \frac{\varphi_1}{\tilde{x}_1} + n_p \ln \frac{\varphi_p}{\tilde{x}_p} \quad \text{Equ. IX- 21}$$

The water activity a_1 is defined by:

$$a_1 = \gamma_1 \cdot \tilde{x}_1 \quad \text{Equ. IX- 22}$$

With Equ. IX- 21, the following expression for a_1 is derived, assuming that $\tilde{V}_1 \ll \tilde{V}_p$:

$$\ln a_1 = \ln \varphi_1 + (1 - \varphi_1) + \chi_{12} (1 - \varphi_1)^2 \quad \text{Equ. IX- 23}$$

3) Water Sorption: Fitting Parameters

	$a_w = \left(\frac{X}{A}\right)^B$ $a_i < 0.2$		$a_w = \frac{1}{\exp\left[\left(\frac{C}{X}\right)^D\right]}$ $a_i > 0.2$	
	A	B	C	D
A-S-1	GAB	GAB	GAB	GAB
A-H-1	0.0325	2.17	0.01725	5.00
AS-H-1a	0.0445	2.17	0.02325	2.86
AS-H-1b	0.0285	2.17	0.01525	5.00
AS-S-1	0.0285	2.17	0.01525	5.00
A-S-2	0.0275	2.17	0.01425	5.00
PU-disp.	-	2.17	-	2.00

Table AVII- 1: A survey of the fitting parameters to describe the sorption isotherms of the different dispersions (to be used in the mathematical model)

Appendix X Saturated Salt Solutions

Conditions of defined water activity in the gasphase can be adjusted above saturated solutions of different salts. The figure below shows a sketch of a sealed box containing a saturated salt solution and polymer films in contact with the gasphase of defined water activity a_w . Such an experimental setup was used to obtain the sorption isotherms from regular gravimetric measurements of the polymer film being in equilibrium with the defined gasphase in the boxes.

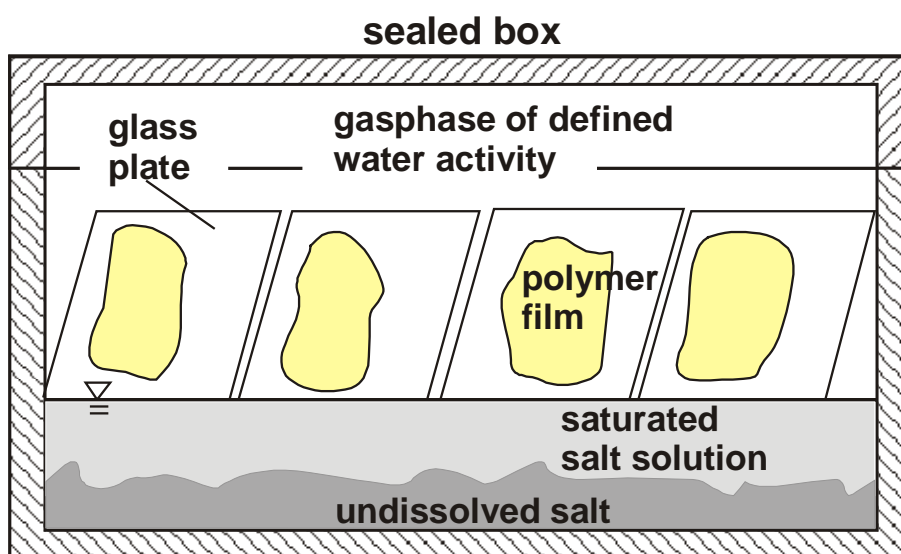


Figure AX- 1: The setup to assure equilibrium between the gasphase of defined water activity a_w and the polymer film

Below is a summary of the salts that were used in this work for the experimental investigation of the sorption equilibria of latex films of different age.

<i>saturated salt solution</i>		<i>relative humidity</i> φ [%]
K₂CO₃	potassium carbonate	43.2
K₂SO₄	potassium sulfate	97.0
KCl	potassium chloride	83.6
KOH	potassium hydroxide	7.4
Mg(NO₃)₂	magnesium nitrate	51.4
MgCl₂	magnesium chloride	32.4
NaNO₃	sodium nitrate	73.1

Table X- 1: The relative humidity above saturated salt solutions at $T = 30$ °C, used to measure sorption isotherms (Greenspan, 1977)

Appendix XI Diffusion Coefficients in Latex Films

The table gives a summary of the initial diffusion coefficients $\delta_{w,p}$, where obtained from a comparison of the experimental data of the different drying, 2-film-, redispersion and water permeation experiments with model calculations. The number of the respective experiment as well as the kind of the dispersion are listed.

A typical initial value of the diffusion coefficient of water in the film during drying is $\delta_{w,p} = 1.95 \cdot 10^{-10} \text{ m}^2/\text{s}$. Water diffusion after the irreversible contact of the latex particles is considerably slower, indicated by a diffusion coefficient which is $\delta_{w,p} \sim 1.8 \cdot 10^{-11} \text{ m}^2/\text{s}$. Depending on whether the network of hydrophilic surface material along the particle interfaces remains intact or not, there is a further decrease in the mobility of water in the coating. When polymer inderdiffusion has resulted in complete coalescence, a typical value of the diffusion coefficient for water in the polymer film is $\delta_{w,p} \sim 4 \cdot 10^{-13} \text{ m}^2/\text{s}$.

<i>experiment</i>	<i>dispersion</i>	$\delta_{w,p} [\text{m}^2/\text{s}]$	
film drying (1 layer)	<i>AS-H-1b</i>	$1.95 \cdot 10^{-10}$	Fig. 7-29
horizontal concentration profiles (1 layer)	<i>A-H-1</i>	$1.94 \cdot 10^{-10}$	Fig. 7-39 Fig. 7-40
horizontal concentration profiles (1 layer)	<i>AS-H-1b</i>	$1.92 \cdot 10^{-10}$	Fig. 7-41 Fig. 7-42
redispersion (before irreversible contact)	<i>AS-H-1b</i>	$1.95 \cdot 10^{-10}$ (drying) $2.58 \cdot 10^{-11}$ (redispersion)	Fig. 7-48
redispersion (after irreversible contact)	<i>AS-H-1b</i>	$2.18 \cdot 10^{-10}$ (drying) $1.14 \cdot 10^{-10}$ (redispersion)	Fig. 7-49
2-film-experiment (before irreversible contact)	<i>AS-H-1b</i>	$1.97 \cdot 10^{-10}$ (drying) $1.83 \cdot 10^{-10}$ (redispersion)	Fig. 7-51
2-film-experiment (after irreversible contact)	<i>AS-H-1b</i>	$1.97 \cdot 10^{-10}$ (drying) $1.79 \cdot 10^{-11}$ (redispersion)	Fig. 7-52
water permeation (1-day-old film)	<i>A-S-1</i>	$3.72 \cdot 10^{-13}$	Fig. 7-54
water permeation (1-week-old film)	<i>A-S-1</i>	$4.65 \cdot 10^{-13}$	Fig. 7-54
water permeation (1 h at T = 150 °C)	<i>A-H-1</i>	$1.71 \cdot 10^{-12}$	Fig. 7-55
water permeation (1 h at T = 150 °C)	<i>AS-H-1b</i>	$6.19 \cdot 10^{-12}$	Fig. 7-55

<i>experiment</i>	<i>dispersion</i>	$\delta_{w,p}$ [m^2/s]	
film drying (1 layer)	<i>AS-H-1a</i> + <i>pigments</i>	$3.36 \cdot 10^{-10}$	Fig. 7-57
water permeation (1-day-old film)	<i>AS-H-1a</i> + <i>pigments</i>	$4.70 \cdot 10^{-12}$	Fig. 7-58
water permeation (1-day-old film)	<i>AS-H-1b</i> (15% <i>Tex</i>)	$6.19 \cdot 10^{-12}$	Fig. 7-62
2-film-experiment (before irreversible contact)	<i>AS-H-1b</i> (<i>pure</i>)	$1.94 \cdot 10^{-10}$ (drying) $1.85 \cdot 10^{-10}$ (redispersion)	Fig. 7-63
2-film-experiment (before irreversible contact)	<i>AS-H-1b</i> (2 nd film: 18% <i>Tex</i>)	$1.94 \cdot 10^{-10}$ (drying) $1.77 \cdot 10^{-10}$ (redispersion)	Fig. 7-64
2-film-experiment (before irreversible contact)	<i>AS-H-1b</i> (1 st film: 18% <i>Tex</i>)	$1.94 \cdot 10^{-10}$ (drying) $1.83 \cdot 10^{-10}$ (redispersion)	Fig. 7-65
2-film-experiment (before irreversible contact)	<i>AS-H-1b</i> (2 films: 18% <i>Tex</i>)	$1.94 \cdot 10^{-10}$ (drying) $1.81 \cdot 10^{-10}$ (redispersion)	Fig. 7-66
water permeation (1-day-old film)	<i>AS-H-1b</i> (15% <i>Tex</i>)	$1.04 \cdot 10^{-12}$	Fig. 7-68
film drying (1 layer)	<i>PU-emulsion</i>	$1.94 \cdot 10^{-10}$	Fig. 7-70
water permeation (1-day-old film)	<i>PU-emulsion</i>	$5.22 \cdot 10^{-14}$	Fig. 7-77

Table XI- 1: A summary of the diffusion coefficients of the different experiments of film drying and film formation

Appendix XII Influence of Different Drying Parameters

The conditions under which many exterior and interior wall paints or varnishes are used are normally ambient and cannot be easily changed. The relative air humidity can be subject to changes, depending on the climate, the season or the weather conditions. Its value can range between $\sim 30\%$ at dry conditions and up to 100% at rain. Inside heated buildings, the air humidity can be very low, but can increase drastically when paint is applied in rooms where the windows are closed. Typically, the temperature range for painting is between 10 and 40 °C, depending on the country, the season and on interior or exterior use. The air movement along the painted walls is generally gentle; it is higher for exterior applications or could be enforced by ventilation. Typical values are between free convection and up to ~ 1 m/s.

A higher air humidity φ increases the partial water pressure in the surrounding drying air. This reduces the gasside concentration gradient that drives water evaporation and results in longer drying times. Increased air humidity has no influence on the gasside mass transfer coefficient $\beta_{w,g}$.

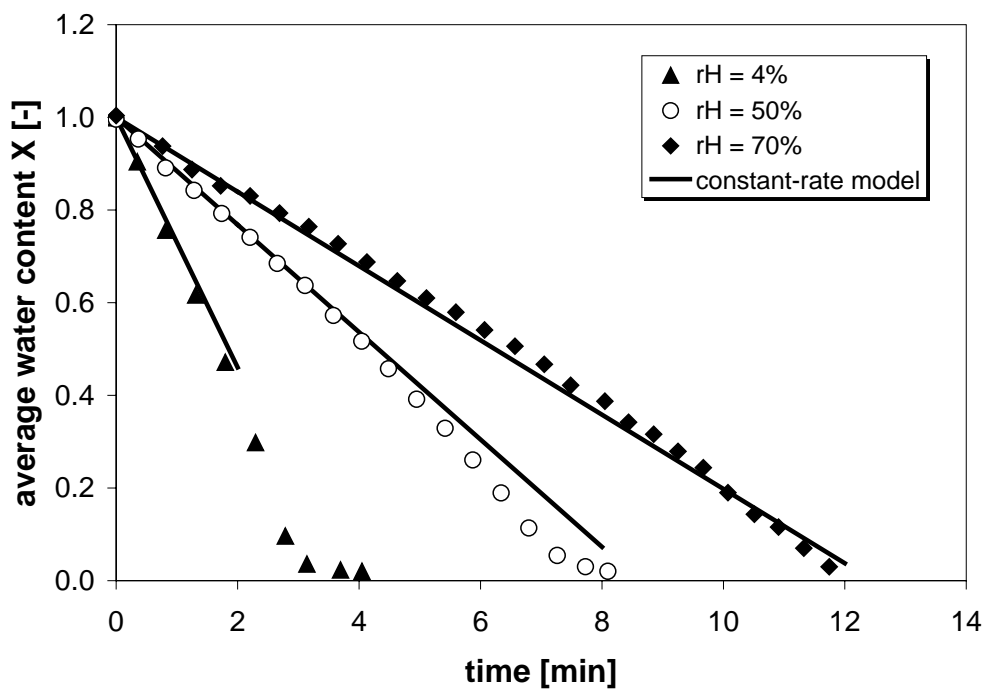


Figure XII- 1: Influence of the relative air humidity φ on the drying curve of AS-H-1b ($X_0 = 1.0$ g water/g pol.; $T = 25$ °C; $u = 0.05$ m/s; $\varphi = 4\%$)

The drying temperature is an important parameter. Generally, the maximum allowed temperature depends on the product characteristics, its temperature sensitivity and the solvent's vapour pressure. In the case of water-based systems, film temperatures above $T = 100$ °C could lead to the formation of bubbles in the film as a result of boiling water and in addition could damage or destroy the latex film. Interior and exterior paints are normally applied at ambient temperatures between 10 – 40 °C; therefore the influence of much higher temperatures on drying is not investigated in this work. High

temperatures increase the drying rate due to the exponential dependence of the water partial pressure on temperature; the mass transfer coefficient $\beta_{w,g}$ is only slightly dependent on T . A larger difference between the drying temperature T and the polymer glass transition temperature $T_g < T$ allows an easier deformation of the polymer particles.

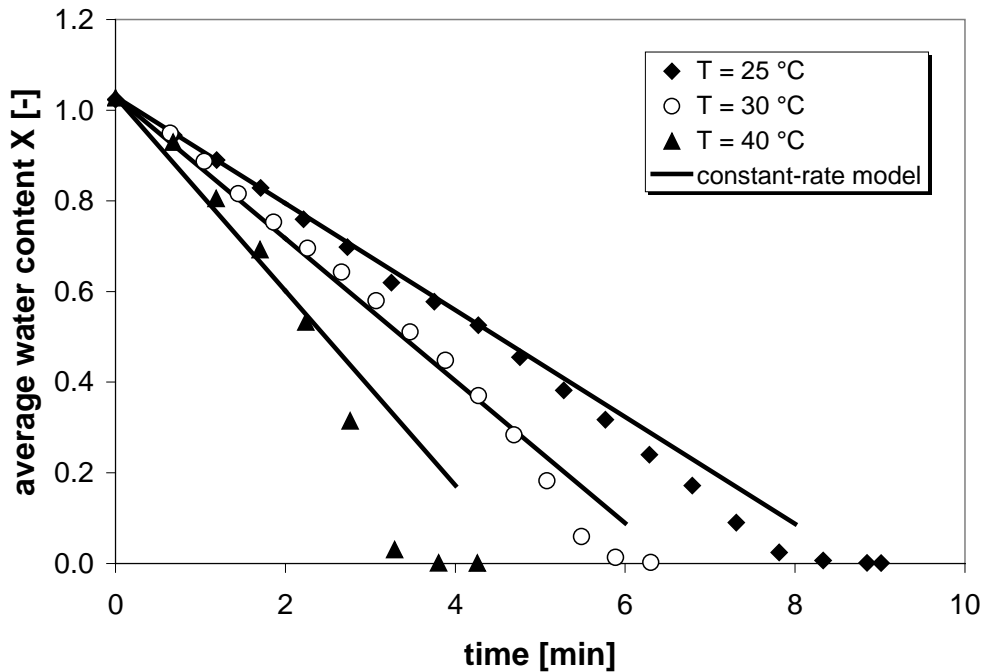


Figure XII- 2: Influence of the drying temperature on the drying curve of A-H-1 ($X_0 = 1.0$ g water/g pol.; $\varphi = 50\%$; $u = 0.05$ m/s)

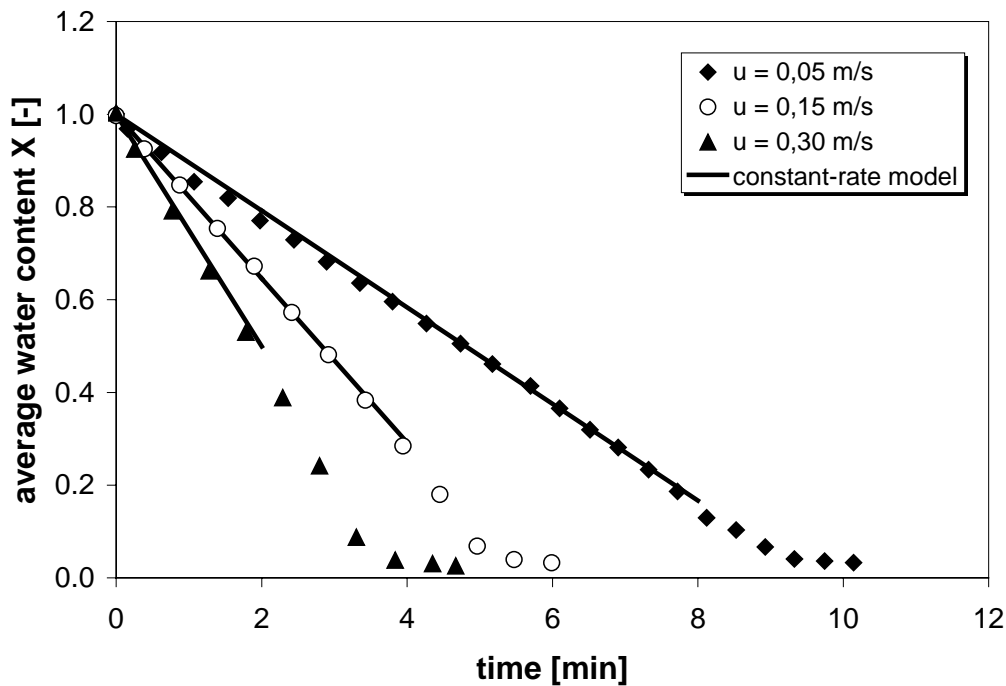


Figure XII- 3: Influence of the air velocity u on the drying curve of AS-H-1b. ($X_0 = 1.0$ g water/g pol.; $T = 25$ °C; $\varphi = 50\%$)

The gasside mass transfer coefficient $\beta_{w,g}$ can be influenced by the air flow rate and the constructive realization of flow above the film, e.g. approaching flow or air foil. Depending on the given application conditions, the air flow rate is only partially adjustable. In industrial driers, high air velocities can be a problem, since high pressure differences and shear forces can deform and damage the coating surface. Generally, an increase of the air velocity u leads to a higher gasside mass transfer coefficient $\beta_{w,g}$ which results in a higher drying rate.

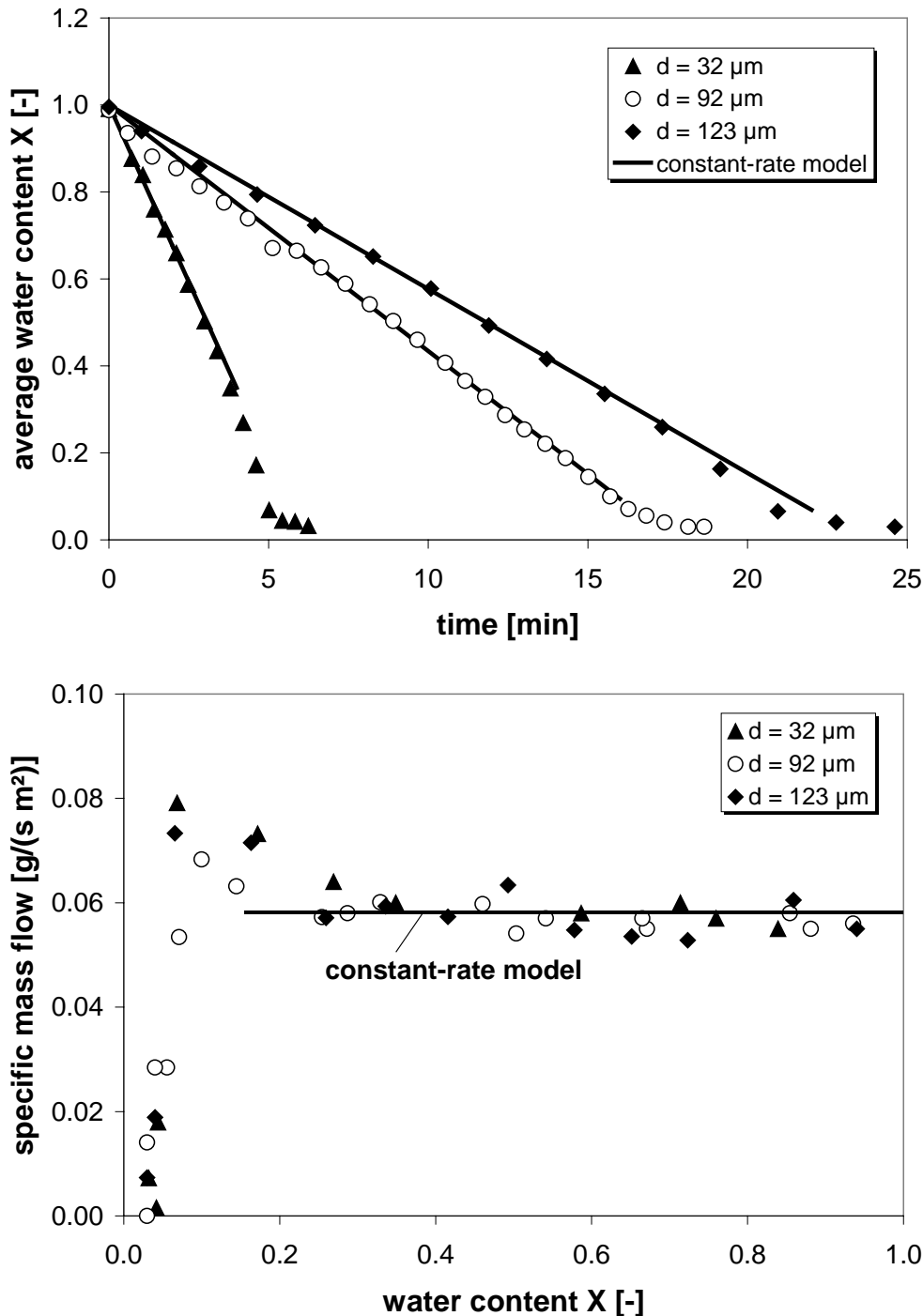


Figure XII- 4: Top: Influence of the initial film thickness on drying of AS-H-1b. Bottom: The specific mass flow of water from the film. ($X_0 = 1.0 \text{ g water/g pol.}$; $T = 25 \text{ }^\circ\text{C}$; $u = 0.05 \text{ m/s}$; $\varphi = 50\%$)

The application of paints by brushing produces film layers of different film thickness, whereas an application by spraying or rolling will give more homogeneous coatings. Therefore, it is important to know the influence of the film thickness on drying, although the thickness cannot be influenced or changed in many application. Since the phase equilibrium and also the gasside mass transfer coefficient $\beta_{w,g}$ are independent of the film thickness, water evaporation in the constant rate period is independent of the initial film thickness.

Appendix XIII Viscosity Models

		<i>A-S-1</i>	<i>A-H-1</i>	<i>AS-H-1a</i>	<i>AS-H-1b</i>	<i>AS-S-1</i>	<i>A-S-2</i>
Einstein $\eta = \eta_0 \left(1 + \frac{5}{2} \phi\right)$	η_0	0.005	0.002	10	0.012	0.002	0.002
	$[\eta]$	2.5	2.5	2.5	2.5	2.5	2.5
Doolittle $\eta = C \exp(b\phi)$	C	0.005	0.002	10	0.012	0.002	0.002
	b	4	5	5	5	5	6
Krieger-Dougherty (modified) $\eta = \eta_0 \left[1 - \frac{p \cdot \phi}{\phi_m}\right]^{-[\eta]\phi_m}$	η_0	0.005	0.002	10	0.012	0.002	0.002
	$[\eta]$	2.5	2.5	2.5	2.5	2.5	2.5
	p	1.31	1.37	1.44	1.45	1.365	1.783
	ϕ_m	0.74	0.74	0.74	0.74	0.74	0.74
Quemada $\eta = \eta_0 \left[1 - \frac{\phi}{\phi_m}\right]^{-2}$	η_0	0.005	0.002	10	0.012	0.002	0.002
	ϕ_m	0.57	0.54	0.513	0.51	0.54	0.415
Percolation $\eta = k(\phi_c - \phi)^{-s}$	ϕ_c	0.57	0.54	0.513	0.51	0.54	0.415
	k	0.0016	0.0006	3.2	0.0035	0.0007	0.0005
	s	2	2	1.8	1.8	1.7	1.8
Mooney $\eta = \eta_0 \exp\left(\frac{A \cdot \phi}{1 - k \cdot \phi}\right)$	η_0	0.005	0.003	10	0.012	0.002	0.002
	A	0.82	1.3	1.3	1.6	0.6	1.9
	k	1.72	1.77	1.88	1.84	1.82	2.3

Table XIII- 1: An overview of the different viscosity models and the parameters used. The best model to fit each dispersion is highlighted in bold letters

Appendix XIV Characteristic Raman Peaks

1) Saturated Hydrocarbons (s = strong; m = medium; w = weak)

$\nu(-\text{CH}_2-)$,	2925, 2850 (s)
$\nu(-\text{CH}_3)$	2960, 2870 (s)
$\nu(\text{C-H})$	2890 – 2880 (w)
$\delta(-\text{CH}_3)$	1390 – 1370 (m)
$\delta(-\text{CH}_2-)$	720 (w)
$\delta(\text{C-H})$	1470 – 1400 (m)
$-\text{C}(\text{CH}_3)_3$	1885 – 1395 (m) 1365 (s)
$>\text{C}(-\text{CH}_3)_2$	~1380 (m)

2) Olefins (s = strong; m = medium; w = weak)

aryl-H	3040 – 3010 (w)
$\nu(\text{C}=\text{C})$	1900 – 1500 (s-m)
$\begin{array}{c} \diagup \\ \text{C}=\text{C} \\ \diagdown \end{array} \text{H}$	3040 – 3010 (m) 1425 - 1375
$\begin{array}{c} \diagup \\ \text{C}=\text{C} \\ \diagdown \end{array} \begin{array}{c} \text{H} \\ \text{H} \end{array}$	3095 – 3075 (m)
$\begin{array}{c} \text{R} \\ \diagdown \\ \text{C}=\text{C} \\ \diagup \\ \text{H} \end{array} \begin{array}{c} \text{H} \\ \text{H} \end{array}$	995 – 985 (s) 940 – 900 (s)
$\begin{array}{c} \text{R} \\ \diagdown \\ \text{C}=\text{C} \\ \diagup \\ \text{H} \end{array} \begin{array}{c} \text{H} \\ \text{R} \end{array}$	970 – 960 (s)
$\begin{array}{c} \text{R} \\ \diagdown \\ \text{C}=\text{C} \\ \diagup \\ \text{R} \end{array} \begin{array}{c} \text{H} \\ \text{H} \end{array}$	895 – 885 (s)
$\begin{array}{c} \text{R} \\ \diagdown \\ \text{C}=\text{C} \\ \diagup \\ \text{R} \end{array} \begin{array}{c} \text{H} \\ \text{R} \end{array}$	840 – 790 (m)
$\begin{array}{c} \text{H} \\ \diagdown \\ \text{C}=\text{C} \\ \diagup \\ \text{R} \end{array} \begin{array}{c} \text{H} \\ \text{R} \end{array}$	730 – 675 (m)

3) Hydroxy Groups (s = strong; m = medium; w = weak)

$\nu(\text{O-H})$	3600 – 3200 (b)	alcohol, phenol
$\nu(\text{O-H})$	3200 - 2400	carboxylic acid
hydrogen bonds	3570 - 3200	
$\begin{array}{c} \diagup \\ \text{C}-\text{OH} \end{array}$	1150 - 1040 (s)	

4) Amines, Amids, Ammonium Salts and Mercaptans (b = broad)

$\nu(-\text{NH})$	3550 - 3350 (<i>b</i>)	<i>amines</i>
$-\text{NH}_3^+$	3130 - 3030 (<i>m</i>) 1600 (<i>s</i>) 1500 (<i>s</i>)	<i>ammonium salts</i>
$\delta(-\text{NH}_2)$	1650 - 1560 (<i>m</i>)	<i>amids</i>
$\delta(-\text{NH})$	1580 - 1490 (<i>w</i>)	<i>prim. and second. amines</i>
$\nu(-\text{SH})$	2600 - 2550 (<i>w</i>)	<i>mercaptans</i>

5) Carbonyl Groups (sat. = saturated; aryl = aryl)

$\nu(-\text{N}=\text{C}=\text{O})$	2275 - 2250 (<i>s</i>)	<i>isocyanates</i>
$\nu(\text{C}=\text{N})$	1680 - 1610 (<i>s</i>)	
$\begin{array}{c} \text{O} \\ \parallel \\ -\text{C} \\ \diagdown \\ \text{O}- \end{array}$	1750 - 1735 (<i>sat.</i>) 1750 - 1730 (<i>aryl</i>)	<i>carboxylic ester</i>
$\nu(-\text{CHO})$	1740 - 1720 (<i>sat.</i>) 1715 - 1695 (<i>aryl</i>)	<i>aldehyde</i>
$\begin{array}{c} \text{H} \\ \diagup \\ -\text{C} \\ \parallel \\ \text{O} \end{array}$	2900 - 2700 (<i>w</i>) (2 peaks, one close to 2720 cm^{-1})	<i>aldehydes</i>
$\nu(\text{C}=\text{O})$	1725 - 1705 (<i>sat.</i>) 1700 - 1680 (<i>aryl</i>)	<i>carbonyl compounds</i>
$-\text{O}-\text{CO}-\text{CH}_3$	1385 - 1365 (<i>s</i>)	<i>ether</i>
$-\text{CO}-\text{CH}_3$	1360 - 1355 (<i>s</i>)	
$\nu(\text{COOH})$	1725 - 1700 (<i>sat.</i>)	<i>carboxylic acid</i>
$\nu(\text{COO}^-)$	1610 - 1550 1420 - 1300	<i>carboxylate ions</i>
$\begin{array}{c} \text{O} \\ \parallel \\ \text{P} \\ \diagdown \\ \text{OH} \end{array}$	2700 - 2560 (<i>m</i>) 1240 - 1180 (<i>s</i>)	<i>phosphoric acid</i>

6) Carbon-Carbon Double-Bonds in Aromatic Molecules

$\nu(\text{C}=\text{C})$	1680 - 1620 (<i>w</i>)	<i>olefines</i>
$\begin{array}{c} \diagdown \text{C}=\text{C} \diagup \\ \quad \quad \quad \text{C}_6\text{H}_5 \end{array}$	~ 1625 (<i>m</i>)	<i>aromatic olefines</i>

$\nu(\text{C}=\text{C})$	~1600 (s) ~1580 (s) ~1500 (m) ~1000 (s)	aromatic ring
mono-substituted	770 - 730 (s) 720 - 680 (s)	aromatic ring (fingerprint)

7) Ether Groups

$\nu(\text{C}-\text{O}-\text{C})$	1150 - 1070 (w) 970 - 800 (m)	ether, ester
$\text{C}-\text{O}-\text{C}=\text{C}$	1275 - 1200 (s) 1075 - 1020 (s)	ether with carboxylic group
$\text{C}-\text{O}-\text{CH}_3$	2850 - 1885 (m)	ether
$-\text{O}-\text{CO}-\text{CH}_3$	1385 - 1365 (s)	ether

8) Bonds with Sulfur, Nitrate and Phosphate

$\nu(\text{C}-\text{F})$	1400 - 1000 780 - 680	
$\nu(\text{S}=\text{O})$	1060 - 1040 (s)	sulfoxides
$\nu(\text{SO}_2)$	1350 - 1310 (s) 1160 - 1120 (s)	compounds with sulfonyl groups
$\nu(-\text{SO}_2-\text{O})$	1420 - 1330 (s) 1200 - 1145 (s)	sulfonates
P-O-alkyl	1050 - 1030 (s)	
P-O-aryl	1240 - 1190 (s)	
$\nu(\text{P}=\text{O})$	1300 - 1250 (s)	
$\nu(\text{SO}_4^{2-})$	1130 - 1080	sulfates
$\nu(\text{NO}_3^-)$	1380 - 1350	nitrates
$\nu(\text{PO}_4^{3-})$	1100 - 1000	phosphates



Institut für Thermische Verfahrenstechnik
Universität Karlsruhe (TH)

ISBN: 978-3-86644-284-9

www.uvka.de

